Załącznik nr 1/1
do Zarządzenia Rektora PG nr 5/2015 z 10 lutego 2015 r.

GDAŃSK UNIVERSITY OF TECHNOLOGY
Faculty of Mechanical Engineering
and Ship Technology

WIMiO

The author of the PhD dissertation: Hanna Pruszko
Scientific discipline: mechanical engineering

DOCTORAL DISSERTATION

Title of PhD dissertation: Hydroelastic properties of the sailing fin – influence of the stiffness distribution on the hydrodynamic forces

Title of PhD dissertation (in Polish): Właściwości hydroelastyczne stateczników – wpływ rozkładu sztywności na siły hydrodynamiczne

Supervisor *signature*	Second supervisor *signature*
Dr hab. inż Tomasz Mikulski	-
Auxiliary supervisor *signature*	Cosupervisor *signature*
Dr inż. Maciej Reichel	-

Gdańsk, year 2024

Page intentionally left blank.

MOST WIEDZY Downloaded from mostwiedzy.pl

STATEMENT

The author of the PhD dissertation: Hanna Pruszko

I, the undersigned, agree/do not agree* that my PhD dissertation entitled: Hydroelastic properties of the sailing fin – influence of the stiffness distribution on the hydrodynamic forces may be used for scientific or didactic purposes.11

Gdańsk,..... .....

signature of the PhD student

Aware of criminal liability for violations of the Act of 4th February 1994 on Copyright and Related Rights (Journal of Laws 2006, No. 90, item 631) and disciplinary actions set out in the Law on Higher Education (Journal of Laws 2012, item 572 with later amendments),22as well as civil liability, I declare, that the submitted PhD dissertation is my own work.

I declare, that the submitted PhD dissertation is my own work performed under and in cooperation with the supervision of Tomasz Mikulski and the auxiliary supervision of Maciej Reichel

This submitted PhD dissertation has never before been the basis of an official procedure associated with the awarding of a PhD degree.

All the information contained in the above thesis which is derived from written and electronic sources is documented in a list of relevant literature in accordance with art. 34 of the Copyright and Related Rights Act.

I confirm that this PhD dissertation is identical to the attached electronic version.

Gdańsk,..... .....

signature of the PhD student

I, the undersigned, agree/do not agree* to include an electronic version of the above PhD dissertation in the open, institutional, digital repository of Gdańsk University of Technology, Pomeranian Digital Library, and for it to be submitted to the processes of verification and protection against misappropriation of authorship.

Gdańsk,..... .....

signature of the PhD student

*) delete where appropriate.

[1] Decree of Rector of Gdansk University of Technology No. 34/2009 of 9th November 2009, TUG archive instruction addendum No. 8.

[2] Act of 27th July 2005, Law on Higher Education: Chapter 7, Criminal responsibility of PhD students, Article 226.

MOST WIEDZY Downloaded from mostwiedzy.pl

Page intentionally left blank.

MOST WIEDZY Downloaded from mostwiedzy.pl

DESCRIPTION OF DOCTORAL DISSERTATION

The Author of the PhD dissertation: Hanna Pruszko

Title of PhD dissertation: Hydroelastic properties of the sailing fin – influence of the stiffness distribution on the hydrodynamic forces

Title of PhD dissertation in Polish: Właściwości hydroelastyczne stateczników – wpływ rozkładu sztywności na siły hydrodynamiczne

Language of PhD dissertation: English

Supervision: Dr hab. inż. Tomasz Mikulski, prof. PG

Auxiliary supervision*: Dr inż. Maciej Reichel

Date of doctoral defense:

Keywords of PhD dissertation in Polish: interakcja płyn-struktura, właściwości hydroelastyczne, analiza wrażliwości, analiza modalna, stateczniki windsurfingowe,

Keywords of PhD dissertation in English: Fluid-Structure Interaction, hydroelastic properties, sensitivity analysis, modal analysis, windsurfing fins

Summary of PhD dissertation in Polish: Niniejsza rozprawa dotyczy problemu wyznaczania sił hydromechanicznych generowanych przez odkształcalne stateczniki windsurfingowe. Badania przeprowadzono na przykładzie kompozytowej płetwy windsurfingowej dla monotypowej klasy RS:X. Pomimo założenia ich identyczności, codzienna praktyka pokazała, że występują różnice we właściwościach hydrodynamicznych i mechanicznych, wpływające na ich osiągi. Niniejsza rozprawa koncentruje się na określeniu różnic między sztywnością płetw windsurfingowych i ilościowym określeniu wynikających z tego różnic w ich charakterystykach hydrodynamicznych. Badanie zostało przeprowadzone głównie przy użyciu metod obliczeniowych wspartych badaniami eksperymentalnymi. Po pierwsze, analiza wrażliwości pierwszego rzędu została wykorzystana do określenia rozkładu sztywności wszystkich analizowanych płetw ze względu na nieznaną strukturę wewnętrzną kompozytu. Następnie utworzono i zweryfikowano zastępczy model RS:X wykorzystując Metodę Elementów Skończonych. Następnie przeprowadzono sprężone obliczenia interakcji płyn-struktura (FSI). Obliczenia FSI miały na celu znalezienie siły nośnej i oporu generowanych przez wszystkie analizowane stateczniki o różnych rozkładach sztywności oraz dla quasi-statycznej deformacji konstrukcji. Obliczenia przeprowadzono dla szerokiego zakresu prędkości i kątów natarcia. Wyniki obliczeń uzyskane dla elastycznych płetw porównano z nieodkształcalnym statecznikiem. Stwierdzono, że płetwy RS:X ulegają wyraźnym deformacją, co ma znaczący wpływ na zmniejszenie ich siły oporu i siły nośnej.

Summary of PhD dissertation in English: This thesis addresses the problem of determining the hydromechanical forces generated by flexible hydrofoils considering their deformation. The research was done on the example of the composite windsurfing fin for the RS:X monotype class. Despite the assumption of their identity, the everyday practice showed that the variations in the hydrodynamic and mechanical properties occur, affecting their performance. This thesis focuses on the determination of differences between the windsurfing fins stiffness and quantify resulting variations in their hydrodynamic characteristics. The study was done using mainly computational methods supported by the experimental investigation. Firstly, the first order sensitivity analysis was used to determine the stiffness distribution of all analysed fins due to unknown internal structure of composite. Then, the substitute Finite Element Method model of the RS:X was created and validated. Further, two-way Fluid-Structure Interaction (FSI) calculations were performed using co-simulation approach. The coupled FSI calculations aimed to find lift and drag forces generated by all analysed fins with various stiffness distributions and for the quasi-static deformation of the structure. The calculations were performed for wide range of speeds and angles of attack. The results of the calculations obtained for flexible fins were compared to the

MOST WIEDZY Downloaded from mostwiedzy.pl

rigid hydrofoil. It was found that RS:X fins can deform significantly, and it has significant impact on the reduction of the drag and lift force.

MOST WIEDZY Downloaded from mostwiedzy.pl

ACKNOWLEDGEMENTS

It is said that it takes the whole village to raise a child. Similarly, this dissertation would not have been completed without the great support of many people. First and foremost, I would like to express my deep gratitude to my supervisor, Professor Tomasz Mikulski, for his scientific guidance and the many hours he spent discussing and explaining, and to my assistant supervisor, Doctor Maciej Reichel, who always gave me his full support. Furthermore, I would like to thank my first formal supervisor Professor Wojciech Litwin, who made it possible for me to start my PhD studies in 2018, and Professor Paweł Flaszyński for his support in the early stages of my research.

I would like to thank Professor Przemysław Krata and Doctor Krzysztof Wołoszyk for the time they spent on the internal review and for their contribution to the final shape and form of my thesis. I owe them also gratitude for valuable scientific discussions and supporting in difficult moments of doubts.

I would like to acknowledge the work of Zbigniew Macikowski, who made the fairing and greatly improved the final 3D model of the fin, and my brother Piotr Pruszko, who helped me prepare the experimental setup. Moreover, I want to thank Mirosław Grygorowicz that the doors to lab and workshop were always wide open for me. I would also like to thank Professor Jerzy Matusiak from Aalto University for sharing with me his programme for lifting line calculations and useful tips for my research.

I want to thank colleagues in my department: Ewelina Ciba, Olga Kazimierska, Paweł Dymarski and Michał Krężelewski, and my colleagues from Department of Marine Structural Engineering: Alicja Bera, Beata Zima, Paweł Bielski, Karol Niklas, Jakub Kowalski and Leszek Samson for their willingness to discuss, help and for their everyday kindness that encouraged me to work.

I would also like to thank the Polish Sailing Association for providing me with the experimental results and RS:X windsurfing fins for testing, and the Comonet company, especially Jerzy Dzierżko, for providing me with the measuring set used in my research.

I would like to express my sincere thanks to CI TASK for allowing me to perform multiprocessor calculations, which greatly accelerated the implementation of the following thesis.

Finally, I would like to thank my boyfriend Finn, my parents, and my best friend Agata, because I have never heard from you that science and engineering are not for women. Instead, I have only heard words of love and support from you, which I really appreciate.

MOST WIEDZY Downloaded from mostwiedzy.pl

Page intentionally left blank.

MOST WIEDZY Downloaded from mostwiedzy.pl

TABLE OF CONTENTS

MOST WIEDZY Downloaded from mostwiedzy.pl

MOST WIEDZY Downloaded from mostwiedzy.pl

1. INTRODUCTION

1.1. Background and motivation

The rapid development of composite materials has resulted in their application in a wide range of engineering structures. The advantages are low mass, high strength related to weight ratio, corrosion resistance, and design flexibility (Navagally 2017). Another feature of the composites is the fact that the type and quality of each component of the laminate, as well as the lamination schedule and manufacturing methods can influence the mechanical properties of the composite structure to a very large extent. This means that the has a significant freedom in selection of the final mechanical properties of the structure, suitable for particular object to be designed. Those undeniable advantages are the reason why composite materials finds an application in variety of engineering constructions. Apart from aerospace and wind turbine industries, composites are widely used in civil engineering applications, for example, the construction of pedestrian bridges (Ferenc and Mikulski 2020b; 2020a; Chróścielewski et al. 2019).

On the other hand, composite material has some disadvantages. One of them is the fact that the process of production can be complicated and significant dependence of the final mechanical properties on the manufacturing conditions is observed. This has one practical implication - in mass production it is difficult to maintain the quality of the laminate and ensure the repeatability of the properties of the composite product. Moreover, during the production process different random factors occurs and as a result the final product will differ from the idealised design.

Nevertheless, the fact that the use of laminate allows tailoring of material properties to the required level found more applications: in widely understood marine industry. Among others, composites are used for production of rigid sail, propellers, and hydrofoil. Those objects have one more thing in common. The principle of their operation is based on the fundamental law of physics which determines the generation of lifting force by the objects with the shape similar to wing section.

The direct consequence of the advantages offered by the composite material is the fact that the performance of the composite hydrofoil can be tailored to the required level. Therefore, the known benefits explain why this material plays such a key role in high performance sailing, for example, as with hydrofoil manufacturing. The application of composite hydrofoils for racing yachts, windsurfing, kitesurfing, and surfing has increased greatly over the years together with the development of composite material. Good example here is application of composite for production of the daggerboards and fins for RS:X Olympic class.

The very best of sportsmen participate in this kind of competition and every smallest detail can have an impact on the final result. The sailing equipment is part of complicated puzzle that need to perform at the level as high as the windsurfer. The RS:X is a monotype class. This means that all pieces of equipment are supposed to be the same to minimise its influence on the final result of the regatta and to let the best windsurfer win. In case of RS:X class, in order to ensure

MOST WIEDZY Downloaded from mostwiedzy.pl

this, all fins have been produced by a single manufacturer. Surprisingly, sailors reported that the performance of the RS:X fins could be very different, according to their feeling and comparison to other competitors. It was noticed that significant differences between the stiffness of the hydrofoils occur, and that fins deform under water.

Composites tend to have a lower Young Modulus than metals commonly used for construction. This results in a greater susceptibility to deformation. It is of note that the water is approximately 800 times denser than the air. Therefore, at the high speeds typical of high-performance vessels, the composite hydrofoils can deform significantly under hydrodynamic loads, which was confirmed by windsurfers for RS:X fin.

The basic analysis of the forces generated by the hydrofoil (namely lift and drag being the effect of the pressure differences on the suction and pressure sides of the hydrofoil) assumes that the hydrofoil is a rigid body. This assumption may be true in numerous cases, like determination of the aluminium keel hydrodynamic forces for slow displacement yacht. However, for certain problems such approach can be hardly found valid. Therefore, the deformation of the hydrofoil and the interaction of the structure with the fluid cannot be neglected. In such cases, the techniques of Fluid-Structure Interaction (FSI) analysis must be employed to obtain a reliable information about the physics of the phenomena. With respect to the hydrofoils there are two groups of phenomena for which FSI analysis is relevant: dynamic instabilities and large deformations of the structure. The first problem was not considered in this thesis, while the latter is addressed herein.

For a flexible hydrofoil, the hydrodynamic loads and forces generated by the foil result in deformation of the lifting body. The changes in geometry result in a variation (usually a reduction) in the hydrodynamic forces generated by the hydrofoil. This leads to a further variation in deformation and forces. Eventually, both phenomena manifest by the coupled interaction to be considered together. This is a non-trivial Fluid-Structure Interaction problem, which will be studied for a composite windsurfing fin of the monotype RS:X class. The numerical and experimental methods are employed to generate appropriate representation of the fin shape and properties. The proposed models must allow to assess the deformation of the fin under hydrodynamic load, differentiate various fins and answer the question to which extent various mechanical properties of the composite fin can affect its hydrodynamic performance.

1.2. State of the art

This thesis addresses the problem of assessing the hydrostructural properties of composite windsurfing fins of the RS:X monotype class. It presents a multidisciplinary approach as it focuses on the coupling of hydromechanical and structural domains. Therefore, the topic and the state of the art are presented against the background of fluid-structure interaction work, with particular emphasis on flexible composite hydrofoils, both in terms of experimental testing and numerical modelling.

The problem of deformation of structures under fluid loads is well understood and described for aerodynamic problems. The phenomenon of vortex induced vibrations began to be

MOST WIEDZY Downloaded from mostwiedzy.pl

studied for bridges and buildings and its importance was to be painfully realised after the failure and collapse of the Tacoma Narrows Bridge (Amman, von Kármán, and Woodruff 1941). It is now common practice to take aerodynamic loads into account when designing bridges or skyscrapers.

It has also been found that deformation under aerodynamic loads plays an important role in aviation. The study of the problems of dynamic instability due to the flow of air around the wings of an aircraft, such as flatter, dates back to the twenties of the last century (Frazer 1929; Greene 1927) and continues to this day (Sinou 2022). There are also numerous studies on optimising the aeroelastic properties of wings taking into account their deformation (Kameyama and Fukunaga 2007; Maute and Allen 2004; Elham and Van Tooren 2016; Rajpal, Kassapoglou, and De Breuker).

A more recent engineering challenge related to the topic of fluid-structure interaction is the design of wind turbine blades. In this case, significant efforts have been made to obtain blades that passively reduce the load during high wind conditions. The tailoring of the composite materials to achieve this has been widely studied (Lackner and Rotea 2011; Hayat and Ha 2015; Capuzzi, Pirrera, and Weaver 2014; Ng et al. 2016; Mangano et al. 2022).

In principle, the most important influence on the mechanical properties of the composite material has the orientation of the fibres, while the influence of the number of plies and resin types is much smaller (Rahmani, Najafi, and Ashori 2014). The manufacturing process is another aspect that strongly influences the mechanical properties of the composite material and introduces uncertainties to the predictions of composite mechanical properties. According to Sun et al. (2018) the differences between tensile and flexural strength for composite specimens can reach up to 42.9% for various manufacturing processes. In addition, the differences in the curing process of the composite material introduce changes in mechanical properties (Zhang et al. 2014). With this in mind, the factors that influence the material properties of the composites can be pointed identified as follows:

- materials – type of resin and reinforcements (carbon, glass, etc.);
- stacking sequence – orientation of the layers, their number and thickness;
- manufacturing technology (prepreg, infusion, RTM);
- curing;
- factors of random nature – especially present in manufacturing methods that involves a significant amount of manual labour.

The idea of controlling the passive aeroelastic behaviour of airplane wings and turbine blades has also been applied to the design of tidal turbines and marine propellers (Herath et al. 2015; Liu and Young 2009; Taketani et al. 2013; Nicholls-Lee, Turnock, and Boyd 2013). It has been found that flexible propellers can delay cavitation inception and could perform better in off-design conditions.

The hydroelastic effects should be also considered when the hydrodynamic impact load on the ship structure is considered. It can play an important role when slamming effects are analysed - for example in the design of planning crafts (Volpi et al. 2016a; Volpi et al. 2016b),

MOST WIEDZY Downloaded from mostwiedzy.pl

catamarans, ships, and offshore structures (Faltinsen 2015; Faltinsen 2000; Hermundstad, Aarsnes, and Moan 1999).

The phenomenon of lift generation by hydrofoils has wide applications in marine propellers and tidal turbines, as mentioned above. It is also a fundamental operating principle of rudders and control surfaces for ships, and of appendages such as fins, daggerboards for yachts, and sails. The hydrodynamic behaviour of rudders and control surfaces is a crucial issue for the manoeuvrability of naval and commercial ships of any size; therefore, this topic is very well studied (Liu and Hekkenberg 2017, Reichel 2019). However, for the small sailboats, dinghies or racing vessels such as windsurfing boards, the research interest has been much lower over the years, especially if we consider the hydroelastic behaviour of rudders, daggerboards, fins, and hydrofoil struts. With the rapid development of modern materials and hull form designs, the high-performance crafts can reach significant speeds. The world of sailing is the witness of the technological race between sports powers that can be observed during America's Cup or Vendee Globe. Yachts can reach increasingly higher speed, and this is directly related to much higher hydrodynamic loads and the growing importance of considering hydro-structural effects. Therefore, the next chapter will focus on the state of the art of hydroelastic properties of hydrofoils in general and with particular interest in application to small, high-performance vessels.

Early work focusing on the hydrodynamic performance and hydroelastic properties of the windsurfing fin dates to nineties of the previous century. At that time, it was noticed that the fins deform under the fluid load, and it is important to study the results of the fin deformation on the hydrodynamic performance. The experimental determination of hydrodynamic characteristics of windsurfing fins with different planform shapes was carried out by Sutherland and Wilson (1994). However, the effect of structural deformation was not considered. The effect of the flexibility of sailboard fin has been investigated using photogrammetry (Chiu, Kalaugher, and Broers 1995). Seven different fins were tested in the circulation tunnel. Each of them had a different ratio of fibreglass to carbon reinforcement. It was found that the most desirable fin was the one that bends the least under normal sailing conditions. At the same time, fin twist should delay stall at high angles of attack. The bending and twisting mechanism described by the Chiu, Kalaugher, and Broers (1995) results from the fin sweep angle and the local centre of lift force in relation to section shear centre. Gourlay and Martellotta (2011) analysed the RS:X windsurfing board as a complete system and estimated the forces and moments acting on the board, sails, and appendages.

Experimental tests of hydrofoil deformation under hydrodynamic loads are performed in the wind or water circulation channels, and suitable measurement techniques have had to be developed for this purpose. One of the most popular techniques is Digital Image Correlation (DIC). This method has been demonstrated on a high-performance curved foil, from a NACRA F20 sailing catamaran (Banks et al. 2015). This technique, together with Particle Image Velocimetry, allows the fluid-structure interaction of the hydrofoil to be assessed experimentally. The results of the experiments performed on the NACRA 20 C-shaped hydrofoil were used to validate the CFD calculations with no deformation and with deformed hydrofoil shape (Marimon Giovannetti et al. 2015). The deformations applied to the hydrofoil were obtained directly from the experiments.

MOST WIEDZY Downloaded from mostwiedzy.pl

This technique was also successfully used to evaluate the fluid loads on the flexible NACA0015 rectangular planform aerofoil, with a span of 0.9 m and an aspect ratio of two (Marimon Giovannetti et al. 2017a).

In many studies, there has been a strong focus on evaluating the problem of the relation between the lay-up of the composite material and its deformation resulting in the variation of hydromechanical properties. Boyd et al. (2015) performed one-way FSI calculations by obtaining the pressure field from the CFD software and applying it in the FEM software. The orientation of the plies within the structural software was modified to check the response of the hydrofoil. It was shown that it is possible to obtain the desired deformation by proper tailoring of the material, however, the strong coupling is necessary to capture the deformation.

For the NACA 0015 hydrofoil profile Marimon Giovannetti et al. (2016) tested three different composite lay-ups characterised with different ply orientations. Experiments were done in the wind tunnel using the DIC technique. Those three tested ply orientations were: 0 deg, for which no bending twist behaviour is expected, -30 deg and 30 deg ply orientation, which introduces bend-twist coupling of the hydrofoils. The tests were carried out for Reynolds number up to 750,000 and as a result the structure deflected more than 10% of its span. The FSI calculations were additionally carried out and their ability to predict the hydroelastic properties of the hydrofoil was confirmed. The hydrofoil with the -30^0 layer was characterised by an increased twisting angle and higher deflection.

The idea of tailoring the hydrofoil performance was used to design a Passive Adaptive Composite (PAC) structure for the Moth foil by Marimon Giovannetti et al. (2018). It was observed that it is favourable for Moth hydrofoils to passively reduce their lift force for high speed. The shape and internal structure of the PAC hydrofoil has been designed, manufactures according to design, and tested in the wind tunnel. Two hydrofoils were tested – one reinforced with E-glass fibre and the other with carbon fibre. The hydrofoils had three different profiles along their length and were evaluated for wind speeds up to 30 m/s. In addition, the experimental conditions were reproduced and fully coupled FSI simulations were performed (Marimon-Giovannetti et al. 2017b). The possibility to achieve the required type of deformations under fluid loads was confirmed. The presented topics has been summarised in the PhD thesis (Marimon Giovannetti 2017c).

Experiments on rigid and flexible hydrofoils in circulating water tunnel have been described by Brandner and Pearce (2012). Hydrodynamic and hydroelastic characteristics of hydrofoils made of aluminium and stainless steel were performed. The investigated hydrofoils profiles were of NACA 0009 section. The geometry of both hydrofoils is an upright or upswept trapezoidal planform with a span of 0.3 m, and an aspect ratio of 3.33. The tests were performed for the Reynolds number ranging from $0.2 \cdot 10^6$ to $1 \cdot 10^6$ with the angles of attack adjusted to avoid the lift force exceeding 1kN. The test campaign was continued by Zarruk et al. (2014). This work was later used as a benchmark by other researchers. Hydrofoils with the same planform shape, but modified NACA 0009 profile made of steel and Carbon Fibre Reinforced Plastic (CFRP) with fibres oriented at 0 deg (CFRP00) and 30 deg (CFRP30) were investigated. The combination of test parameters was the same. In addition, the natural frequencies in air and water were evaluated

MOST WIEDZY Downloaded from mostwiedzy.pl

for all tested hydrofoils. It was found that the composite hydrofoils experienced significantly greater deflection and twist deformation under hydrodynamic loads than the stainless steel and aluminium hydrofoils. Mild positive twisting was observed for the CFPR00 hydrofoil. Strong negative bending twist coupling was seen for CFRP30 hydrofoil, resulting in a reduction of the lift force slope. This study was later continued by Young et al. (2018a) when the aluminium hydrofoil was replaced by a hydrofoil with a ply orientation of -30 degrees. Depending on the ply orientation nose-up (increase of angle of attack) or nose-down twist deformation (decrease of angle of attack) occurred. It is shown that the type of bend-twist coupling depends on the lay-up of the structure. A simplified numerical model has been developed to predict bending and coupling of the elastic hydrofoil.

The bend-twist coupling phenomena could also be predicted using computational methods. Liao et al. (2019) performed a numerical FSI simulation of flat plate and CFRP hydrofoil to validate the hydro-structural solver and better understand the load-dependent bend-twist coupling. The calculations were performed for the same hydrofoil shape as evaluated by Young et al. (2018a) and Zarruk et al. (2014), but for the composite layer direction from -45 deg to +45 deg.

The knowledge of the basic hydrostructural mechanism has been used to develop methods and workflows to optimise the hydroelastic properties of composite hydrofoils. Garg et al. (2017) performed the hydroelastic optimisation of the hydrofoil shape starting from trapezoidal aluminium hydrofoil with NACA 0009 section and validated it against experiments (Zarruk et al. 2014). The aim of the optimisation was to reduce drag. It was shown that it was necessary to include hydroelastic effects and the optimisation process resulted in an overall efficiency increase of 11%. The results for the optimised hydrofoil shape were later validated with experimental results (Garg et al. 2019). The optimised hydrofoil was tested in the circulation tunnel under the same conditions. The experiments confirmed the numerical findings that optimised hydrofoil was characterised by delayed cavitation inception. Volpi, Diez, and Stern (2017) also performed FSI-based calculations of a 3D flexible trapezoidal hydrofoil with NACA 0009 profile. The objective of the study was to develop the multidisciplinary design optimisation architecture for high-fidelity fluid-structure interaction problems. The results were validated against the experimental results presented in Zarruk et al. (2014).

The process of optimising the composite lay-up orientation was described by Herath et al. (2017). The objective was to design the composite lay-up of the hydrofoil to obtain a specific deformation under the selected conditions. The hydrofoil was manufactured, and calculations were validated against the results of the free vibration experiments and the static load tests. This process was used by Herath et al. (2021) to design, manufacture, and test composite hydrofoil. Both the composite plies schedule and shape with pre-twist were the subject of optimisation and further testing. The aim of the study was to maximise the lift to drag ratio (L/D) and reduce the risk of cavitation. The scope of tests was again like presented by Zarruk et al. (2014). The experiments were complemented by FSI calculations. It was shown that for selected operating conditions significant improvements could be achieved, such as higher L/D values and reduced

MOST WIEDZY Downloaded from mostwiedzy.pl

loss of lift after stall. This study was continued by investigating the deflection of the composite hydrofoil under the quasi-static load using the embedded single optical fibre (Maung et al. 2017). The numerical model of the composite structure was created and compared with experiment. The optical sensor was also used to evaluate the added mass effect, damping and natural frequencies in air and water for composite hydrofoil with NACA 0009 profile. Maung et al. (2021) presented the study on 1.35-metre span hydrofoil manufactured using automatic fibre placement. The natural frequencies and deformations under static loads were evaluated. For strain measurements the surface and embedded optical sensors were used together with strain gauges. The experiments were compared with the computation results of the FEM model based on the equivalent single layer approximation. Pernod et al. (2019) used the strain measurement technique, via a fully distributed optic fibre sensor directly embedded within the composite layers to evaluate the deformations and vibrations of the composite hydrofoil under the fluid loads. The experiments were performed on the NACA 66-206 trapezoidal hydrofoil with span of 180 mm in the circulation tunnel for angles of incidence between -10 and 10 degrees and Reynolds numbers between $9 \cdot 10^4$ and $5.4 \cdot 10^5$. Three different flow regimes were identified: unsteady dominated by von Karman vortex shedding, quasi-steady and pre-stall quasi unsteady regime. Tightly coupled high-fidelity fluid-structure interaction calculations were performed as well.

Temtching Temou et al. (2018) experimentally evaluated the trapezoidal NACA 0015 hydrofoil made of polyacetate in the cavitation tunnel. The span of the hydrofoil was 0.15 m, the aspect ratio was equal to 2.3, and the range of measurements covered Reynolds numbers from $0.3 \cdot 10^6$ to $0.7 \cdot 10^6$ and angles of incident of 2 degrees, 6 degrees and 10 degrees. The material was soft, and the experiments resulted in a maximum deformation of the tip equal to 4.5% of the span. In addition to the lift and drag forces, the flow induced vibrations were investigated and the response of the hydrofoil was assessed numerically by coupling Vortex Lattice Method (VLM) potential flow code, Athena Vortex Lattice (AVL) code, and an in-house structural code based on beam theory by Finite Element Method (FEM). Temtching Temou, Augier, and Paillard (2021) studied numerically and experimentally the effect of the composite lay-up on the hydrodynamic performance of the surface-piercing hydrofoil in presence of large displacements (up to 10% of the span). Four hydrofoils with different composite lay-up and materials (glass or carbon reinforcement) but identical geometry parameters were evaluated. The hydrofoils had a span of 1.350 m and a chord of 0.114 m. The experiments were carried out in a circulation tunnel with velocities of 0.7m/s and 0.9 m/s and angles of incidence between 3 degrees and 9 degrees. The FSI calculations were performed using two different approaches: the potential code coupled with the beam theory FEM solver and the OpenFOAM Volume of Fluid solver coupled with ASTER FEM solver, which is based on the theory of the mechanics of continuous media.

An important aspect of hydroelastic analysis relates to flow-induced vibrations, which can arise from several sources: shed vortices, also observed in aerodynamic problems, as well as laminar separation bubbles and cavitation. The latter is unique to hydrodynamic problems, as cavitation does not occur in air. Ausoni et al. (2007) experimentally investigated the influence of cavitation on Karman vortex shedding and hydrofoil vibration. The experiments were performed

MOST WIEDZY Downloaded from mostwiedzy.pl

for the 2D hydrofoil and high Reynolds number Re = $2.5 \cdot 10^4$ - $6.5 \cdot 10^4$. The structural response of the hydrofoil in different flow regimes, including the cavitating regime, and subjected to static and transient pitching motions was determined by Ducoin, André Astolfi, and Sigrist (2012). The experiments were performed for cantilevered NACA 66212 hydrofoils at Reynolds number of $0.75 \cdot 10^6$. Ducoin, André Astolfi, and Gobert (2012) analysed the vibration of a NACA 66312 hydrofoil at angles of attack ranging from 2 to 4 degrees of incidence and Reynolds number between $4.5 \cdot 10^5$ and $1.2 \cdot 10^6$ caused by laminar-to-turbulent transition and Laminar Separation Bubbles. The numerical and theoretical investigation of flow-induced vibrations was performed by Chae, Akcabay, and Young (2017). The influence of flow-induced bend–twist coupling on the vibration response of flexible hydrofoils was evaluated, and the influence of viscous effects was investigated for cantilevered hydrofoil. The influence of inflow velocity, angle of attack, and solid-to-fluid added mass ratio on the vibration frequencies and damping characteristics was investigated numerically and experimentally by Chae et al. (2016). Akcabay et al. (2014) determined the influence of cavitation on the vibration of the NACA66 hydrofoil at 8 degrees angle of attack at Re=$0.75 \cdot 10^6$ through experimental measurements and numerical simulations. Yao et al. (2014) experimentally investigated how the application of the Donaldson trailing edge affects the hydrodynamic damping for flow-included vibrations. Similarly, Bergan et al. (2019) experimentally measured and numerically evaluated how the shape of the trailing edge can affect the hydrodynamic damping for a wide range of flow velocities.

In case of hydrofoil struts or surface piercing rudders, the effect of the free surface could also have a considerable influence on the hydroelastic performance. The development of the measurement method that allowed for determination of the hydroelastic properties of the surface piercing strut was described in detail by Young, Harwood, and Ward (2018).

The effect of surface waves and the ventilation on the dynamic response of a surface piercing cantilever hydrofoil was investigated experimentally e.g. by Young et al. (2018). The experiment was conducted for different submergence ratios, angles of incidence, wave lengths, and wave amplitudes. The results show that, in general, the natural frequencies of the hydrofoil decrease with increasing submergence and ventilation developed for high angles of attack (above 12 degrees).

The effect of immersion and ventilation on the resonant frequencies, added mass and mode shapes of the surface piercing strut was investigated experimentally and numerically by Harwood et al. (2019). It was shown that the ventilation causes the reduction of the added mass and therefore, increase the resonant frequencies values, compared to fully wetted strut.

The Fluid-Structure Interaction methods are applicable and useful in the optimisation and analysis of various sailing appendages and rigid sails. Sacher et al. (2018) performed an optimisation of the hydrofoil of the 35th America's Cup high-speed racing yacht. The aim of the optimisation was to reduce the lift and avoid cavitation by adjusting the non-deformed shape and the material properties of the hydrofoil. This was achieved by deforming the trailing edge of the hydrofoil. The FSI method was also used to optimise the appendages of high-speed racing yacht (Balze et al. 2017). The 3D lifting line theory was coupled with modified beam method to optimise

MOST WIEDZY Downloaded from mostwiedzy.pl

the mass and stiffness of the daggerboard of the America's Cup flying catamaran. Sacher et al. (2020) coupled Abaqus software with lifting line – based flow model to calculate the forces and deformations of semi-rigid yacht sails. Banks et al. (2016) used the DIC method to evaluate the torsion and deflection of Moth class composite hydrofoil under quasi-static load. The obtained material property values were used to evaluate the deformation of the hydrofoil during sailing. Furthermore, the system for capturing the sailor's dynamic pose was developed with the intention of evaluating the impact of unsteady human motions and loads on the hydrofoil performance. Ponte, Sutherland, and Garbatov (2022), based on the information provided by the manufacturer of the Moth sail yacht, produced, and build an FEM model of the main strut with the purpose of further FSI testing. They found a good agreement between the Abaqus FEM model and the experimental results. Giovannetti et al. (2022) performed the experiments to evaluate the performance and deformation of the NACRA 17 hydrofoil in the cavitation tunnel for different combinations of water speed, leeway, and rake angle. The FSI calculations were also performed finding good agreement with the drag and lift forces, however, some discrepancies were found for the twisting angles.

There has been little work on the problems of Fluid-Structure Interaction for windsurfing fins, so far. Sutherland et al. (2022) and Cardoso de Brito et al. (2022) investigated the hydroelastic performance of a commercial windsurfing fin and performed two-way FSI analysis of the influence of ply orientation on the tip torsion. A slalom fin with the span of 0.37 m was studied for a range of speeds from 10 knots to 35 knots and angles of attack from 2 degrees to 6 degrees. The differences between the one-way and two-way FSI couplings were also evaluated.

1.3. Knowledge gap identification

Despite significant effort put in the understanding of the hydroelastic properties of the composite hydrofoil and significant achievements in this field, there are still some areas that remain not sufficiently explored. The previous works that investigated the performance of the composite hydrofoils focused mainly on the influence of the material and stacking sequence on the hydroelastic properties. None of them considered the other factors i.e. the manufacturing methods or the influence of random production errors, which may also have non-negligible influence on the material and hydrodynamic properties of the composite hydrofoil.

Moreover, what is common for majority of the up-to-date investigations is the fact that they are valuable from the designer point of view. The designer deals with the idealised object – both from geometrical and structural point of view. However, the actual final hydrofoils after manufacturing are not free from any defects, or deviations from the design. Moreover, the designer has the exact knowledge about the composite lay-up and manufacturing technology. Current state-of-the-art proves the feasibility to predict the hydroelastic properties of the hydrofoils for a given set of all the necessary data regarding the shape, composite lay-up and production process details. This, however, is not the case in practical applications since perfectly repeatable industrial processes are hardly achievable, thus the flawless reproduction of the design remains a theoretical ideal.

MOST WIEDZY Downloaded from mostwiedzy.pl

Therefore, from an end-user point of view, it has to be admitted that such accurate and credible data are simply not available, and **hydroelastic modelling using reverse engineering methods is hardly addressed at all.** So far, only one work focused on numerical investigation of the hydroelastic properties of the hydrofoil with a completely unknown internal structure (Giovannetti et al. 2022). However, it investigated one sample only. Nevertheless, this is a valuable case study, but it is not the systematic investigation. Furthermore, it is challenging to identify the stiffness of an object when the incomplete data on it are available. High-accuracy methods of stiffness identification have not yet been reported for use in hydrofoil research.

The previously described differences may apply to both geometry and mechanical properties. In case of the serial production of sailing equipment those differences vary within some particular, but unknown range. In the light of hydrostructural properties of flexible hydrofoil **the range of mechanical properties alteration for a composite fin has not been investigated.** Moreover**, it remains unexplored, how those variations affect the hydrodynamic properties of a flexible lifting structure.**

Those three aspects were identified as the knowledge gap, and they will be addressed in this thesis.

1.4. Research question

In the light of the current state-of-the-art and the identified knowledge gaps, the following research questions were formulated:

1. What are the suitable reverse engineering methods and modelling approaches to develop the substitute numerical hydroelastic model of a flexible composite hydrofoil with an unknown composite schedule?
2. What is the range of structural stiffness alterations of the investigated windsurfing fins?
3. How the stiffness alterations resulting from the manufacturing processes influence the hydroelastic properties of the flexible windsurfing RS:X fin?

1.5. Aim and Scope

The ultimate goal of this research is to determine the hydroelastic properties range of variability for the flexible composite windsurfing RS:X fins.

The specific goals leading to meet the ultimate objective include:

- development and verification of the framework for analysis of the hydroelastic properties of windsurfing fins whit unknown composite lay-up;
- identification the range of variations in the mechanical properties of the hydrofoils;
- determination of the composite material constituents of the fins;
- development of the substitute Finite Element Method model of the hydrofoil internal structure;
- modelling the flow around the fin by means of high fidelity unsteady CFD calculations;

MOST WIEDZY Downloaded from mostwiedzy.pl

- coupling CFD and FEM solvers to perform Fluid-Structure Interaction calculations;
- determination of the influence of the structural stiffness on the hydromechanical characteristics of the hydrofoil.

The scope of the research comprises both experimental and numerical investigations. It includes 3D scanning and post processing to obtain digital representation of the object. It covers also implementation of the method for identifying the fin stiffness distribution. The scope includes also the static and dynamic experimental investigation to validate the substitute model, CFD calculations of the flow around the undeformed structure, and finally, the Fluid-Structure Interaction calculations.

The structure of the thesis reflects presented aim and scope of the work to achieve the research objectives.

1.6. Thesis structure

The remaining part of the thesis is structured as follows, Chapter 2 presents materials and methods used to answer the research questions. Chapter 2 is divided into seven subsections which characterise the object of study, present the entire workflow of the investigation and describe applied experimental and numerical methods together with theoretical fundamentals of each. Subchapter 2.1 describes in detail the investigated analyse its internal structure that facilitated creation of the Finite Element Method (FEM) model for further calculations. Subchapter 2.2 presents the method overview and workflow of the investigation. It is followed by Subchapter 2.3 that describes the 3D scanning procedure and further actions that ended with 3D model of the analysed windsurfing fin. Subchapter 2.4 describes the experimental investigation, the static deformation measurements, the free vibrations tests, and determination of structure damping coefficients. Subchapter 2.5 focuses on the principles of Computational Fluid Dynamics (CFD), numerical model, validation, and verification study. Subchapter 2.6 describes the FEM principles, generation of numerical model and identification study. The last subchapter 2.7 describes the principles of Fluid-Structure Interaction calculations, numerical set-up, verification study and matrix of calculations.

Chapter 3 is divided into five subchapters that describe the results of experimental and numerical investigations in the same order as they were introduced in Chapter 2. Subchapter 3.1 presents the results of 3D scanning. Subchapter 3.2 describes the results of experimental investigation for static deformation, free vibrations experiments and assessment of damping coefficient. In Subchapter 3.3 results of CFD verification and validation study are presented, while in Subchapter 3.4 the FEM results are described. Finally in Subchapter 3.5 the results of FSI investigation are summarized.

The last two chapters, i.e. Chapter 4 and Chapter 5 present the discussion of the results and conclusions with remarks for future work, respectively. The structure of the thesis is presented in Figure 1.1.

MOST WIEDZY Downloaded from mostwiedzy.pl

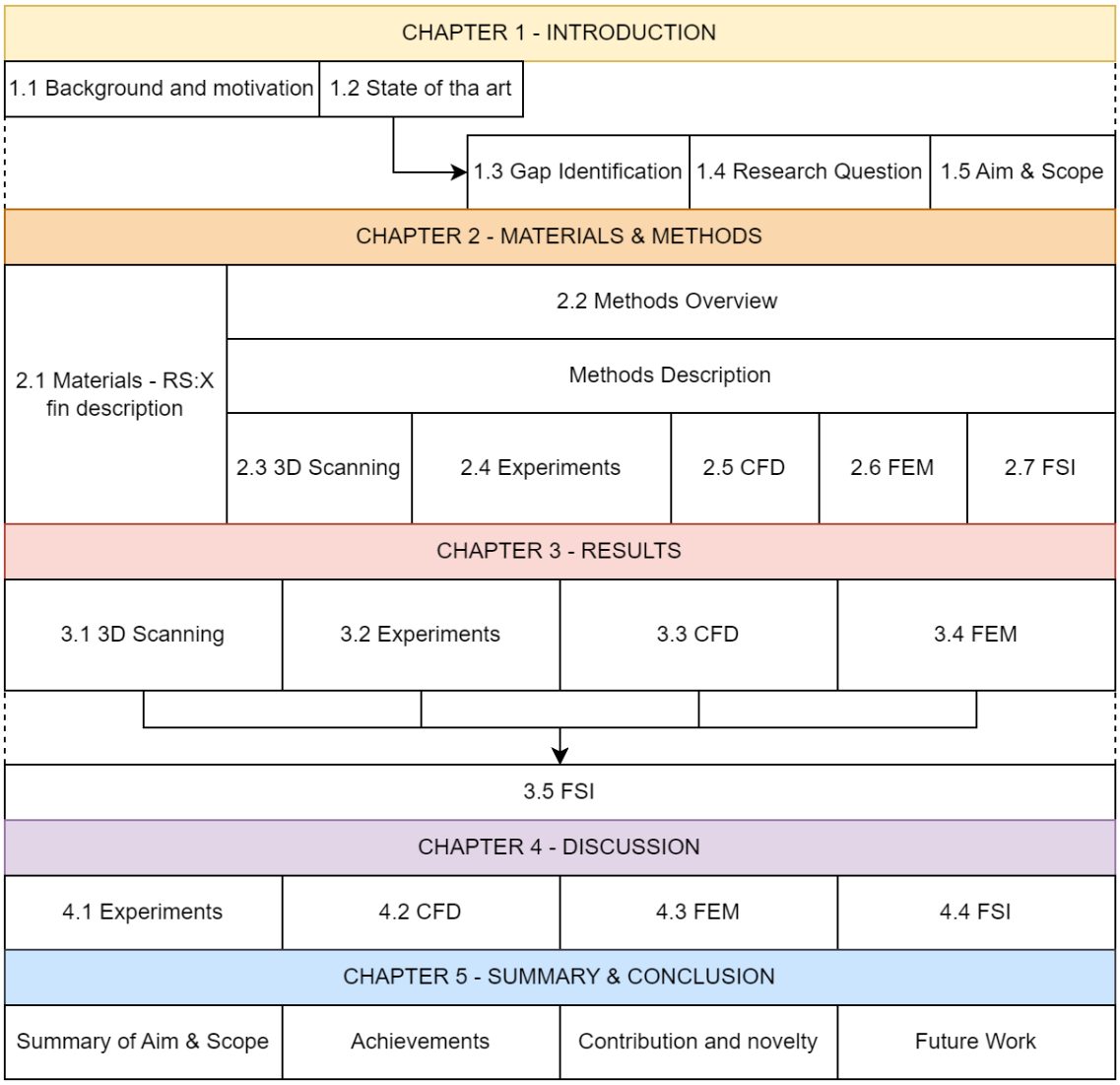

Figure 1.1Thesis structure.

MOST WIEDZY Downloaded from mostwiedzy.pl

2. MATERIALS & METHODS

2.1. Materials RS:X fin characteristics

The subject of the research is the windsurfing fin for the racing board RS:X. The RS:X is so called monotype class, what has two implications. Theoretically, all the fins should be the same, however, the differences in the performance are felt by windsurfers themselves. Additionally, the internal lay-up, materials, and manufacturing details are the producer's commercial-in-confidence intellectual property and are unknown. Therefore, direct modelling of the composite plies, their orientation and number is not possible in the presented case. The lack of knowledge about the manufacturing processes details enforces the necessity to find the alternative model of the composite structure to study the differences between windsurfing fins.

It was observed that the windsurfing fins deform during sailing in heavy wind conditions. Above a given speed of the board, the fin is the only control surface responsible for generating the side force that allows keeping the course of the board – Figure 2.1. This hydrodynamic side force balances the aerodynamic sail force, but at the same time results in bend-twist deformation of the fin. This, and the fact of observed differences between various fins, was the main motivation for conducting this research.

Figure 2.1 Sailing in heavy wind condition with retracted daggerboard (Sailing Energy)

Four fins were selected for deep investigation. The motivation and selection criteria are widely explained in Chapter 2.4. The span of the fin for male competitors is equal to 0.66 m, and chord next to the head is equal to 0.13 m. The fin planform shape resembles ellipse, but it has not pure elliptic shape. The exact 3D geometry of the fin was created using reverse engineering tools.

One of the investigated fins was cut into twelve sections to determine the unknown internal structure. Three sections are shown in Fig. 2.2 The structure consists of carbon fibre reinforced skin and carbon fibre reinforced core with polyethylene medium to distribute resin inside the mould during the lamination process.

MOST WIEDZY Downloaded from mostwiedzy.pl

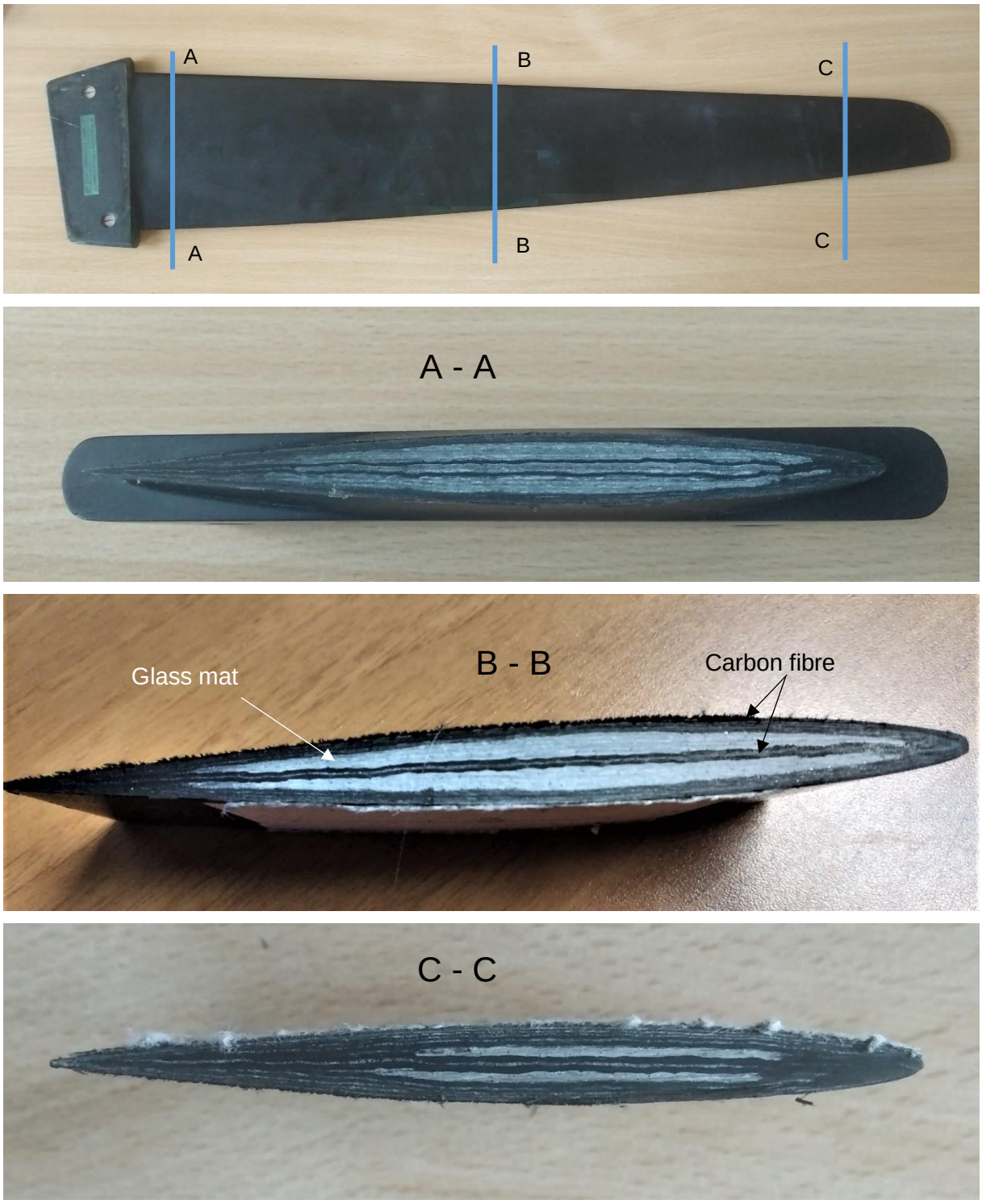

Figure 2.2 Internal composite structure of RS:X fin.

The section was "peeled" ply by ply to assess plies' orientation. However, it was possible to do it only for the first four plies, and their orientation was estimated to be +/-75 and +/- 15 with the symmetrical lay-up. The medium was made of randomly orientated cut fibres of glass. The amount of medium inside the fin varies along the span off the fin, decreasing closer to the tip. It was not possible to assess the number and orientation of all plies. Therefore, instead of directly modelling each ply's thickness, orientation, and mechanical properties, an alternative method was used to

MOST WIEDZY Downloaded from mostwiedzy.pl

predict fin structural behaviour. The numerical model of fins' structure is described in detail in Chapter 2.6.5.

2.2. Method overview

Combination of experimental and numerical methods was used to solve the defined problem. The first step was to digitalise the shape of the windsurfing fin, it was done with the use of 3D scanning method. The digital model in .igs file format was used for both CFD and FEM simulations.

The verification study of mesh sensitivity was done for the CFD model and various turbulence models were also compared. The results the CFD hydrodynamic calculations were validated against the literature data described by Zarruk et al. (2014). The CFD calculations were performed using Finite Volume Method, and STAR-CCM+ software was used for both CFD and FSI calculation.

For the FEM model it was necessary to create the substitute model of the internal structure. Two types of experiment were done to assess the stiffness of the windsurfing fin and gain validation data for the FEM model. At the first stage the structural calculations were performed using Femap software.

The first type of experiments was the measurement of the displacement under the static load. At this stage, from a population of seventy-nine fins, four of them with different stiffness characteristics were selected for identification. The identification of the stiffness distribution of each fin was done based on the displacement measurements. The second test was the evaluation of the structure acceleration during the free vibration tests. The results of this tests were eigenfrequencies, eigenmodes, and damping coefficients. Free vibration tests were performed for one fin to confirm the accuracy of the identification based on the static load. The free vibrations experiments were also performed in water.

After confirming credibility of CFD and FEM models, the next step was to couple both of them – fluid and structural domain. This was done by performing two-way coupled FSI simulations. For the sake of FSI simulations, the FEM model was exported to Abaqus, and this software was used for coupled calculations. The mesh and time step verification study were performed once again.

Finally, for four fins with quite different stiffness properties the hydro-elastic performance was assessed. All those steps are graphically presented in Figure 2.3, and they are described in detail in following chapters.

MOST WIEDZY Downloaded from mostwiedzy.pl

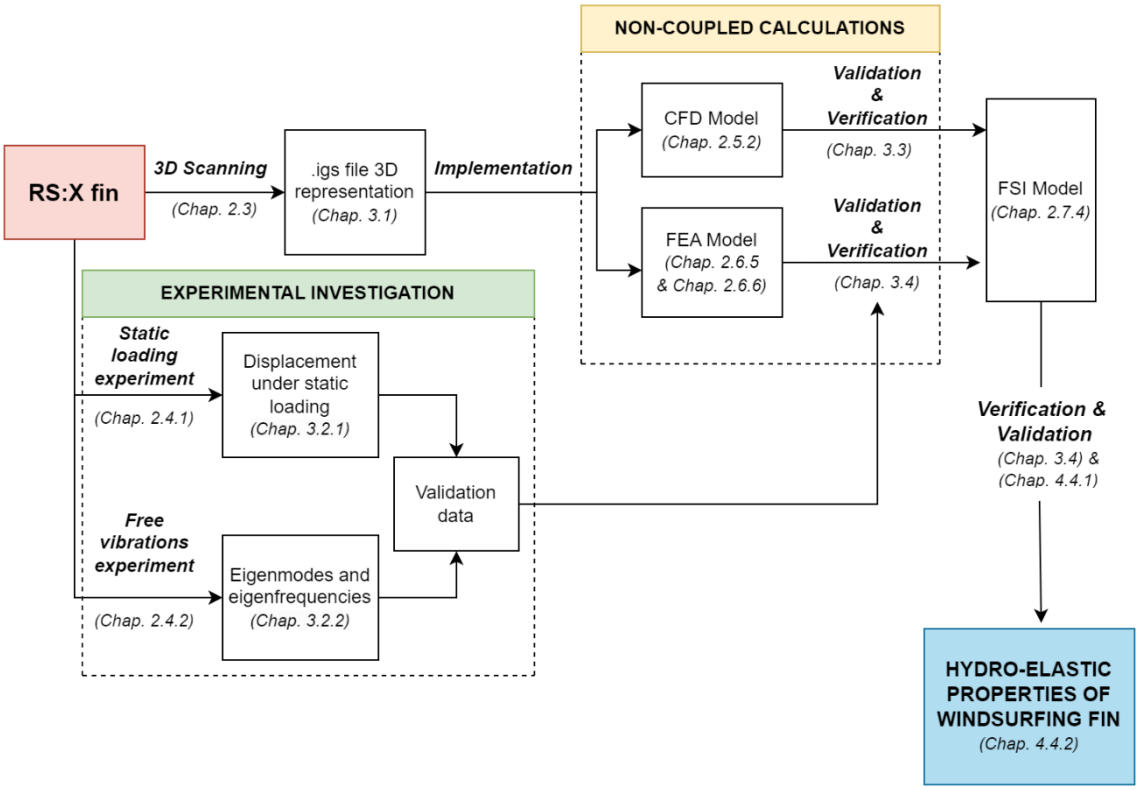

Figure 2.3 The workflow of the research.

2.3. 3D scanning

The first part of the research included creating computer files with fin 3D geometry using reverse engineering. The laser scanner with the measuring arm was used to create the cloud of points that was later transferred into the final geometry of the fin used for computations. The Cloud Compare software was used to generate the. stl triangle mesh of raw geometry from the cloud of points. Two sides of the fin were measured separately, and the coordinates of the points were imported from the text file containing coordinates of points to Cloud Compare software. At first, the cloud was cleaned from scattered points. Next, both sides of the fin were matched to each other. The characteristic points on the head and tip of the fin were used for correct assembly. The cloud of points was transferred into triangle mesh using the Poisson Surface Reconstruction tool implemented into the Cloud Compare software. The process of scanning and the cloud of points was presented in Figure 2.4.

MOST WIEDZY Downloaded from mostwiedzy.pl

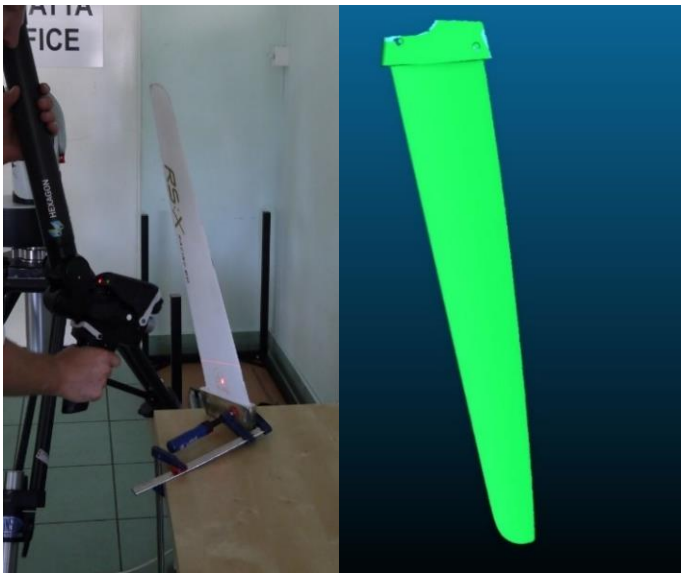

Figure 2.4 Reconstruction of the RS:X fin 3D geometry.

At the next stage of the 3D model preparation, the cross-sections of the cloud of points were generated and faired. Based on those sections, the NURBS surfaces were created using Siemens NX software. The surfaces were merged together in a way to assure smooth and continuous surface. Finally, the 3D model ready to use for structural and hydrodynamic calculations was obtained.

2.4. Experiments

2.4.1. Static deformation determination

The measurement setup for static deformations was developed and build by Polish Sailing Association with the purpose of comparing the fins with each other. The simplified measurement setup is presented in Figure 2.5.

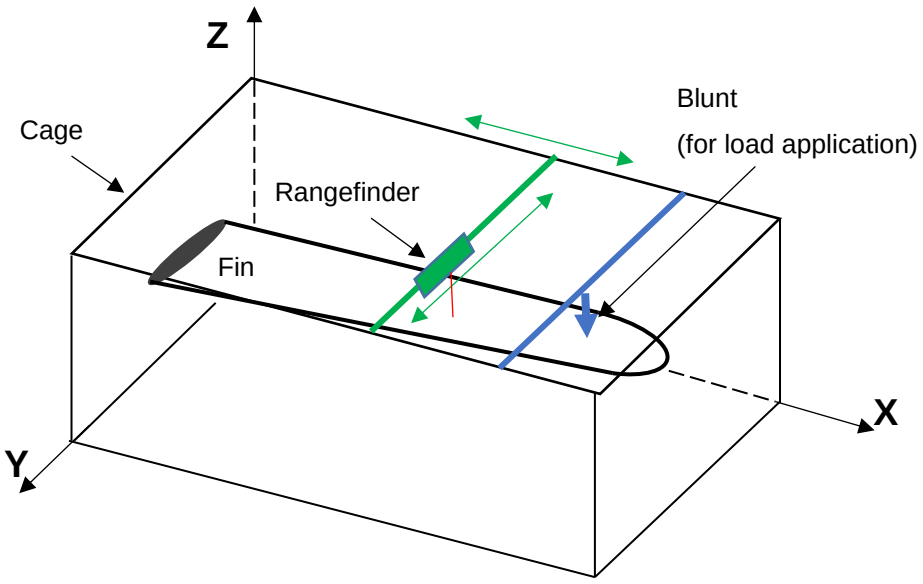

Figure 2.5 Schematic setup for windsurfing fin displacement measurements.

MOST WIEDZY Downloaded from mostwiedzy.pl

During the experiment, the fins were rigidly clamped by the head to allow obtaining cantilevered beam schema. The force was applied by pressing the stamp at the distance of 0.6 m from the head. The applied load was adjusted manually with the knob, and magnitude of that load was displayed by the digital screen for the sake of recording. The position of the load application is presented as the blue arrow in the Figure 2.5. Each of the tested fins were loaded with the force equal to 130 N. The force was controlled with the precision of 0.1N. The load was applied to avoid local stress concentration and deformations of the skin. The displacement of the fin was measured by the laser rangefinder, presented in the Figure 2.5 as a green box. The rangefinder was mounted on the rails. It allowed to measure the distance from the base to any point on the fin surface. The precision of the rangefinder measurements was equal to 0.1 mm. The displacement was measured at positions X_1 = 30 cm, X_2 = 50 cm, and X_3 = 59 cm away for the fin head. Along Y-axis the measurement point corresponded to the maximum thickness of the fin at given X-coordinate. Checking the displacements in multiple places allowed for an accurate assessment of mechanical properties of the entire structure.

Based on the measurements of a large population (79 fins) four of them were selected for further study. The first (FIN1) represented the flexible structure, second (FIN2) the stiff structure, the third (FIN3) and the fourth (FIN4), moderate ones. The displacements in three different points were measured for fins numbered one to three (FIN1, FIN2, FIN3), and in two points for the fin number four (FIN4).

2.4.2. Free vibrations experiment

The first part of this experiment was dedicated to design and prepare the experimental setup. This included the proper realization of the boundary conditions and development of research measuring and acquiring equipment.

The free vibration test of the FIN4 was conducted to confirm the accuracy of the stiffness identification and obtain experimental data for validation of the proposed method for stiffness distribution identification. The reason for selection just one fin was that at a time of performing the tests if was available for experimental testing.

The investigation of vibrations provides additional information about the structure compared to static displacement measurement. Besides the stiffness of the structure, it also allows to control if the mass distribution assumed in FEM model is correct. Moreover, the structural damping can be also identified. Finally, the analysis of vibration allows to determine eigenfrequencies of the structure. The experiments were conducted in air and in water.

In case of the measurements in the air the acceleration and angular velocity were measured at various locations on the fin in three directions, X, Y, and Z. The accelerations in water were measured only at the tip of the hydrofoil. The free vibration test was conducted only for FIN4. The time history of the acceleration was processed, and with the use of Fast Fourier Transform (FFT) analysis, the natural frequencies of the composite structure were determined.

In order to accurately represent the way that fin is fixed to the windsurfing board in real-life conditions, the mounting block made of MDF material was milled by a CNC machine. This is

MOST WIEDZY Downloaded from mostwiedzy.pl

shown in Figure 2.6. To conduct the experiments in the air two screws marked with squares were used to fix the fin inside the block. There are two threaded holes at the head of the fin, and those screws were used for holding the fin top head. The fin is attached to the board in the same way. The bolts marked with triangles were used for joining together two parts of the mounting block.

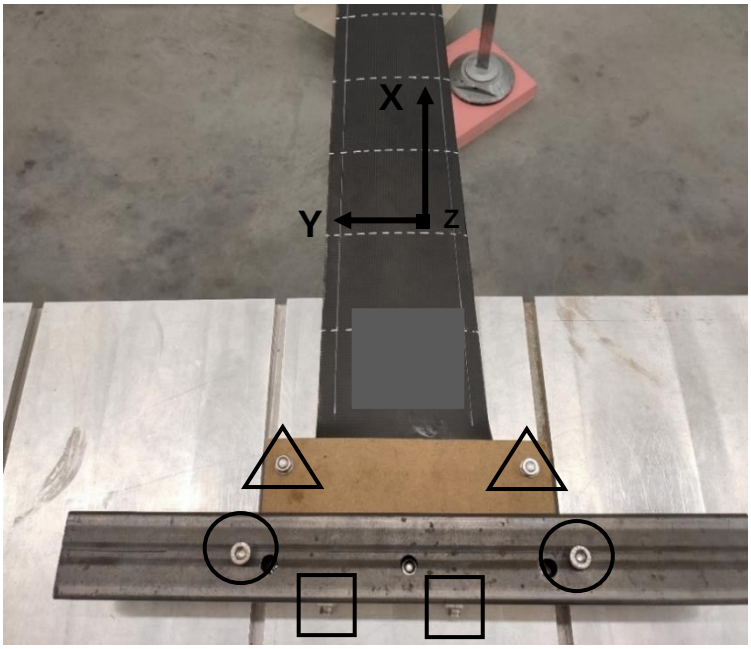

Figure 2.6 The cantilever beam conditions.

The last two bolts (marked in Fig. 2.6 with the solid circles) were used for attaching the mounting block with a fin to the solid table. Mounting in such a way, allowed to achieve the cantilever boundary conditions.

The set of six microplates with micro-accelerometers and micro-gyroscopes yielded measurements of the vibrations. They were attached to the surface of the fin in equidistant separation from each other. The accelerations and angular velocities were recorded for each accelerometer in three directions X, Y, and Z. The X-axis ran from the top to the tip of the fin. The Y-axis corresponded to the direction from the leading to the trailing edge. The Z-axis corresponded to the vertical direction – the same as the direction of the gravity acceleration vector. The experimental setup is presented in Fig. 2.7.

MOST WIEDZY Downloaded from mostwiedzy.pl

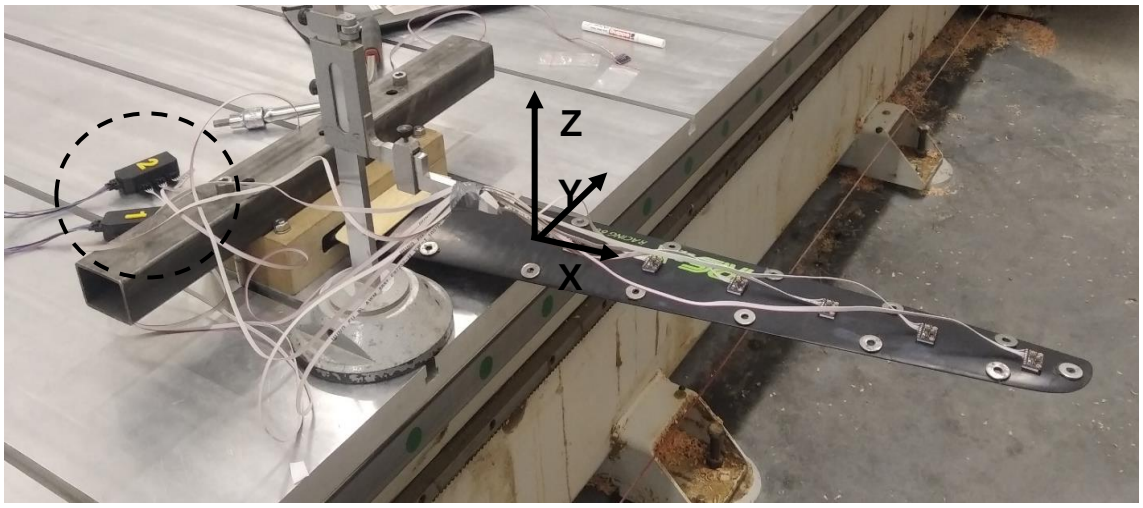

Figure 2.7 Experimental setup for measurements of the accelerations in air.

The signal from the three sensors was acquired by one transducer (marked in Fig. 2-7 with the dashed circle) and then sent to the transmitter. In total, two transducers were used to support six accelerometers and gyroscopes. Transmission to the receiver connected with the computer can be realized via cable or radio waves. The frequency of data acquisition was set to 1000 Hz. The resolution of the sensor was equal to 0.001 G (G – gravity acceleration). The precision of the sensor was estimated to be equal to 0.019 G, and accuracy was equal to 0.007 G. The measurement range was ∓16 G. The duration of each measurement was 2 seconds. The initial bending of the fin generated the free vibrations. Then, the free vibration chart was plotted. Based on the time history of accelerations using FFT, the eigenfrequencies and damping coefficients were found. The precision and accuracy were estimated for the sensor before the actual measurement, while it was placed flat. Ideally, the measurement along Z-axis should yield value 1G. The accuracy of the sensor was determined by comparing the mean value of the measurement within 0.1 to value of 1G. The precision was determined as the standard deviation of the 100 samples. The same procedure was repeated for the accelerometer used in water.

The experimental setup for determining the damped vibration in water is presented in Figure 2.8. The investigated fin was fixed under the towing carriage to the runner which allowed to adjust the draft of the fin. The plate with the dynamometer was connecting the runner with the fin mounting plates. The waterproof accelerometer was placed at the tip of the hydrofoil. The time history of the accelerations was recorded on the SD card inside the accelerometer. The sensor had the measurement range equal to ∓16G and sampling frequency of 200Hz, which allows to determine the eigenfrequencies up to 100 Hz. The resolution of the sensor is equal 0.001 G. The precision of the sensor was equal to 0.009 G and accuracy was equal to 0.007G.

MOST WIEDZY Downloaded from mostwiedzy.pl

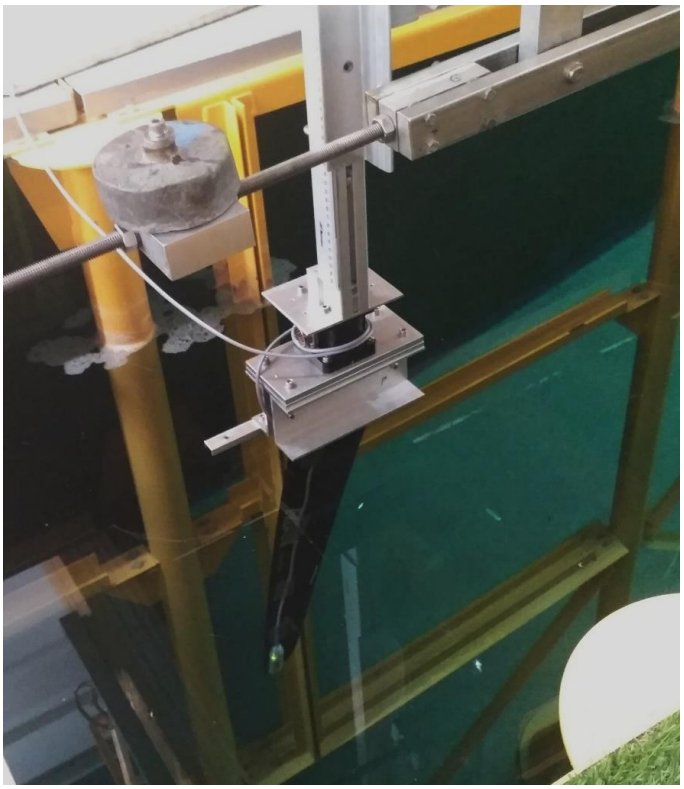

Figure 2.8 Experimental setup for measurements of the accelerations in water.

The detail of the mounting scheme is presented in Figure 2.9. Two C-section plates are connected with each other with another two plates of 7 millimetres thickness. C-section plates and flat plates are connected with each other using set of twelve bolts. Another four bolts connect dynamometer with the flat plate. It resulted in rigid and tight fitting the fin inside the mounting nest.

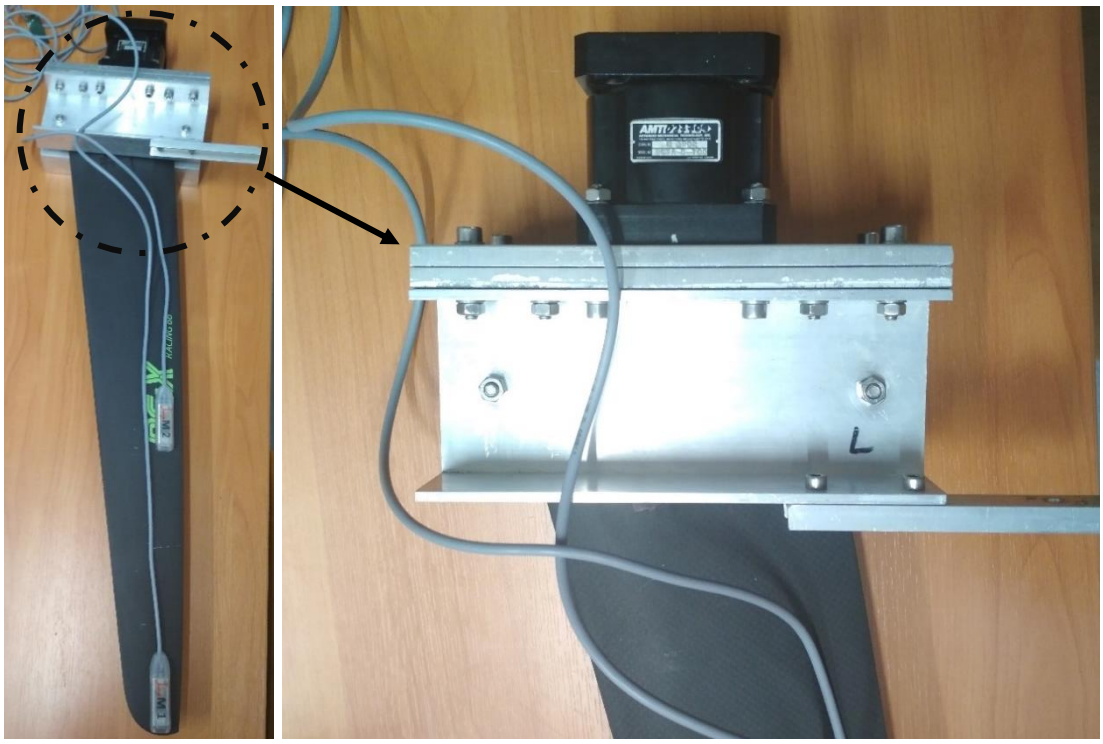

Figure 2.9 Rigid fixing the fin inside the mounting nest.

MOST WIEDZY Downloaded from mostwiedzy.pl

Again, the free vibrations experiment was performed to determine the accelerations of the structure and based on that the modes and corresponding eigenfrequencies in water. Due to expected damping of the motions only the acceleration in the direction normal to fin surface were analysed. It corresponds to bending motion of the fin. The time history of the accelerations was also used to determine the damping coefficient and the eigenfrequency in water.

2.4.3. Determination of structural damping based on the free vibrations experiment

The damping of the vibrating system using Rayleigh damping can be written as:

$$\mathbf{C} = \alpha \boldsymbol{M} + \beta \boldsymbol{K} \tag{2.1}$$

Where:

C – damping matrix

M – mass matrix

K – stiffness matrix

α – mass proportional damping

β – stiffness proportional damping

The Rayleigh damping is the sum of stiffness proportional damping and mass proportional damping. The rate of damping is related to the natural frequency of the vibrating object. The Rayleigh damping coefficient is expressed as:

$$\lambda_R = \frac{1}{2}\left(\frac{\alpha}{\omega_i} + \beta\omega_i\right) \tag{2.2}$$

Where ω_i is the i-th natural frequency of the object.

For FEM dynamic calculations the damping coefficients are important material constants. They can be obtained from the free vibrations experiment based on the analysis of the vibration time history. It is important to isolate (filter) each frequency that seems crucial for particular object and evaluate its damping ratio separately. Most often the first two eigenfrequencies are sufficient (Patel 1988).

The damping coefficients α and β are expressed as:

$$\alpha = \frac{2\omega_i\omega_j}{\omega_j^2 - \omega_i^2}(\zeta_i\omega_j - \zeta_j\omega_i) \tag{2.3}$$

$$\beta = \frac{2\left(\zeta_i\omega_i - \zeta_j\omega_j\right)}{\omega_j^2 - \omega_i^2} \tag{2.4}$$

Where:

ω_i , ω_j - the i-th and j-th eigenfrequency

ζ_i, ζ_j – the damping coefficient for i-th and j-th eigenfrequency

The general formula for the damping coefficient of i-th frequency is as follows:

MOST WIEDZY Downloaded from mostwiedzy.pl

$$\zeta_i = \frac{1}{\sqrt{1 + \left(\frac{2\pi}{\Lambda_i}\right)^2}} \tag{2.5}$$

Where Λ_i is the logarithmic damping decrement for i-th eigenfrequency. The time history of the typical dampened signal is presented in the Figure 2.10.
The logarithmic decrement of damping is defined as:

$$\Lambda = \frac{1}{n} ln \frac{x_A(t)}{x_A(t + nT)} \tag{2.6}$$

Where T is the period of dampened vibrations and n is the number of analysed cycles.

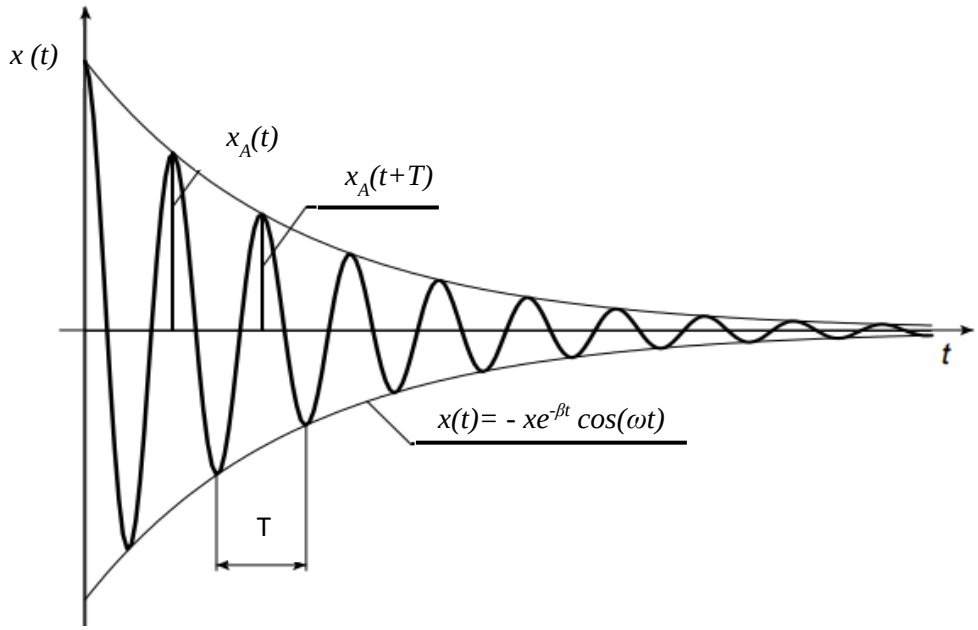

Figure 2.10 The example of the free vibrations damping (Stasiak 2005).

Therefore, the following procedure was applied to obtain damping coefficients for the first two eigenfrequencies of the windsurfing fin:

- the first four eigenfrequencies were identified based on the Fast Fourier Transform of the fin accelerations measurements;
- the first frequency time history was isolated using low-pass filter for the registered signal of fin accelerations;
- the second frequency was isolated using first the high-pass filter to remove the first eigenfrequency from the signal and then the low-pass filter to remove higher orders eigenfrequencies;
- the logarithmic decrement was calculated for each eigenfrequency;
- the damping coefficients ζ_1 and ζ_2 were calculated;
- the damping coefficients α and β were evaluated.

MOST WIEDZY Downloaded from mostwiedzy.pl

Obtained damping coefficients were later used for definition of the material constants in the FEM and FSI calculations.

2.5. Application of the Computational Fluid Dynamics methods

2.5.1. Computational Fluid Dynamics Principles

The Computational Fluid Dynamics is a rather wide term that includes computational methods of different fidelity that are used to obtain information about flow field. The Unsteady Reynolds Averaged Navier-Stokes Equations (U-RANS) with Finite Volume Method is used for the majority of calculations and lifting-line code for the sake of comparison.

The Navier-Stokes Equations describes all the real flow phenomena, and assuming incompressible flow model they are described by the mass and momentum conservation equations. The mass conservation equation states that in the closed volume the amount of the fluid that flow inside is the same as the amount of fluid that exits the control volume (Çengel and Cimbala 2018). The mass conservation equation is presented in Eq. 2.7 described below:

$$\nabla \cdot \mathbf{v} = 0 \tag{2.7}$$

What can be written in following form:

$$\frac{\partial u}{\partial x} + \frac{\partial v}{\partial y} + \frac{\partial w}{\partial z} = 0 \tag{2.8}$$

Where:
$\mathbf{v}$ – vector of velocity

u, v, w – velocity components in x, y, z direction

∇- vector differential operator defined as:

$$\nabla = \vec{\mathrm{i}}\frac{\partial}{\partial x} + \vec{\mathrm{j}}\frac{\partial}{\partial y} + \vec{\mathrm{k}}\frac{\partial}{\partial z} \tag{2.9}$$

The momentum conservation law is presented in Equation 2.10:

$$\rho\frac{D\mathbf{v}}{Dt} = -\nabla p + \rho\vec{g} + \mu\nabla^2\mathbf{v} \tag{2.10}$$

Where:

$\frac{D}{Dt}$ is the material derivative expressed as: $\frac{D}{Dt} = \frac{\partial}{\partial t} + (\mathbf{v} \cdot \nabla)$,

p – pressure,

ρ – fluid density,

$\vec{g}$ – acceleration of gravity,

μ – dynamic viscosity of the fluid.

The analytical solutions for Navier-Stokes equation are only known for simplified models of fluid (for example stationary and laminar) and involving very simple geometries. For more complex geometries, turbulent and unsteady flow, the numerical solutions are necessary.

MOST WIEDZY Downloaded from mostwiedzy.pl

Most of the CFD codes are based on the Finite Volume Method (FVM). The numerical domain is divided (discretised) by the finite amount of the different size control volumes (CV) bounded by the control surfaces (CS) that constitutes the numerical mesh. The computational node is located at the centroid of each CV, at which the variables are computed. The interpolation is used to calculate the variables at the CS. As a result, the conservation equations are solved in each of the mesh cells. The mass and momentum conservation equation in 2.7 and 2.10 in FVM are implemented in their integral version that is defined as follows:

$$\frac{\partial}{\partial t}\int_{CV} \rho dV + \int_{CS} \rho \mathbf{v} \cdot \mathbf{n}\, dS = 0 \tag{2.11}$$

$$\frac{\partial}{\partial t}\int_{CV} \rho \mathbf{v} dV + \int_{CS} \rho \mathbf{v}\mathbf{v} \cdot \mathbf{n}\, dS = \sum \boldsymbol{f} \tag{2.12}$$

$\sum \boldsymbol{f}$ is the sum of the forces acting on the body, such as buoyancy, and surface forces – (normal and shear stresses) (Ferziger and Peric 2002).

Therefore, the equation 2.12 can be written as:

$$\frac{\partial}{\partial t}\int_{CV} \rho \mathbf{v} dV + \int_{CS} \rho \mathbf{v}\mathbf{v} \cdot \mathbf{n}\, dS = \int_{CS} \mathbf{T} \cdot \mathbf{n}\, dS + \int_{CV} \rho \mathbf{b}\, dV \tag{2.13}$$

Where **T** is the stress tensor defined as:

$$\mathbf{T} = -\left(P + \frac{2}{3}\mu \nabla \cdot \mathbf{v}\right)\mathbf{I} + 2\mu \mathbf{D} \tag{2.14}$$

I is the unit tensor and **D** being the rate of strain defined as:

$$D = \frac{1}{2}[\nabla \mathbf{v} + (\nabla \mathbf{v})^T] \tag{2.15}$$

The analysed object is operating in the regime of laminar-to-turbulent transition flow, and turbulent flow regime, therefore high-fidelity method will be applied. The available approaches for modelling turbulence are:

- Direct Numerical Simulations (DNS) that aims to solve both large- and small-scale turbulent eddies, however, due to required mesh size this approach is completely unfeasible for high Reynolds number flows;
- Large Eddy Simulation (LES) – turbulent eddies have various dimensions, in the LES approach only the larger scale eddies mainly in the region of the turbulent wake are directly resolved, and small-scale eddies near the wall are modelled by wall functions;
- Reynolds Averaged Navier-Stokes Equations (RANS) with turbulence models;

MOST WIEDZY Downloaded from mostwiedzy.pl

- Detached Eddy Simulations (DES) – this is the blend of LES and RANSE, whenever the mesh resolution is fine enough, the LES is applied, either way, the RANSE in applied.

In principle LES and DES simulations are applied when behaviour of turbulent wake is the key interest of the simulation. Moreover, LES simulation is able to predict position and strength of vortices for highly separated flow with much greater accuracy (Visonneau, Guilmineau, and Rubino 2018).

At the early stage of my study, I compared four different turbulence models: $k-\varepsilon$ model and $k-\omega$ SST, Reynolds Stress Transport (RST) turbulence model, and DES approach, which is LES blended with $k-\omega$ SST turbulence model. Those models are characterised below, and in the Chapter 2.5.2 and 2.5.3 I am comparing the results of simulations using DES with different RANSE turbulence models for accuracy of the prediction of drag and lift forces.

The RANSE approach assumes that in turbulent flow instantaneous velocity can be expressed as the mean velocity and fluctuating component, so that for u, v, and w components of velocity vector $\mathbf{v}$:

$u = U + u'$

$v = V + v'$

$w = W + w'$

Then, RANS equation can be written as:

$$\rho\frac{D\mathbf{v}}{Dt} = -\nabla p + \rho\vec{g} + \mu\nabla^2\mathbf{v} + \nabla\cdot\rho\tau_{ij\,T} \tag{2.16}$$

Where:

$$\tau_{ij\,T} = \begin{pmatrix} \overline{u'^2} & \overline{u'v'} & \overline{u'w'} \\ \overline{u'v'} & \overline{v'^2} & \overline{v'w'} \\ \overline{u'w'} & \overline{v'w'} & \overline{w'^2} \end{pmatrix} = -\overline{u'_\iota u'_j}$$

$\tau_{ij\,TURBULENT}$ is so-called - Reynolds stress tensor that represents transfer of momentum due to turbulent fluctuations (Çengel and Cimbala 2018).

In tensor notation the Reynolds stress tensor can be written and defined as:

$$-\rho\overline{u'_\iota u'_j} = \mu_t\left(\frac{\partial\overline{u}_\iota}{\partial x_j} + \frac{\partial\overline{u}_j}{\partial x_j}\right) - \frac{2}{3}\rho\delta_{ij}k \tag{2.17}$$

Where δ_{ij} is Kronecker delta, μ_t is the eddy viscosity, and k is the turbulent kinetic energy, defined as:

$$k = \frac{1}{2}\overline{u'_i u'_\iota} = \frac{1}{2}(\overline{u'u'} + \overline{v'v'} + \overline{w'w'}) \tag{2.18}$$

Equitation 2.18 is the eddy viscosity model for the Reynolds stress. Introducing Reynolds stress tensor brings additional unknowns to the system of equations and require turbulence model to allow for closure of the problem.

One of the most common turbulence models that bounds turbulent kinetic energy k with eddy viscosity and turbulence dissipation ε is $k-\varepsilon$ that is defined as:

MOST WIEDZY Downloaded from mostwiedzy.pl

$$\frac{\partial(\rho\varepsilon)}{\partial t}+\frac{\partial(\rho u_j\varepsilon)}{\partial x_j}=C_{\varepsilon1}P_k\frac{\varepsilon}{k}-\rho C_{\varepsilon2}\frac{\varepsilon^2}{k}+\frac{\partial}{\partial x_j}\left(\frac{\mu_t}{\sigma_\varepsilon}\frac{\partial\varepsilon}{\partial x_j}\right) \tag{2.19}$$

Where $P_k$is the production rate defined as:

$$P_k=-\rho\overline{u_i'u_j'}\frac{\partial\overline{u}_i}{\partial x_j}=\tau_{ij}\frac{\partial u_i}{\partial x_j}\approx\mu_t\left(\frac{\delta\overline{u}_i}{\delta x_i}+\frac{\delta\overline{u}_j}{\delta x_i}\right)\frac{\delta\overline{u}_j}{\delta x_j} \tag{2.20}$$

The eddy viscosity is then defined as:

$$\mu_t=\rho C_\mu\frac{k^2}{\varepsilon}$$

Where C_μ is an empirical constant equal to 0.09. Other constants in Eq. 2.19 are:

$\sigma_k=1.00;\qquad \sigma_\varepsilon=1.30;\qquad C_{1\epsilon}=1.44;\qquad C_{2\epsilon}=1.92$

In general, the constants used in various turbulence models are the result of data fitting for a wide range of turbulent flows and validation against experiments. This is one of the reasons why some turbulence models are better suited for particular CFD applications than the others.

The second widely used turbulence model is $k-\omega$ SST. The standard $k-\omega$ turbulence model is defined as (Blazek 2015):

$$\frac{\partial(\rho k)}{\partial t}+\frac{\partial(\rho\overline{u}_j k)}{\partial x_j}=P_k-\rho\beta^*k\omega+\frac{\partial}{\partial x_j}\left[(\mu+\mu_t\sigma_k^*)\frac{\partial k}{\partial x_j}\right] \tag{2.21}$$

$$\frac{\partial(\rho\omega)}{\partial t}+\frac{\partial(\rho\overline{u}_j\omega)}{\partial x_j}=\alpha\frac{\omega}{k}P_k-\rho\beta\omega^2+\frac{\partial}{\partial x_j}\left[(\mu+\mu_t\sigma_\omega^*)\frac{\partial\omega}{\partial x_j}\right] \tag{2.22}$$

The eddy viscosity is dependent on the specific dissipation rate ω as follows:

$$\mu_t=\frac{\rho k}{\omega} \tag{2.23}$$

The constant values in the Eq. 2.21 and 2.22 are:

$\alpha=\frac{5}{9};\qquad \beta=0.075;\qquad \beta^*=0.09;\qquad \sigma_k^*=\sigma_\omega^*=0.5;\quad \varepsilon=\beta^*\omega k$

The modification of the $k-\omega$ of the turbulence model that was proposed by Menter (1994). The $k-\omega$ SST model was introduced in two steps: first creating the base line model that blends together standard $k-\omega$ model in the boundary layer with $k-\varepsilon$ in the region of wake and free shear layers, then the constants in the base model were modified to obtain $k-\omega$ SST model:

$$\frac{\partial(\rho k)}{\partial t}+\frac{\partial(\rho\overline{u}_j k)}{\partial x_j}=P_k-\rho\beta^*k\omega+\frac{\partial}{\partial x_j}\left[(\mu+\mu_t\sigma_k^*)\frac{\partial k}{\partial x_j}\right] \tag{2.24}$$

MOST WIEDZY Downloaded from mostwiedzy.pl

$$\frac{\partial(\rho\omega)}{\partial t}+\frac{\partial(\rho\overline{u_j}\omega)}{\partial x_j}=\alpha\frac{\omega}{k}P_k-\ \rho\beta\omega^2+\frac{\partial}{\partial x_j}\left[(\mu+\mu_t\sigma_\omega^*)\frac{\partial\omega}{\partial x_j}\right]+2\rho(1-F_1)\sigma_{\omega2}\frac{1}{\omega}\frac{\partial k}{\partial x_j}\frac{\partial\omega}{\partial x_j} \tag{2.25}$$

Then the eddy viscosity model $\vartheta_t=\frac{\mu_t}{\rho}$ can be redefined as:

$$\vartheta_t=\frac{a_1k}{\max(a_1\omega;\Omega F_2)} \tag{2.26}$$

Where F_1 and F_2 function can be defined as:

$$F_1=\tanh\left[min\left[max\left(\frac{\sqrt{k}}{0.09\omega y};\frac{500v}{y^2\omega}\right);\frac{4\rho\sigma_{\omega2}k}{CD_{k\omega}y^2}\right]\right] \tag{2.27}$$

$$F_2=\tanh\left(max\left(2\frac{\sqrt{k}}{0.09\omega y};\frac{500v}{y^2\omega}\right)\right) \tag{2.28}$$

Where:

$$CD_{k\omega}=\max\left(2\rho\sigma_{\omega2}\frac{1}{\omega}\frac{\partial k}{\partial x_j}\frac{\partial\omega}{\partial x_j},10^{-20}\right) \tag{2.29}$$

And applied constants are:

$\beta=0.075;\quad \beta^*=0.09;\quad \sigma_k=0.85;\quad \sigma_\omega=0.5;\quad a_1=0.31;\quad \alpha=0.553;$

The Reynold Stress Models directly calculate the components of the Reynolds stress tensor by solving their governing transport equations. RST models have the potential to predict complex flows more accurately than eddy viscosity models because the transport equations for the Reynolds stresses naturally account for the effects of turbulence anisotropy, streamline curvature, swirl rotation and high strain rates (Manceau and Hanjalić 2002). The RST turbulence model is presented in Eq. 2.30.

$$\frac{\partial(\rho\tau_{ij})}{\partial t}+\frac{\partial(\rho\overline{u_k}\tau_{ij})}{\partial x_k}=\nabla\cdot\mathbf{D}+\mathbf{P}-\frac{2}{3}\mathbf{I}\gamma_M+\Pi_{ij}-\rho\varepsilon_{ij} \tag{2.30}$$

Where:

$\overline{u_j}$ is the mean velocity.

D is the Reynolds Stress Diffusion.

P is the Turbulent Production.

I is the identity tensor.

γ_M is the Dilatation Dissipation.

Π_{ij} is the pressure-strain tensor.

ε_{ij} is the dissipation tensor.

MOST WIEDZY Downloaded from mostwiedzy.pl

Where:

$$\mathbf{D} = \mu \frac{\partial \tau_{ij}}{\partial x_k} + C_{ijk} \tag{2.31}$$

$$C_{ijk} = \rho \overline{u_i' u_j' u_k'} + \overline{p' u_i'} \delta_{ik} + \overline{p' u_j'} \delta_{ik} \tag{2.32}$$

The term **D** was simplified as follows (Lien and Leschziner 1994):

$$\mathbf{D} = \left(\mu + \frac{\mu_t}{\sigma_k}\right) \frac{\partial \tau_{ij}}{\partial x_k} \tag{2.33}$$

$$\mu_t = \rho C_\mu \frac{k^2}{\varepsilon} \tag{2.34}$$

Where, generally the turbulence dissipation rate tensor can be defined as:

$$\varepsilon_{ij} = 2v \overline{\frac{\partial u_i'}{\partial x_k} \frac{\partial u_j'}{\partial x_k}} \tag{2.35}$$

According to Lien and Leschziner (1994) turbulence dissipation rate ε is defined as:

$$\frac{\partial(\rho u_i \varepsilon)}{\partial x_i} = \frac{\partial}{\partial x_i}\left[\left(\mu + \frac{\mu_t}{\sigma_\varepsilon}\right)\frac{\partial \varepsilon}{\partial x_i}\right] + \frac{\varepsilon}{k}(C_{\epsilon 1} P_k - C_{\epsilon 2 \rho} \varepsilon) \tag{2.36}$$

and turbulence production **P** as:

$$\mathbf{P} = -\rho\left(\tau_{ik}\frac{\partial u_j}{\partial x_k} + \tau_{ij}\frac{\partial u_i}{\partial x_k}\right) \tag{2.37}$$

The dilatation dissipation is defined as:

$$\gamma_M = \frac{\rho C_M k \varepsilon}{c^2} \tag{2.38}$$

c – speed of sound

$C_M = 2; \quad \sigma_k = 1; \quad \sigma_\varepsilon = 1; \quad C_{\epsilon 1} = 1.44; \quad C_{\epsilon 2} = 1.92; \quad C_\mu = 0.07$

The pressure strain tensor Π is generally defined as:

$$\prod_{ij} = \overline{p'\left(\frac{\partial u_i'}{\partial x_j} + \frac{\partial u_j'}{\partial x_i}\right)} \tag{2.39}$$

The pressure strain tensor was modelled choosing the elliptic blending model proposed by Lardeau and Manceau (2012):

$$\Pi_{ij} - \varepsilon_{ij} = (1 - \alpha^3)\left(\Pi_{ij}^w - \varepsilon_{ij}^w\right) + \alpha^3(\Pi_{ij}^h - \varepsilon_{ij}^h) \tag{2.40}$$

It is based on the assumption made by Durbin (1991) and Manceau and Hanjalić (2002) that the pressure-strain tensor can be modelled as a blend of near-wall and weakly

MOST WIEDZY Downloaded from mostwiedzy.pl

inhomogeneous models for the pressure-strain and dissipation. Where the blending parameter α can be defined according to the equation:

$$L^2\nabla^2\alpha = 1 \tag{2.41}$$

Where L is the length scale defined as:

$$L = C_l \max\left(\frac{k^{\frac{3}{2}}}{\varepsilon}, C_\eta \frac{v^{\frac{3}{4}}}{\varepsilon^{\frac{1}{4}}}\right) \tag{2.42}$$

Where C_l and C_η are model coefficients equal to 0.133 and 80, respectively.

In the outer region the model proposed by Speziale, Sarkar, and Gatski (1991) is applied according to equation:

$$\Pi_{ij}^h = -\left(C_1 + C_1^*\frac{p}{\varepsilon}\right)\varepsilon a_{ij} + \left(C_3 - C_3^*\sqrt{a_{kl}a_{kl}}\right)kS_{ij} + C_4 k\left(a_{ij}S_{jk} + a_{jk}S_{ik} + \frac{2}{3}a_{lm}S_{lm}\delta_{ij}\right) + C_5 k(a_{ik}W_{jk} + a_{jk}W_{ik}) \tag{2.43}$$

Where S_{ij} and W_{iji} are strain-rate and rotation rate tensor, respectively, and a_{ij} is the anisotropy tensor. The coefficients of the model are as follows:

$C_1 = 1.7;$ $C_1^* = 0.9;$ $C_3 = 0.8;$ $C_3^* = 0.65;$ $C_4 = 0.625;$ $C_5 = 0.2$

The near-wall formulation was as follows:

$$\Pi_{ij}^w = -5\frac{\varepsilon}{k}\left[\overline{u_\iota u_k}n_j n_k + \overline{u_j u_k}n_i n_k - \frac{1}{2}\overline{u_k u_l}n_k n_l\left(n_i n_j + \delta_{ij}\right)\right] \tag{2.44}$$

Where wall normal direction n_k can be computed as:

$$n_k = \frac{\frac{\partial\alpha}{\partial x_k}}{\sqrt{\frac{\partial\alpha}{\partial x_l}\frac{\partial\alpha}{\partial x_l}}} \tag{2.45}$$

The dissipation tensors are:

$$\varepsilon_{ij}^w = \frac{\overline{u_\iota u_k}}{k}\ \varepsilon_{ij}^h = \frac{2}{3}\varepsilon_{ij} \tag{2.46}$$

Where the ε is solved as it has place for $k-\varepsilon$ model.

The turbulent time scale T is equal to:

$$T = \max\left(\frac{k}{\varepsilon}, C_t\sqrt{\frac{v}{\varepsilon}}\right) \tag{2.47}$$

Where $C_t = 6$

The additional source term is added to transport equation according to equation:

MOST WIEDZY Downloaded from mostwiedzy.pl

$$E = A_1 v\overline{u_k u_l} n_k n_l \frac{k}{\varepsilon} (1 - \alpha^3) \left(\frac{\partial \left| \left| S_{ij} n_i \right| \right| n_k}{\partial x_j} \right)^2 \tag{2.48}$$

Where $A_1 = 0.115$

For DES approach, the LES was coupled with $k - \omega$ SST model. The LES approach allows to resolve greater scales, while small scales are modelled using RANS approach (Çengel and Cimbala 2018). The DES allows for combining advantages of both approaches. It uses the RANS formulations inside the boundary layer of the body and switches to LES in the detached region (Menter and Kuntz 2004). Such an approach allows reducing orders of magnitude of computing resources.

2.5.2. Computational Fluid Dynamics - Verification study

Verification study has a purpose of comparing the lift and drag curves for three meshes of different resolution and four different turbulence models. Flow around the fin was modelled as a single-phase, turbulent, viscous, and incompressible. Three RANS turbulence models were used for the computations: $k - \varepsilon$ model and $k - \omega$ SST, RST turbulence model, and DES approach (LES blended with $k - \omega$ SST turbulence model).

The size of the domain was set according to International Towing Tank Conference guidelines (ITTC 2011, ITTC 2014). According to them, if a significant lift force is generated by the lifting surface, then the upstream boundary plane should be placed at least ten chord lengths c in front of the body and the downstream boundary twenty chord lengths behind it. This rule was used for the simulations, but, due to so small chord of the fin it was decided to additionally extend the domain length so that it was equal to 6 meters. Side boundaries were placed two meters from the fin. The top boundary was overlapping with the head of the fin. The bottom boundary was placed 0.84 meters below the tip. For the upstream and bottom boundaries, the velocity inlet condition was selected. The downstream boundary had assigned the pressure outlet condition. The symmetry condition was assigned to the top and side boundaries.

The implicit unsteady solver was used with the first order temporal discretisation scheme. The time step was selected so that the Courant number was kept below 5 for majority of the cells around the fin. The resulting time step was equal to 0.001 s.

To capture the relevant features of the flow, mesh refinements were applied on the tip and nose of the fin, in the proximity of the model, and in the wake region including the area of tip vortex generation. The mesh coarsening was applied on the outside domain boundaries, where the high number of cells is unnecessary. The mesh sensitivity analysis was performed by varying the value of y^+, which is defined as:

$$y^+ = \frac{u^*}{\vartheta} \tag{2.49}$$

Where u^* stands for the friction velocity, y is the distance to the wall, and ϑ is the kinematic viscosity. For obtaining the desired y^+, the value of y needs to be estimated. The STAR CCM+

MOST WIEDZY Downloaded from mostwiedzy.pl

software was used for computation. Defining the mesh topology using prism layers allows for accurate resolving of the boundary layer and saving of computational resources.

The mesh sensitivity study can also be done by systematic variation of the base size element and maintaining the same mesh resolution in the area of prism layer. It was decided that in presented case, the boundary layer resolution is more influential parameter, and the general mesh resolution is good.

The prism layer cells have thickness significantly smaller than the remaining dimensions (Siemens PLM Software 2017). For defining the mesh resolution with prism layers, the total thickness, the number of layers, and thickness growth ratio (stretch factor) must be specified.

The thickness of the first layer can be specified using the formula for the first term of geometric series:

$$y_1 = \frac{\delta_X(1-r)}{1-r_n} \tag{2.50}$$

Where:

δ_X– thickness of a boundary layer,

r - common ratio – stretch factor,

n – number of terms – number of prism layers.

The length-dependent thickness of the boundary layer was estimated according to the formula:

$$\frac{\delta_X}{x} = 0.37\, Re_X \tag{2.51}$$

Where:

x - position in the longitudinal direction (length of the body along the vector of the flow velocity),

Re_X – Reynolds number.

It can be noticed that there are three ways for controlling the y^+: the thickness of the prism layer, the number of prisms, and the modification of the stretch factor. It was decided that the parameter that controlled the value of y^+ was the number of prism layers. Too high stretch factor can result in calculation divergence, whereas the thickness of the prism layer should at least closely reflect the physical thickness of the boundary layer. Table 2.1 gives the details about the mesh resolution.

Table 2.1. Summary - mesh resolution.

	M1	**M2**	**M3**
Cell Count	5.4 M	7.1 M	7.8M
Number of prisms	8	14	20
Stretch factor.	1.3	1.3	1.25
y^+	40	3.8	1.8

MOST WIEDZY Downloaded from mostwiedzy.pl

Due to convergence issues, the M3 had the stretch factor equal to 1.25, while the remaining meshes had the stretch factor equal to 1.3. The computational mesh is presented in Figure 2.11.

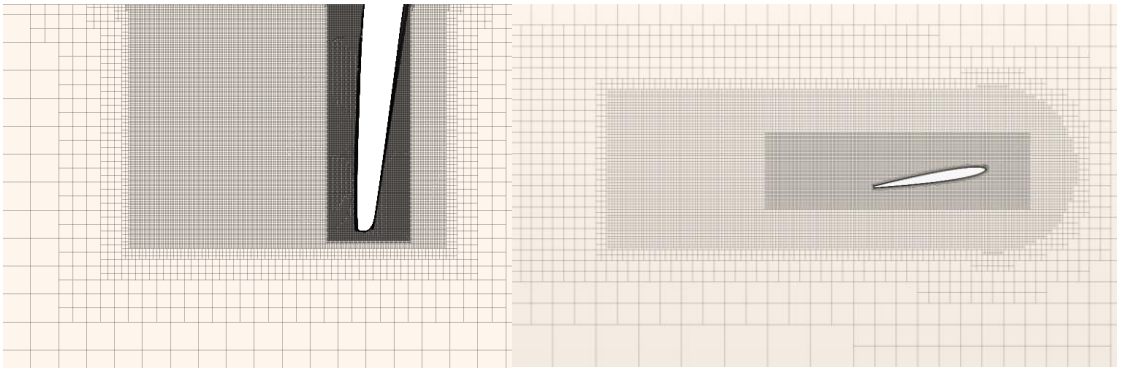

Figure 2.11 Computational mesh used for numerical simulations.

During the calculations, the mesh was slightly adjusted, especially in the region of the hydrofoil leading edge so that the volumetric refinements followed the new position of the leading edge after updating the angle of attack. The verification study was done for a wide range of angles of attacks: from 2 degrees, up to 10 degrees angle of attack. Within this range of angle of attack the occurrence of the critical angle of attack (stall angle) is expected. The calculations were performed for the speed of 10 m/s, which corresponds to Reynolds number of $Re = 1.2 \cdot 10^6$ and justifies the selection of the turbulent flow model.

2.5.3. Computational Fluid Dynamics - Validation study

In order to perform due diligence in the conducted research as well as due to the limitations of the Gdańsk University of Technology hydrodynamic laboratory it was decided to perform additionally a validation study for an object similar to RS:X with a published and well documented experimental study. The towing tank at the Gdańsk University of Technology has a length of 40 meters and maximum speed of the towing carriage is equal to 2.5 m/s. This speed is well below the speed of the RS:X windsurfing board that it within the interest of this research. The forces that can be measured for such object are small and yielding high level of uncertainty.

The requirement for the similar tested object was that it has to be the tapered hydrofoil with a symmetrical profile and similar to RS:X fin aspect ratio. Additional requirements included the experimental conditions – the hydrofoil had to be tested at a high Reynolds number. It needed to be placed inside the measurement zone so that only the top edge of the object is attached to the channel wall. The experiments in Zarruk et al. (2014) fulfil all the requirements above. The main goal of this part of the investigation was to study again the various turbulence model with the reference to the experimental results.

The trapezoidal wing with modified NACA 0009 profile was generated using Siemens NX software. The chord length at the head of the foil was equal to 0.12 m, while at the root, it was equal to 0.06 m. The span was equal to 0.3 m. The 3D model of the hydrofoil used for the validation study is presented in Figure 2.12.

MOST WIEDZY Downloaded from mostwiedzy.pl

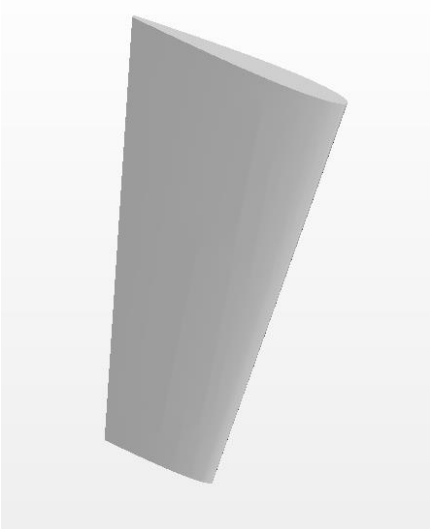

Figure 2.12 3D model of hydrofoil for the CFD validation study.

The numerical simulations were performed both using unsteady RANS solver and DES approach. Four turbulence models were compared with each other: $k-\varepsilon$ model and $k-\omega$ SST, RST turbulence model, and DES approach.

Flow around the fin was again modelled as a single-phase, turbulent, viscous, and incompressible. The free stream water velocity corresponding to the Reynolds number equal to Re = $0.6*10^6$ was taken as a reference for the validation data. During the experiment, the hydrofoils of various materials were tested. The rigid stainless steel hydrofoil was chosen for the benchmark because it can be treated as realistically non-deformable. The inlet boundary conditions were specified based on the data presented in the article. Therefore, the velocity of the free stream was equal to 5.94 m/s, and turbulence intensity was equal to 0.005. The size of the domain was the same as for the RS:X fin verification study, so was the boundary conditions.

The numerical mesh used for the validation study was similar to the one described in Chapter 2.5.2. The resolution inside the region of the boundary layer was the same as for the Mesh 2 of verification study (M2 – See Chapter 2.5.2). First of all, it seemed to be a reasonable compromise between the mesh quality and computational time. Secondly, due to the lower Reynolds number of the validation case, the result in y^+ value was equal to the y^+ = 1.5. It complies with necessity to keep $y^+ \approx 1$ for accurate stall prediction (Siemens PLM Software 2017). The calculations were performed for the range of angle of attack from 9 degrees to 12 degrees. According to the experimental findings, the stall occurred at the 10.5 degree angle of incidence. Therefore, the selected range of tested angles of attack was considered the most challenging for accurate resolving.

2.5.4. Lifting Line Theory

The CFD model was compared with the potential flow model of lifting line based on the Prandtl lifting line theory. It is based on the idea that the three-dimensional wing with particular span and aspect ratio AR can be replaced by the straight line. It is assumed that the circulation about the wing section, which is associated with the lift production is replaced by a vortex filament

MOST WIEDZY Downloaded from mostwiedzy.pl

located along that straight line. The strength of the vortex is proportional to the local intensity of lift at each spanwise location. The Helmholtz theory states that the vortex filament cannot terminate in the fluid. Therefore, it is assumed that the variation of the vortex strength along the lifting line is the superposition of some number of horseshoe-shaped vortices. The vortices that lie along the span are the bound vortices, and the downstream vortices are called the trailing vortices. There are schematically presented in Figure 2.13.

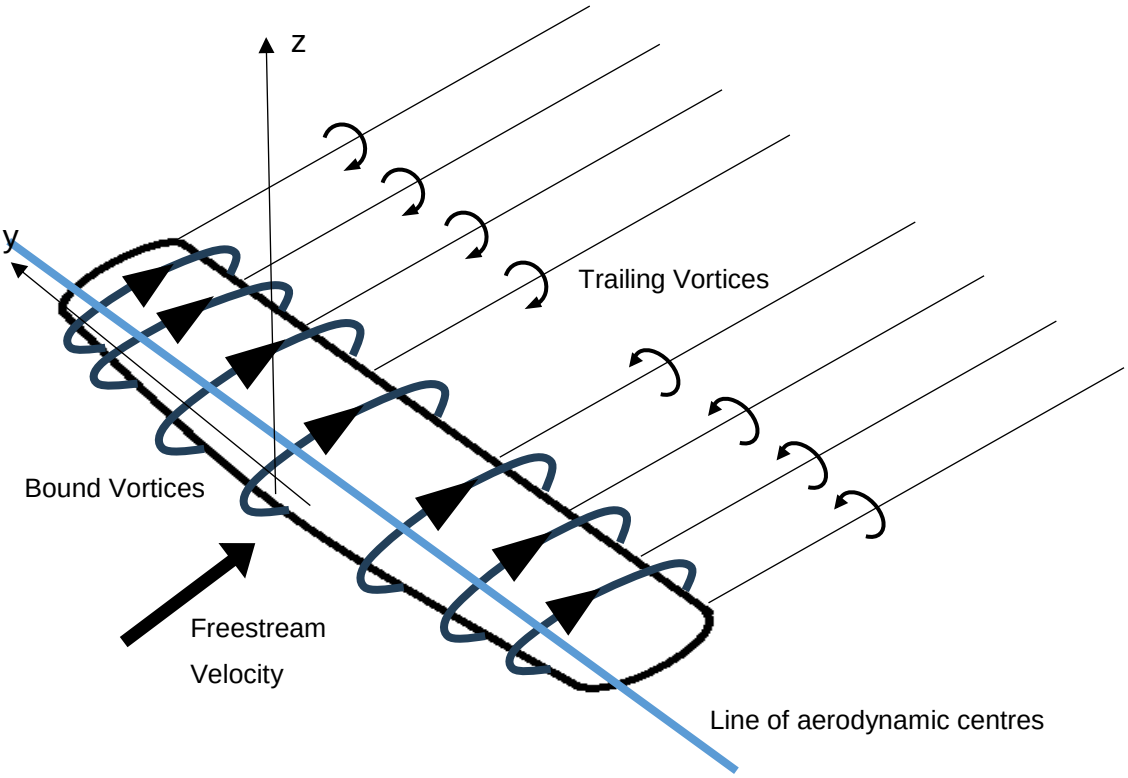

Figure 2.13 Trailing and bound vortices

Usually the bound vortices (circulation Γ(y)) are placed on a line located along the leading edge of the lifting plane at a distance equal to 25% of the chord c.

The spanwise definition of the lift coefficient is defined as follows:

$$C_l(y) = \frac{F_Z(y)}{\frac{\rho}{2}U^2(y)c(y)} = \frac{2\Gamma}{U(y)c(y)} \tag{2.52}$$

The circulation Γ around the lifting surface can be written as:

$$F_Z(y) = \rho U\, \Gamma(y) \tag{2.53}$$

For small angles of attack, the circulation and lift force coefficient depend linearly on the lifting surface angle of attack, therefore:

$$C_l(y) = 2\pi[\alpha(y) - \alpha_0(y)] \tag{2.54}$$

MOST WIEDZY Downloaded from mostwiedzy.pl

Where $\alpha(y)$ is the angle of attack, i.e. the angle formed by the incoming flow and the vortex line, and $\alpha_0(y)$is the so-called angle of zero lift force.

Assuming the elliptical shape of the wing yielding elliptical lift spanwise distribution the lift and induced drag coefficients of the entire wing can be written as:

$$C_L = \frac{2\pi}{1+\frac{2}{AR}}(\alpha_{2D} - \alpha_0) \quad C_{Di} = \frac{1}{\pi AR} C_L^2 \tag{2.55}$$

Where α_{2D} is the two-dimensional flow ange of attack. The induced drag is attributed to generation of the lift by the three-dimensional wing. At the tips of the wing occurs vortices that generates down wash. The down wash causes variation of the local angle of attack and additional component in the aerodynamic force facing downstream, which is called induced drag. For the square or trapezoidal-shaped wing section the lift distribution is different than for the elliptical wings, and the induced drag is greater than for the elliptical-shaped wing section.

The lifting line approximation were applied by Matusiak (2022) in the Vortex Lattice Method to calculate the lift and drag force of the wing. The Vortex Lattice Method bases on the assumption that continuous distribution of circulation around the wing can be discretised after implementing boundary conditions at so-called control points, and the discrete vortexes intensities can be obtained. The bound vortices are represented by the discrete distribution of circulation parallel to the lifting surface.

The lifting surface is approximated by the lifting line located parallel to the leading edge on the distance of 25% of the chord length c. Unknown bound vortices Γ_i are placed on the lifting line. For each i-sector, it is assumed that the bound circulation intensity is constant. Each segment is represented by horseshoe vortex, and it includes a collocation point. It is located at a distance of 0.75 ci from the leading edge, i.e. $c_i/2$ at a distance from the bound vortex. The induced velocity w_k at the collocation point *k* is the sum of the induced velocities of all horseshoe vortexes, i.e.:

$$w_k = \sum_{i=1}^{N}(w_{k,i}^b + w_{k,i}^f) = \sum_{i=1}^{N}(a_{k,i}^b + a_{k,i}^f)\Gamma_i = \sum_{i=1}^{N} a_{k,i}\Gamma_i \tag{2.56}$$

Where $a_{k,i}$ are the influence coefficients dependent on the lifting surface geometry and its discretisation. Superscript b stands for bound vortex and superscript f for the effect of free vortices.

The vortices Γ_i are calculated using the kinematic boundary condition:

$$w_k = U_k(-\alpha_{2D,k} + \alpha_{0,k}) \tag{2.57}$$

Therefore, the set of equations for all collocation points can be constructed, and in the matrix form it can be written as:

$$[a]\{\Gamma\} = \{U(-\alpha_{2D} + \alpha_0)\} \tag{2.58}$$

MOST WIEDZY Downloaded from mostwiedzy.pl

Where $[a]$ is a matrix composed of a-coefficients and $\{\Gamma\}$ is a matrix of unknown values of circulation formed vector. The solution of equation (2.58) produces circulation values at all collocation points:

$$\{\Gamma\} = [a]^{-1}\{U(-\alpha_{2D} + \alpha_0)\} \tag{2.59}$$

If the incoming flow is uniform the values of lift and drag coefficient are calculated according to the formula:

$$C_L = \frac{F_z}{\frac{1}{2}\rho U^2 A} = -\frac{\sum_{k=1}^{N} \Gamma_k \Delta y_k}{UA} \tag{2.60}$$

$$C_D = \frac{F_X}{\frac{1}{2}\rho U^2 A} = \frac{\sum_{k=1}^{N} \Gamma_k \, w_{\infty,k} \, \Delta y_k}{UA} \tag{2.61}$$

Where:

$$w_{\infty,k} = \sum_{i=1}^{N} c_{k,i} \, \Gamma_i \tag{2.62}$$

is the flow rate induced by free vortices far downstream. Coefficients $c_{k,i}$ are equal to:

$$c_{k,i} = -\frac{1}{4\pi}\left[\frac{1}{y_k - \left(y_i - \frac{\Delta y_i}{2}\right)} - \frac{1}{y_k - \left(\frac{\Delta y_i}{2}\right)}\right] \tag{2.63}$$

and y_k is the y-coordinate of k control point, y_i is the y-coordinate of the middle of i-th section, Δy_i is the width of the section.

The calculations of the hydrodynamic forces were performed using *lifting line* programme by Matusiak (2022). One of the limitations was the selection of the hydrofoil planform shape. Only trapezoidal or elliptical shape can be chosen. Following the suggestion of the programme's author, the trapezoidal section was selected to represent the simplified shape of the RS:X fin. Moreover, programme perform the calculations for foil with two free tips, while the RS:X fin has only one free tip. As a result, the effective aspect ratio AR_{Ef} of the RS:X fin is twice as large as geometric aspect ratio AR which is calculated according to formula:

$$AR = \frac{s^2}{A} \tag{2.64}$$

To correct these differences, the span of the hydrofoil that modelled the RS:X fin in *lifting line* programme has been doubled. As a result, the effective aspect ratios, crucial for hydromechanical calculations, of both hydrofoils are the same. Figure 2.14 presents the comparison of the RS:X fin with the simplified shape defined in *lifting line* programme.

MOST WIEDZY Downloaded from mostwiedzy.pl

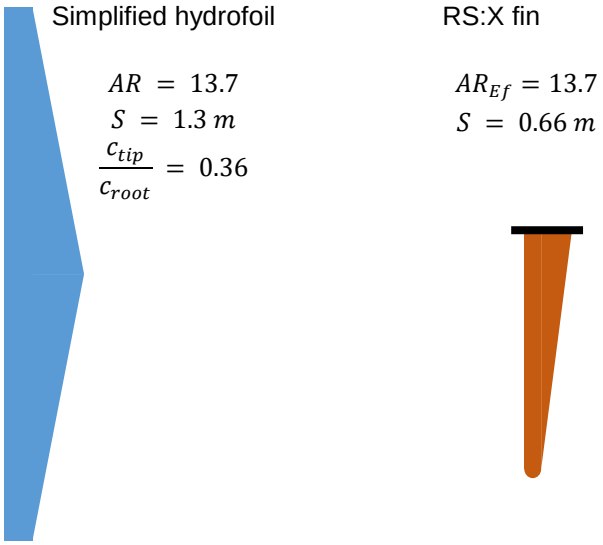

Figure 2.14 The geometry comparison – lifting line and CFD.

The outputs of the *lifting line* programme are lift coefficient $C_L(\alpha)$ and induced drag coefficient $C_{DI}(\alpha)$.

The total drag coefficient C_D, which is directly obtained from the CFD calculations can be decomposed into the sum of the profile drag C_{DP}, induced drag C_{DI} and skin friction drag C_F. As aforementioned, the *lifting line* programme provides only with the values of induced drag coefficient C_{DI}. To compare the results of CFD and *lifting line* calculations, the remaining components of the drag coefficient need to be determined. The value of friction drag coefficient C_F can be calculated according to formula:

$$C_F = \frac{0.075}{(\log Re - 2)^2} \tag{2.65}$$

which is ITTC-57 skin friction line. The profile drag $C_{DP}(\alpha)$ will be taken for NACA 0009, according to findings by Hansen, Gourlay, and King (2011) that profile of the RS:X resembles NACA 0009. The profile drag $C_{DP}(\alpha)$ characteristics are presented by Abbott and Von Doenhoff (1959).

2.6. Finite Element Method

2.6.1. Finite Element Method Principle

The Finite Element Method (FEM) is somewhat similar to Finite Volume Method, since it is based on the idea of discretization, which is dividing large and complex system into smaller elements. The individual behaviour of each element is integrated, and it allows to obtain the wider knowledge about the entire system (Zienkiewicz, Taylor, and Zhu 2013). The FEM is the method developed for solving complex systems of non-linear differential equations and find its application in the field of mechanical engineering. Application of FEM allows to study the displacement, forces, and stresses of the structure.

The discretization in FEM bases on dividing the structure into the finite number of elements (it is related to the complexity of the problem) with simplified geometric and physical

MOST WIEDZY Downloaded from mostwiedzy.pl

parameters and computational nodes which connects neighbouring elements (Rakowski and Kacprzyk 2016).

The system contains a finite number of elements and nodes. If forces acting on the structure are reduced to forces acting on the nodes it is possible to define the vector of nodal forces according to Eq. 2.66:

$$\boldsymbol{R} = \{\boldsymbol{R}_1 \boldsymbol{R}_2 \dots \boldsymbol{R}_n\} \tag{2.66}$$

With $\boldsymbol{R}_i$ being the elements of vector $\boldsymbol{R}$ containing components of forces and moments. The reaction of the construction is the displacement which is represented as a vector of nodal displacements:

$$\boldsymbol{u} = \{\boldsymbol{u}_1 \boldsymbol{u}_2 \dots \boldsymbol{u}_n\} \tag{2.67}$$

If the element is characterised by linear elastic behaviour, the relation between forces and displacement can be written as:

$$\boldsymbol{K} \cdot \boldsymbol{u} - \boldsymbol{Q} = \boldsymbol{R} \tag{2.68}$$

Where $\boldsymbol{K}$ is the stiffness matrix, and $\boldsymbol{Q}$ are the forces required to balance loads acting on the elements. If the displacements are continues and compatible in each node, and if in each node occurs equilibrium then the Eq. 2.68 can be simplified to:

$$\boldsymbol{K} \cdot \boldsymbol{u} = \boldsymbol{R} \tag{2.69}$$

Equation 2.69 is a system of equations binding forces and displacements in each node. After applying boundary conditions and solving such a system, the deformation of the entire structure can be determined.

2.6.2. Stress-strain relationship

For the three-dimensional problem, the displacement field in the Cartesian coordinate system is given by:

$$\mathbf{u}(\mathbf{x}, t) = \begin{Bmatrix} u_S(x, y, z, t) \\ v_S(x, y, z, t) \\ w_S(x, y, z, t) \end{Bmatrix} \tag{2.70}$$

Whereas the six independent components of the strain matrix can be written as:

$$\varepsilon = \begin{bmatrix} \varepsilon_x \\ \varepsilon_y \\ \varepsilon_z \\ \gamma_x \\ \gamma_y \\ \gamma_z \end{bmatrix} \tag{2.71}$$

Where first three elements are the linear strains and last three are angular strains.

MOST WIEDZY Downloaded from mostwiedzy.pl

For the small displacement problem, the strains are the derivatives of displacements are defined as:

$$\varepsilon = \begin{bmatrix} \varepsilon_x \\ \varepsilon_y \\ \varepsilon_z \\ \gamma_x \\ \gamma_y \\ \gamma_z \end{bmatrix} = \begin{bmatrix} \frac{\partial}{\partial x} & 0 & 0 \\ 0 & \frac{\partial}{\partial y} & 0 \\ 0 & 0 & \frac{\partial}{\partial z} \\ \frac{\partial}{\partial y} & \frac{\partial}{\partial x} & 0 \\ 0 & \frac{\partial}{\partial z} & \frac{\partial}{\partial y} \\ \frac{\partial}{\partial z} & 0 & \frac{\partial}{\partial x} \end{bmatrix} \begin{Bmatrix} u_S \\ v_S \\ w_S \end{Bmatrix} \tag{2.72}$$

The stresses in the three-dimensional body are presented in Figure 2.15. There are two kinds of components: normal stresses σ_x, σ_y and σ_z and shear stress components: $\tau_{xy}, \tau_{yx}, \tau_{yz}, \tau_{zy}, \tau_{xz}$ and τ_{zx}. However, the shear stresses are symmetrical, and it can be written:

$$\tau_{xy} = \tau_{yx}, \qquad \tau_{yz} = \tau_{zy}, \qquad \tau_{xz} = \tau_{zx}$$

Therefore, the stress matrix can be written like strain matrix as:

$$\sigma = \begin{bmatrix} \sigma_x \\ \sigma_y \\ \sigma_z \\ \tau_{xy} \\ \tau_{yz} \\ \tau_{xz} \end{bmatrix} \tag{2.73}$$

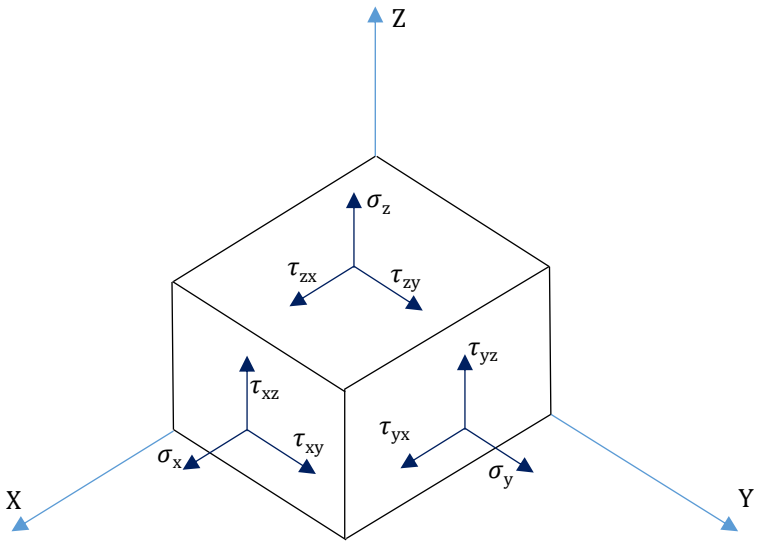

Figure 2.15 Normal and shear stresses for the finite element.

For isotropic material, the relation between the stress and strain is presented in Equation 2.74:

MOST WIEDZY Downloaded from mostwiedzy.pl

$$\begin{Bmatrix} \varepsilon_x \\ \varepsilon_y \\ \varepsilon_z \\ \gamma_x \\ \gamma_y \\ \gamma_z \end{Bmatrix} = \frac{1}{E} \begin{bmatrix} 1 & -v & -v & 0 & 0 & 0 \\ -v & 1 & -v & 0 & 0 & 0 \\ -v & -v & 1 & 0 & 0 & 0 \\ 0 & 0 & 0 & 2(1+v) & 0 & 0 \\ 0 & 0 & 0 & 0 & 2(1+v) & 0 \\ 0 & 0 & 0 & 0 & 0 & 2(1+v) \end{bmatrix} \begin{Bmatrix} \sigma_x \\ \sigma_y \\ \sigma_z \\ \tau_{xy} \\ \tau_{yz} \\ \tau_{zx} \end{Bmatrix} \tag{2.74}$$

Where E is Young Modulus and v is the Poisson ratio. For the linear elastic material, the Shear Modulus G is calculated according to Eq. 2.75:

$$G = \frac{E}{2(1+v)} \tag{2.75}$$

Since for modelling the fin structure the isotropic material was selected presented material constants are the main parameters describing the material and necessary of obtaining stress-strain-displacement fields. The reason for choosing the isotropic material approximation for modelling composite material is deeply discussed in Chapter 2.6.5.

2.6.3. Types of elements in Finite Element Method

There are many different types of elements with different complexity and for various purposes, in this section I will focus on those that are the most common for Finite Element Method coupled with aero and hydrodynamic solvers.

- 1-D beam element

This approach bases on the Euler-Bernoulli or Timoshenko beam theory. The 3D structure is simplified into a 1D structure which is concentrated along the elastic axis of the beam (Hansen et al. 2006). This approach is quite common for modelling the wind turbine blades deformation under the aerodynamic loads (Malcolm and Laird 2003). For blade turbines it is sufficient to use the classical beam theory since the turbine blades are relatively stiff. The structural properties are assumed to vary linearly along the beam length. However, for more flexible objects, such as helicopter blades, the non-linear beam models were also introduced (Hansen et al. 2006), (Kunz 1994).

- Plate element

The plate elements are the elements whose thickness t is significantly smaller than remaining two dimensions ($t << a \cup b$) and forces are acting perpendicular to mid-plane. There are two types of formulation for plate elements: thick and thin, the plate is considered as thin if the thickness is less 0.1 of greater of remaining span directions. Plate element is subjected to torsion and bending in two directions (Rakowski and Kacprzyk 2016). There are two kinds of basic plate elements: three and four nodded elements. Displacement *w* along Z-axis and angular rotation of nodes φ_x, φ_y is the result of force W and moments M_x and M_y acting on the element. This is schematically presented in Figure 2.16.

MOST WIEDZY Downloaded from mostwiedzy.pl

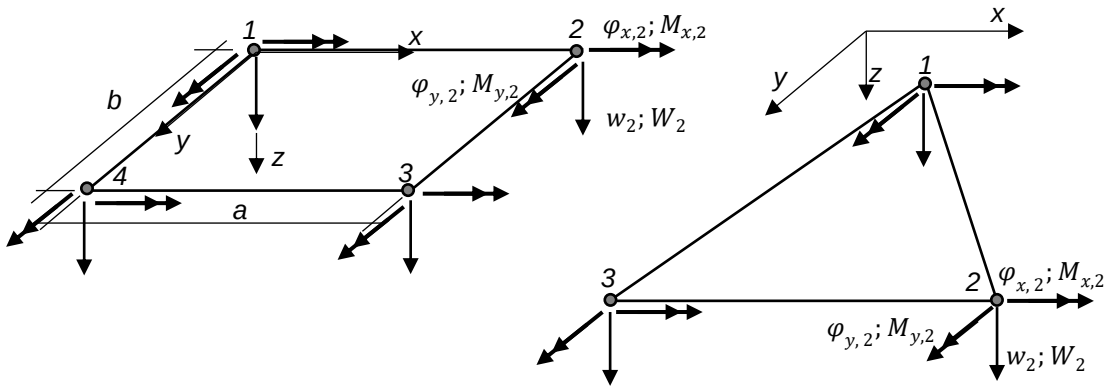

Figure 2.16 Plate elements degrees of freedom.

For the four-nodded element the stiffness matrix has 12 x 12 components, while for three-nodded element it is 9 x 9 component matrix. For the three nodded element the stiffness matrix is:

$$\boldsymbol{K} = A\frac{E\,t^3}{(1-\nu^2)}\begin{bmatrix} k_{11} & k_{12} & \cdots & k_{19} \\ k_{21} & k_{22} & \cdots & k_{29} \\ \vdots & & & \vdots \\ k_{91} & k_{92} & & k_{99} \end{bmatrix} \tag{2.76}$$

Where *A* is element area, *t* is plate thickness and E is Young Modulus.

- Shell element

The shell elements unlike the plane elements could be also curved, however, similar to them, the thickness is much smaller than remaining two dimensions. Shell element is the combination of the plate and membrane. Therefore, the stress acting on the middle surface of the shell has tangential and normal components. For the basic formulation of shell elements, three and four nodded elements are used. Shell elements were used for modelling the outer layer of the analysed fin structure laminate.

- 3D elements

There are several types of 3D elements, which include tetrahedral elements, wedges, pyramids, and hexahedral elements. The tetrahedral elements were used for modelling of windsurfing fin, and they are briefly characterized in this point.

The simplest tetrahedral elements have four nodes, and the displacement field has three components that is dependent on three variables: $u_S(x,y,z)$, $v_S(x,y,z)$ and $w_S(x,y,z)$. In FEM the higher order tetrahedral elements are also used, one of the examples is 10-noded tetrahedral.

In simple tetrahedral elements stress and strains are constant inside the element. In higher order elements this limitation is eliminated.

Figure 2.17 a) presents typical tetrahedral element, and b) is an example of ten-nodded tetrahedral elements.

MOST WIEDZY Downloaded from mostwiedzy.pl

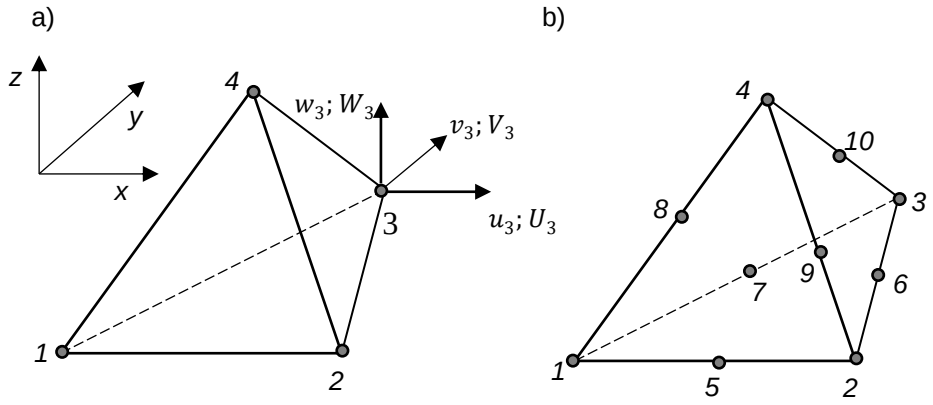

Figure 2.17 Tetrahedral elements.

Tetrahedral elements enable to model objects with various and more complicated shapes, and application of higher order elements allows for application of coarser mesh, compared to standard hexahedral elements.

2.6.4. Modelling composite materials

Composite materials are made of two or more different immiscible materials, with various properties, which form one non-uniform structure. Typically, in the mechanical engineering field composite materials consist of matrix and reinforcement. The former is responsible for transferring the loads between the reinforcements and binding the fibres together, which plays the role of stiffener of the structure. There are different types of materials that can be used as constituents of composite structures – metal, ceramic or polymeric. In general, the composites are considered anisotropic material, which mean that the mechanical properties vary in each direction. The special case of anisotropic material is orthotropic material, which show a symmetry between two planes (Müzel et al. 2020). This study focuses on composites with composites polymeric matrix and reinforcements made of carbon and glass fibre, namely Carbon Fibre Reinforced Polymers (CFRP) and Glass Fibre Reinforced Polymers (GFRP).

Two types of fibre reinforcements are in practice used: unidirectional and bi-directional plies (bi-directional woven). The unidirectional fibres exhibit anisotropy, since the strength in the in-fibre direction is significantly greater than in perpendicular to fibre direction. The bi-directional woven ply has the major stiffness in both directions. The laminate can also have quasi-isotropic properties if plies are orientated in multiple directions [0^0/ 45^0/ 90^0/ -45^0] regarding to the object main axes (Xu, Mkaddem, and El Mansori 2016).

There are two main approaches for describing the properties of laminate:

- specifying the constitutive equations;
- specifying laminate stacking sequence.

MOST WIEDZY Downloaded from mostwiedzy.pl

Composite structures are mostly modelled shells; therefore, their description is based on the shell theory. To obtain composite structure with desired properties the laminate consists of multiple layers (uni- or bi-directional) of different orientation with regard to the main material axes. According to Barbero (2013) the laminate constitutive equations are derived by employing the definition of stress resultants, which are the stress components integrals through the thickness of the shell, as presented in Eq. 2.77.

$$\begin{Bmatrix} N_x \\ N_y \\ N_{xy} \end{Bmatrix} = \sum_{k=1}^{N} \int_{z_{k-1}}^{z_k} \begin{Bmatrix} \sigma_x \\ \sigma_y \\ \sigma_{xy} \end{Bmatrix}^m dz$$

$$\begin{Bmatrix} V_x \\ V_y \end{Bmatrix} = \sum_{k=1}^{N} \int_{z_{k-1}}^{z_k} \begin{Bmatrix} \sigma_{yz} \\ \sigma_{xz} \end{Bmatrix}^m dz$$

$$\begin{Bmatrix} M_x \\ M_y \\ M_{xy} \end{Bmatrix} = \sum_{k=1}^{N} \int_{z_{k-1}}^{z_k} \begin{Bmatrix} \sigma_x \\ \sigma_y \\ \sigma_{xy} \end{Bmatrix}^m z\, dz \tag{2.77}$$

Where:

σ_x, σ_y are normal stresses and $\sigma_{xy}, \sigma_{xz,}\sigma_{yz}$ and are shear stress components.

N_x, N_y, N_{xy} are in-plane forces per unit length.

M_x, M_y, M_{xy} are in-plane moments per unit length.

V_x, V_y are shear forces per unit length.

N is number of layers.

m is number of analysed layers.

z is z-coordinate.

To obtain constitutive equations, the plane stress version of the constitutive equations needs to be replaced by shell coordinates at each layer, and then integrated. As a result, the following relation is obtained:

$$\begin{Bmatrix} N_x \\ N_y \\ N_{xy} \\ M_x \\ M_y \\ M_{xy} \end{Bmatrix} = \begin{bmatrix} \mathrm{A}_{11} & \mathrm{A}_{21} & \mathrm{A}_{16} & \mathrm{B}_{11} & \mathrm{B}_{21} & \mathrm{B}_{16} \\ \mathrm{A}_{12} & \mathrm{A}_{22} & \mathrm{A}_{26} & \mathrm{B}_{12} & \mathrm{B}_{22} & \mathrm{B}_{26} \\ \mathrm{A}_{16} & \mathrm{A}_{26} & \mathrm{A}_{16} & \mathrm{B}_{16} & \mathrm{B}_{26} & \mathrm{B}_{66} \\ \mathrm{B}_{11} & \mathrm{B}_{21} & \mathrm{B}_{16} & \mathrm{D}_{11} & \mathrm{D}_{12} & \mathrm{D}_{16} \\ \mathrm{B}_{12} & \mathrm{B}_{22} & \mathrm{B}_{26} & \mathrm{D}_{12} & \mathrm{D}_{22} & \mathrm{D}_{26} \\ \mathrm{B}_{16} & \mathrm{B}_{26} & \mathrm{B}_{66} & \mathrm{D}_{16} & \mathrm{D}_{26} & \mathrm{D}_{66} \end{bmatrix} \begin{Bmatrix} \epsilon_x^0 \\ \epsilon_y^0 \\ \gamma_{xy}^0 \\ \kappa_x \\ \kappa_y \\ \kappa_{xy} \end{Bmatrix}$$

$$\begin{Bmatrix} V_x \\ V_y \end{Bmatrix} = \begin{bmatrix} H_{44} & H_{45} \\ H_{45} & H_{55} \end{bmatrix} \begin{Bmatrix} \gamma_{yz} \\ \gamma_{xz} \end{Bmatrix} \tag{2.78}$$

Where:

$$A_{ij} = \sum_{m=1}^{N} \left(\bar{Q}_{ij}\right)_m t_m \;\; i,j = 1,2,6$$

$$B_{ij} = \sum_{m=1}^{N} \left(\bar{Q}_{ij}\right)_m t_m \bar{z}_m; \;\; i,j = 1,2,6$$

MOST WIEDZY Downloaded from mostwiedzy.pl

$$D_{ij} = \sum_{m=1}^{N} \left(\bar{Q}_{ij}\right)_m \left(t_m \bar{z}_m^2 + \frac{t_m^3}{12}\right) \; i,j = 1,2,6$$

$$H_{ij} = \frac{5}{4} \sum_{m=1}^{N} \left(\bar{Q}_{ij}^*\right)_m \left[t_m - \frac{4}{t^2}\left(t_m \bar{z}_m^2 + \frac{t_m^3}{12}\right)\right] \; i,j = 4,5$$

Where:

$\bar{Q}_{ij}$ – are coefficients in laminate coordinates of the plane-stiffness matrix for layer m and $\bar{z}_k$coordinate of the middle surface of m-th layer.

A_{ij}- is the coefficient representing in-plane stiffness.

B_{ij} - is bending-extension coupling.

D_{ij}- is the bending stiffness.

H_{ij}- is the interlaminar shear stiffness.

The former mentioned approach for specifying the properties of laminate is defining the stacking sequence – the number and thickness of layers with their orientation with the regard to the main material axes. Moreover, the elastic properties of laminate constituents need to be specified.

Modelling and analysis of composite material covers investigation in different material behaviour in relation to the scale of the object presented in Figure 2.18, According to Tan et al. (2018), three scales can be distinguished:

- microscale;
- mesoscale;
- macroscale.

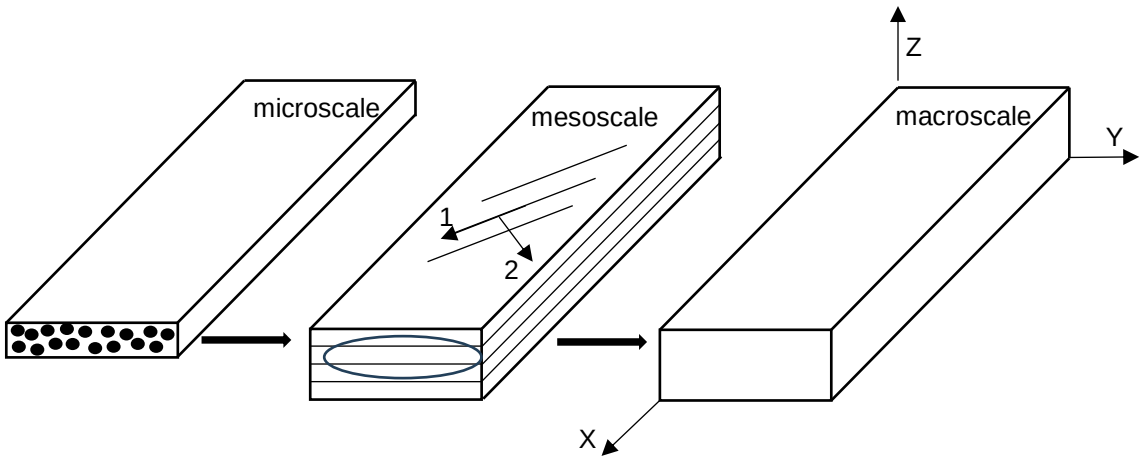

Figure 2.18 Macro, meso and microscale of composite structure.

In microscale the properties of composite constituents are characterised, for example fibre volume fraction and spatial distribution, properties of matrix and fibre and interface between them. The fibre and matrix are modelled separately together with connection between them. Microscale analysis allows to study stress and strains at the constituent levels, as well as

MOST WIEDZY Downloaded from mostwiedzy.pl

complicated failure mechanism. The result of a microscale analysis can be used to specify the properties of a singular ply (lamina) at the mesoscale level.

If the information about stress and strains in each lamina is desired, then it is necessary to perform the mesoscale analysis. At this level different plies are included: the interlaminar properties, ply behaviour and laminate lay-up (stacking sequence). In meso-models the composite is assumed to be formed by stack of single lamina with unidirectional fibres. It allows to study numerous types of non-linear phenomena and damages related to matrix failure modes, interlaminar failure mechanisms and fibres failures (Toledo, Nallim, and Luccioni 2008). The result of the meso-scale analysis can be used to obtain the properties of the homogenized laminate. The calculation of stresses in lamina constituents allows to obtain the global stresses and strains for laminate elastic properties determination (Mustafa, Suleman, and Crawford 2015).

The largest length scale is the macroscale which focuses on assembly of different laminate components. It includes properties and shape of the structure components and connection between various parts. The elements of the structure are considered as a homogeneous equivalent material. This approach is desired when the displacements, buckling loads and modes or vibration frequencies and modes are wanted, whereas the stresses inside the material are not the main interest. The result of macroscale analysis is the characterization of the structural behaviour of the entire large composite object, such as wind turbine blade or windsurfing fin.

In the multiscale analysis, the macro mechanical model accounts for the intrinsic micro- and meso-structure of the material (Stier, Simon, and Reese 2015). The important aspect of multiscale analysis is the homogenization, since it allows to transfer the information about the material to higher level analysis (Mustafa, Suleman, and Crawford 2015). The composite is a heterogeneous material, and its mechanical properties are obtained using the properties of each component including topological distribution. Multiscale numerical homogenisation is based on the concept of representative volume element (RVE) and Representative Unit Cell (RUC) that is employed to determine the properties for homogenised macroscale. The RVE is a microstructural region that is representative for the entire subscale (Otero et al. 2015). There are several methods for laminate homogenisation, such as Rule of Mixtures, asymptotic homogenisation technique or Mori-Tanaka. In general, homogenisation provides an information about the larger scale structure given the properties of composite constituents.

A common approach for modelling the composites is the Equivalent Single Layer (ESL) Model. The single-layer panel represents the entire laminate. The macro-mechanical properties are estimated based on the weighted average of the mechanical properties of each lamina. The ESL model combined with Kirchhoff-Love's thin shell plate' theory is known as the Classical Lamination Theory (CLT) (Kreja 2007). According to CLT, the assessment of the stiffness matrix is obtained by summation of lamina plies having thicknesses, stacking sequence, and elastic constants transformed from the material direction into arbitrary axes according to the ply orientation (Chaphalkar and Kelkar 2001).

MOST WIEDZY Downloaded from mostwiedzy.pl

Finite Element Method allows calculations to be carried out at all scales - from micro to macro scale, and different level of detail can be obtained. Usually, shell elements are used to describe laminate. They offer the possibility to compute the laminate properties based on the defined stacking sequence. Composite structure can be also discretized using 3D elements, especially in the regions where rapid variations in stress and strain are expected (Barbero 2013).

The investigation presented in this monograph focuses only on the macroscale behaviour of the composite structure. The microscale and mesoscale analysis are neglected. To conduct the micro- and mesoscale analysis the detailed information about the material is necessary. Moreover, such approach is often used to study complicated failure mechanisms, which are outside the scope of this thesis. The main interest is to study the behaviour of entire composite structure using the homogenized material, with the special interest in the structure displacement, therefore the macroscale model is sufficient.

2.6.5. Numerical model of the RS:X windsurfing fin structure

In this thesis the approach in which composite structure is modelled as an isotropic material is proposed. The calculations that included such simplification were presented by Kreja and Sabik (2019). The optimization of the sandwich composite footbridge with a U-shaped cross-section modelled parts of the bridge as an isotropic material was found in Ferenc and Mikulski (2020a) and such simplification proved its usefulness. It was found that the core material of hydrofoil is quite often modelled as isotropic, and equivalent single layer based on shell element or 3D hexahedral element is used to model outer skin (Maung et al. 2021; Pernod et al. 2019). It is also common to treat a hydrofoil as isotropic beam (Temtching Temou, Augier, and Paillard 2021; Temtching Temou et al. 2018). As mentioned before, the laminate can be considered quasi-isotropic when it consists of layers in various directions with regard to the main material axes. According to Figure 2.2 and information provided in Chapter 2.1 the structure is made of +/-75 degrees and +/-15 degrees plies at the outer surface, inner layers of unknown direction and glass mate, which can be considered isotropic. The precise definition of stacking sequence is not possible. Moreover, the fact that another fin can have different stacking sequence justifies searching for different approach for modelling structure. Finally, laminate homogenization, according to the shell theory for the laminate with a particular lay-up, often gives predictions different from the experiments done for specimens with the same stacking sequence (Carvelli et al. 2004).

For windsurfing fin, the global bending effects are dominant. Local skin bending is negligible and does not occur in this case, as well as the delamination, see Figures 2.19 a) and 2.19 b). The maximum chord of the fin is 130 mm, while the skin thickness was measured to be equal to about 1.5 mm. Such proportion of the dimensions and high stiffness of the skin increased by the core stiffness, eliminates the risk of local deformations and wrinkling.

MOST WIEDZY Downloaded from mostwiedzy.pl

a)

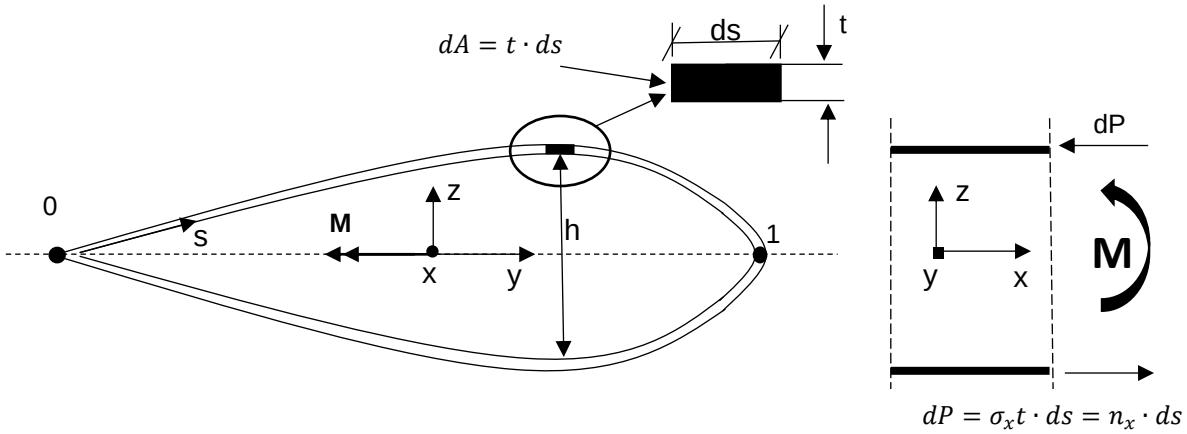

b)

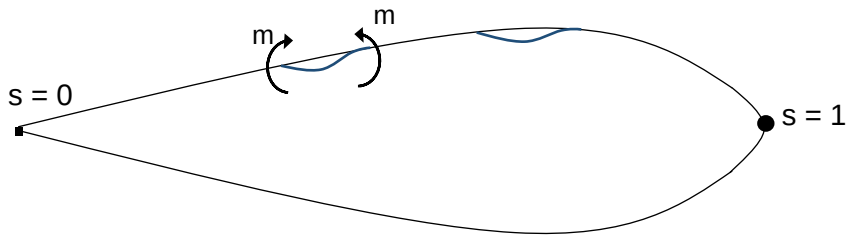

Figure 2.19 Global and local effects due to bending of the fin.

The moment of inertia about the Y-axis of the presented in Figure 2.19 a) elemental cross-section dA can be described as follows:

$$dI_y = 2\left[\frac{ds \cdot t^3}{12} + \left(\frac{h(s)}{2}\right)^2 \cdot t \cdot ds\right] \tag{2.79}$$

$$t \ll h \;\Rightarrow\; \frac{ds \cdot t^3}{12} \approx 0 \;\rightarrow\; dI_y \cong 2 \cdot \left(\frac{h(s)}{2}\right)^2 \cdot tds = \frac{1}{2}h^2(s) \cdot tds \tag{2.80}$$

Therefore, the moment of inertia about the Y-axis can be written as:

$$I_{y0} = \int_0^{s_1} \frac{1}{2}h^2(s)tds = \frac{1}{2}t\int_0^{s_1} h^2(s)\,ds \tag{2.81}$$

The cross-section does not undergo any local deformations – the example of such is shown in Figure 2.19 b), so the cross-sections deformations are negligible. Therefore, the integral expression $\int_0^{s_1} h^2(s)\,ds = const$ is considered valid in this case. It was assumed that the internal structure can be simplified to the core and to the skin. The FEM model consisted of solid elements representing the core and shell elements modelling the skin.

Because of problematic features of geometry, i.e., leading, and trailing edges, the core of the RS:X fin was modelled using 3D solid tetrahedral 10-noded elements. Triangular and quadratic 2D shell elements represented the skin. The 3D solid tetrahedral 10-noded elements

MOST WIEDZY Downloaded from mostwiedzy.pl

were generated using existing nodes of 2D shell elements. The nodes coincidence was checked, and coincident nodes were merged. As a result, all shell elements nodes were common with the 3D solid tetrahedral nodes. Such an approach could be found also in Chróścielewski et al. (2019) and Ferenc and Mikulski (2020b). The thickness of the shell was assessed based on the measurements of fin sections. A similar approach was proposed by Maung et al. (2021); however, the outer laminate was modelled as a hexahedral solid element.

The total count of the elements in presented numerical model was equal to 22705 and included seventy-six triangular elements, 4147 quadratic elements, and 18482 tetrahedral 10-noded elements. The model had 33084 nodes. The numerical mesh is presented in Fig. 2.20.

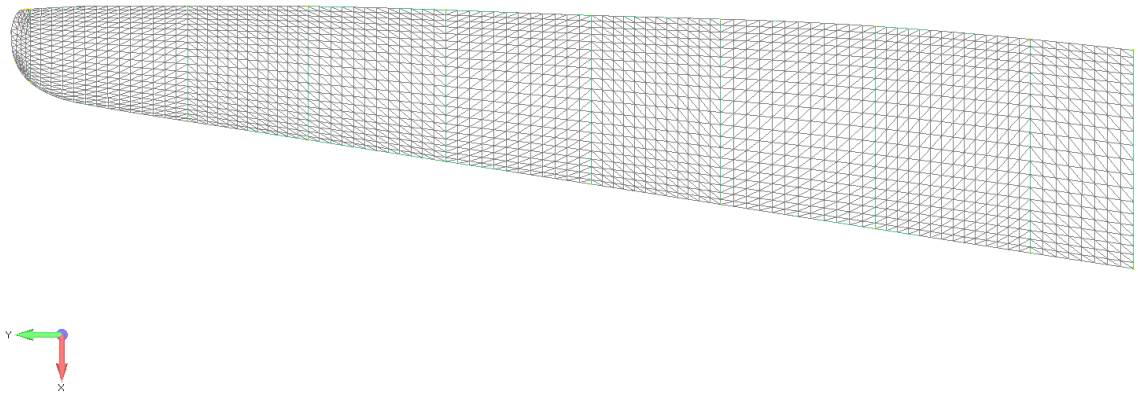

Figure 2.20 FEM mesh of the fin.

Thanks to the investigation into the internal structure, it was possible to notice that the lay-up varies across the length of the fin. Consequently, the mechanical properties change as well. It was assumed that these variations in lay-up affect only Young Modulus. To correctly represent the changes of the Young Modulus along the fin, it was divided into eight sections.

The boundary condition, load, and control points were applied in the FEM model - schematically presented in Fig. 2.21. The fixed boundary conditions were applied to the upper fin section to represent the experimental conditions.

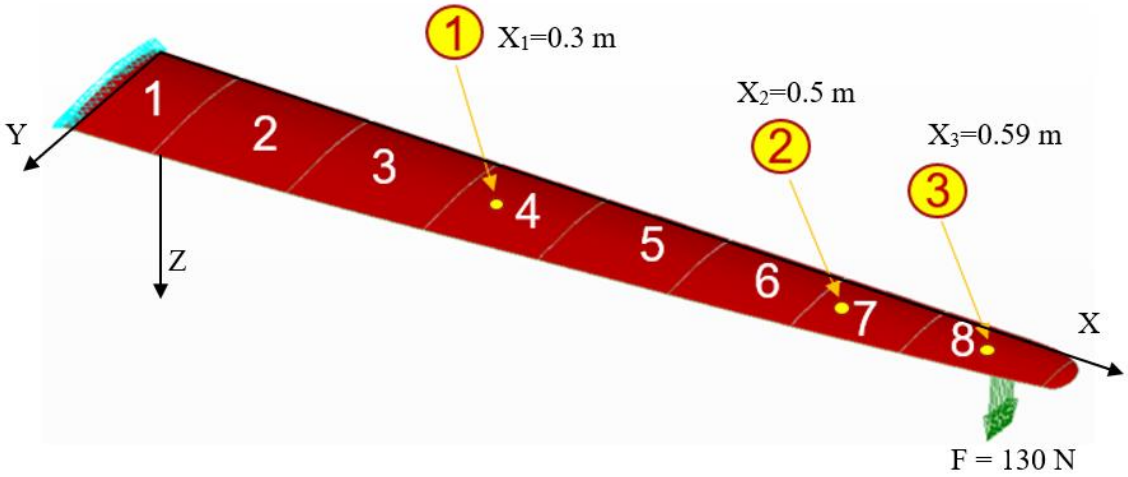

Figure 2.21 Scheme of the 1st stage validation study – sections of various property.

MOST WIEDZY Downloaded from mostwiedzy.pl

The result of calculations was the displacement of control points. The yellow dots numbered from 1 to 3 are marked as the control points in which the displacement under given load were measured and calculated. The load was applied at the distance of 0.6 m away from the fin head. The coordinates of the points along the fin were equal to X_1 = 0.3 m, X_2 = 0.5 m, and X_3 = 0.59 m away for the fin head, respectively.

2.6.6. Stiffness distribution identification study

Combination of experimental and numerical methods were used to evaluate the FEM model of the RS:X windsurfing fin with unknown lay-up. First stages included 3D scanning and investigation into internal structure, which allowed to build initial FEM model (FEM Model Stage 1).

In parallel, the experimental investigation was done. The purpose of the tests was to determine the displacement of the structure under static load and the eigenfrequencies based on the free vibration experiments.

Results of static load experiment were used as an objective goal to Femap build-in optimisation procedure; therefore, the FEM Model Stage 2 was obtained. Next, the exact identification of the stiffness distribution was done, also using the measurements of the displacement of the structure as a benchmark data –the FEM model Stage 3 was obtained. The eigenmodes of FEM Model – Stage 3 were compared with experimentally evaluated eigenmodes and very good agreement was achieved – see Subchapter 3.4.3. Therefore, the FEM model can be considered as validated. This entire workflow is graphically presented in Figure 2.22.

MOST WIEDZY Downloaded from mostwiedzy.pl

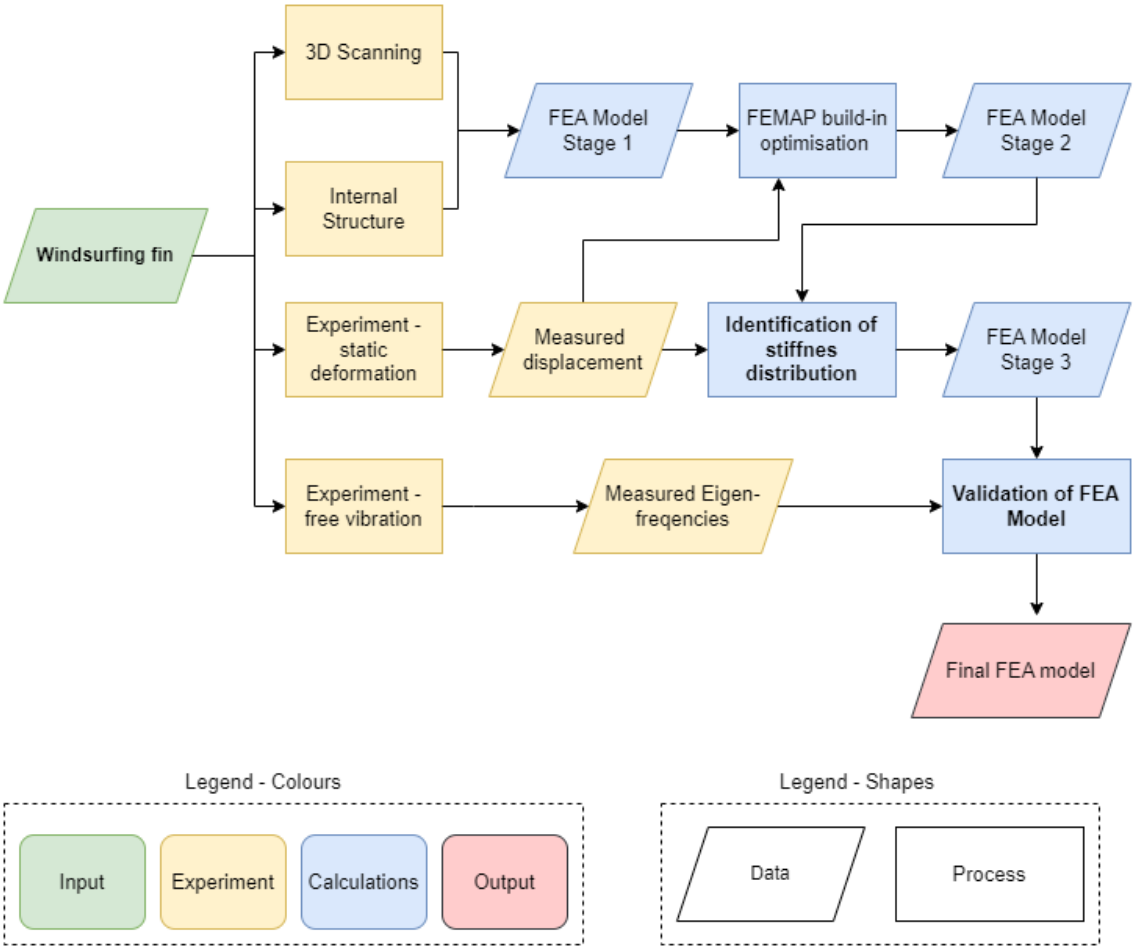

Figure 2.22 Schematic workflow of the structural investigation.

To summarise, the procedure of validation based on the static deformations had three stages:

Stage 1 – primary and simplified identification for finding approximate values of Young Moduli of particular fin sections;

Stage 2 – initial identification of the stiffness distribution realised by the variations of shells thickness using Femap build-in optimisation tool;

Stage 3 – identification through the optimization procedure using the first order sensitivity analysis and least square objective function based on the variations of the Young Modulus values.

The identification process aimed to find proper values of skin Young Modulus for each section so that the displacements obtained numerically agree with the measured ones.

The quantity responsible for higher or lower susceptibility for deformations is the global bending stiffness EI_y. Using Eq. 2.81 EI_y it can be expressed as:

$$EI_y = \int_0^{s_1} E\frac{1}{2}h^2(s)tds = Et\left[\frac{1}{2}\int_0^{s_1} h^2(s)\,ds\right] \tag{2.82}$$

Where Et [N/m] is the membrane shell stiffness.

MOST WIEDZY Downloaded from mostwiedzy.pl

It can be noticed that any changes to the membrane shell stiffness can be realized by modifications of the Young Modulus E or shell thickness t, according to the equation:

$$\delta EI_y = \delta(Et)\left[\frac{1}{2}\int_0^{s_1} h^2(s)\,ds\right] \tag{2.83}$$

Therefore, the variations in the membrane bending stiffness can be written as follows:

$$\delta(Et) = E\cdot\delta t \;\; or \;\; \delta(Et) = \delta E\cdot t \tag{2.84}$$

Stage 2 of the identification study uses the first approach (variable thickness) to quickly obtain the first approximation of the possible stiffness distribution. Stage 3 is based on the variations of the Young Modulus values using as the starting point values of the membrane shell stiffness obtained from Stage 2. The process of identification including all three stages Is described below.

- Stage 1

FEM model of the RS:X windsurfing fin was built according to description presented in Section 2.6.5. The initial check of the model correctness was done by running linear analysis under the load equal to mass of the fin. The model was verified positively, therefore, it was possible to proceed to further stages of the identification study.

- Stage 2

The values of skin for Young Modulus were selected at the starting point of the identification and were kept constant all the time at this stage of the identification study. For all sections, it was equal to 30MPa, while the shell thickness t_j of each section was changed. Therefore, the variations of plate membrane stiffness were realized through modification of plate thickness, according to Eq. 2.85.

$$\mathrm{E} = \mathrm{const} \Rightarrow \delta EI_y \rightarrow \delta t \tag{2.85}$$

Calculations were performed using software Femap 10.1 with NX Nastran solver. The program allows for running a simple optimization function, and this ability was used to estimate the stiffness of the fins. Programme allows for varying the thickness of the shell element. The limits for the optimization were target displacement in the three control points. As a result, various shell thickness values $t_j = \{1,2,..,8\}$ for all eight sections were obtained.

- Stage 3

In the case of identification based on the static deformations, both mentioned approaches are acceptable. However, the object's mass is an important design parameter for the validation based on the free vibration measurements. Modifications of the membrane stiffness by the shell thickness variations affects mass of the fin. Therefore, the variations of the plate membrane stiffness had to be realized through Young Modulus E_j. modification according to Eq.2.86:

$$\mathrm{t} = \mathrm{const} \Rightarrow \delta EI_y \rightarrow \delta E \tag{2.86}$$

MOST WIEDZY Downloaded from mostwiedzy.pl

The Femap optimization (Stage 2) resulted in varying the plate thickness t_{j0} for $j = 1,2,..,8$, and E_{j0} equal to 30MPa for all sections. Using Eq. 2.86, the Young Modulus of each section was evaluated to transform the constant Young Modulus to constant plate thickness:

$$E_{j0}t_{j0} = E_j t \quad \rightarrow \quad E_j = E_{j0}\frac{t_{j0}}{t} \tag{2.87}$$

In this equation, E_{j0} corresponds to the Young Modulus and t_{j0} to the plate thickness of the j-th section after the primary optimization using Femap built-in optimization procedure. The E_j corresponds to the Young Modulus of the j-th section after the transformation that aimed to express the membrane stiffness by variations of Young Modulus, t is the final plate thickness. It was assumed that the final plate thickness was equal to 1.5 mm, 2 mm, 1.8 mm, and 1.5 mm for all sections for FIN1, FIN2, FIN3 and FIN4, respectively.

The further identification of the model parameters was performed with the method of construction identification described in detail by Szymczak and Mikulski (2004). The method was utilized to assess the variance of design variables for the bell tower. It was used in the primary stage of the design and after finalization of construction. The measured state variables were the free vibration frequencies. The method is based on the minimization of differences between measured and calculated values of state variables by modifying the design variables. The design variables (in that case, the Young Modulus of stone and brick wall together with the spring constant of the subsoil) were changed iteratively to achieve a convergence of state variables – in the described case; there were the free vibration frequencies. For the efficiency of the solution, the first-order sensitivity analysis was used. It was proven that such an approach is valid for the problem of the identification of the construction design variables.

A similar approach was used for assessing the stiffness properties of composite RS:X fin. In this study, two kinds of state variables were considered. The first was measured deformations in selected control points under a given static loading. The second was the eigenfrequencies of the first four modes, and the design variables were the material constants of the fin sections.

In general, the model for the identification study can be described by constant parameters and design variable vector **x**. In this case, the identified parameters were the Young Modulus of fin sections for $\mathbf{x_j}$ $j = 1,2,..,8$, so the proper values of model parameters need to be derived. They can be evaluated and validated by comparing the measured state variable $\hat{q}_i$ with state variables obtained numerically q_i for $i = 1,2,3$. The measured variable $\hat{q}_i$ was the displacement in the control point *i*, and q_i was the displacement in the control point *i* identified with FEM calculations. The optimization procedure based on the sum of the least square method described below was applied for the problem of validation and identification of each section stiffness properties. The identification problem was formulated as follows:

$$\min F(\delta\mathbf{x}) = \sum_{i=1}^{3}[\,(q_i + q_i(\delta\mathbf{x})) - \hat{q}_i]^2 \tag{2.88}$$

Where $q_i(\delta\mathbf{x})$ – is the state variable change due to design variable vector **x** variations**.**

MOST WIEDZY Downloaded from mostwiedzy.pl

The first order sensitivity method was used to solve the identification problem. In structural mechanics, sensitivity analysis focuses on evaluating the direct dependency between structure response variations due to variation of design variables. If the design variables form a set of numbers, the state variable is described by the characteristic function $q(\mathbf{x})$ where $\mathbf{x}$ is a vector of design variables. In a great majority of the problems, the direct relation between the state variable function $q(\mathbf{x})$ and design variables $\mathbf{x}$ is unknown.

The sensitivity analysis is based on the development of the characteristic function s (state variable) into the Taylor series around the initial solution defined by the initial value of the design variables.

$$q(x_0 + \delta x) \cong q(x_0) + \delta q(x_0) + \delta^2 q(x_0) + \cdots \tag{2.89}$$

The first order sensitivity analysis takes into account only linear increment; therefore, the behaviour of the construction can be approximated with linear function around the initial value of the solution for the design variable x_0. The idea of the first order method is outlined in the Figure 2.23.

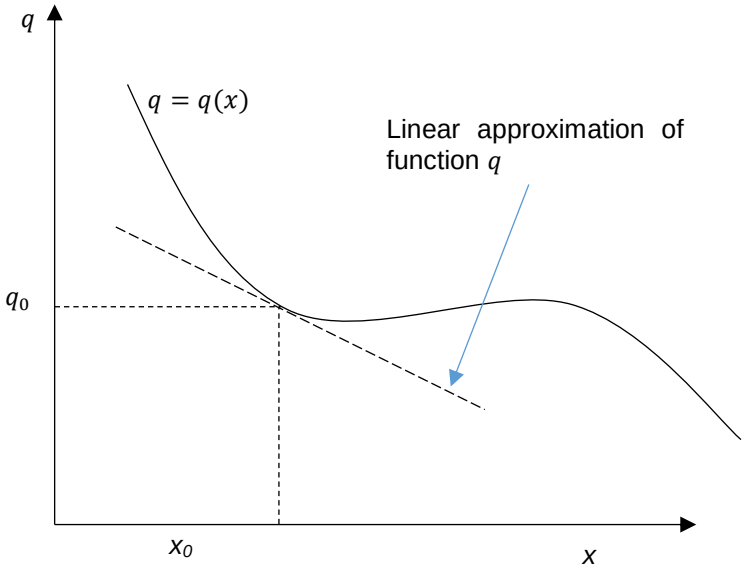

Figure 2.23 First-order sensitivity analysis – one dimensional problem.

The next step is to introduce the first-order sensitivity vector according to Equation 2.90 and 2.91:

$$\mathbf{w_i} = \{w_{i1}, w_{i2}, .., w_{ij}, .., w_{i8}\}^T \tag{2.90}$$

$$\mathbf{w_i} = \left\{\frac{\delta q_i}{\delta x_1}, \frac{\delta q_i}{\delta x_2}, .., \frac{\delta q_i}{\delta x_j}, .., \frac{\delta q_i}{\delta x_8}\right\}^T \tag{2.91}$$

The first order sensitivity vector $\mathbf{w_i}$ expresses the vector of variation in the displacement of control point *i* $\delta\mathbf{q}_\mathrm{i} = \{\delta q_1,\ \delta q_2,\ \delta q_3\}^T$ due to variations of Young Modulus of sections *j=1,2,…,8* described as $\delta\mathbf{x}_\mathrm{j} = \{\delta x_1,\ \delta x_2, ..,\ \delta x_8\}^T$.

MOST WIEDZY Downloaded from mostwiedzy.pl

To achieve the numerical efficiency, the normalized vectors $\delta\overline{\mathbf{q}}$ and $\delta\bar{\mathbf{x}}$ were applied:

$$\delta\overline{\mathbf{q}} = \left\{\frac{\delta q_1}{q_1}, \frac{\delta q_2}{q_2}, \frac{\delta q_3}{q_3}\right\}^T \tag{2.92}$$

$$\delta\bar{\mathbf{x}} = \left\{\frac{\delta x_1}{x_1}, \frac{\delta x_2}{x_2}, .., \frac{\delta x_8}{x_8}\right\}^T \tag{2.93}$$

The normalized first-order vector of the sensitivity can be written as:

$$\overline{\boldsymbol{w}}_{\boldsymbol{i}} = \left\{\frac{\delta\overline{q_i}}{\delta\bar{x}_1}, \frac{\delta\overline{q_i}}{\delta\bar{x}_2}, .., \frac{\delta\overline{q_i}}{\delta\bar{x}_j}, .., \frac{\delta\overline{q_i}}{\delta\bar{x}_8}\right\}^T \tag{2.94}$$

At this point, it becomes clear that the components of the vector of sensitivity need to be evaluated. It was necessary to assess the sensitivity of the displacement due to the variations of the Young Modulus. Therefore, the parametric identification study using the sensitivity analysis was done. At this stage, the influence of Young Modulus variations of each section on the deformation in control was checked. The Young Modulus of each section was systematically changed by the value $\Delta\bar{\mathbf{x}}_{\boldsymbol{j}}$ =+/-0.05$E_{j0,}$ where E_{j0} is the Young Modulus of section j at the start point of the identification study.

For the new value of E_j, the difference in the construction displacement in a particular control point was evaluated. The procedure was done for the mechanical properties of the skin.

The normalized vector of state variable variation can be expressed as the product of the normalized first-order sensitivity vector and normalized vector of state variables variations, according to Eq. 2.95:

$$\delta\overline{\mathbf{q}}_{\mathbf{i}} = \overline{\mathbf{w}}^{\boldsymbol{T}}{}_{\mathbf{i}} \cdot \delta\bar{\mathbf{x}} \tag{2.95}$$

The variation of Young Modulus of each section was evaluated to x_j =+/-0.05E_{j0} changes. This represents the central differential method.

$$\delta q_i \cong \frac{q_i\left(x_j + 0.05x_j\right) - q_i\left(x_j - 0.05x_j\right)}{0.1\delta x_j} \cdot \delta x_j \quad \rightarrow \quad \delta q_i = w_{ij} \cdot \delta x_j \tag{2.96}$$

$$\delta\mathbf{q}_{\mathbf{i}} = \mathbf{w}_{\mathbf{i}}^{\mathbf{T}} \cdot \delta\mathbf{x} \tag{2.97}$$

After introducing normalized design parameter variations and normalized state variable variance, the equation is expressed as follows:

$$\frac{\delta q_i}{q_i} \cong \frac{q_i\left(x_j + 0.05x_j\right) - q_i\left(x_j - 0.05x_j\right)}{0.1 \cdot q_i} \cdot \frac{\delta x_j}{x_j} \quad \rightarrow \quad \delta\overline{\mathbf{q}}_i = \overline{\mathbf{w}}_{\boldsymbol{i}}^{\mathbf{T}} \cdot \delta\bar{\mathbf{x}} \tag{2.98}$$

The problem of validation using the procedure of optimization based on the least square method defined by Eq. 2.88 can be expressed using relative values:

MOST WIEDZY Downloaded from mostwiedzy.pl

$$\min F(\delta\bar{\mathbf{x}}) = \sum_{i=1}^{3} \left(\frac{\delta q_i}{q_i} - \frac{\hat{q}_i - q_i}{q_i} \right)^2 \tag{2.99}$$

Using Eq. 2.98 and Eq. 2.99 the optimization function can be written as:

$$\min F(\delta\bar{\mathbf{x}}) = \sum_{i=1}^{3} \left(\bar{\mathbf{w}}_i^T \cdot \delta\bar{\mathbf{x}} - \frac{\hat{q}_i - q_i}{q_i} \right)^2 \tag{2.100}$$

Where $\frac{\hat{q}_i - q_i}{q_i}$ and the vectors $\bar{\mathbf{w}}_i$ were evaluated based on the FEM calculations.

The Matlab optimization toolbox was used to solve the optimization problem defined in Eq. (2.100) and determine the components of design variable vector variations $\delta\bar{\mathbf{x}}$ of the objective function. The least-square linear solver (*lsqlin* solver) with the interior-point algorithm was used to find the minimum of the expression. The optimization problem could be classified as searching the function minimum without constraints. The presented issue is not a typical optimization problem; however, the optimization tool is used to find the components of design variable vector variations on each step of the identification problem. It allowed to obtain the target modifications of Young Modulus values for each section.

The scheme of the procedure is presented in Fig. 2.24. It corresponds to process named 'Identification of stiffness distribution' in Figure 2.22. Within this procedure the first step was a determination of the control points displacements ('START' in Figure 2.24). Then, the Young Modulus of each section was modified individually, and each time the new displacements of control point was determined. It allows to calculate the sensitivity vector – namely how variation of each section bending stiffness influences the magnitude of control points displacement. For example, variation in stiffness of sections near the head influences the displacements of all control points, while changing the stiffness of the sections closer to the tip has an impact only on the last control point. Sensitivity vectors describe this relation. High values of sensitivity vectors indicate significant impact of the section stiffness on the given control point displacement.

The sensitivity vector and difference between the calculated and experimentally obtained displacements are the input to the optimisation procedure. The output is the desired modifications of the Young Modulus values of each section.

After evaluating the target modifications of material properties, the FEM analysis was rerun with new sections properties to verify whether the improvement was achieved. The entire procedure was repeated several times: the new components of the sensitivity vector were evaluated by systematic modifications of the Young Modulus of each section. Then the Matlab optimization script was run to find the target modifications of the section Young Modulus values. The FEM analysis was rerun to check if the solution is converging to the target values of the state variables.

MOST WIEDZY Downloaded from mostwiedzy.pl

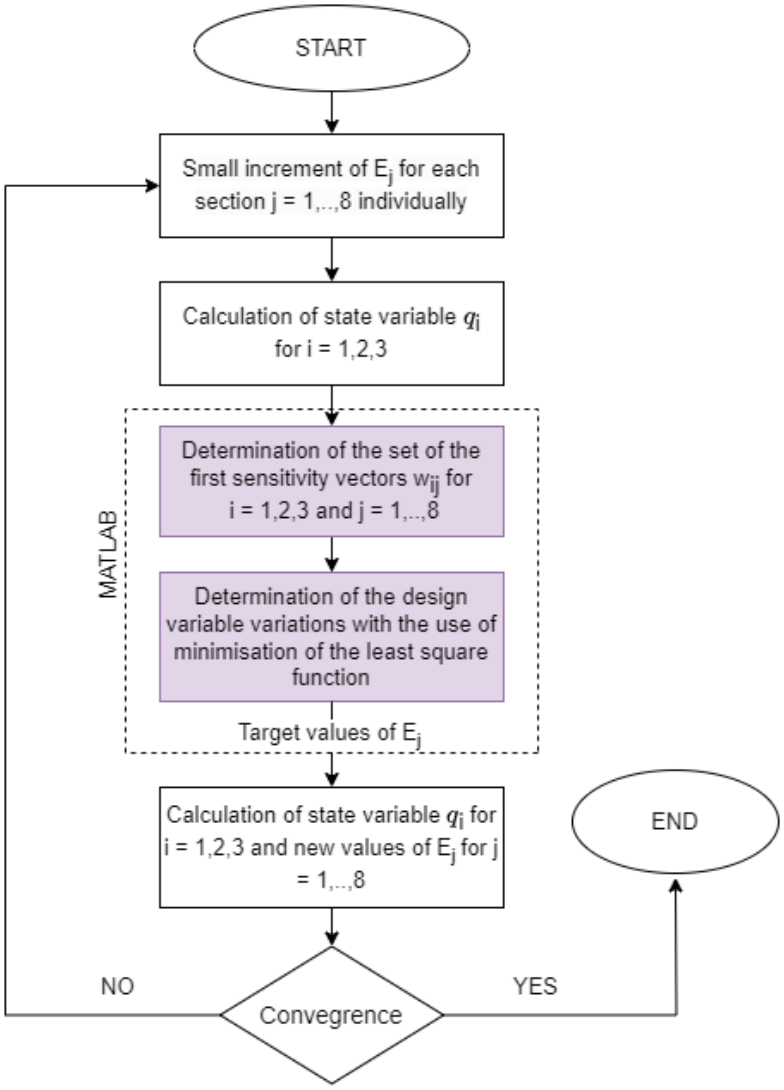

Figure 2.24 Block scheme of material properties identification using optimization procedure.

By following this procedure, it was possible to identify the stiffness along the fin axis. It also needs to be emphasized that this method does not allow for identifying material properties as such.

Finally, the numerical model obtained after application of stiffness identification procedure was used to determine the eigenmodes. The weight of the fin and the centre of mass were checked before the experiments. The density of the materials used in FEM analysis was set to fit the mass of the measured structure. The Normal Modes/Eigenvalue analysis was run to determine the eigenmodes and corresponding frequencies.

MOST WIEDZY Downloaded from mostwiedzy.pl

2.7. Fluid-Structure Interaction

2.7.1. Fluid-Structure Interaction Principles

In fluid mechanics computation the solid is treated as a boundary, and the nature of the solid is not the object of the interest (in this approach the material of which the hydrofoil is built of does not influence the nature of the flow). On the contrary to mechanics, when the main goal of the calculations are computations of stresses and displacements of the solid under various loads. The load can come from the fluid as well; however, the nature of the flow is neglected. The fluid-structure interaction analysis is employed for phenomena, which cannot be solved independently, so this field of science deals with investigating into mutual influence of the fluid and solid deformable body on each other.

For fluid-structure interaction problems the governing equations are:

- Navier-Stokes Equations;
- continuum mechanics equations such as stress – strain – displacement relation or modal shape approximation;
- dynamic and kinematic boundary conditions at the interface of the two domains.

The Fluid-Structure Interaction domain is therefore a sum of two non-overlapping domains: solid domain Ω^S, and fluid domain Ω^F sharing common interface Γ. In the case of hydoelasticity, the unknowns of the fluid field are velocity **v**, pressure p, and for the solid boundary the displacement **u** (Küttler and Wall 2008). The kinematic boundary conditions yield that velocities at the interface between domains are equal and the fluid domain changes in time according to the interface velocity, therefore, no mixing of sliding occurs. The dynamic boundary condition assumes that the stresses $\boldsymbol{\sigma}$ at the interface are equal, according to the dime dependent interface normal vector $\mathbf{n}$. In this context $\boldsymbol{\sigma}$ is the generalised stress resulting from action of the fluid forces $\boldsymbol{\sigma}_\Gamma^F$ and the reaction of the solid body on the external load in the form of material stress at the interface $\boldsymbol{\sigma}_\Gamma^S$. Therefore, the kinematic and dynamic boundary conditions at the interface can be written as:

$$\mathbf{v}_\Gamma = \frac{d\mathbf{u}_\Gamma}{dt} \qquad \boldsymbol{\sigma}_\Gamma^S \cdot \mathbf{n} = \boldsymbol{\sigma}_\Gamma^F \cdot \mathbf{n} \tag{2.101}$$

The fluid forces are the result of pressure and viscous forces, and these are the forces acting on solid, which are balanced by structure internal forces.

The general equation of the motion for the vibrating body in one degree of freedom can be written as:

$$M\ddot{x} + C\dot{x} + Kx = F \tag{2.102}$$

Where x is position of the body, M is mass, C is structural damping and K is structural stiffness, whereas F is the excitation force. As the body vibrates in the fluid, the interaction occurs, therefore, the equation can be written as:

MOST WIEDZY Downloaded from mostwiedzy.pl

$$(M + m_{add})\ddot{x} + (C + c_{add})\dot{x} + (K + k_{add})x = F \tag{2.103}$$

Where m_{add} is the fluid added mass, c_{add} is the fluid added damping, and k_{add} is the fluid added stiffness.

In this context several of non-dimensional numbers that are used to describe and classify the interaction between fluid and solid domain can be defined. The reduced velocity is defined as the ration between the solid and fluid time scale, and is defined as:

$$U_R = \frac{T_{SOLID}}{T_{FLUID}} \tag{2.104}$$

The solid time scale T_{SOLID} is a time at which analysed phenomena occurs. With the relation to equation 2.104 the solid time scale is the period of oscillations. The fluid time scale is defined as:

$$T_{FLUID} = \frac{L}{U_0} \tag{2.105}$$

Where U_0 is the free stream velocity. The fluid time scale is associated with the convection in the fluid and describes the time that fluid particle requires to travel the distance equal to body characteristic length L.

The mass number defined as the ratio of the fluid over solid density:

$$M = \frac{\rho}{\rho_s} \tag{2.106}$$

The Cauchy number bounds the dynamic pressure with the stiffness of structure and is defined as:

$$C_y = \frac{\rho U_0^2}{E} \tag{2.107}$$

E is the Young Modulus of the body; L is the characteristic length of the body and ρ_s is the solid density.

The problems of fluid-structure interaction can be classified depending on the reduced velocity U_R number:

- U_R << 1;
- U_R >1;
- U_R >>1.

Depending on the class of the problem some of them can be solved by applying some simplifications. For the first approach the timescale of the solid is much smaller than the timescale of the fluid – for example, the period of the solid oscillations is much smaller than the convection of the fluid. In this case the flow is considered to be at rest, so the solid is moving in the still fluid. For small reduced velocities, the added damping can be neglected, and it is important to include

MOST WIEDZY Downloaded from mostwiedzy.pl

the effects of added mass and added stiffness in the analysis of the phenomena. For example, this is the case of free oscillations of the cylinder in the water. The added stiffness is related to the increase of the buoyancy, whereas the added mass is related to water that moving cylinder disturbs.

For the second case, the frequency of oscillations or eigenfrequencies of the solid are similar to fluid time scale. Under assumption that that fluid convection is quicker than the structure oscillation, the motion of the solid can be linearized, and solid velocity can be assumed constant. In this framework the added damping needs to be included, as it is dominant effect.

For the very large reduced velocities, the fluid convection is much quicker, therefore the motion of the solid can be neglected, and the fluid stiffness force has a major effect on the fluid-solid interaction.

For the scope of the calculation presented in this work, the range of analysed fluid velocities is between 4 m/s and 10 m/s. It corresponds to fluid timescale between 0.01 s and 0.025 s.

The eigenfrequency of the first mode in the air is equal to 24 Hz (see Chapter 3.4.3). According to De La Torre et al. (2013), the ratio of the oscillations frequency in water and air can be approximated according to formula:

$$\frac{f_{fluid}}{f_{air}} \cong \sqrt{\frac{1}{\left(1+\frac{m_{add}}{M}\right)}} \tag{2.108}$$

According to Brennen (1982), the increase of moment of inertia for plate rotating about one edge is equal to 4/3 of moment of inertia in the air. This is good approximation of the first mode vibrations of the fin, therefore the frequency of oscillations in fluid is approximately equal to 15.7 Hz. It corresponds to 0.064 s of the period of oscillations, for the following modes the oscillation time is even smaller. The timescale of the fluid is between 0.01 s and 0.02 s. Based on the first mode frequency, the reduced velocity for analysed case is then estimated to be within a range of $4 < U_R < 8$. As it will be further presented and discussed, the measured frequency of oscillations in the water is even smaller.

For small displacement it is possible to apply some approximations and solve two domains separately, neglecting other effects, than dominant for particular phenomena. However, in presented case, the expected displacement is large, and the object of interest more complex therefore, more sophisticated methods should be applied.

The numerical methods for fluid-structure interaction can be classified in terms of different approach for exchange of data between the domains. The schematic division of the approaches is presented in Figure 2.25.

MOST WIEDZY Downloaded from mostwiedzy.pl

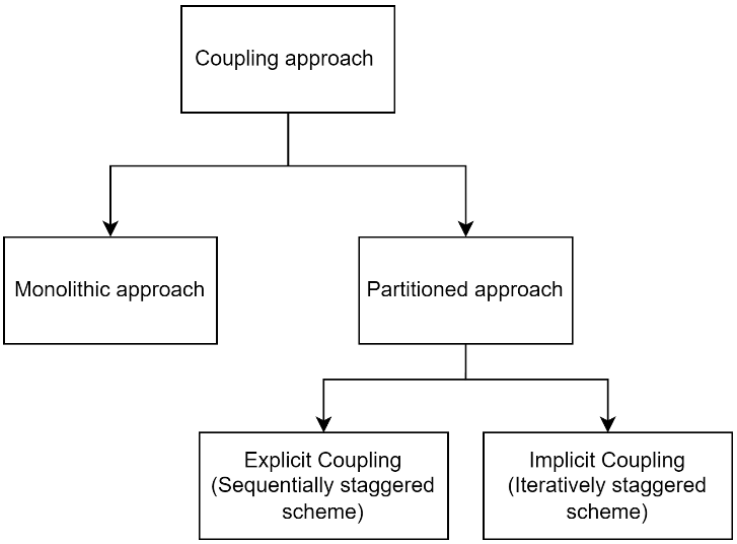

Figure 2.25 Summary of the coupled Fluid-Structure Interaction methods.

As can it be noticed, there are two ways to deal with interaction: monolithic and partitioned. In the monolithic approach, the governing equations are solved simultaneously (Degroote, Annerel, and Vierendeels 2010). While the other partitioned approach uses two separate already existing solvers, one for fluid domain and other for solid domain and a coupling algorithm is required. In this approach the large system of equations is solved by means of solvers for sub-systems using known methods such as block-Jakobi, block-Gauss-Seidel or related relaxation methods (Matthies, Niekamp, and Steindorf 2006).

The partitioned approach can be further divided into explicit coupling (sequentially staggered) and implicit coupling (iteratively staggered). The sequentially staggered schemes are characterised by the loose (weak) coupling. It requires only one solution of either field per time step in a sequentially staggered way, without inner iteration between solvers, which makes it very efficient approach. According to Degroote, Annerel, and Vierendeels (2010) most of the aeroelasticity problems can be solved using weak coupling. In this case the equilibrium on the fluid-structure interface is not enforced strictly. However, at the same time the explicit coupling algorithms are prone to instabilities. Förster, Wall, and Ramm (2007) indicated that sequentially staggered algorithm can become unstable due to artificial added mass effect. It was argued that for sufficiently high mass number the stability of calculation is extremely difficult to obtain. However, they indicated that for aeroelastic problems, the sequentially staggered algorithms could be conditionally stable. As a solution to instabilities, they propose application of iteratively staggered (strong coupling) schemes.

The implicit coupling utilises subiteration over the single field and converge to the solution of the monolithic system (Förster, Wall, and Ramm 2007). A coupling algorithm is required to find a position of the interface for which the stress of both sides of the interface will be in equilibrium. (Degroote, Annerel, and Vierendeels 2010). If the structure deformation is significant with the great influence of the fluid part, most probably the interface correction via the subiterations to obtain right position of the interface is necessary. The strong coupling scheme iterates until coupled problem is solved (Küttler and Wall 2008).

MOST WIEDZY Downloaded from mostwiedzy.pl

For either type of coupling most often the Dirichlet-Neuman partitioning is used. For aero or hydroelastic calculations the fluid becomes the Dirichlet partitioning with prescribed interface velocities $\mathbf{v}_\Gamma$ and the structural field becomes Neuman partition loaded with the interface forces $\mathbf{f}_\Gamma$. In this approach the black box solvers can be used. Moreover, the Dirichlet-Neuman partitioning prescribes definite interface displacement, and the Navier-Stokes equation is solved on the domain with prescribed motion (Küttler and Wall 2008).

The Navier-Stokes equation that govern the fluid behaviour was written in Eq. 2.11 and in Eq. 2.12 in its' integral form. For FSI problems the fluid domain varies in time as a result of moving interface $\boldsymbol{\Gamma}$, therefove, the Navier-Stokes equation in arbitrary Lagrangian-Eulerian (ALE) framework in the moving fluid domain can be written as:

$$\left.\frac{\partial \mathbf{v}}{\partial t}\right|_{X_0} + \mathbf{c}\cdot\nabla\mathbf{v} - \frac{1}{\rho_f}\nabla\cdot\mathbf{T}^F = \mathbf{b}_f \tag{2.109}$$

Where ρ_f is fluid density, and $\mathbf{b}_f$ is the body force vector. The ALE velocity is given as $\mathbf{c} = \mathbf{v} - \mathbf{v}^{\mathrm{G}}$ and $\mathbf{v}^{\mathrm{G}}$ is the interface velocity. The stress tensor T^F is defined according to Eq. 2.14.

The changes in the fluid domain are taken into account by mapping, so that the interface position corresponds to the equation:

$$\mathbf{x} = \varphi(\mathbf{u}_\Gamma, \mathbf{x}_0, t) \tag{2.110}$$

Where $\mathbf{u}_\Gamma$ is the interface displacement, and $\mathbf{x}_0$ is the starting position of the interface.

In principle, the FSI explicit procedure can be explained by the scheme presented in Figure 2.26.

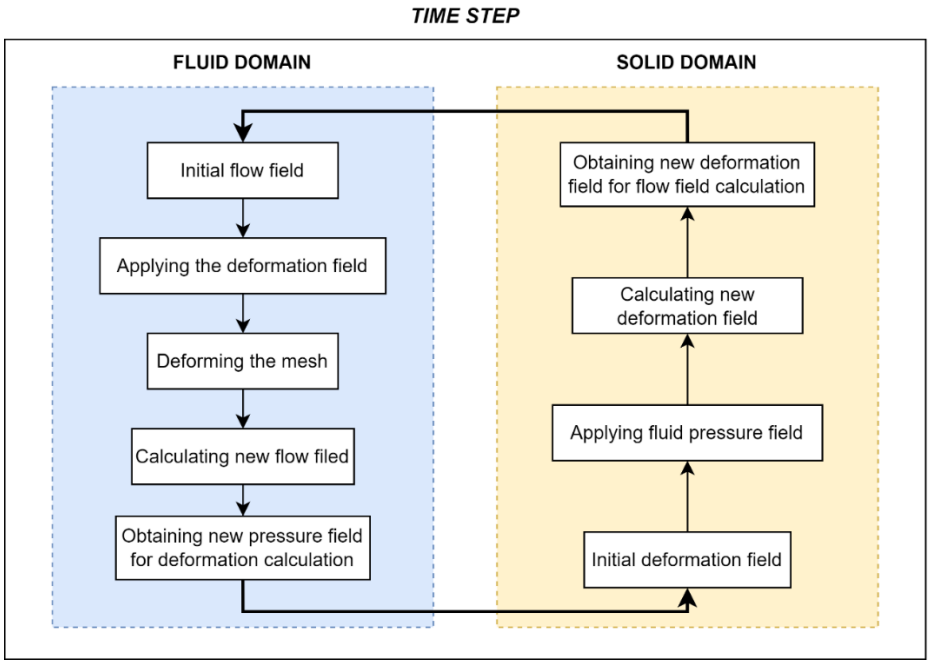

Figure 2.26 Scheme for explicit coupling method.

MOST WIEDZY Downloaded from mostwiedzy.pl

There are two most popular numerical schemes for the exchange of fields, which is Gauss-Seidel scheme and Jacobi scheme. According to Degroote, Annerel, and Vierendeels (2010) the Gauss-Seidel scheme can be explained by following steps that solvers perform, where k is the coupling iteration within the time step:

- solve the flow governing equation for the new velocity v^{k+1} and pressure p^{k+1} with a given geometry deformation d^k;
- solve solid governing equation for the new geometry deformation d^{k+1} with the pressure p^{k+1} from the preceding step;
- increase k and return to step 1 if the iterations have not yet converged.

It means that this scheme uses the information about the flow field data as soon as they are available. This scheme is also known to converge faster that Jacobi scheme.

For the Jacobi coupling, the calculations of the pressure, velocity and displacement are performed for the same iteration number k. The prediction for the following time step is made based on the extrapolation from the previous steps (Matthies, Niekamp, and Steindorf 2006).

2.7.2. Mesh morphing

The deformation of the body inside fluid domain could be performed by the mesh morpher. It is necessary to use deformable mesh for fluid domain. To do so, the mesh morphing was applied in FSI calculations presented in this work. The mesh morpher redistributes the mesh vertices in the response to the displacement boundaries. The movement that the morpher imposes in the mesh is defined through a set of control points, which originate from the mesh vertices on the morphing boundary. The displacement vector is associated with each control point. Using this displacements vector, morpher constructs an interpolation field and calculates displacement of all mesh vertices. Then, morpher uses interpolation field to translate the mesh vertices to their new positions. The Radial Basis Functions (RBF) morpher was used for calculations in this research.

The interpolation field is generated via system of equations that are based on specified displacements of the control points, where the displacement u'_i of each vertex **i** as expressed as:

$$u'_i = \sum_{j=1}^{N} f_{b,j}\left(r_{ij}\right)\lambda_j + \boldsymbol{\alpha} \tag{2.111}$$

The radial basis function is defined as:

$$f_{b,j}\left(r_{ij}\right) = \sqrt{r_{ij}^2 + c_j^2} \tag{2.112}$$

Where r_{ij} is the distance between two vertices x_i and x_j , λ_j is the expansion coefficient, c_j is the basis constant, and $\boldsymbol{\alpha}$ is the constant vector.

In the Finite Volume Method, the governing equations that take into account the mesh motion via morphing can be written as:

MOST WIEDZY Downloaded from mostwiedzy.pl

$$\frac{\partial}{\partial t}\int_{CV} \rho dV + \int_{CS} \rho(\mathbf{v} - \mathbf{v_g}) \cdot \mathbf{n}\, dS = 0 \tag{2.113}$$

$$\frac{\partial}{\partial t}\int_{CV} \rho \mathbf{v} dV + \int_{CS} \rho \mathbf{v}(\mathbf{v} - \mathbf{v}_g) \cdot \mathbf{n}\, dS = \int_{CS} \mathbf{T} \cdot \mathbf{n}\, dS + \int_{CV} \rho \mathbf{b}\, dV \tag{2.114}$$

Where $\mathbf{v}_g$ is the velocity of mesh motion. It can be noticed that these equations are analogous to eq. 2.11 and 2.13.

2.7.3. Fluid-Structure Interaction - Validation study

To confirm the accuracy of the STAR-CCM+ with Abaqus coupling through co-simulations engine, and the validity of numerical model, the calculation results have been compared with the relevant experimental ones. To do so, the experiments described by Zarruk et al. (2014) were reproduced numerically again, however, for the flexible hydrofoil. The CFD model with $k - \omega$ SST turbulence, described in Chapter 2.5.3, was coupled with the structural one. Also, the base size of the mesh cell was slightly increased, with decreasing the minimum element size to keep smooth leading edge. The total number of elements for CFD calculations was equal to 3.1M.

The aluminium hydrofoil was selected for the study, since it is an isotropic material with lower Young Modulus than steel, therefore, more susceptible for bending. The validation study was performed for two conditions:

- Case 1: Re = $1 \cdot 10^6$ and angle of attack AoA = 6 degrees;
- Case 2: Re = $0.6 \cdot 10^6$ and angle of attack AoA = 8 degrees.

The structural mesh was based on the 10-noded tetrahedral solid elements. The model had 57390 elements and 92880 nodes. The fixed boundary condition was applied on the nodes lying on the top surface of the hydrofoil. The properties of aluminium material are presented in Table 2.2

Table 2.2. Material properties of the aluminium hydrofoil.

Property	**Symbol**	**Value**
Density	ρ	2700 kg/m^3
Young Modulus	E	71 GPa
Poisson Ratio	v	0.33

The non-linear implicit solver was used. The maximum time increment was equal to 0.002 s, which was the same as the time step in CFD calculations, and so was the coupling interval between solvers. The iteratively staggered approach was used, and the Gauss-Seidel scheme was selected, so solvers exchanged the data within one time step several times. The number of exchanges depended on the value of the normalised displacement residual that aimed to drop below 0.01. For stability of calculations the pressure field was ramped to obtain linearly increasing load during the first 0.1s of calculations. The calculations aimed to determine drag and lift forces, and the displacement of the tip of the hydrofoil.

MOST WIEDZY Downloaded from mostwiedzy.pl

2.7.4. Fluid-Structure Interaction - Numerical setup to determine the hydroelastic properties of RS:X fins

The final setup consisted of a coupled CFD and FEM models, each of them were in details described in Chapter 2.6.5 and Chapter 2.5.2. Therefore, in this chapter, only the details about the coupled calculations are presented. The numerical setup of the FSI simulations was done following the current state of the art. The flow was modelled as a single-phase, turbulent, viscous, and incompressible with $k-\omega$ SST turbulence model and wall functions. STAR-CCM+ was coupled with Abaqus using the SIMULIA Co-simulation engine. The FEM model was primary generated in Femap, and for the sake of FSI calculations it was implemented to Abaqus and checked for differences.

The SIMULIA Co-simulation engine allows to exchange the information between the solvers and obtain flow velocity and pressure, and structure deformations. Due to large unsteadiness of the flow, the implicit second order temporal discretisation was applied for the fluid domain. The implicit solver was also used for Abaqus calculations. Since significant deformations of the structure were expected, the non-linear structural theory for calculation of deformations was applied.

In this study two types of coupling were compared – sequentially staggered and iterative. Majority of the studies presented here were actually performed for explicit coupling, however, for comparison and control reasons, selected cases were also calculated with application of implicit coupling. Both for the sequential and iterative coupling the Gauss-Seidel scheme was selected. The exchange of the data fields for the explicit coupling was after ten inner iterations of the fluid solver, whereas, for Abaqus it was forced by maximum time step size and coupling time. The minimum time step of the structural solver was equal to $2 \cdot 10^{-7}$ s, the maximum time step was equal to 0.004 s, and the total number of increments was equal to $1 \cdot 10^{6}$. The global maximum time of the calculations was set to 15 seconds. Additionally, the time step verification study for FSI coupling was done. Three time steps were considered: 0.001 seconds, 0.002 seconds, and 0.004 seconds. Since little influence of the time step on the results was found, as aforementioned, the greatest analysed time step was used. The details on time step sensitivity study are presented in Chapter 3.5.

For iterative coupling further conditions were applied for inner iterations. Additional stopping criterion was applied to reinforce iterating until the residual of structural displacement dropped below the value of 0.01. Minimum number of coupling exchanges was set to 3, and coupling iterations were equal to 5. Additionally, according to findings of Küttler and Wall (2008) the dynamic relaxation was applied, which increase the stability and convergence of inner iterations. Due to increased coupling accuracy, only 8 seconds of simulation time was required to obtain converged results.

The data obtained by fluid solver were fluid pressure and velocity. Based on the pressure on the structure (both normal and viscous stress) the traction vectors were obtained. Then the traction vectors were recalculated to nodal forces and applied in a structural solver. The data

MOST WIEDZY Downloaded from mostwiedzy.pl

imported from structural solver were structure displacements, and for implicit coupling also structure velocity.

The calculations were performed for a wide combination of the angles of attack and velocity of the fluid. Therefore, the wide range of load scenarios was simulated. The calculations were done for angles of attack 2 degrees, 4 degrees and 6 degrees. The range of speed was from 4 m/s up to 10 m/s. The calculations matrix is presented in Table 2.3. The implicit coupling was applied also for the velocity of 8 m/s and angle of attack equal to 6 degrees (In Table described as 6-I). The calculations were performed for all four compared fins. The calculations with implicit coupling scheme were conducted for FIN4 only.

Table 2.3. Calculation matrix.

Case Id.	**Velocity [m/s]**	**Angle of Attack [deg]**
1 - 3	4	2, 4, 6
4 - 6	6	2, 4, 6
7 - 9	8	2, 4, 6 / (6-I)
10 - 12	10	2, 4, 6

The size of the domain was the same as described in Section 2.5.2. The total length of the domain was equal to 60 meters. Side boundaries were placed two meters from the fin. The top boundary overlapped the head of the fin, and in structural solver the fixed boundary condition was applied to that surface. The bottom boundary was placed 0.84 meter below the tip. For the upstream, the velocity inlet condition was selected. The downstream boundary had assigned the pressure outlet condition. The symmetry condition was assigned to the bottom and side boundaries. The top boundary was a slip-wall. The boundary conditions and domain dimensions are presented in Figure 2.27.

As described in the Chapter 2.7.1, in FSI calculations interface of two domains occurs, therefore it was necessary, that in both solvers the fin surface was identically oriented with regard to main coordinate system. For Abaqus, the surface of the fin that served as the interface was defined using the computational mesh faces.

MOST WIEDZY Downloaded from mostwiedzy.pl

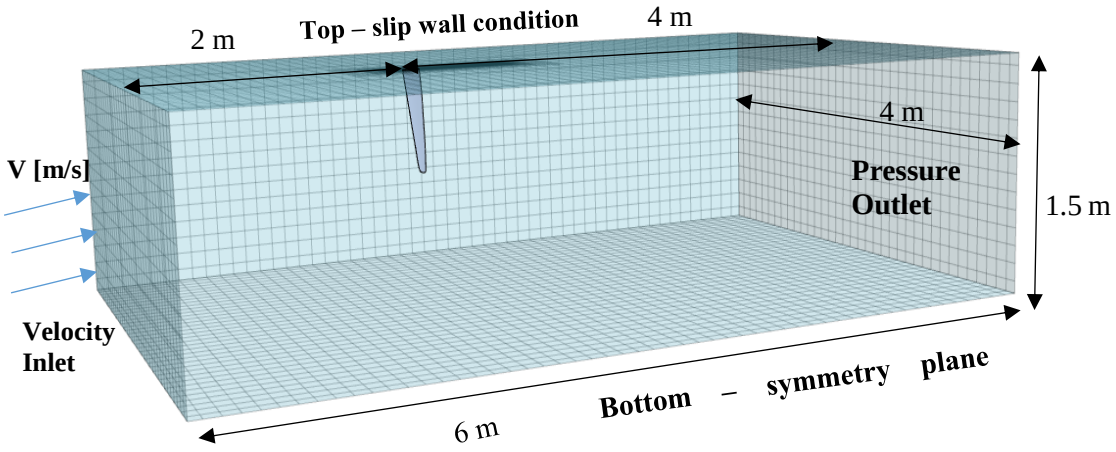

Figure 2.27 Boundary conditions and domain size for FSI calculations.

The fluid mesh resolution had to be high enough to accurately represent the geometry, especially leading and trailing edges, and capture all the flow relevant features. On the other hand, it should not be too expensive, due to high computational resources related to FEA-CFD coupling. Mesh refinements were applied on the tip and nose of the fin, in close proximity to the model and the wake region, including the expected area of tip vortex generation. The mesh coarsening was applied on the outside domain boundaries, where a large number of cells is unnecessary. The mesh morpher based on RBF was used to deform the mesh according to the displacement field function imported from Abaqus after every time step.

The final fluid mesh was a result of the systematic mesh sensitivity study. The FEA mesh remained the same as described in Section 2.6.5, because the FEA validation study confirmed the high credibility of proposed mesh and model. Apart from the influence of the mesh resolution in the boundary layer region (see Chapter 2.5.2 and 3.3.1) on the lift and drag characteristics, the influence of the mesh size on the accuracy of the FSI calculations was performed. The starting point for the mesh sensitivity study was the mesh obtained from the CFD study, however, it was decided that the base size element would be increased. The reason for this was the computation time. It took more than three days to perform FSI calculation for the single case with the mesh resolution corresponding to CFD Mesh 2 (see Table 2.1). After further consideration also the resolution inside the boundary layer was changed. As mentioned above, the viscous layer was not resolved directly, because selected range of angle of attack is below the stall angle and the y^+ has a major effect mainly on the stall angle prediction. Finally, the $k-\omega$ SST turbulence model was selected because the numerical mesh needs to be fine enough to benefit from DES approach, which otherwise for selected base model would be $k-\omega$ SST anyway.

There were eight prism layers with a maximum thickness of 0.002 m and prism layer stretching equal to 1.3. The values of y^+ were slightly above 30 for the highest speed case. Three mesh base sizes were used, the subsequent values of mesh base size varied from each other by factor of $\sqrt{2}$, resulting in mesh cell count equal to 1.2 M cells, 2.6 M cells and 5.7 M cells. The results of the mesh sensitivity study for FSI calculations are presented in Chapter 3.5.

MOST WIEDZY Downloaded from mostwiedzy.pl

The numerical fluid mesh used to evaluate the hydroelastic properties of the chosen windsurfing fin is presented in Figure 2.28.

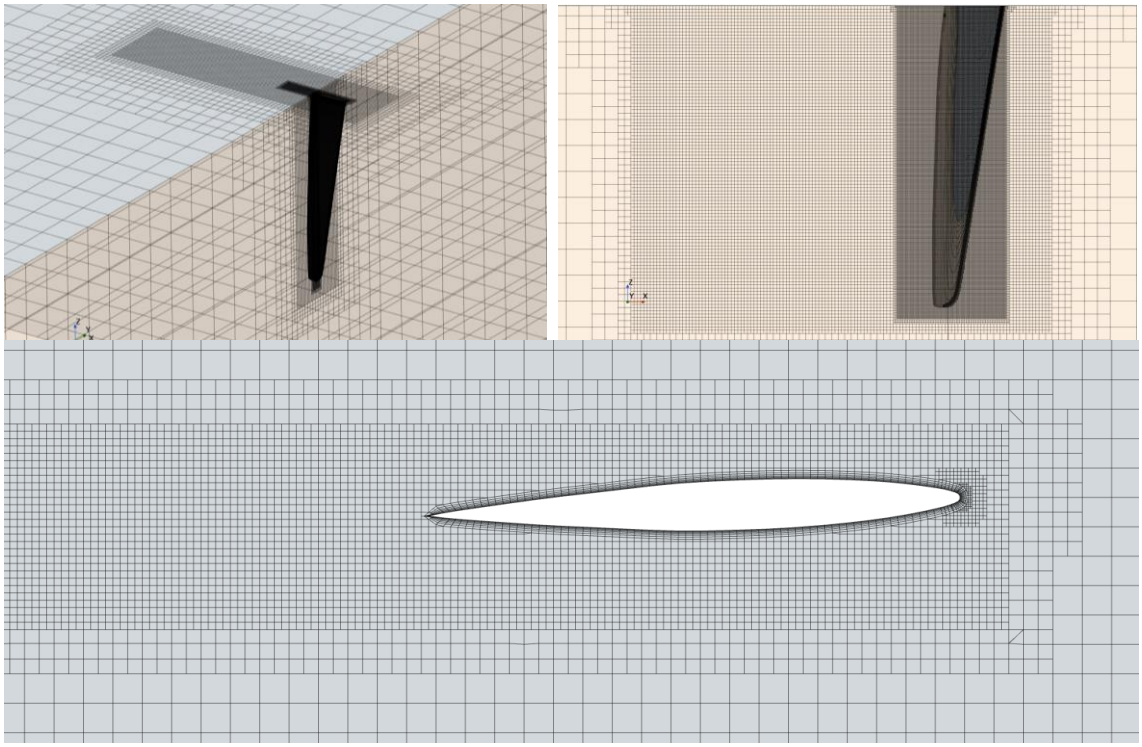

Figure 2.28 Numerical fluid mesh for FSI calculations.

For the structural calculations three types of elements were used in Abaqus: the shell elements were S4R and S3R which are and 3- and 4-noded shell element with reduced integration and a large-strain formulation. For the 3D elements the modified quadratic tetrahedral element (C3D10M) was chosen.

The last part was specification of the mechanical properties of the fins. To match the measured weight of the structure, for 3D elements that modelled the core of the fin the density equal to 950 kg/m^3 was assigned. The Poisson ratio was equal to 0.24. The plate elements had the material density equal to 1280 kg/ m^3, and Poisson ratio was equal to 0.32. The Poisson ratio and material stiffness were assumed constant along the entire span of the fin. The Young Moduli and plate thickness was specified as it is shown in Table 3.8 in Chapter 3.4.2. The last material constant necessary to specify was the material damping determined according to Rayleigh damping model, as described in Chapter 2.4.3 and Chapter 3.3.2. However, for the values of material damping found from experimental measurements it was not possible for large fluid loading to obtain stable calculations, despite application of strong coupling. To mitigate the problem, material damping was artificially increased, and the consequences are discussed in Chapter 4.

MOST WIEDZY Downloaded from mostwiedzy.pl

3. RESULTS

3.1. 3D scanning

The span of RS:X fin was equal to 0.66 m, and the chord at the head was equal to 0.129 m. Identifying the windsurfing RS:X profile indicated significant similarities to NACA 65-009 section (Hansen, Gourlay, and King 2011). The final 3D model of the RS:X windsurfing fin is shown in Figure 3.1.

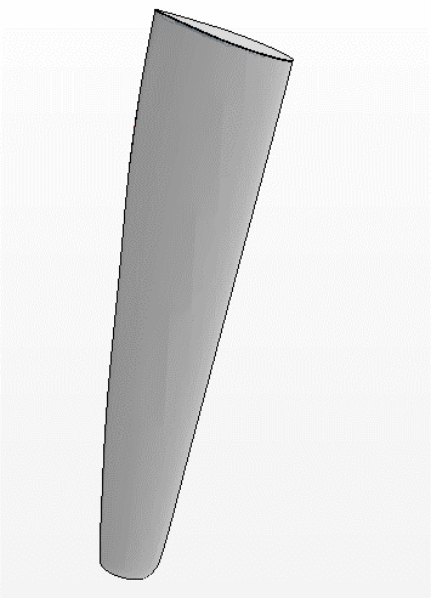

Figure 3.1 3D model of the windsurfing fin.

3.2. Experiment

This chapter presents the results of experimental investigation that served as a data source for stiffness identification of each fin – the assessment of displacement under the static loading is presented in Chapter 3.2.1. The FIN4 was selected for the free vibrations test. The results of this experiment are described in Chapter 3.2.2. The results of free vibration tests were used to confirm the accuracy of the stiffness identification procedure based on the static displacement measurements.

3.2.1. Static deformation trial

The results of the static load experiment are presented in Figure 3.2, in the form of displacement lines. The displacement is presented for four fins. It could be noticed that even for moderate loading equal to 130 N of concentrated force the displacement of the tip can vary from 48.6 mm to 67.4 mm. At the first control point the displacement varied between 12.3 mm and 16.7 mm. The displacement measured in the second control point was between 46.9 mm and 34.2 mm.

MOST WIEDZY Downloaded from mostwiedzy.pl

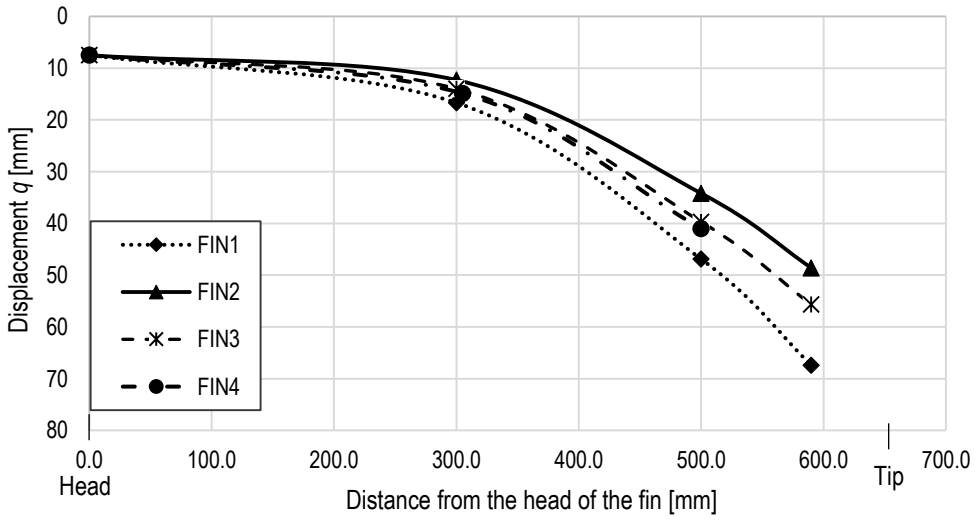

Figure 3.2 The results of the static load experiment - measured displacements.

Presented results were used as a benchmark data for identification of stiffness distribution of analysed RS:X windsurfing fins.

3.2.2. Free vibrations experiment

The direct results of the measurements were the time history of the accelerations and angular velocities in all six degrees of freedom from six sensors that were placed along the fin X-axis. Figure 3.3 presents the time history record registered by all the accelerometers in the Z-direction. The accelerometer numeration was one to six, starting with one closest to the head and six at the tip. The accelerometer 1 was places 5 mm from the tip, and the following sensors were placed 100 mm from each other, therefore, the last accelerometer was positioned 60 mm from the head (span of the fin is equal to 0.66 m).

It can be easily noticed that the accelerations are the highest at the tip of the fin. At the beginning of the measurement, the accelerations recorded by accelerometer 6 (6_Az) reached the 16 G measurement range, but it was quickly damped.

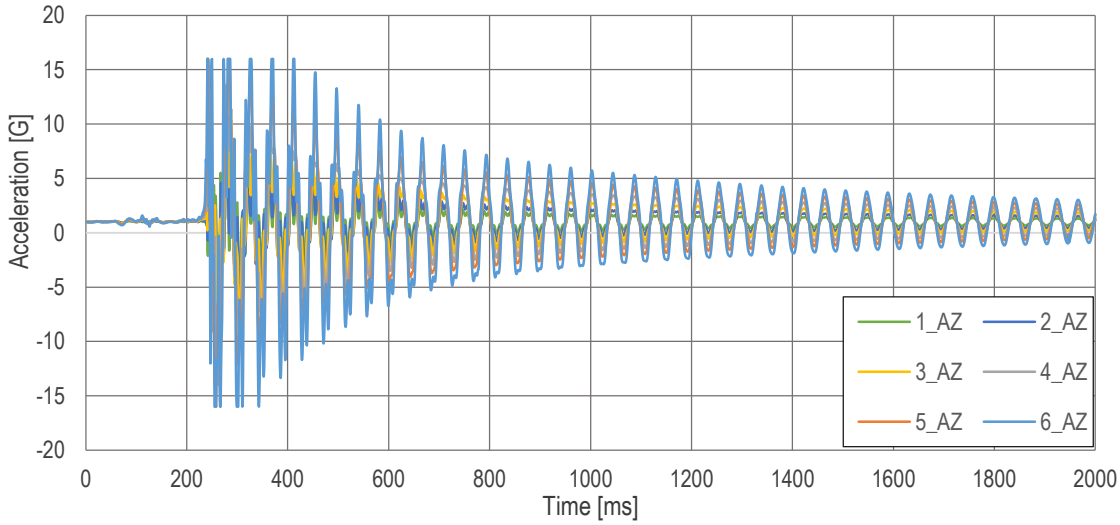

Figure 3.3 Time history of the accelerations in the Z-direction.

MOST WIEDZY Downloaded from mostwiedzy.pl

Table 3.1 summarizes the results of the measurements. The signal amplitude was calculated for the ten following periods, starting from 500 ms of the measurement. It can be noticed that the accelerations measured in the X-direction are less dependent on the position of the accelerometer than for the Y-direction and Z-direction accelerations. Moreover, the accelerations along X-axis are the secondary effect for extensive translations along Z-axis. The main reason for low accelerations in X and Y-direction is the high bending stiffness in this direction. It is worth noting that the X-axis is not the axis of symmetry. Therefore, the pure bending modes of the fin will almost never be observed. The accelerations in the Z-direction will be coupled with X-axis torsional accelerations. For Y and Z-direction accelerations, some variations in the mean value of the signal can be observed for various accelerometer locations.

Table 3.1. Results of the free vibration acceleration measurements.

	Z - direction	**X-direction**	**Y-direction**
Sensor number	Amplitude AZ [G]	Amplitude AX [G]	Amplitude AY [G]
1	0.5	0.032	0.019
2	0.87	0.045	0.031
3	1.32	0.059	0.044
4	1.87	0.058	0.064
5	2.45	0.059	0.07
6	3.12	0.067	0.12

The correct processing of the signal remained the crucial for this study. The Fourier Transform was used to transfer the signal from the time into the frequency domain. This ability was used to assess the natural frequency of the analysed composite structure. Figure 3.4 presents the spectral power density plot of the accelerations measured by the accelerometer A6. The function peak corresponds to the natural frequencies of the composite structure. The analysis was performed for the time history of the accelerations in all three directions. The right vertical axis corresponds to the value of power spectral density of accelerations in the Z-direction, while the left axis to the accelerations in directions X and Y.

The values on the right axis are about twenty times larger than those on the left axis, showing the domination of the accelerations along the Z-axis.

The first natural frequency is equal to 23.99 Hz, and the second is equal to 94.45 Hz. Those modes are dominated by the Z-direction accelerations and correspond to the first two bending modes. The plot requires a closer look for the determination of the higher frequencies. The third bending mode occurs for the frequency 222.9 Hz.

Here, the accelerometers were positioned along one line. Therefore, the time history of angular velocity from sensor A6 according to the X-axis was analysed to assess torsional modes accurately. The power spectral density of those signals is presented in Fig. 3.5.

MOST WIEDZY Downloaded from mostwiedzy.pl

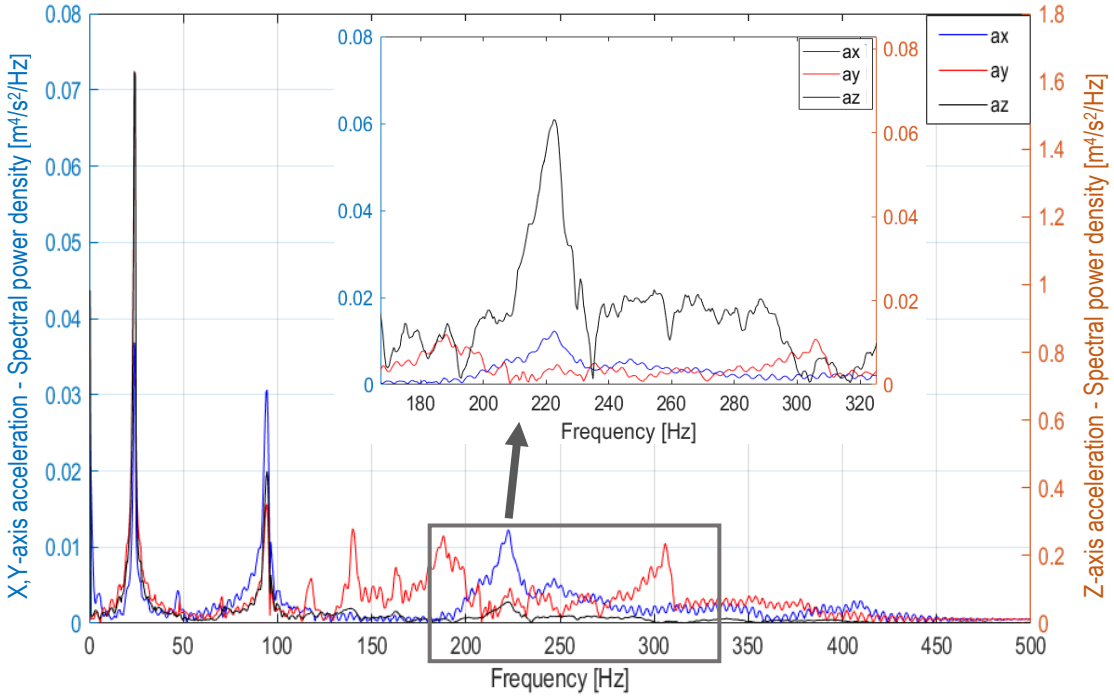

Figure 3.4 FFT of the accelerations time history based on the sensor A6 measurement.

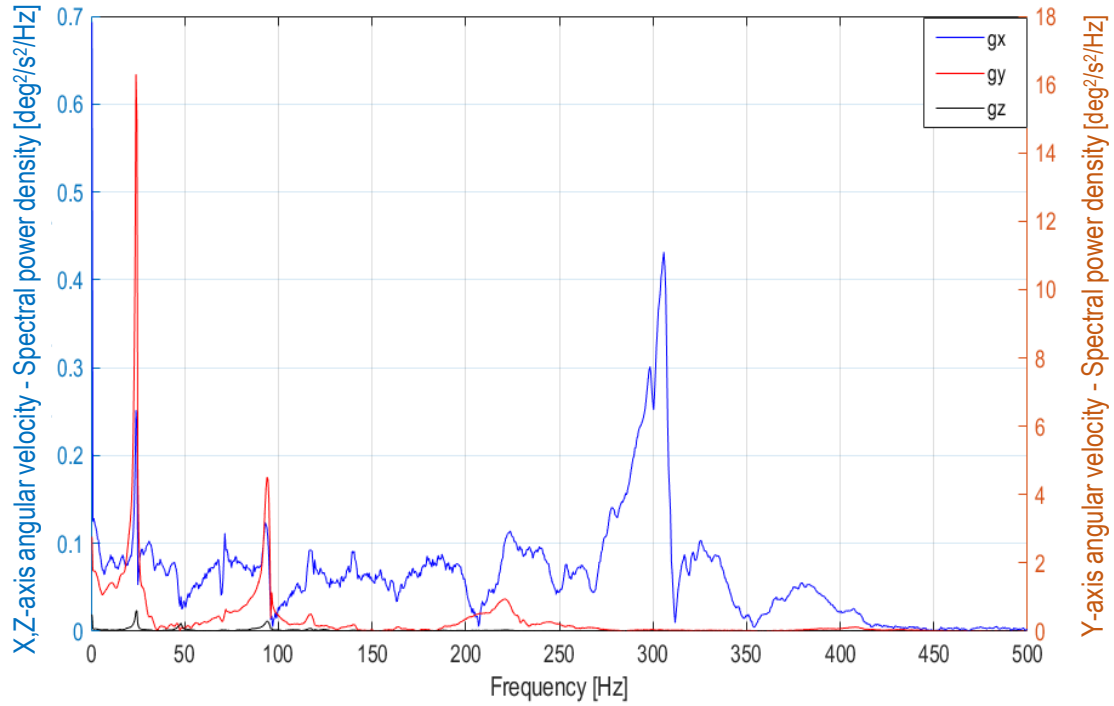

Figure 3.5 FFT of the angular velocity time history based on the sensor A6 measurement.

The rotation around the Y-axis corresponds to the bending motion, while torsion is the rotation around the X-axis. The spectral power density resultant from measured angular velocity of the structure due to bending (gy) is on the right axis, and torsional motion (gx and gz) is on the left axis. The spectral power density of angular velocity around the Y-axis is about ten times greater than the spectral power density of angular velocity around the X-axis. This proves the

MOST WIEDZY Downloaded from mostwiedzy.pl

domination of bending deformations. It is understandable since the bending stiffness is the smallest due to low cross-section moment of inertia about the Y-axis.

According to Fig. 3.5, the first three bending modes could be distinguished from angular velocity measurement. The rotation around Z-axis is negligible. This is related to the considerable stiffness for bending around Z-axis, which is perpendicular to the fin mid surface. Additionally, the bending modes are coupled with the torsional effects due to X-axis.

The fourth eigenmode corresponds to 305.8 Hz frequency, which can be considered almost pure torsional mode.

Figure 3.6 presents the time history of the accelerations along the Z-axis in water. It can be noticed that compared to the Figure 3.3 the values of the accelerations are more than one order of magnitude lower than in the air. Additionally, the oscillations are more quickly dampened.

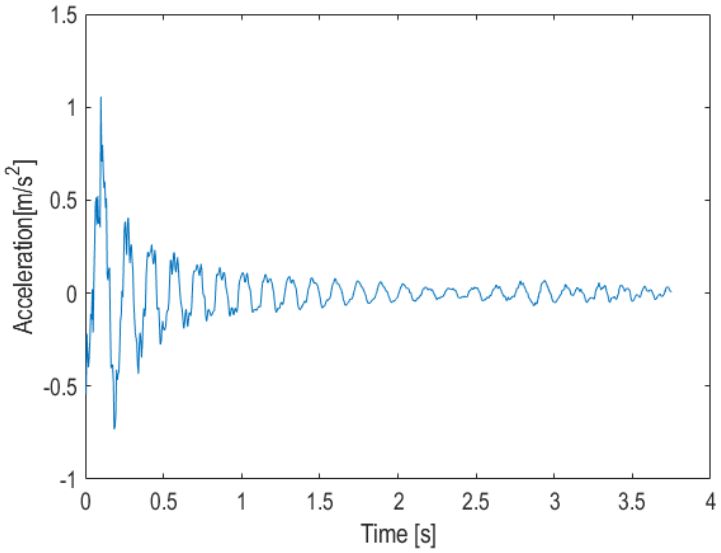

Figure 3.6 Time history of the accelerations along the Z-axis in water.

Based on the time history of the signal the FFT analysis was done, which allowed to indicate values of the eigenfrequencies in water. The result is presented in Figure 3.7.

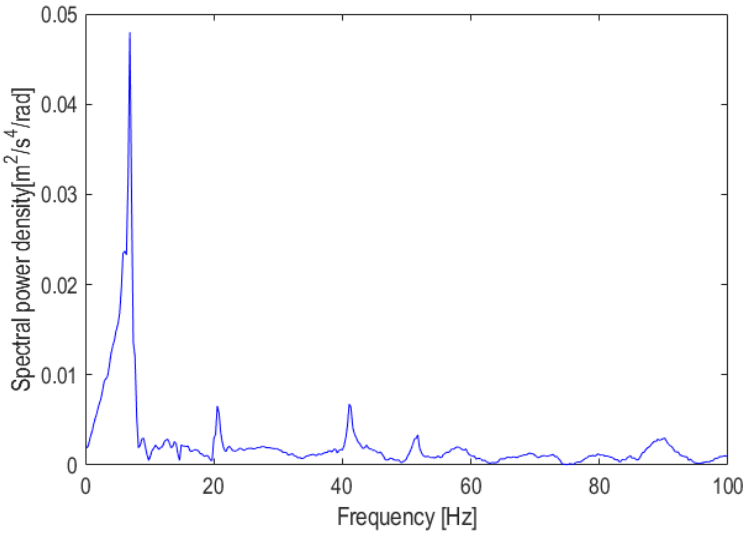

Figure 3.7 Spectral power density plot of the accelerations time history in water.

MOST WIEDZY Downloaded from mostwiedzy.pl

The results of the free vibrations test in air and in water are summarised in Table 3.2. It can be noticed that the values of eigenfrequencies in water are significantly smaller than in air. It is the result of the presence of the added mass, which is accelerated by the oscillating hydrofoil.

Table 3.2. Eigenfrequencies in water and in air.

Mode	Eigenfrequency in air	Eigenfrequency in water
1	23.99 Hz	6.933 Hz
2	94.45 Hz	20.53 Hz
3	222.9 Hz	41.07 Hz
4	305.8 Hz	-

As mentioned earlier in this chapter the first three modes in the air are dominated by the bending motion and the fourth mode is almost pure torsional mode. For the vibrations in water no torsional mode was detected, and the first three modes are dominated by bending. The strength of the power spectrum for the frequencies higher than the third eigenfrequency is rather small, therefore they were not considered.

3.2.3. Damping coefficients

Following the procedure described in Chapter 2.4.3 first two eigenfrequencies were isolated. In the Figure 3.8 a) is presented the time history of Z-axis accelerations for the first eigenfrequency. To verify the correctness of the filtration, the FFT of the obtained signal was calculated. It is presented in the Figure 3.8 b). It can be noticed that only one peak corresponding to the frequency equal to 23.99 Hz occurs. Therefore, the procedure is correct and the time history of the Z-axis accelerations for the first eigenfrequency was obtained.

a) b)

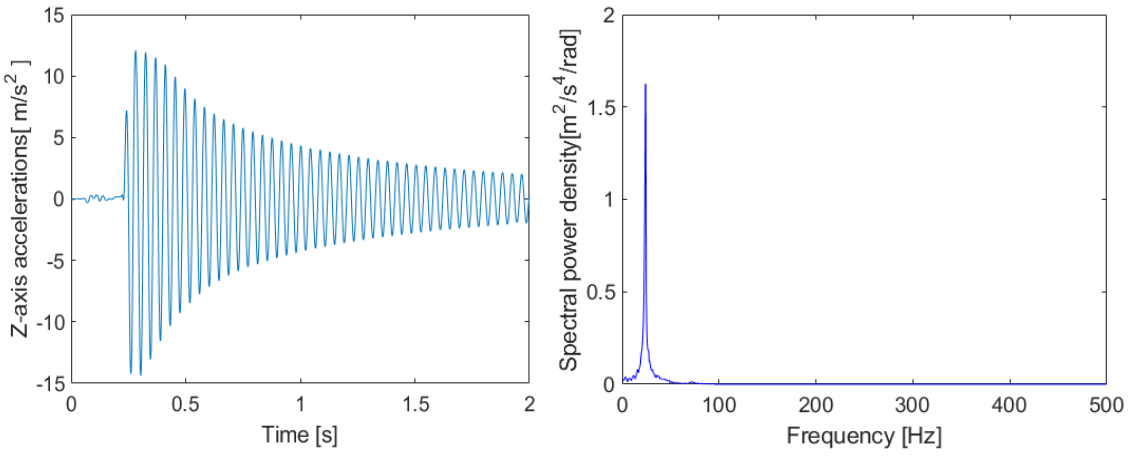

Figure 3.8 a) Time history of the accelerations in air b) FFT of the filtered signal for the first eigenmode.

The same procedure was applied to obtain the time history of accelerations for the second eigenfrequency. The time history of accelerations of the second eigenfrequency and FFT of the filtrated signal are presented in Figure 3.9. The peak in the acceleration spectrum corresponds to the frequency equal to 94.45 Hz.

MOST WIEDZY Downloaded from mostwiedzy.pl

a) b)

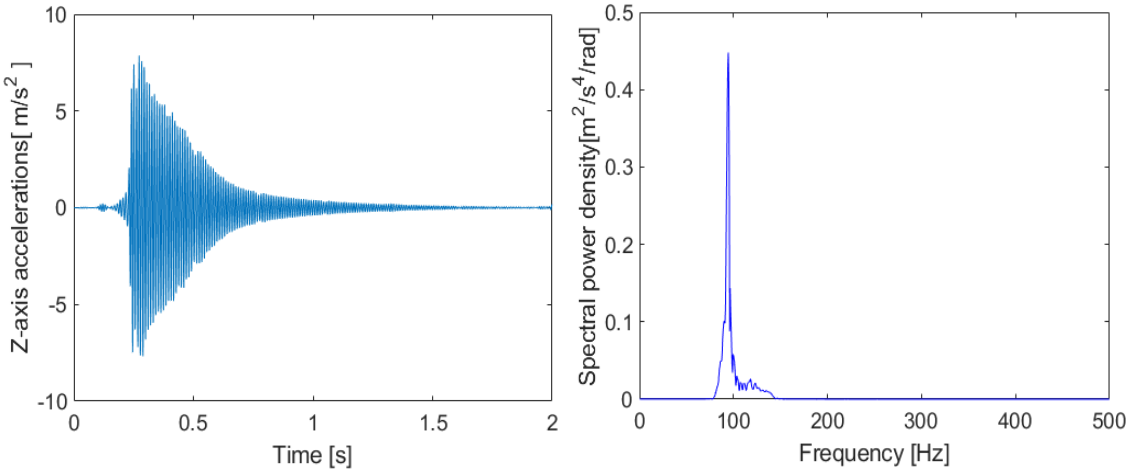

Figure 3.9 a) Time history of the accelerations in air b) FFT of the filtered signal for the second eigenmode.

The time history of accelerations along the Z-axis of the first two eigenfrequencies was used to obtain logarithmic decrements of those eigenfrequencies, damping coefficients ζ_1 and ζ_2 according to Eq. 2.5. The logarithmic decrements were calculated according to Eq. 2.6 based on the value of the maximum amplitude X_{A1} and the first amplitude which value dropped below 0.14 X_{A1}. Then the number of periods of oscillation were calculated and damping coefficients for each eigenfrequency were evaluated. The results were presented in the Table 3.3.

Table 3.3 Damping ratio in air.

	Eigenfrequency 1	**Eigenfrequency 2**
n – number of cycles	40	38
Λ – logarithmic decrement of damping	0.0504	0.0519
ζ – damping coefficient	0.00802	0.00826

Finally damping coefficients α and β, namely mass and stiffness proportional damping coefficients, were calculated according to Eq. 2.3 and Eq. 2.4, and they are equal to:

$$\boldsymbol{\alpha = 1.34} \qquad \boldsymbol{\beta = 2.24 * 10^{-5}}$$

The same procedure was used to determine the damping coefficients in water. Figure 3.10 a) presents the time history of the signal processed with the low pass filter equal to 7 Hz, giving the time history of the accelerations for the first mode. Figure 3.10 b) presents the FFT of the signal presented in Figure 3.10 a).

MOST WIEDZY Downloaded from mostwiedzy.pl

a) b)

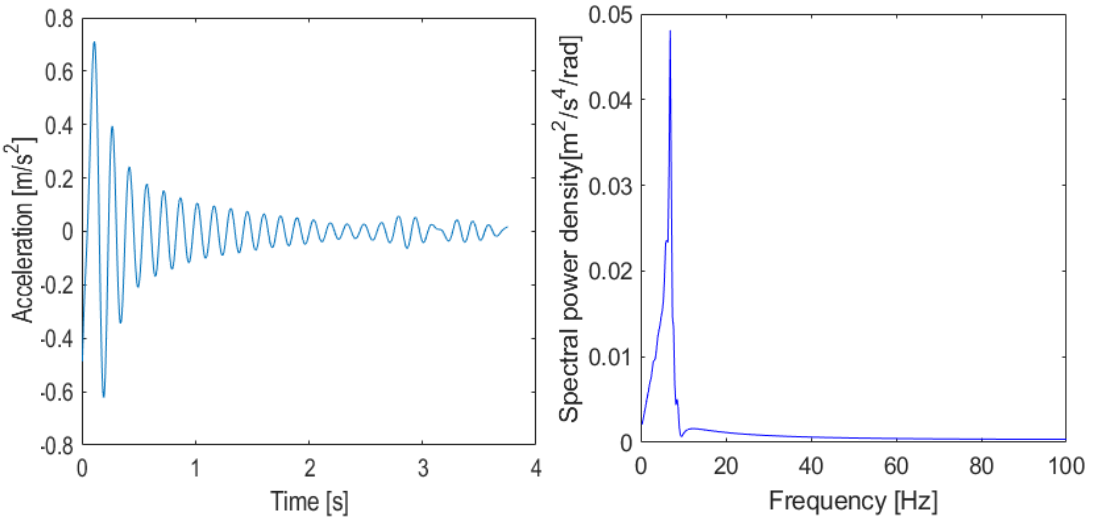

Figure 3.10 a) Time history of the accelerations in water – first mode b) FFT of the filtered signal for the first eigenmode.

Figure 3.11 a) presents the time history of the signal processed with the low pass filter equal to 21 Hz, and then high pass filter with the threshold of 19 Hz. It gives the time history of the accelerations for the second mode. Figure 3.11 b) presents the FFT of the signal presented in Figure 3.11a).

a) b)

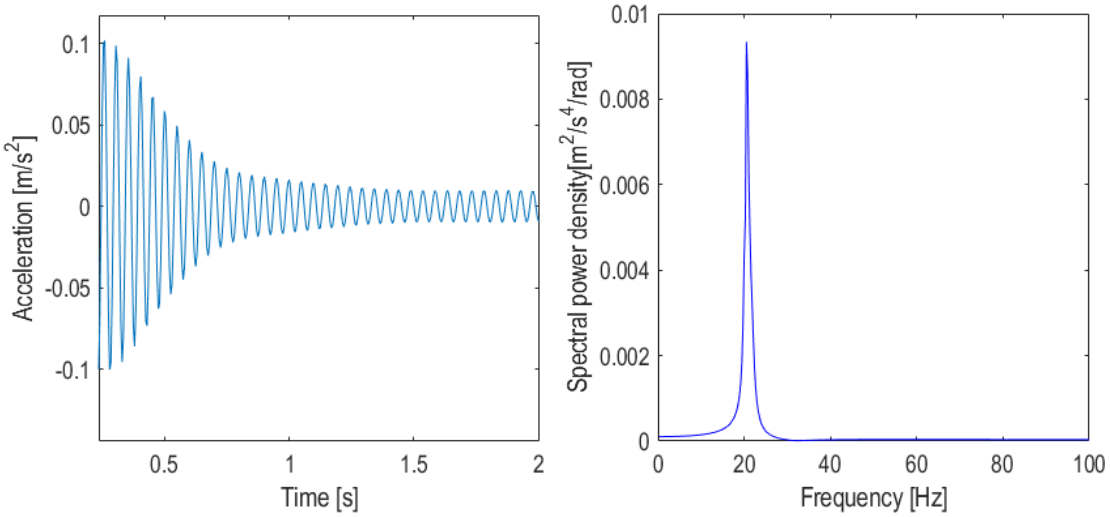

Figure 3.11 a) Time history of the accelerations in water – second mode b) FFT of the filtered signal for the second eigenmode.

Table 3.4 Damping ratio in water.

	Eigenfrequency 1	**Eigenfrequency 2**
n – number of cycles	7	18
Λ – logarithmic decrement of damping	0.114	0.295
ζ – damping coefficient	0.0182	0.0469

MOST WIEDZY Downloaded from mostwiedzy.pl

Finally damping coefficients α and β, namely mass and stiffness proportional damping coefficients, they are equal to:

$$\boldsymbol{\alpha = 3.86} \qquad \boldsymbol{\beta = 3.88 * 10^{-5}}$$

Both values (determined in water and airt) were used in FSI calculations, however, due to issues with stability of calculation discussed in Section 4.4.2 different values were used in the end. It can be noticed that the damping coefficient $\boldsymbol{\alpha}$ for water is about two times larger than for water. It is believed that this is caused by the effect of added mass, which artificially increased the mass proportional damping in this case.

3.3. Computational Fluid Dynamics

3.3.1. Validation study results

Figure 3.12 presents the drag and lift coefficient plots against the angle of attack (AoA) for the experiments (EFD – Experimental Fluid Dynamic) by Zarruk et al. (2014) and CFD calculations. The values of lift and drag forces were normalized to obtain lift coefficient C_L and drag coefficient C_D. They are defined as follows:

$$C_L = \frac{L}{0.5\rho V^2 S} \qquad C_D = \frac{D}{0.5\rho V^2 S} \tag{3.1}$$

The planform area *S* of the hydrofoil was equal to 0.027 m^2, and free stream velocity V was calculated based on the Reynolds number value.

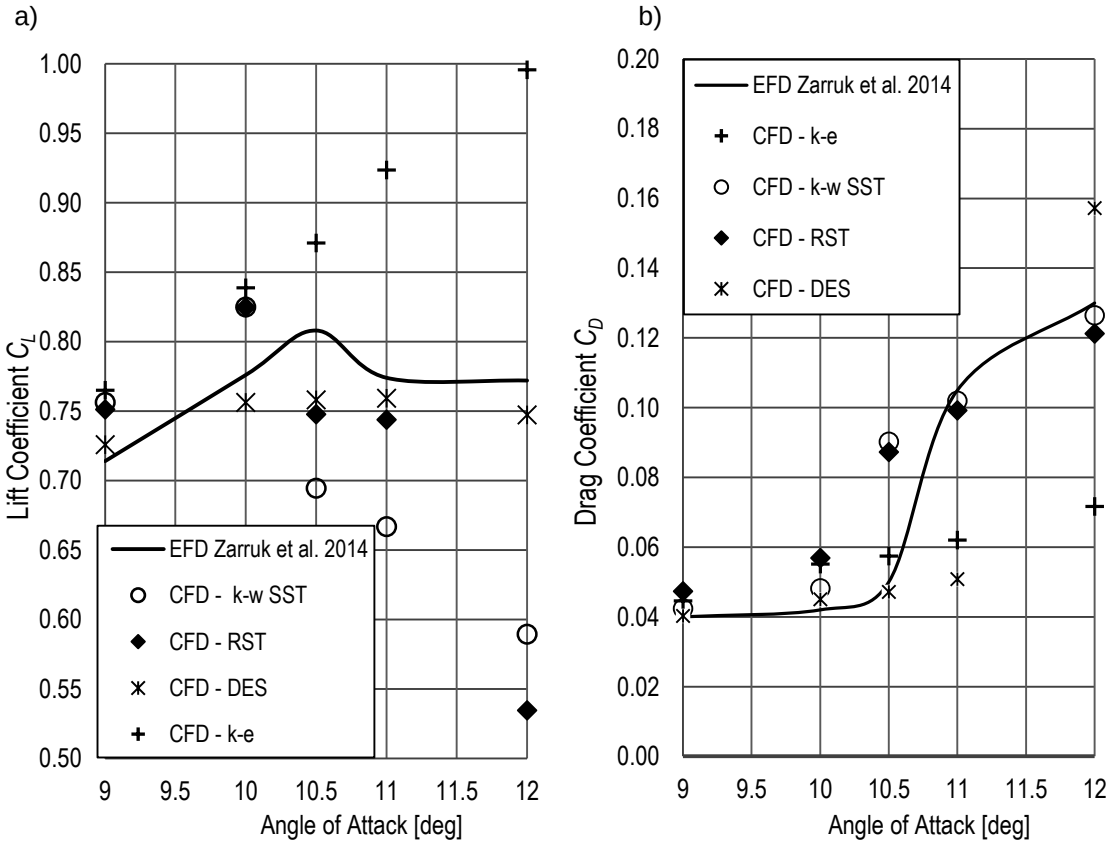

Figure 3.12 Validation Study a) lift coefficient comparison b) drag coefficient comparison.

MOST WIEDZY Downloaded from mostwiedzy.pl

In Table 3.5, the relative error between the experimental data and numerical simulations is included. The error is defined as $(R_{CFD} - R_{EFD})/R_{EFD}$ where R correspond to CFD of EFD result.

Table 3.5 Validation of the CFD calculations **-** comparison with EFD results.

	$k-\varepsilon$		RST		$k-\omega$ SST		DES	
AoA [deg]	% diff C_L	%diff C_D	%diff C_L	% diff C_D	% diff C_L	% diff C_D	% diff C_L	% diff C_D
9	7.14%	11.38%	5.20%	18.27%	5.90%	5.91%	1.66%	0.54%
10	8.07%	31.18%	6.26%	35.44%	6.31%	14.65%	-2.56%	7.13%
10.5	7.80%	14.86%	-7.46%	74.47%	-14.05%	80.32%	-6.18%	-5.68%
11	19.31%	-40.91%	-3.92%	-5.54%	-13.86%	-2.95%	-1.92%	-51.64%
12	28.97%	-44.86%	-30.76%	-6.75%	-23.67%	-2.71%	-3.22%	20.93%

According to Figure 3.12, both $k-\omega$ SST and RST model underpredicted the value of the stall angle. For the $k-\omega$ SST, the problem of accelerated separation is well known. The modifications into the *gamma-theta* transition model were applied according to suggestions of Siemens PLM Software (2017). However, it did not help mitigate this problem. Both models overpredicted lift and drag for lower angles of attack. Nevertheless, above the stall angle, both models predicted drag with remarkably high accuracy. Although the lift force for the low angles of attack is well predicted, it is underestimated past the stall.

The $k-\varepsilon$ turbulence failed to predict the value of stall angle. Both the drag and lift coefficient raised almost linearly for the entire range of angles of attack. It proves that for the separated flow the $k-\varepsilon$ turbulence model cannot be chosen. However, for the linear region, the accuracy is comparable to both the $k-\omega$ SST and RST models. Moreover, reduction of the computation time compared to the $k-\omega$ SST and RST model is quite significant. For this particular study, it was equal to 18% and 96%, respectively. The DES approach required 37% more time than the $k-\varepsilon$ for completing a time step.

In terms of lift force prediction, the DES approach was characterized by good accuracy for the entire range of analysed angles of attack. The drag force prediction was less accurate due to delayed stall angle compared to the experimental finding. The drag curve predicted by CFD is much steeper for the highest values of analysed angles of attack compared to the experimental results. According to the validation study results, none of the turbulence models managed to predict the stall angle "on point". Additionally, none of them managed to predict both drag and lift accurately for the entire range of analysed angles of attack. Although, in general, the accuracy of the DES approach was found to be the highest, but other models have also their advantages.

3.3.2. Fluid mesh verification study results

The numerical simulations were run until convergence of the result. In case of high angles of attack until sufficient number data – the time history of lift and drag were gathered for averaging the simulation solution. The values of the lift coefficient C_L and drag coefficient C_D were obtained.

The planform area *S* of the windsurfing fin was equal to 0.061 m^2, and free stream velocity V = 10m/s. It corresponds to Reynolds number around Re≈10^6. Figure 3.13 presents the drag and lift curves comparison. Each chart corresponds to a different turbulence modelling approach.

MOST WIEDZY Downloaded from mostwiedzy.pl

The differences between meshes are presented as well (for the record – M1, M2 and M3 corresponds to the coarse, medium, and fine mesh, respectively – see Table 2.1). Meshes differ by total cell element number due to various number of prism layers. It results in different values of y^+.

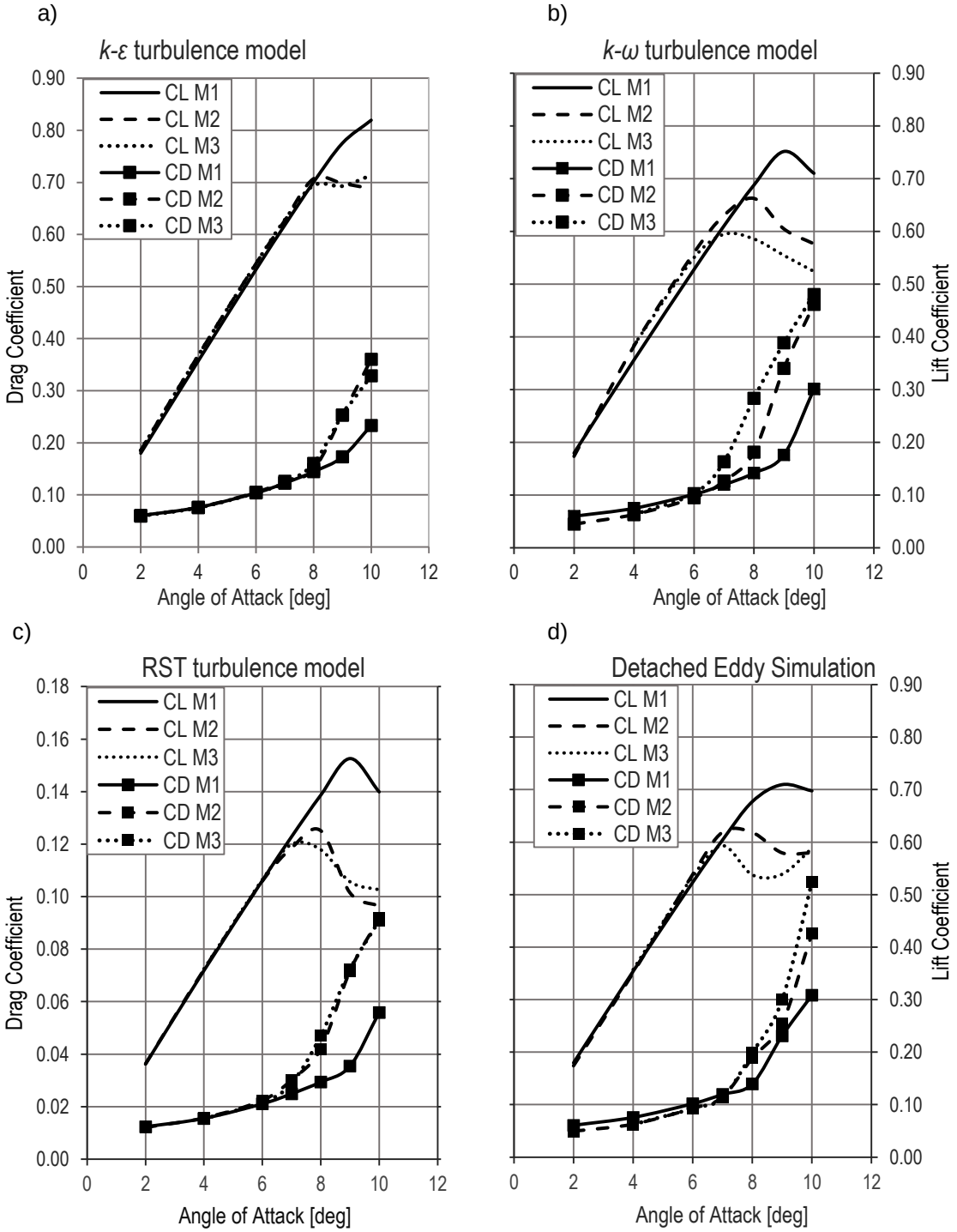

Figure 3.13 Mesh dependence study a) $k-\varepsilon$ turbulence model, b) $k-\omega$ SST turbulence model, c) Reynolds's Stress Transport turbulence model, d) Detached Eddy Simulation.

According to Figure 3.13 for the $k-\varepsilon$, before the separation occurs, the value of y^+ had a minor influence on the drag and lift curve. The value of stall angle predicted by the coarsest grid was significantly higher than for the remaining meshed. For M2 and M3 the stall angle was equal

MOST WIEDZY Downloaded from mostwiedzy.pl

to 8 degrees. The coarsest mesh did not predict the occurrence of the stall angle at all for the tested range of angles of incidence.

For the $k-\omega$ SST model, the strong dependency of lift and drag curves from the y^+ value could be observed. With decreasing y^+, the stall angle and corresponding value of maximum lift decreased as well. In the past stall regime, the drag increased with the increasing mesh resolution. Therefore, the lower y^+, the higher the drag value. For the M3, M2, and M1 the values of stall angle were equal to 7 degrees, 8 degrees, and 9 degrees, respectively.

For the RST turbulence model, the values of lift and drag coefficients up to the value of 6 degrees angles of attack were almost identical. Both low y^+ meshes predicted similar post-stall behaviour in terms of lift and drag values. The sensitivity on the y^+ value is smaller than for the $k-\omega$ SST model. The coarsest mesh overpredicted the stall angle compared to finer meshes. Therefore, for the angle attack above 6 degrees the drag value was lower and lift higher than for the remaining M2 and M3 grids. Obtained values of the stall angle were equal to 7 degrees, 8 degrees, and 9 degrees for M3, M2, M1, respectively.

For the DES, the same pattern of over predicting the stall angle by the coarsest mesh can be noticed, with similar relations as described for the remaining cases. The dependency on the y^+ could also be observed for angles of attack greater than 7 degrees. The stall angles were equal to 7 degrees, 7.5 degrees, and 9 degrees for M3, M2, M1, respectively. Therefore, the influence of the y^+ on the stall angle is smaller than for the remaining three approaches.

Figure 3.14 presents the comparison between the results obtained using CFD for various models and lifting line method. Mesh 2 was selected for the comparison. Since lifting line method does not account for stall, the results were compared only for the angle of attack up to 7 degrees.

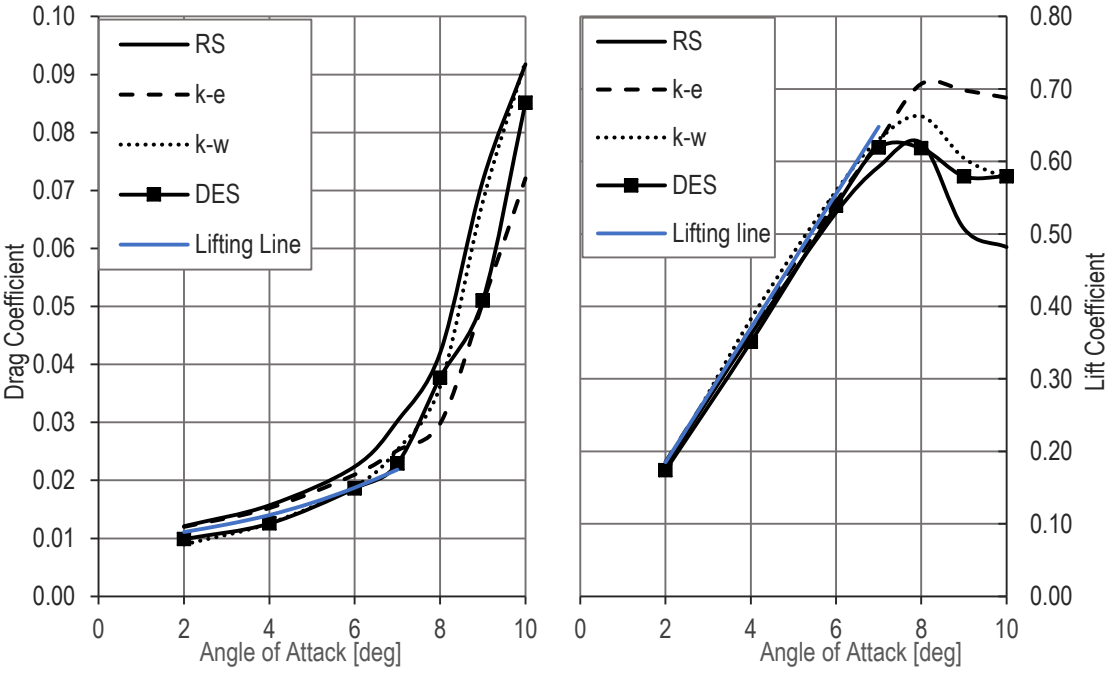

Figure 3.14 Comparison of lifting line results with CFD for all turbulence models and Mesh 2.

MOST WIEDZY Downloaded from mostwiedzy.pl

It can be noticed that the agreement between lift coefficients values obtained by CFD, and the lifting line method are very similar, proving that obtained values are credible. There are some discrepancies between values of drag coefficient obtained using various turbulence models. Drag coefficient obtained with lifting line method lies between extreme results of CFD based drag coefficient.

The mesh resolution in the boundary layer region has a major influence on the prediction of the hydrofoil hydrodynamic characteristics. Applying the wall functions prevents accurate prediction of the stall angle. The differences between the turbulence models and DES could be observed as well. For better understanding, the turbulent kinematic energy fields were compared for all three meshes and all four approaches for turbulence modelling for RS:X windsurfing fin at 8 degrees angle of incidence. The results were presented in Figure 3.15 with increasing mesh resolution from left to right (M1, M2, and M3, respectively).

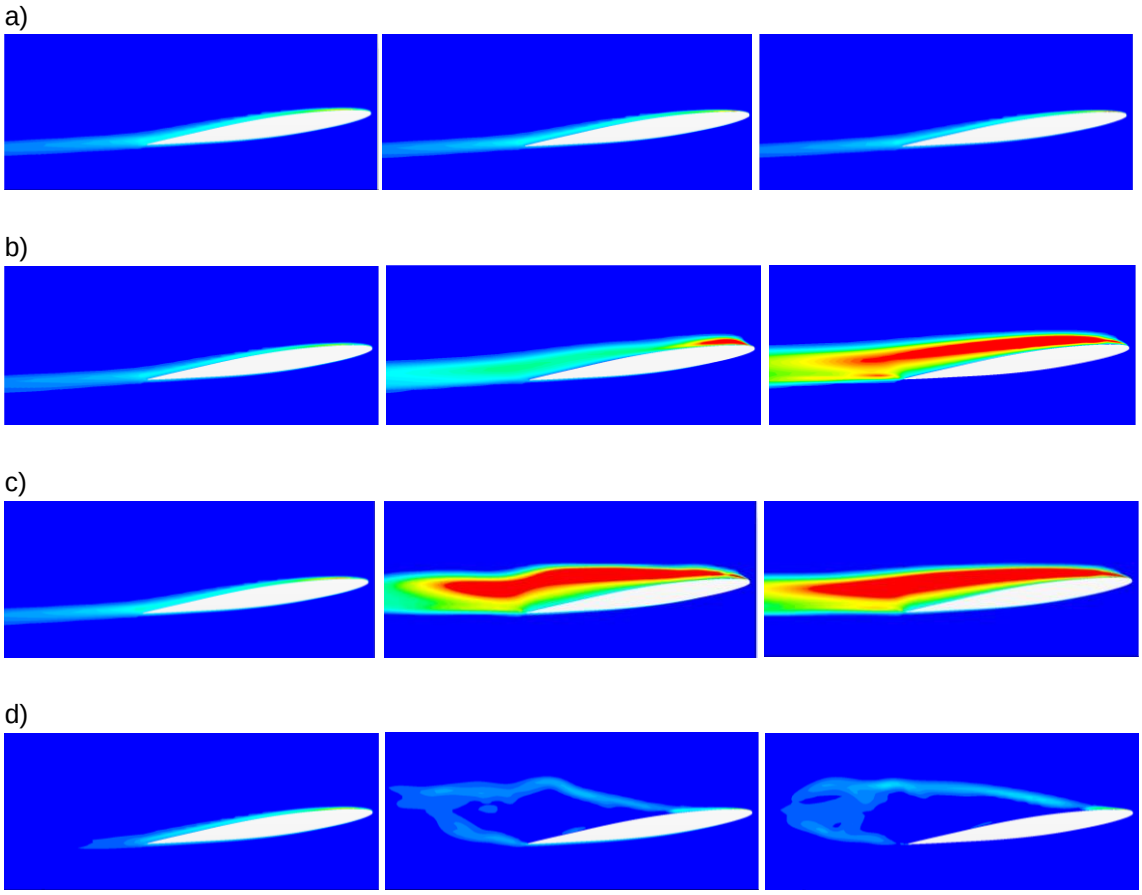

Figure 3.15 Turbulence kinetic energy field a) $k-\varepsilon$ model b) $k-\omega$ SST model c) RST model d) DES and y^+ = 40 (left), y^+ = 3.8 (middle), y^+ = 1.8 (right).

It could be noticed that the turbulence intensity is the highest for the finest mesh for the RST model. It might explain the low values of lift and high values of drag for this angle of incidence. At the same time, a low level of turbulence energy for $k-\varepsilon$ could explain the delay of the predicted stall, high values of lift, and low drag. The turbulence kinetic energy field for DES significantly differs from RANS-based simulations.

MOST WIEDZY Downloaded from mostwiedzy.pl

In terms of the Fluid-Structure interaction assessment of the RS:X windsurfing fin, the proper calculation of the lift force is of major interest. The lift is about one order of magnitude greater than the drag and buoyancy force generated by the fin. Therefore, the lift force is the major load on the structure. The bending cross-sectional index of the horizontal cross-section is the smallest compared to other directions. It means that the bending deformations in the lift force direction will be dominating. Therefore, the accurate prediction of the lift force is believed to have a priority over accurate drag assessment. In the end it was decided to use the $k-\omega$ SST turbulence model and that the hydroelastic calculations will focus on the linear region. The latter allows to apply less conservative approach for the y^+ value. Despite advantages of DES in terms of accuracy, it was decided that the FSI calculations would be too time consuming. For the coarse mesh DES would use in the end $k-\omega$ SST formulation anyway.

3.4. Finite Element Method

3.4.1. Identification of stiffness distribution – stage 1

This Chapter presents the results of stiffness optimisation procedure based on variation of plate element thickness. In the workflow diagram (Figure 2.22) it corresponds to the box Femap build-in optimisation, and the result of this step was the FEM model – Stage 2. As mentioned before, in this stage the Young Modulus of the sections was constant and plate thickness was searched by Femap optimisation tool.

Table 3.6 presents results of primary optimization with relative differences of the displacements in control points compared to experimental data. It can be noticed that this straightforward approach allowed for obtaining quite satisfactory results. The percentage difference between the experimental and computational displacements was varied between 0% and 4.66%.

MOST WIEDZY Downloaded from mostwiedzy.pl

Table 3.6 Results of the identification procedure – Stage 1.

FIN1			
Displacement in control point	q_1 [m]	q_2 [m]	q_3 [m]
Experiment	0.0167	0.0469	0.0674
FEM	0.0167	0.0471	0.0647
Difference	0%	-0.43%	4.01%
Sum of least squares	$1.623 * 10^{-6}$		
FIN2			
Displacement in control point	q_1[m]	q_2 [m]	q_3 [m]
Experiment	0.0123	0.0342	0.0486
FEM	0.0120	0.0344	0.0473
Difference	2.71%	-0.48%	2.58%
Sum of least squares	$1.345 * 10^{-6}$		
FIN3			
Displacement in control point	q_1 [m]	q_2 [m]	q_3 [m]
Experiment	0.0140	0.0397	0.0557
FEM	0.0141	0.0402	0.0553
Difference	-0.86%	-1.36%	0.66%
Sum of least squares	$0.303 * 10^{-6}$		
FIN4			
Displacement in control point	q_1 [m]	q_2 [m]	-
Experiment	0,0149	0,0410	-
FEM	0.0142	0.0419	-
Difference	-4.66%	2.20%	
Sum of least squares	$1.298 * 10^{-6}$		

The membrane stiffness Et obtained for each section was used to as a starting point for next stage of the identification.

3.4.2. Identification of stiffness distribution – stage 2

The procedure described in Chapter 2.6.2 was followed to obtain displacements in control points for all fins. For FIN1 and FIN4 five iterations were necessary to obtain convergence. The results of static deformation for FIN2 and FIN3 converged after two iterations. The stiffness distribution was precisely identified for all fins. Following figures presents the convergence plots for each iteration step for FIN4. In Fig. 3.16, the convergence of the deformations in control points one and two are presented.

MOST WIEDZY Downloaded from mostwiedzy.pl

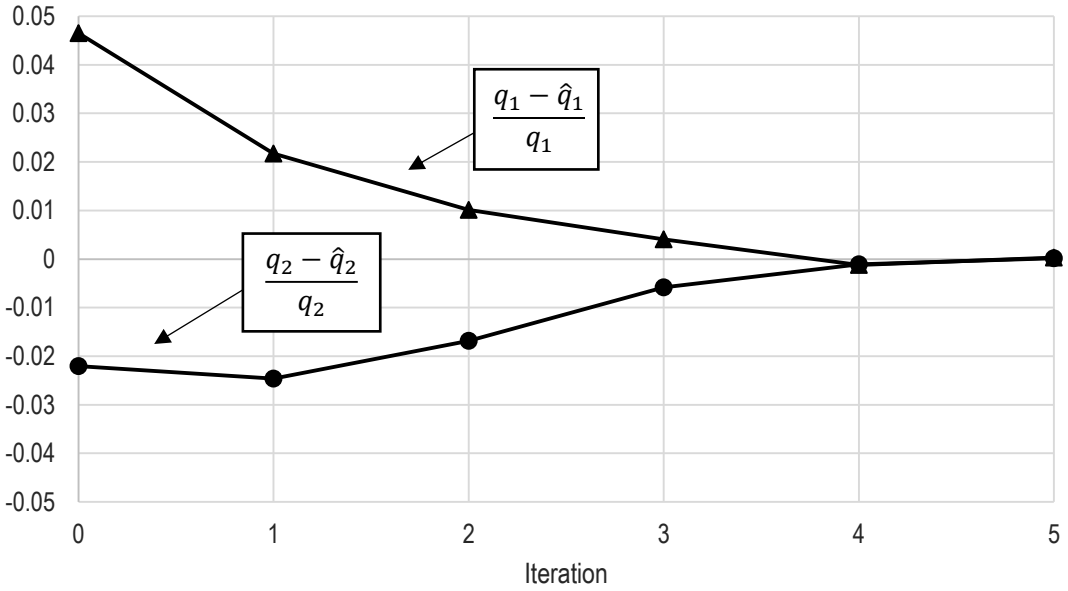

Figure 3.16 The convergence plot for the normalized state variable variations.

Figure 3.17 presents the convergence of the values of Young Modulus for sections from one to eight for the FIN4 and the final values of Young Modulus for each section. The influence of properties E_7 and E_8 was negligible thus was not identified in this stage, nevertheless, they were included in the Fig. 3.17.

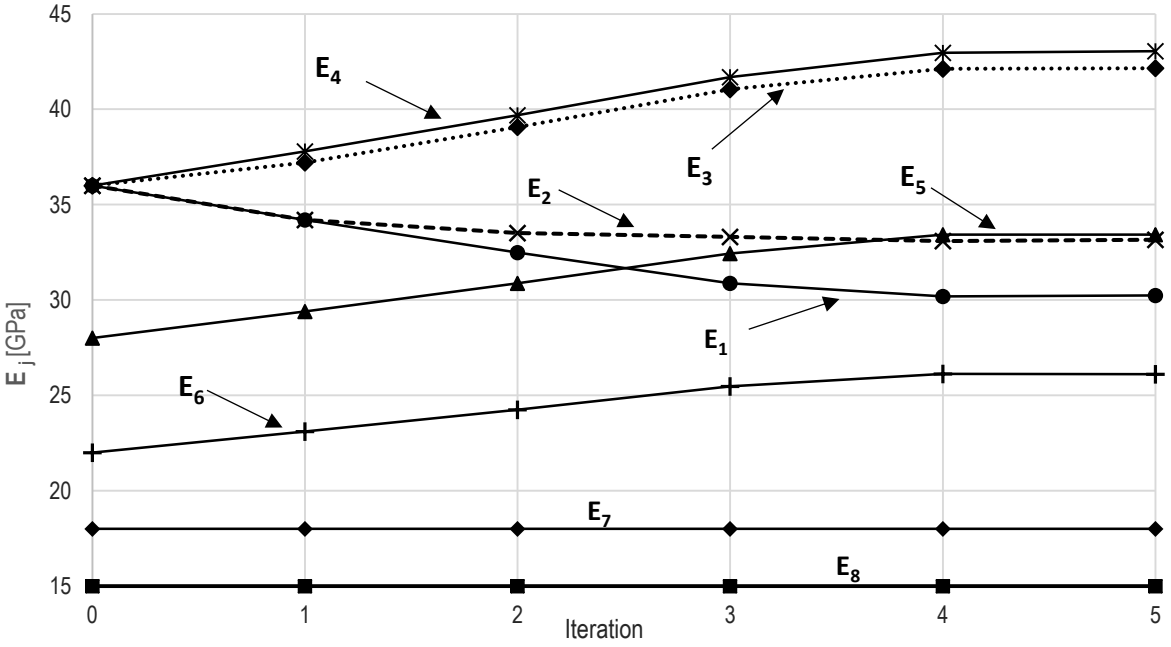

Figure 3.17 Identification of the design variables process.

Figure 3.18 a) presents the variations of the sensitivity vector $\bar{\mathbf{w}}_{\mathbf{1i}}$ for the first control point, and Figure 3.18 b) shows the variations of the sensitivity vector $\bar{\mathbf{w}}_{\mathbf{2i}}$ for the second control point. Both apply to FIN4. It is essential to mention that the Young Modulus of sections from five to eight does not influence the deformation in the control point one; therefore, they were not included in Figure 3.18 a). In Figure 3.18 b) sections seven and eight were neglected for the same reasons.

MOST WIEDZY Downloaded from mostwiedzy.pl

a)

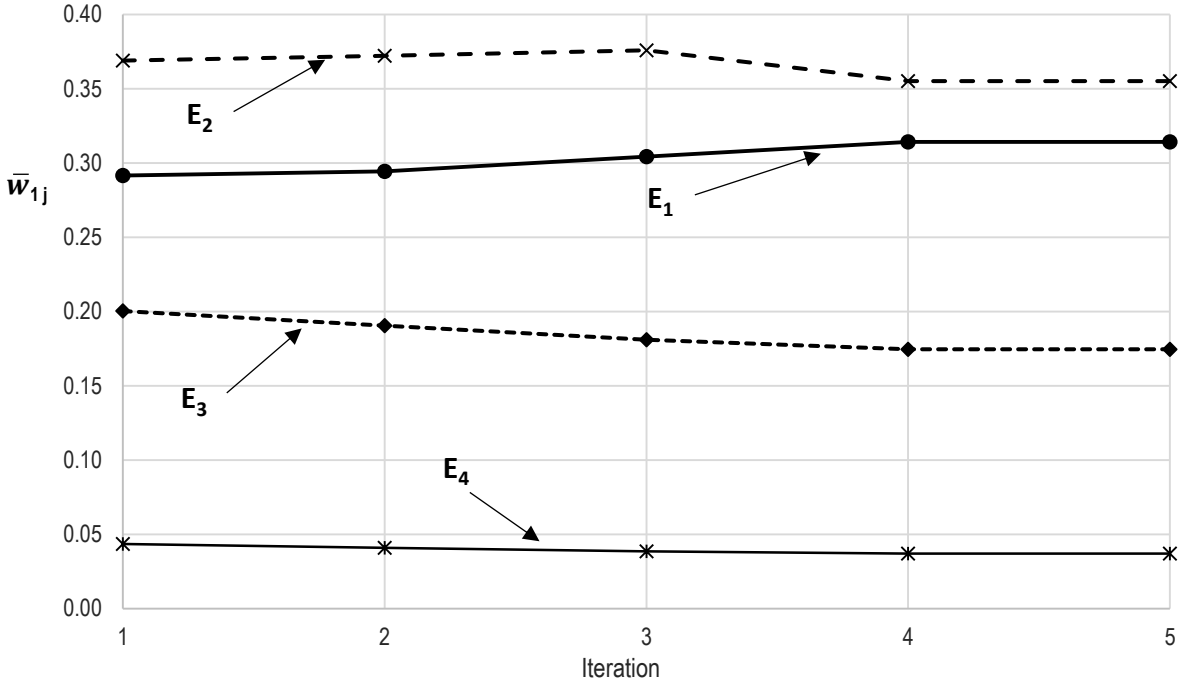

b)

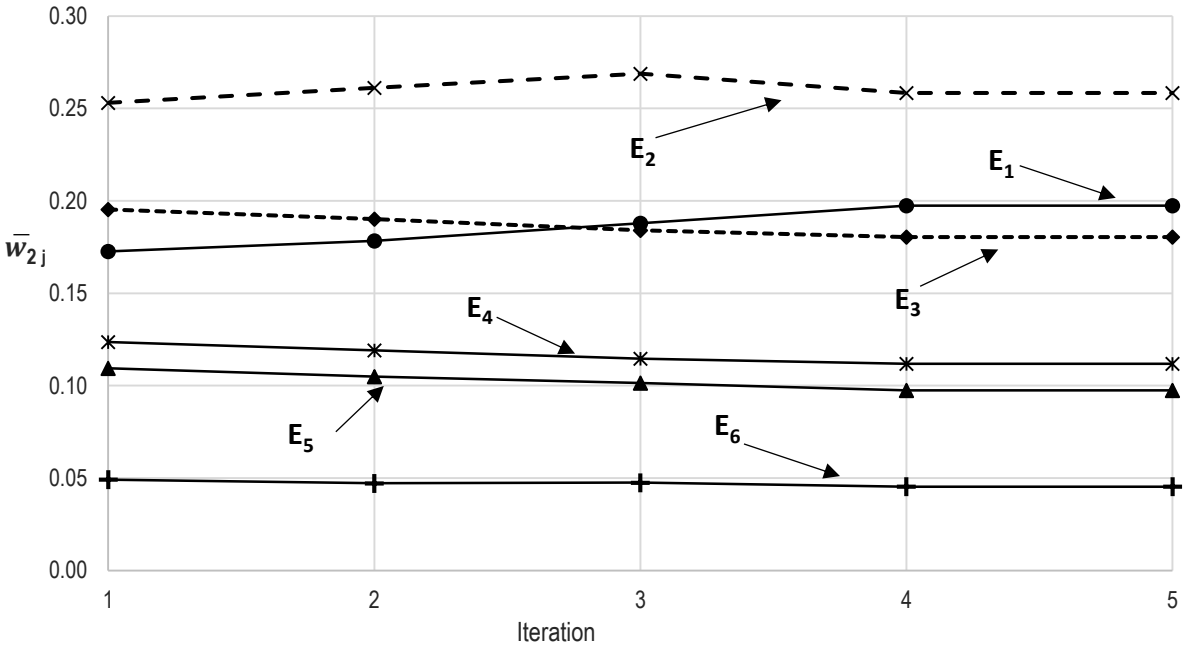

Figure 3.18 Convergence of sensitivity vectors for state variables: a) q_1 and b) q_2.

It can be noticed that the searched model parameters achieved convergence, and the difference between the numerical and experimental values are very slight. An excellent agreement was achieved already after the first four iterations. It also proved that the presented procedure allows obtaining an accurate solution quickly.

Table 3.7 presents the results of the identification procedure.

MOST WIEDZY Downloaded from mostwiedzy.pl

Table 3.7 Results of the identification procedure – Stage 2.

FIN1			
Displacement in control point	q_1 [m]	q_2 [m]	q_3 [m]
Experiment	0,0167	0,0469	0,0674
FEM	0,0167	0,0473	0,0670
Difference	0%	0,9%	-0,7%
Sum of least squares	$4.1 * 10^{-7}$		
FIN2			
Displacement in control point	q_1[m]	q_2 [m]	q_3 [m]
Experiment	0.0123	0.0342	0.0486
FEM	0.0123	0.0348	0.0484
Difference	-0.25%	1.29%	-0.58%
Sum of least squares	$2.741 * 10^{-7}$		
FIN3			
Displacement in control point	q_1 [m]	q_2 [m]	q_3 [m]
Experiment	0.0140	0.0397	0.0557
FEM	0.0140	0.0401	0.0555
Difference	0.0%	1.11%	-0.04%
Sum of least squares	$2.549 * 10^{-7}$		
FIN4			
Displacement in control point	q_1 [m]	q_2 [m]	-
Experiment	0.0149	0.0410	-
FEM	0.0149	0.0410	-
Difference	-0.03%	0.02%	-
Sum of least squares	$7.4 * 10^{-11}$		

The values of measured and computed displacement for fitted values of Young Modulus for each section together with percentage difference were included. The highest discrepancy was equal to 1.29%, which is less than 1 mm in the absolute numbers.

Ultimately, for each fin the Young Modulus for every section was obtained. The results of identification are presented in Table 4. The final plate thickness was equal to 1.5 mm, 2 mm, 1.8 mm, and 1.5 mm for all sections for FIN1, FIN2, FIN3 and FIN4, respectively. In the Table 3.8 are presented values of each section membrane stiffness *Et.*

Table 3.8. Membrane shell stiffness *Et* [N/m] for various sections.

	Et_1	**Et_2**	**Et_3**	**Et_4**	**Et_5**	**Et_6**	**Et_7**	**Et_8**
FIN1	$3.59 \cdot 10^6$	$5.01 \cdot 10^6$	$5.24 \cdot 10^6$	$5.26 \cdot 10^6$	$3.94 \cdot 10^6$	$2.71 \cdot 10^6$	$2.07 \cdot 10^6$	$1.92 \cdot 10^6$
FIN2	$5.98 \cdot 10^6$	$6.33 \cdot 10^6$	$6.72 \cdot 10^6$	$6.72 \cdot 10^6$	$5.88 \cdot 10^6$	$4.87 \cdot 10^6$	$3.42 \cdot 10^6$	$2.56 \cdot 10^6$
FIN3	$5.14 \cdot 10^6$	$5.59 \cdot 10^6$	$5.65 \cdot 10^6$	$5.65 \cdot 10^6$	$4.78 \cdot 10^6$	$4.10 \cdot 10^6$	$4.10 \cdot 10^6$	$3.96 \cdot 10^6$
FIN4	$4.54 \cdot 10^6$	$4.97 \cdot 10^6$	$6.32 \cdot 10^6$	$6.45 \cdot 10^6$	$5.01 \cdot 10^6$	$3.91 \cdot 10^6$	$2.7 \cdot 10^6$	$2.25 \cdot 10^6$

3.4.3. Free vibrations test as a validation of the Finite Element Method Model

The results obtained from the modal FEA analysis were Eigenmodes and corresponding eigenfrequencies. The results of the analysis were compared to the experimental findings presented in Table 3.2 for the frequencies in the air. The first four modes were compared. Table 3.9 presents the results of the calculations with isotropic material compared to the experimental results, with the percentage difference between the calculation and experiment.

MOST WIEDZY Downloaded from mostwiedzy.pl

Table 3.9. Estimation of prism layers distribution.

	Eigenmode 1	**Eigenmode 2**	**Eigenmode 3**	**Eigenmode 4**
EXPERIMENT	**23.99 Hz**	**94.45 Hz**	**222.9 Hz**	**305.8 Hz**
FEM ISOTROPIC	23.87 Hz	99.42 Hz	237.4 Hz	321.4 Hz
DIFFERENCE	0.63%	4.71%	6.11%	4.64%

According to Table 3.9, excellent accuracy was achieved for the first mode; and sufficient for the following three modes. It proves the usefulness of the presented approach. However, a qualitative comparison also had to be done to ensure that the numerical calculations predicted the same types of modes. The results of the FEM computations are presented in Fig. 3.19. The undeformed fin was also plotted with the grey colour for a more straightforward interpretation.

1st bending mode – 23.87 Hz

2nd bending mode – 99.42 Hz

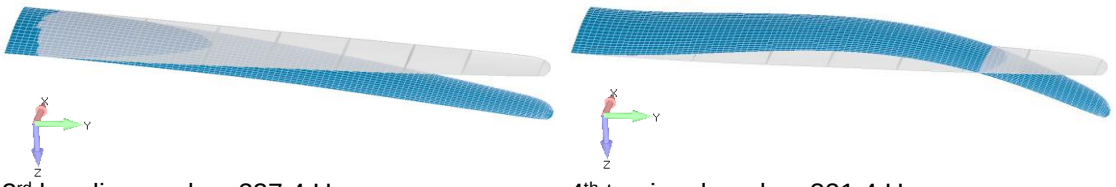

3rd bending mode – 237.4 Hz

4th torsional mode – 321.4 Hz

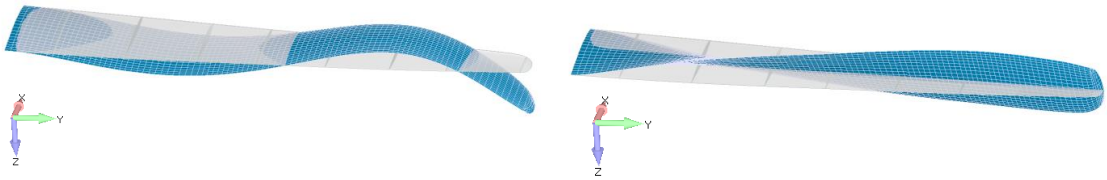

Figure 3.19 First four Eigenmodes of the RS:X fin.

According to Figure 3.19 the first three modes are bending modes, and the fourth one is the torsional mode. This is in line with the experimental findings, in which the first three modes were dominated by acceleration due to bending. The fourth frequency was dominated by the motions about the longitudinal axis corresponding to torsion motion. It means that proposed numerical model can be considered valid and represents well the properties of the real object.

3.5. Fluid-Structure Interaction

3.5.1. Validation study

In the benchmark paper by Zarruk et al. (2014) the results of the forces generated by the hydrofoil and static displacement were presented in the non-dimensional form. The tip displacement q was normalised by the Young Modulus E, base section second moment of inertia I, hydrodynamic force normal to the chord line F_N and hydrofoil span s according to formula:

$$q' = \frac{qEI}{s^3 F_N} \tag{3.2}$$

MOST WIEDZY Downloaded from mostwiedzy.pl

Hydrodynamic forces were presented in the form of lift and drag coefficient, which have already been defined. The results of the calculations were normalised in the same way, and the comparison of the numerical and experimental fluid dynamic (EFD) vales for both cases are presented in Table 3.10. The Case 1 corresponds to angle of attack AoA = 6 degrees and Re = $1 \cdot 10^6$, while Case 2 to Re = $0.6 \cdot 10^6$ and AoA= 8 degrees.

Table 3.10. Validation of FSI calculations – comparison with EFD.

	Case 1			**Case 2**		
	C_L	C_D	$\frac{qEI}{s^3 F_N}$	C_L	C_D	$\frac{qEI}{s^3 F_N}$
Exp. acc. to Zarruk et al. (2014)	0.521	0.025	0.221	0.651	0.036	0.225
FSI Calculations	0.546	0.028	0.222	0.681	0.037	0.191
Difference in %	4.8%	+12%	1.6 %	4.6%	3.1%	-15.1%

It can be noticed that in terms of lift forces the discrepancy between numerical and experimental results is rather small. The differences between drag forces are moderately high for the Case 1 and in particularly good agreement with experiments for Case 2. Some differences could be also noticed for stand-alone CFD calculations indicating that the source of discrepancies might be the fluid solver as such, not the co-simulation engine. For the Case 1, the displacement is in excellent agreement. In terms of the absolute values, the tip displacement obtained experimentally was equal to $q_{\mathrm{Exp.}}$ = 12.5 mm, and numerically q_{FSI} = 12.7 mm. Therefore, the difference between experiment and calculations is equal to 0.2 mm. For the Case 2, the difference in terms of absolute values is similar, however, due to small values of the displacement (q_{FSI} = 3.7 mm) any relative differences are much greater. Moreover, it was indicated that for small displacements, the experimental measurement uncertainty is much greater.

In the Figure 3.20 it is presented the displacement field which in every time step is obtained from FEM Abaqus calculations. On the right, there is the front view at the hydrofoil together with the undeformed shape contour for the comparison. It can be noticed that for this case the displacement is rather insignificant compared to the span of the hydrofoil. It can be noticed that the colour contour is not parallel to the chord line indicating small twisting angle, which results from asymmetry of the hydrofoil due to longitudinal axis. Nevertheless, the twist angle was not compared. They were not reported in the experimental findings due to its small values. The deformation of the hydrofoil in Figure 3.20 is presented in actual scale.

MOST WIEDZY Downloaded from mostwiedzy.pl

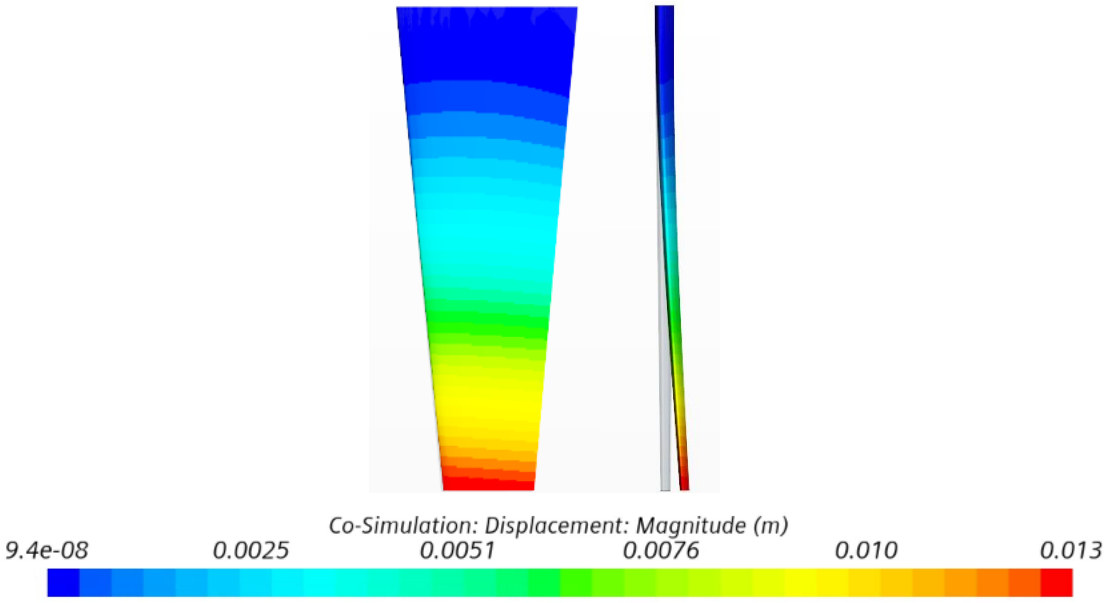

Figure 3.20 Validation study results - displacement of the hydrofoil.

Figure 3.21 presents the FSI traction vectors in directions X and Y, which in the picture are described as 0 and 1, respectively.

The typical pressure distribution on the hydrofoil can be clearly noticed. The red colour corresponds to the high pressure, whereas the blue to low pressure zone.

MOST WIEDZY Downloaded from mostwiedzy.pl

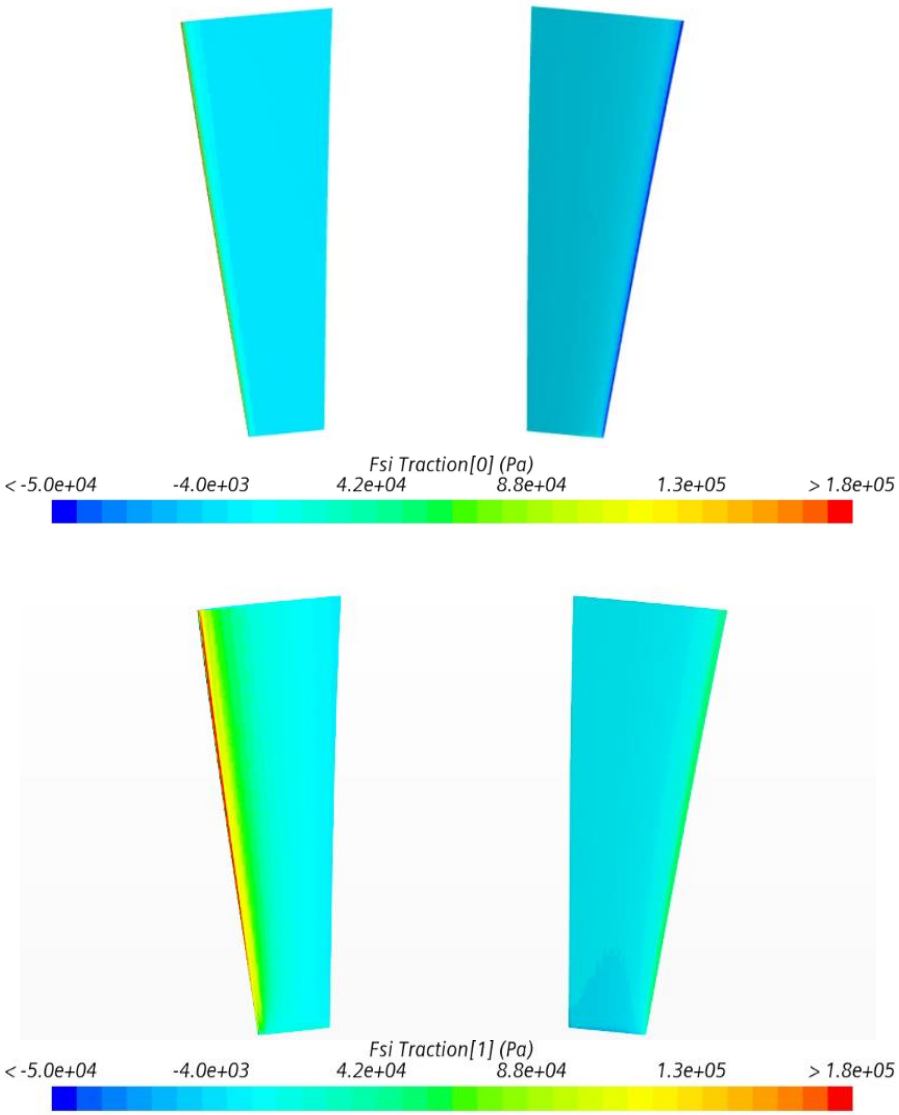

Figure 3.21 Pressure field used for mapping the loads onto the solid structure.

The results presented indicates that the solvers are capable of effective and correct exchange of data, and it can be used for the further FSI calculations of the fins.

3.5.2. Verification study of the RS:X model for FSI calculations

This chapter presents the results of the time step and mesh resolution verification study. The verification study was performed for the angle of attack equal 4 degrees and velocity equal to 8 m/s. For mesh sensitivity study thee meshes were checked, and Figure 3.22 presents the relation between the number of elements and drag force, while the Figure 3.23 presents the relation between lift force and number of fluid mesh elements. The time dependence study was performed for the coarsest mesh, and the mesh dependence study for the largest time step.

MOST WIEDZY Downloaded from mostwiedzy.pl

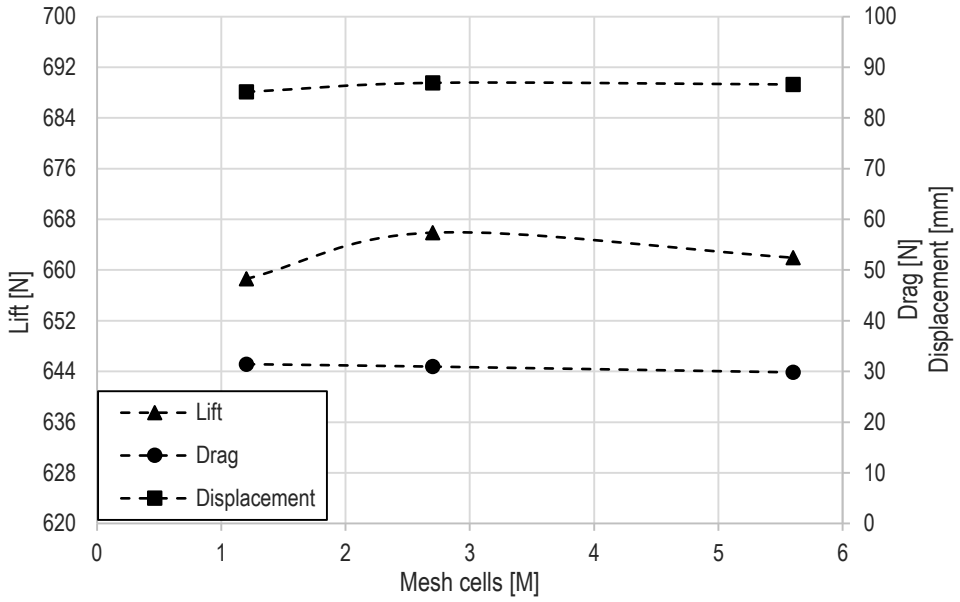

Figure 3.22 Mesh sensitivity study.

According to Figure 3.22 for the lift force, the oscillatory convergence can be noticed. The coarsest mesh underestimate lift by 0.5% compared to the finest mesh, while the medium density mesh overestimates lift by 0.6%. According to ITTC (2008) the simulation uncertainty U_i for the oscillatory convergence can be defined as follows:

$$U_i = \frac{1}{2}(S_U - S_L) \tag{3.1}$$

Where S_U is the maximum value of the solution, and S_L is the solution minimum. In this case, the mesh uncertainty of the lift force is equal to 3.68 N which is 0.5% of the value of the lift force for the finest mesh. The prediction of the lift force is of the great importance, because fin deformation depends on it, and the numerical uncertainty due to mesh size in this case is little.

For the displacement, the difference between the coarsest and the finest grid is equal to 1.5 mm, and 0.3 mm between the medium mesh and fine mesh. Since it depends on the lift force it is also characterised by oscillatory convergence. The difference between coarse and fine mesh corresponds to the 1.7% of the tip displacement obtained for the fine mesh, and between medium and fine 0.3%. Therefore, for the medium mesh obtained displacement can be considered rather mesh independent.

According to Figure 3.22 for the drag force, the difference between meshes is the highest. Drag is 3.9 % overestimated by the medium mesh, and 5.5% by the coarsest mesh, compared to the finest mesh. Formally, the solution for drag force is diverging because the difference between coarse and medium mesh is smaller than between medium and fine mesh. Therefore, the uncertainty cannot be evaluated based on the presented results. If the calculations would be done for one finer mesh the convergence behaviour may change. However, it would result in the mesh that is not practical for the FSI simulations of RS:X fin in the range of angles of attack below stall.

Lift and displacement are characterised by little uncertainty and good agreement for the medium mesh. Therefore, the larger differences between obtained drag forces were accepted.

MOST WIEDZY Downloaded from mostwiedzy.pl

It was decided that the medium mesh is the good compromise between the accuracy of the solution and the computation time. Especially, that numerous cases will be analysed, and numerical efficiency is an important factor to consider.

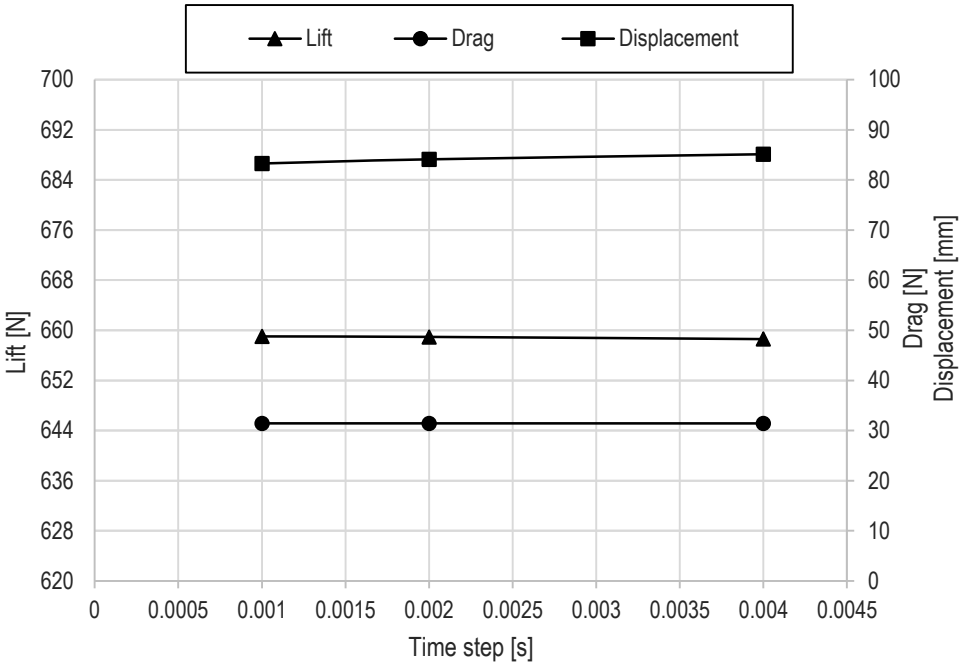

Figure 3.23 Time step sensitivity study.

According to Figure 3.23 the forces are rather time step independent, whereas the displacement is more sensitive to the time step. Lift forces are converging with decreasing time step; however, the differences are less than 0.1%. Therefore, the greatest time step was selected. Choosing smallest time step would greatly increase the computation time and the benefit from the higher accuracy is small. Taking into account the influence of mesh size and time step, it was decided to perform the calculations with the medium mesh and greatest time-step. In such a case small loss of accuracy is expected.

3.5.3. Results of Fluid-Structure Interaction calculations for RS:X fin – forces and deformations

This chapter presents the results of FSI calculation in terms of obtained deformation and forces generated by the fin for various angles of attack and velocities. Figure 3.24 presents the results for all fins and velocity V = 4 m/s.

MOST WIEDZY Downloaded from mostwiedzy.pl

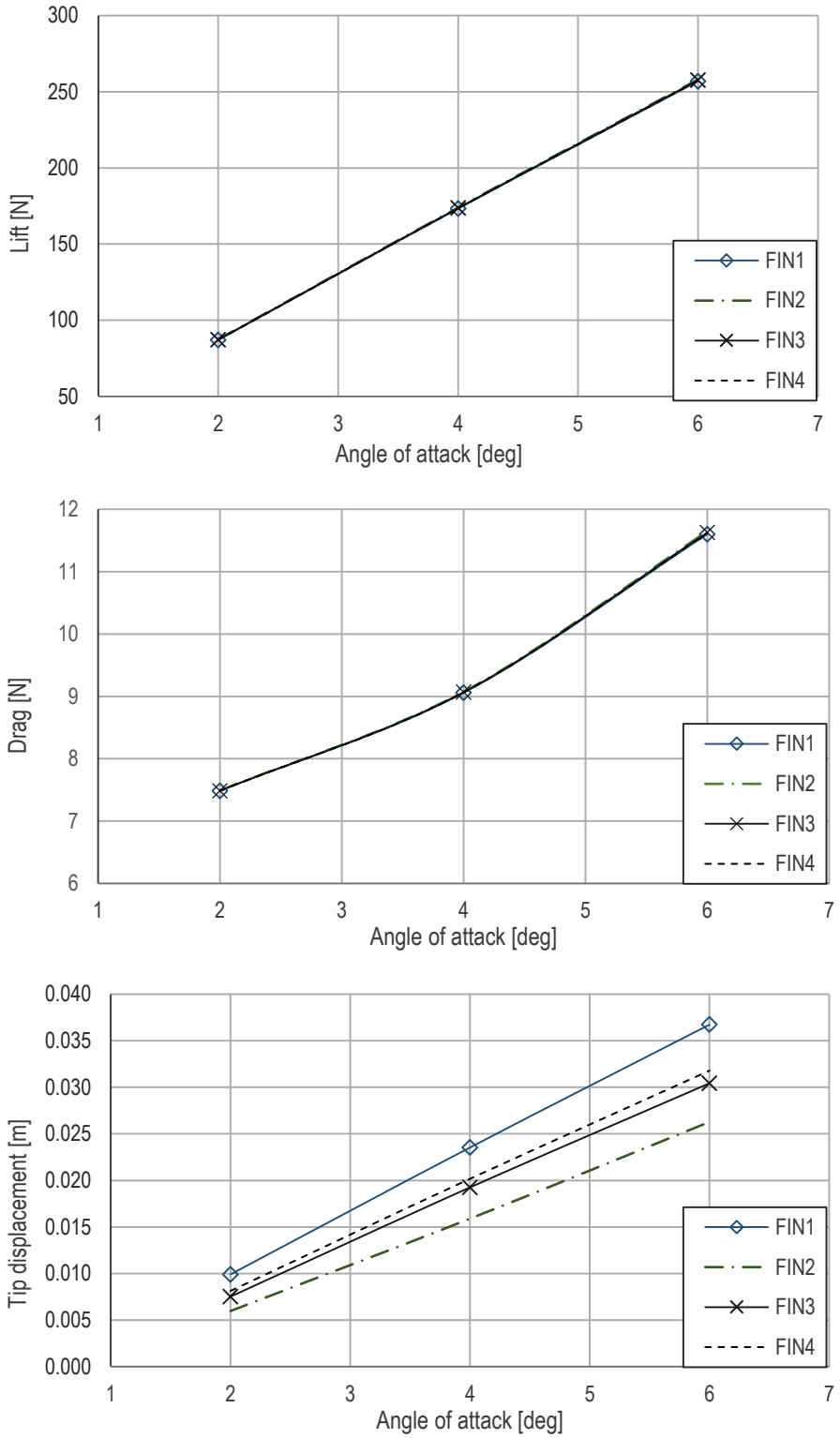

Figure 3.24 Results for velocity v=4m/s, lift force (top), drag force (middle), tip displacement (bottom).

Figure 3.25 presents the comparison of forces and displacement for all fins and velocity V = 6 m/s.

MOST WIEDZY Downloaded from mostwiedzy.pl

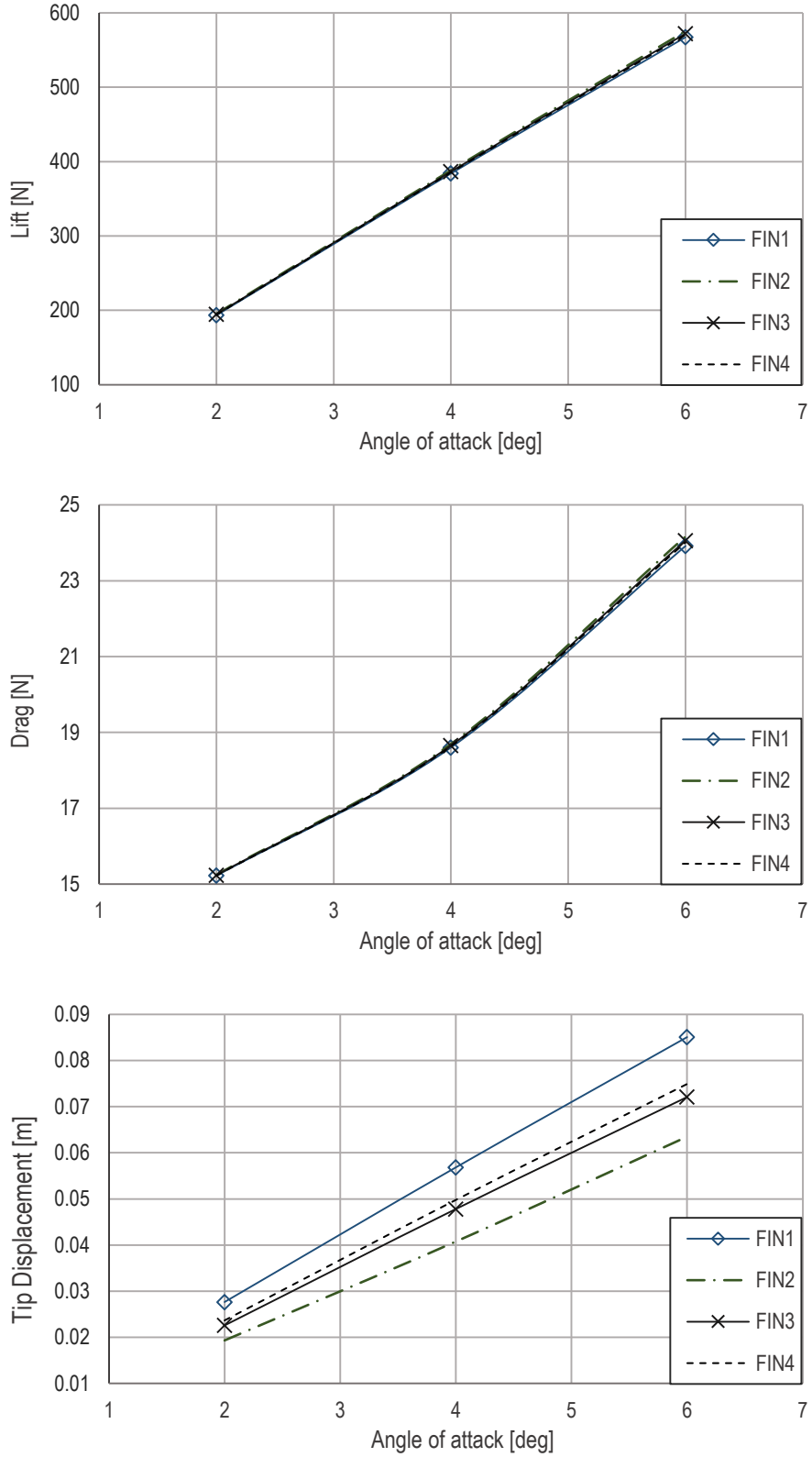

Figure 3.25 Results for velocity v=6m/s, lift force (top), drag force (middle), tip displacement (bottom).

Figure 3.26 presents the comparison of forces and displacement for all fins and velocity V = 8 m/s.

MOST WIEDZY Downloaded from mostwiedzy.pl

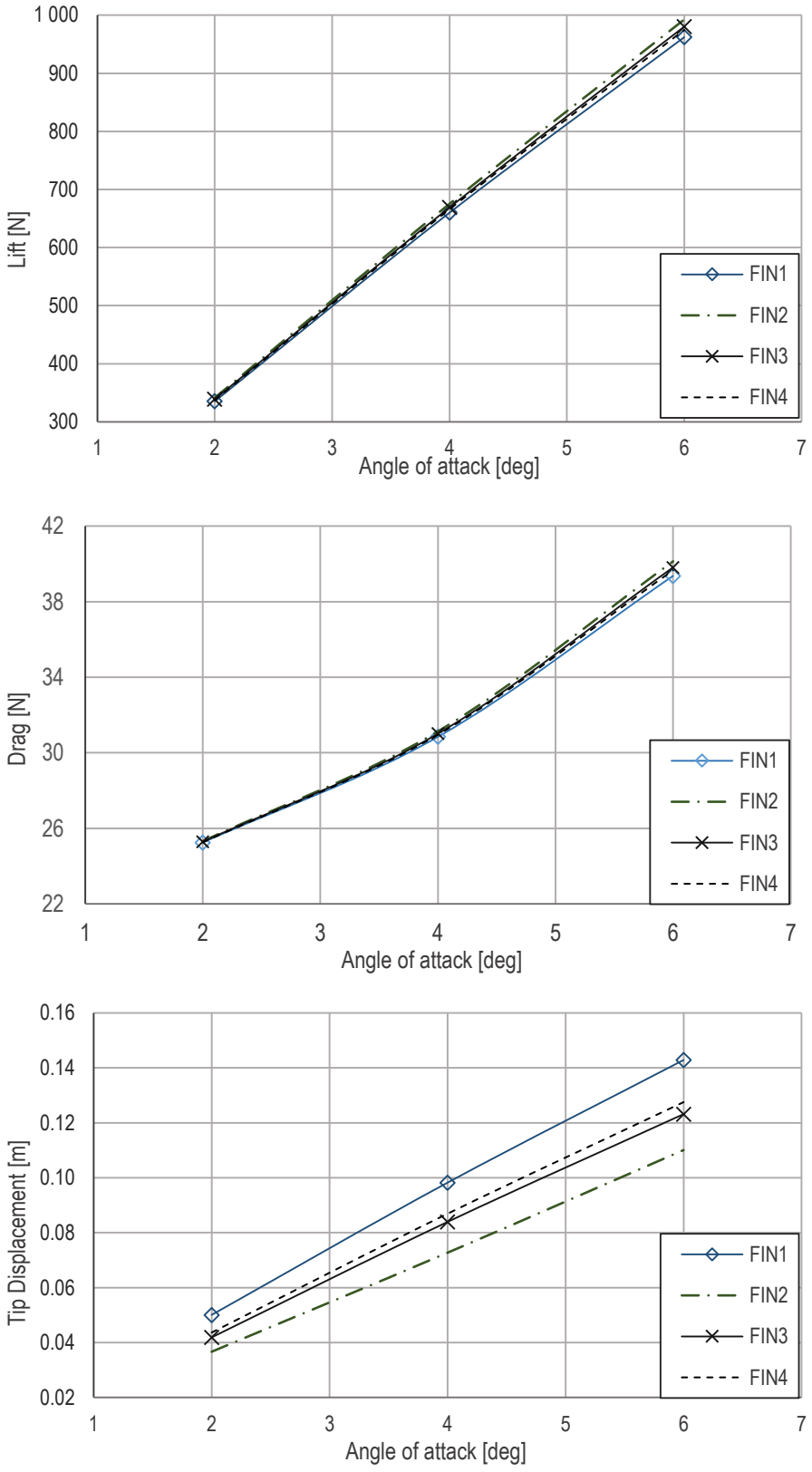

Figure 3.26 Results for velocity v=8 m/s, lift force (top), drag force (middle), tip displacement (bottom).

Figure 3.27 presents the comparison of forces and tip displacement for all fins and velocity V = 10 m/s. Additionally, the results for the undeformed fin are presented for comparison.

MOST WIEDZY Downloaded from mostwiedzy.pl

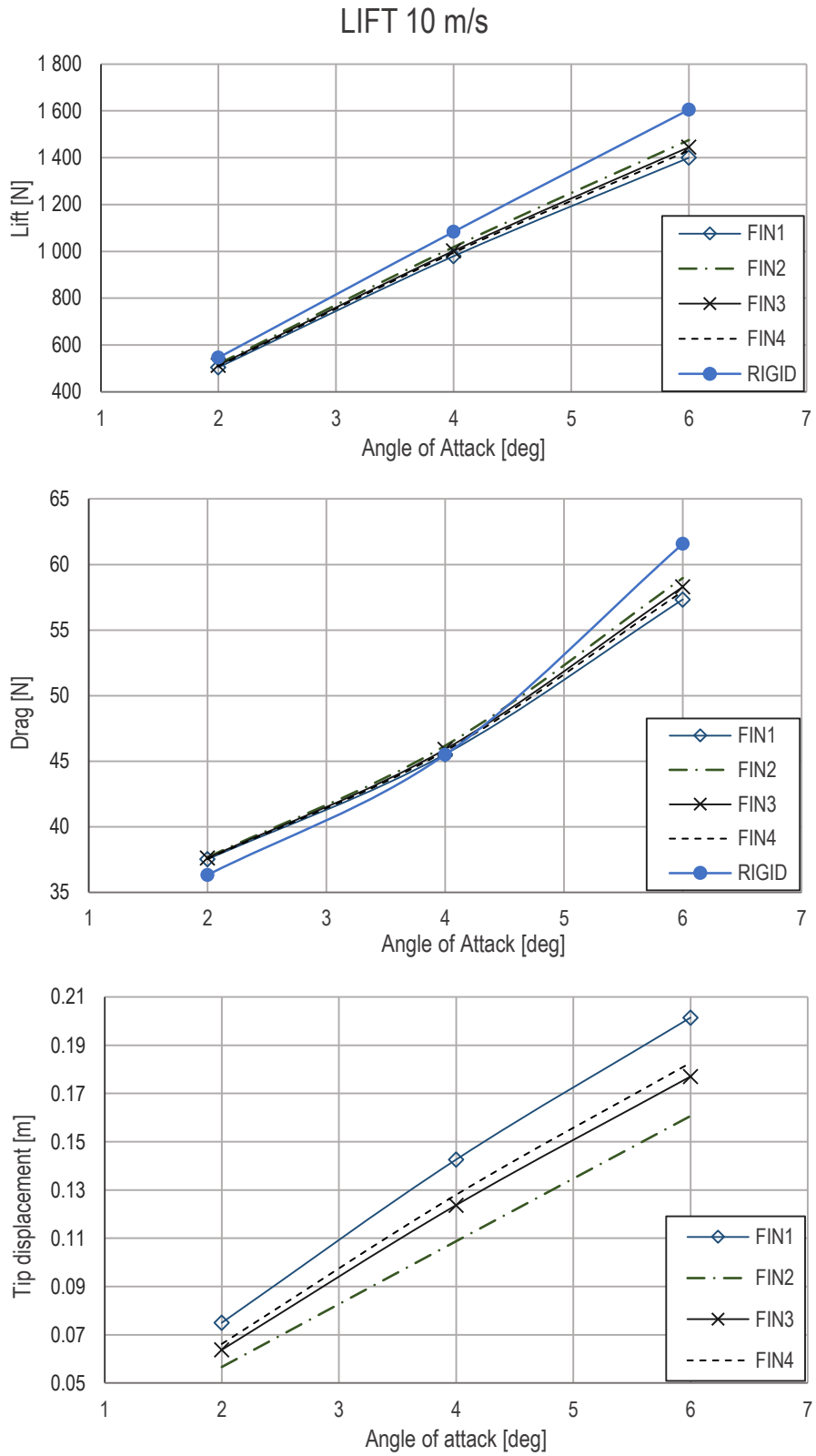

Figure 3.27 Results for velocity v=10 m/s, lift force (top), drag force (middle), tip displacement (bottom).

It can be noticed that the lift force of the undeform hydrofoil is significantly larger than if the effect of fin flexibility is considered.

For higher values of the angle of attack it causes also the reduction of the drag forces, presumably, due to reduced induced drag.

MOST WIEDZY Downloaded from mostwiedzy.pl

Figure 3.28 presents the relation between lift force and displacement. It can be noticed that for all fins, it follows almost linear trend, and the slope of the line defines the stiffness of the fin. In Figure 3.28 the colour of the sign indicates to which fin obtain value is corresponding, while the shape of the sign indicates the angle of attack (AoA).

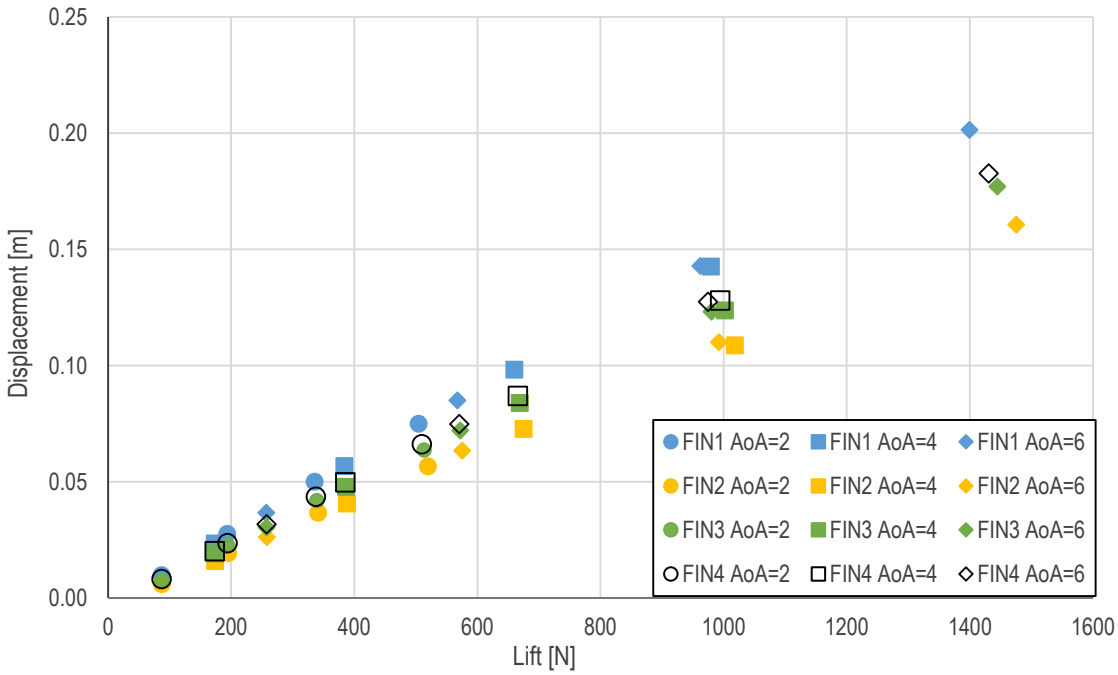

Figure 3.28 Relation between the lift force and tip displacement for the RS:X fin.

Figure 3.29 presents the relation between the tip displacement and the drag force. For constant angle of attack and varying speed the relation between displacement and drag has a non-linear trend.

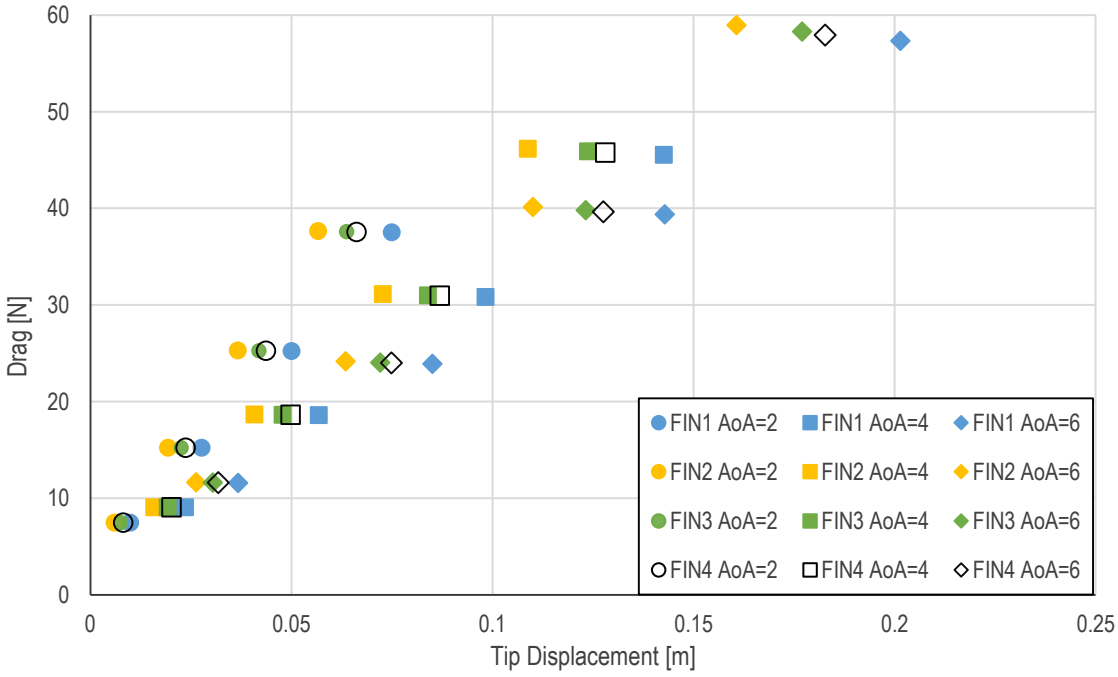

Figure 3.29 Relation between the tip displacement and the drag force for the RS:X fin.

MOST WIEDZY Downloaded from mostwiedzy.pl

Figure 3.30 presents the displacement magnitude scalar field for *V* = 8 m/s and *AoA* = 4 degrees, while Figure 3.31 for V = 10 m/s and *AoA* = 6 degrees. Both of these images show the deformation of the RS:X fins at the actual scale. The dominant is the displacement in Y-direction corresponding to bending. Maximum tip displacement for lower fluid velocity corresponds to 98.2 mm for FIN1, whereas the minimum tip displacement occurred for the FIN 2 and was equal to 72.7 mm.

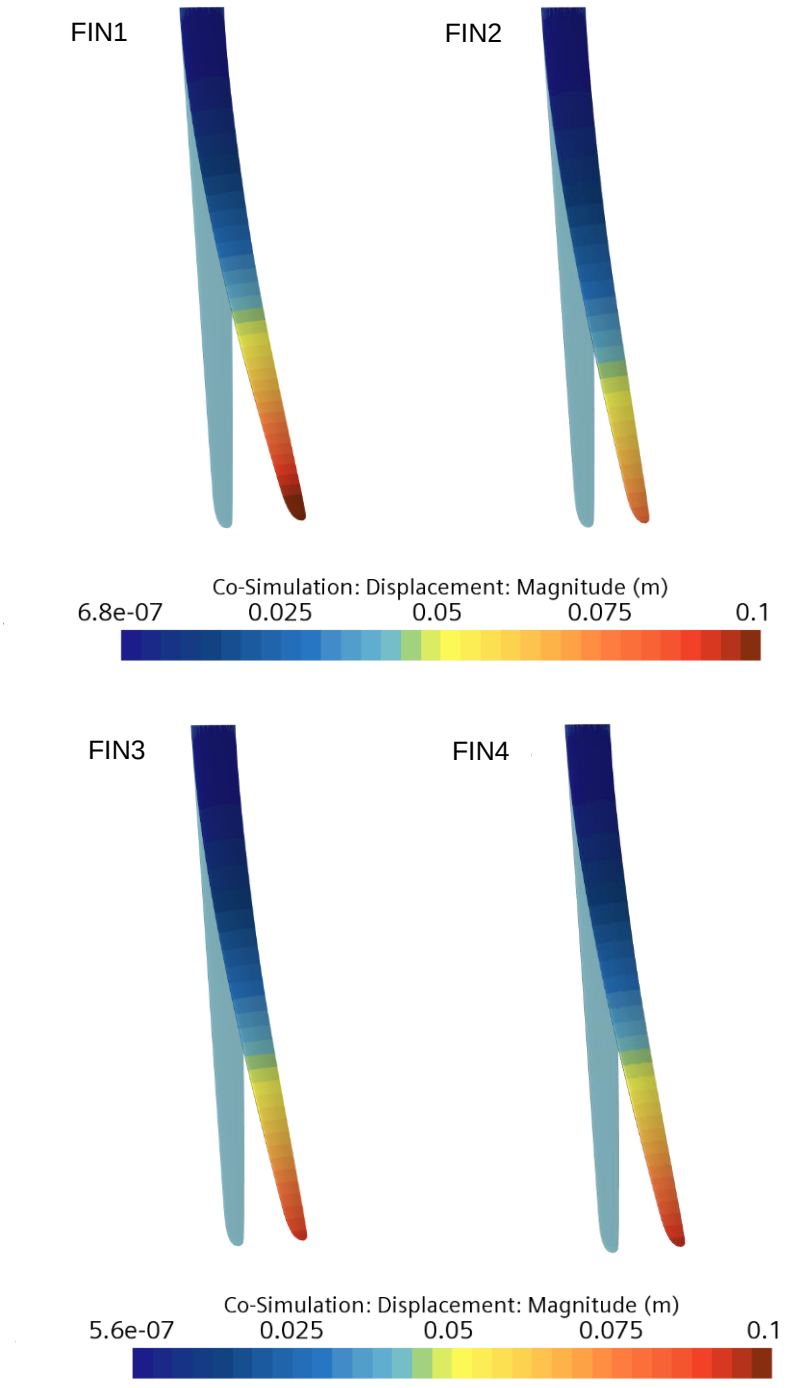

Figure 3.30 Displacement field function for V = 8 m/s and AoA = 4 degrees.

MOST WIEDZY Downloaded from mostwiedzy.pl

For the highest fluid velocity, the differences between tip displacements are significant and they vary between 160.6 mm for FIN2 and 201.4 mm for FIN1.

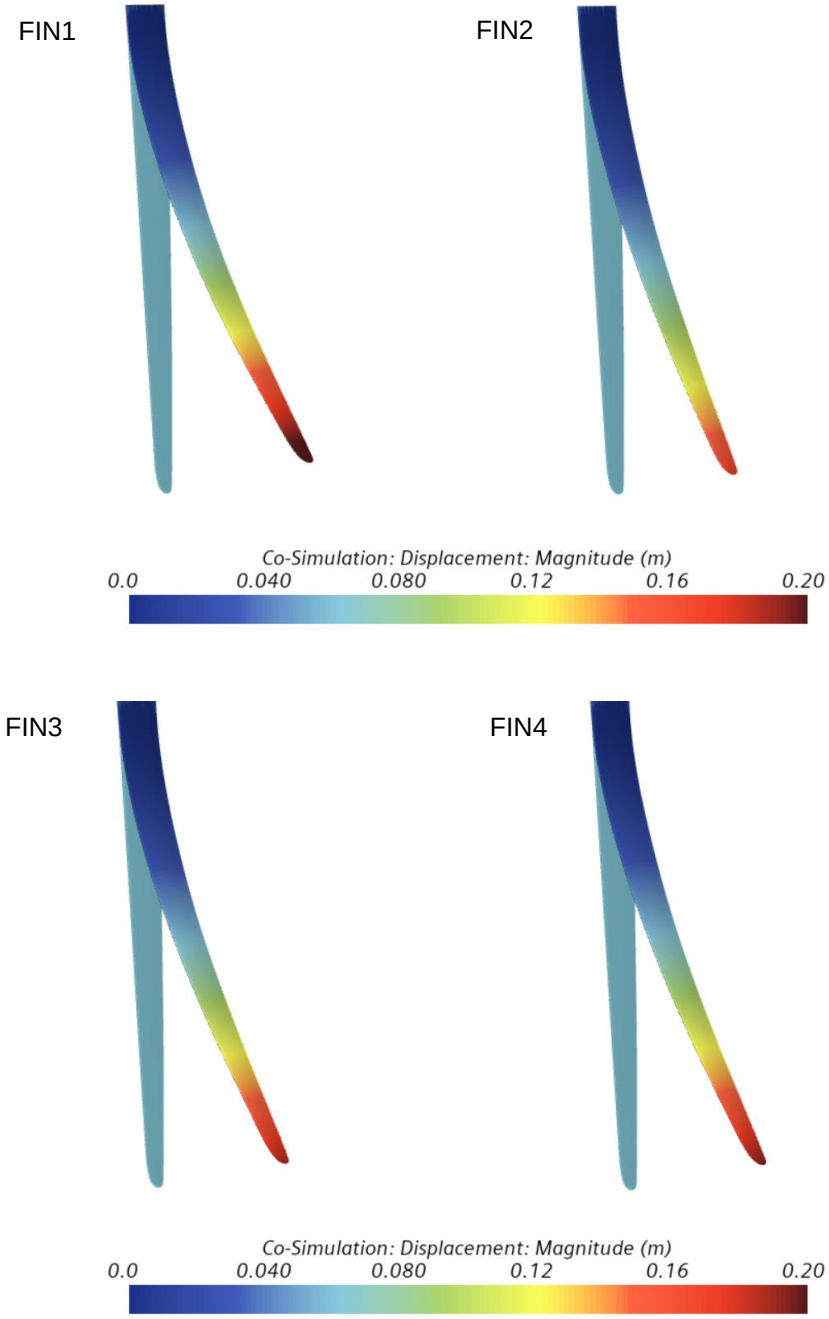

Figure 3.31 Displacement field function for V = 10 m/s and AoA = 6 degrees.

The differences between the forces generated by the fins of various stiffness distribution are not significant. Thus, only very minor alterations in the pressure field for each fin can be observed. It is the explanation of little force differences. A bit better insight into differences in the pressure values offer the plots of the pressure field on selected cross-section cuts. The cross-sections were done at the distance of 0.2 m, 0.4 m, and 0.6 m away from the fin head and the plots in Figure 3.32 present the pressure coefficient for those sections, respectively. On the X-axis is non-dimensional chord length, Y/c = 0 corresponds to trailing edge, while Y/c = 1

MOST WIEDZY Downloaded from mostwiedzy.pl

corresponds to the leading edge. Values of pressure coefficient below 0 indicates the pressure lower than in the free stream (suction side of the hydrofoil), and values of pressure coefficient above 0 indicates the high pressure zone (pressure side of the hydrofoil)

a)

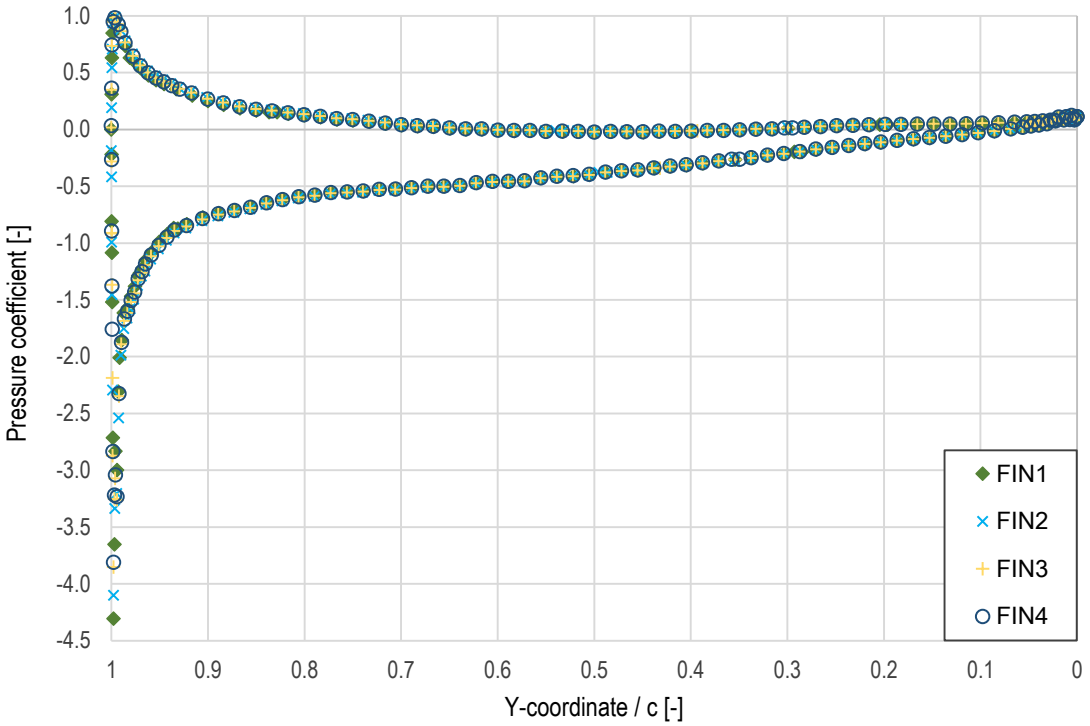

b)

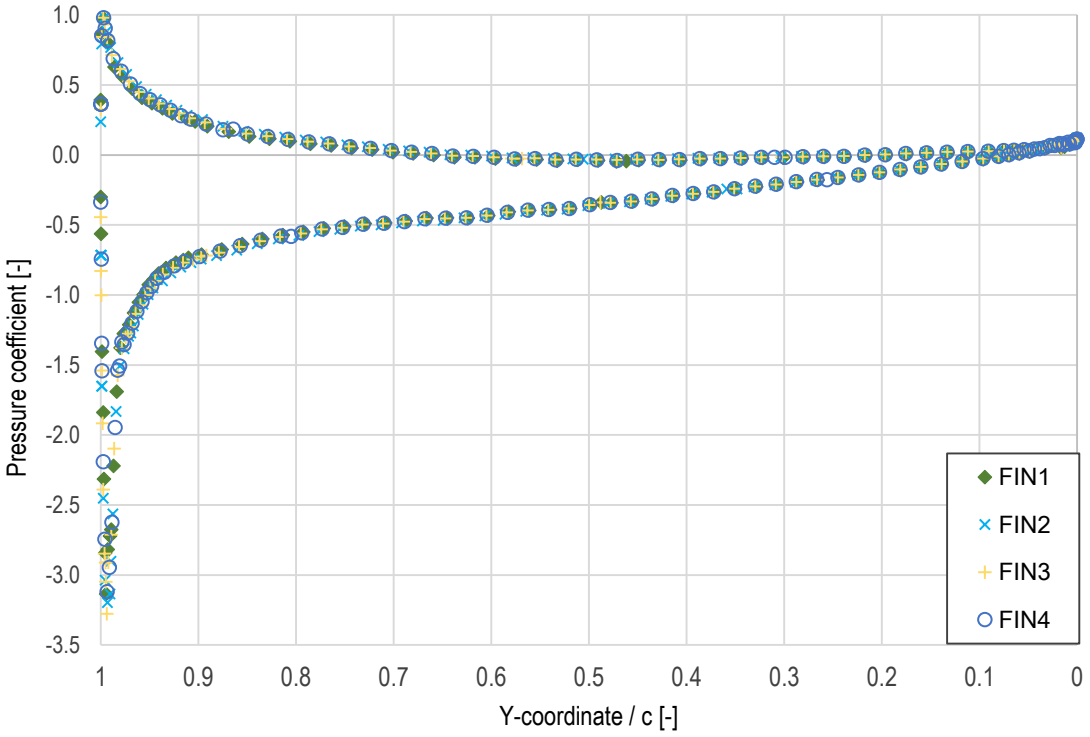

MOST WIEDZY Downloaded from mostwiedzy.pl

c)

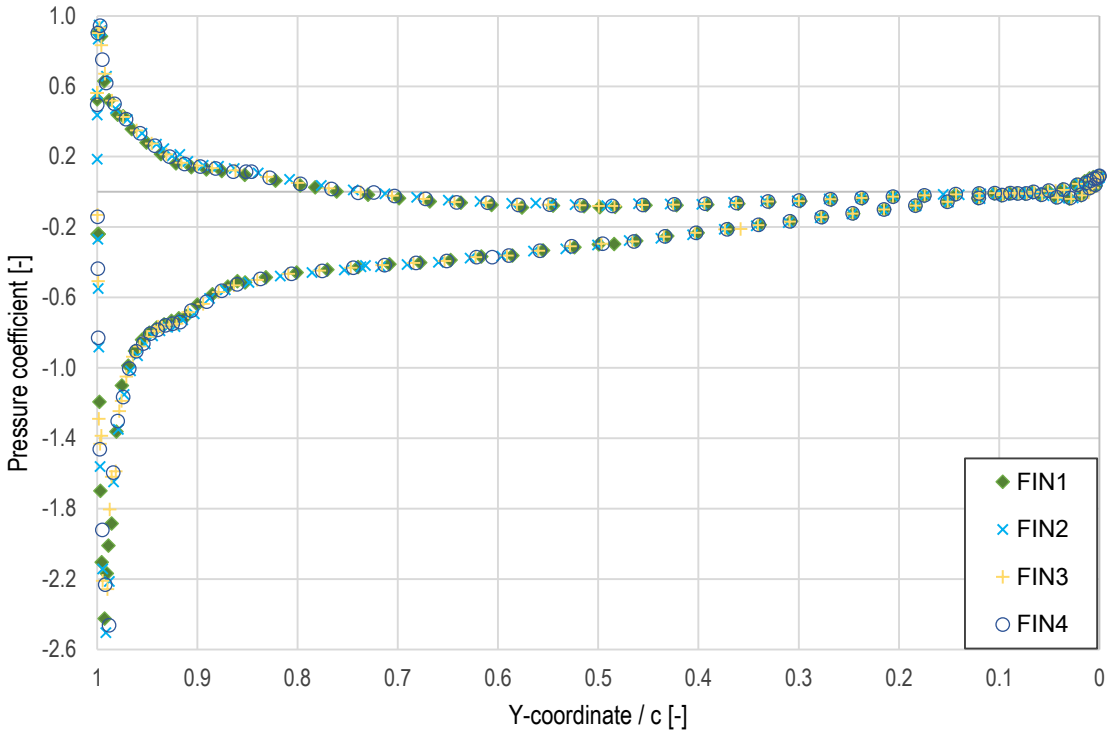

Figure 3.32 Pressure coefficient plot along the chord of the RS:X windsurfing fin for sections along fin span: a) X = 0.2 m, b) X = 0.4 m, c) X = 0.6 m.

It can be noticed in Figure 3.32b) and 3.32c), that for the FIN2 the values of the pressure coefficient are only slightly different than for the remaining fins. It explains why marginally higher lift force was reported for FIN2. At the same time those variations, which are difficult to notice, justifies why the differences in lift forces between analysed fins are minor.

Forces generated by the fins were normalised and Tables 3.11 – 3.14 present the values of the lift and drag coefficients for all analysed fins, across the entire range of speeds and angles of attack.

Table 3.11. Forces coefficients - FIN1.

	***AoA* = 2 deg**		***AoA* = 4 deg**		***AoA* = 6 deg**	
	C_L	C_D	C_L	C_D	C_L	C_D
V = 4 m/s	0.179	0.0154	0.357	0.0187	0.529	0.0239
V = 6 m/s	0.177	0.0139	0.352	0.0170	0.519	0.0219
V = 8 m/s	0.173	0.0130	0.340	0.0159	0.495	0.0203
V = 10 m/s	0.166	0.0124	0.323	0.0150	0.461	0.0189

MOST WIEDZY Downloaded from mostwiedzy.pl

Table 3.12. Forces coefficients - FIN2.

	***AoA* = 2 deg**		***AoA* = 4 deg**		***AoA* = 6 deg**	
	C_L	C_D	C_L	C_D	C_L	C_D
V = 4 m/s	0.180	0.0154	0.358	0.0187	0.532	0.0240
V = 6 m/s	0.179	0.0140	0.355	0.0171	0.527	0.0221
V = 8 m/s	0.176	0.0130	0.348	0.0160	0.511	0.0207
V = 10 m/s	0.171	0.0124	0.336	0.0152	0.486	0.0194

Table 3.13. Forces coefficients - FIN3.

	***AoA* = 2 deg**		***AoA* = 4 deg**		***AoA* = 6 deg**	
	C_L	C_D	C_L	C_D	C_L	C_D
V = 4 m/s	0.180	0.0154	0.358	0.0187	0.531	0.0240
V = 6 m/s	0.178	0.0139	0.354	0.0171	0.524	0.0220
V = 8 m/s	0.175	0.0130	0.345	0.0160	0.505	0.0205
V = 10 m/s	0.169	0.0124	0.330	0.0151	0.476	0.0192

Table 3.14. Forces coefficients - FIN4.

	***AoA* = 2 deg**		***AoA* = 4 deg**		***AoA* = 6 deg**	
	C_L	C_D	C_L	C_D	C_L	C_D
V = 4 m/s	0.179	0.0154	0.357	0.0187	0.530	0.0239
V = 6 m/s	0.178	0.0139	0.353	0.0171	0.522	0.0220
V = 8 m/s	0.174	0.0130	0.343	0.0159	0.502	0.0204
V = 10 m/s	0.168	0.0124	0.328	0.0151	0.472	0.0191

Figure 3.33 presents the comparison of the values of the lift coefficient for all four fins for the entire combination of analysed angles of attack and velocity of the water. Each surface represents another fin. It can be noticed that the differences for small velocities and small angles of attack are minor. The greatest discrepancy between the hydrofoils occurs for the speed of 10 m/s and angle of incidence equal to 6 degrees. The decrease of the lift coefficient proportionally to the increase of the fluid loads can be observed. The highest drag coefficient has FIN2, whereas the lowest one has FIN1.

MOST WIEDZY Downloaded from mostwiedzy.pl

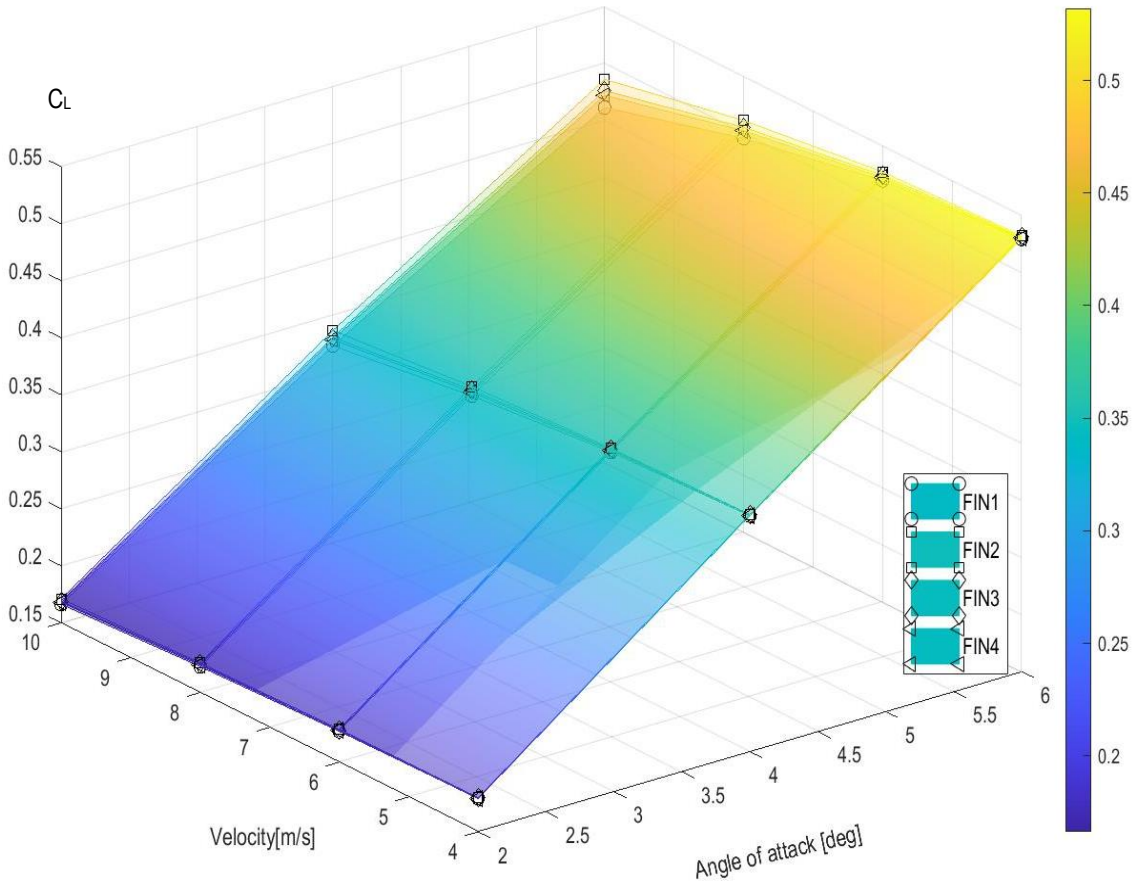

Figure 3.33 Comparison of the lift coefficient for all fins.

Figure 3.34 presents similar comparison for the drag coefficient. The differences between fins become even less pronounced. What is interesting, though, is the clear trend of significant decrease of the drag coefficient with the increase of the fluid loads.

MOST WIEDZY Downloaded from mostwiedzy.pl

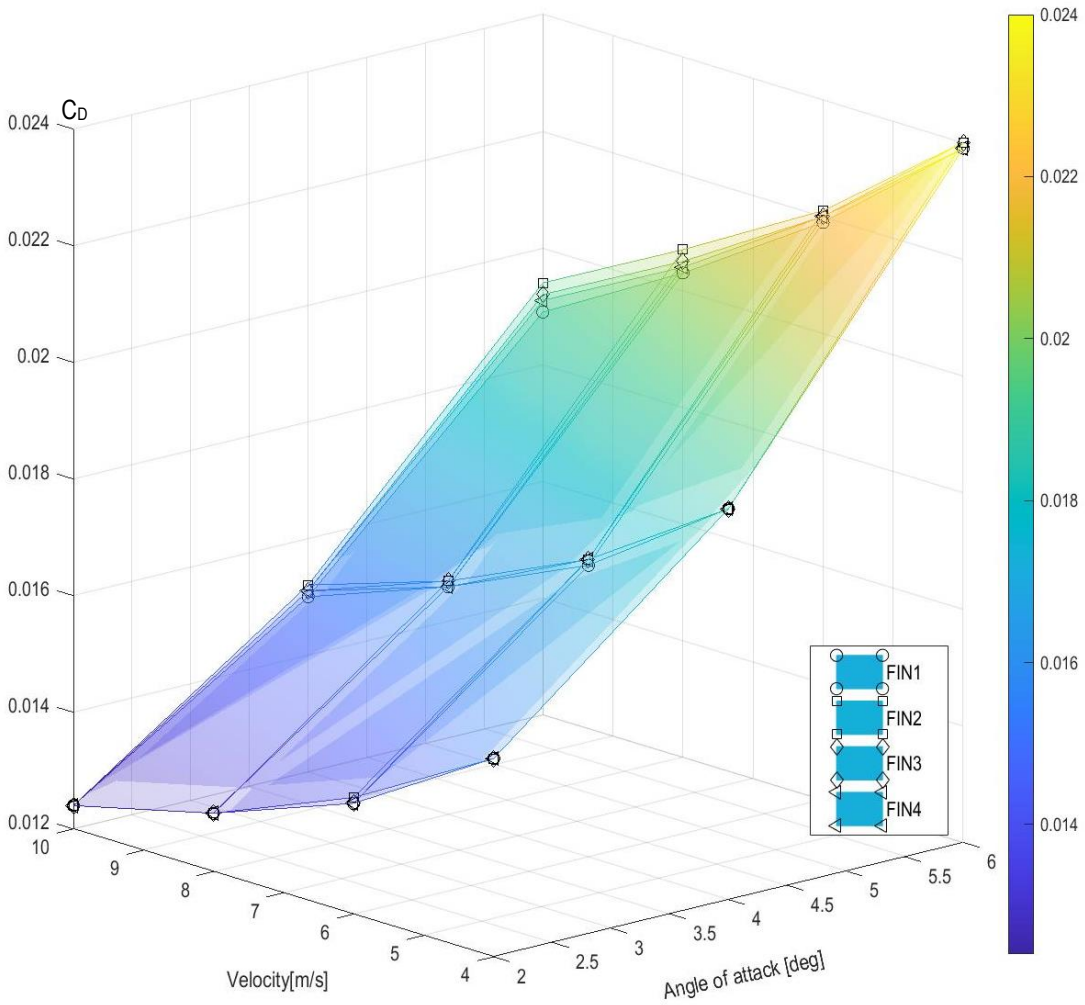

Figure 3.34 Comparison of the drag coefficient for all fins.

It is believed that the main reason for this, is the decrease of the lift coefficient and related loss of the induced drag. Therefore, the highest drag coefficient has the FIN2, and the lowest has FIN1.

Figure 3.35 presents the relation between the fluid velocity, angle of attack and tip displacement for all analysed fins.

MOST WIEDZY Downloaded from mostwiedzy.pl

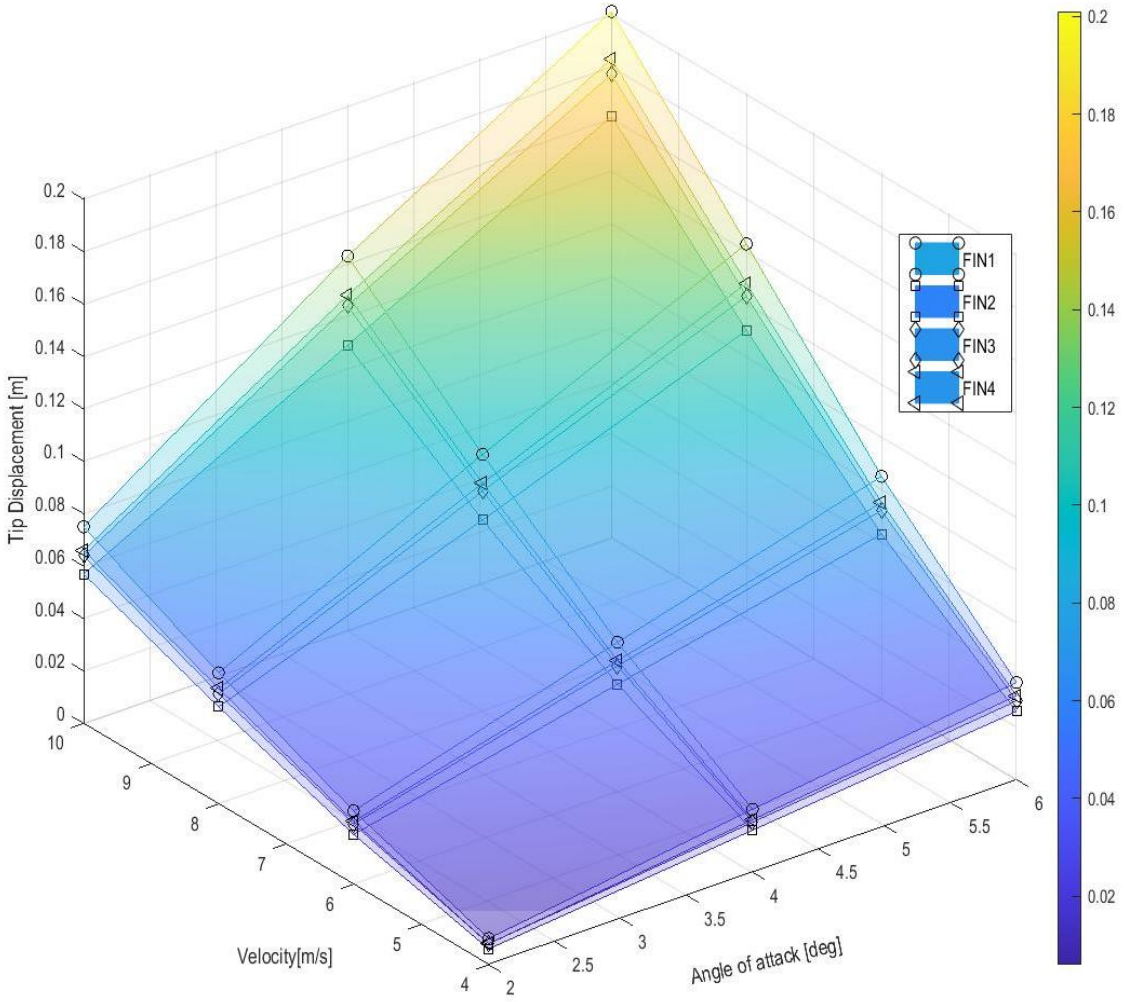

Figure 3.35 Comparison of tip displacement for all fins.

It can be clearly noticed that visible differences in the tip deflection occur even for the minimum analysed speed and smallest angle of attack. However, it was expected, since the experimental results presented in Chapter 3.2.1 reveal that for the load as small as 130 N the differences between tip displacement may reach 20 mm. Therefore, the presented difference of the tip displacement reaching up to 40 mm should not come as a surprise. It can be clearly seen that the stiffest is the FIN2 and the most susceptible to bending is FIN1. Finally, it can be noticed that the significant differences in tip deflection have limited effect on the values of the generated forces.

MOST WIEDZY Downloaded from mostwiedzy.pl

4. DISCUSSION

4.1. Static displacement and free vibrations experiments – discussion of results

According to the results presented in Chapter 3.2.1, the tip deflections of the selected fins are significantly different from each other, even for the load as small as 130 N. Table 4.1 presents the percentage difference between the displacements for all fins in control points. Values of displacement of FIN1 were taken as the reference. Presented results clearly show significant differences between the fins.

Table 4.1. Results of the FSI calculations for RS:X fin - comparison of the displacements.

Control point	FIN1	FIN2		FIN3		FIN4	
	q [m]	q [m]	% diff	q [m]	% diff	q [m]	% diff
P1	0.0167	0.0123	-26.3%	0.0140	-16.2%	0.0149	-10.8%
P2	0.0469	0.0342	-27.1%	0.0397	-15.4%	0.0410	-12.5%
P3	0.0674	0.0486	-27.8%	0.0557	-17.4%	-	-

According to Gourlay and Martellotta (2011), the lifting force generated on the fin during sailing can reach up to 1000 N of distributed hydrodynamic pressure. Nevertheless, the hydrodynamic pressure centre is in actual use closer to the board, resulting in a smaller lever than in the experimental case. Nevertheless, the deformations in water can be much larger than those observed in experiments. Therefore, the variations in fin bending displacements are more significant than those observed in the experimental study.

The experimental method for determining fin displacement under a given load is rather simple and straightforward. The resolution of the rangefinder was 0.1 mm and, based on the repeated measurements, the accuracy of the measurement was 0.4 mm. Considering that the differences between the measured tip displacements of the fins are much greater, the accuracy of the measurements is sufficient. It allows to clearly differentiate various measured fins and indicate variation in susceptibility to bending. Moreover, the measurements of the fin displacement in multiple points allows to obtain unambiguous stiffness distribution along the span of the fin.

The measurements of the free vibrations provided validation data to confirm the process of the stiffness identification based on the measurements of the static displacement. Based on the repeated seven measurements of the free vibrations excited with various initial loads it was found that each time the same eigenfrequency was obtained for the first mode. For the second mode the standard deviation based on the seven measurements was equal to 0.23 Hz, and for the third mode it was equal to 4.28 Hz. Therefore, the measurement results are repeatable and accurate. Thus, they can be used for validation of the calculations.

Slightly more problematic was the assessment of the damping coefficient. The damping coefficient was evaluated as a single number based on the value of the logarithmic decrement for certain number of periods of oscillations. However, the damping coefficient is not constant across the entire process of oscillations decay. It decreases, as the amplitude of motions is smaller in

MOST WIEDZY Downloaded from mostwiedzy.pl

the further phase of the experiment. Therefore, its values are different depending on the number of periods of oscillations taken for the determination of the damping coefficient value. Thus, it should be treated as an approximate value. Especially, because, as it is discussed later in this chapter, its value has limited influence on the accuracy of the results.

4.2. Computational Fluid Dynamics - discussion of results

The stand-alone numerical CFD simulations were performed for the same fin of the RS:X windsurfing class. For the RS:X fin the calculations were done for the angle of attack between 2 degrees and 10 degrees and the speed of 10 m/s. Three meshes and four turbulence modelling approaches were compared. The CFD calculations of the RS:X windsurfing fin were also compared to the results of the calculations that were based on the lifting line theory and were done for the similar trapezoidal hydrofoil.

Additionally, the validation study was performed. The calculations were carried out for hydrofoil with modified NACA 0009 profile, and the results of computations were compared with experimental findings (Zarruk et al. 2014).

It was noticed that the influence of the mesh resolution on the results was greater than the influence of the turbulence modelling approach. The primary CFD study focussed on the stall angle prediction and accuracy of the hydrodynamic forces predictions. The calculations have revealed that a high y^+ value makes it impossible to predict stall accurately, however, for low angles of attack, all the turbulence approaches predict similar values of lift and drag. Also, within the linear region of the lift curve, the mesh resolution did not play a significant role. For detached flow $k-\varepsilon$ fails to predict drag and lift accurately since the value of the stall angle is greatly overestimated. Results obtained for RST and $k-\omega$ SST turbulence model were similar. However, the validation study showed better accuracy for the latter one. The $k-\omega$ SST turbulence model was characterized by the highest sensitivity on the mesh resolution. According to the results of the validation study, the DES was characterized by excellent accuracy in predicting the lift and good accuracy in drag prediction. The mesh sensitivity study proved little to gain from the further increase of y^+ value. The coarsest grid and $k-\varepsilon$ model do not allow to correctly capture the separation. For the same reason, despite its robustness, they are not applied as well for further FSI calculations in presented study. Based on the validation study and mesh sensitivity study, it was concluded that the accuracy of the RST approach seems to be too poor compared to the required computational resources. The $k-\omega$ SST model provided similar predictions; however, it required a significantly shorter computation time. According to the validation study, the $k-\omega$ SST underpredicted the stall angle, whereas the DES overpredicted it. In the mesh sensitivity study for corresponding meshes, the predictions of stall angle values were the same for both approaches. There is no gain in the accuracy compared to the M3 in the linear region, and the difference between the values of stall angle predictions is little. In the validation study, the DES was characterized by too steep drag curve.

The validation and verification study allowed for confirming the accuracy of the selected numerical CFD model. The comparison of the CFD-based results with the lifting line findings

MOST WIEDZY Downloaded from mostwiedzy.pl

within the linear region also confirmed the accuracy of the calculations. It can be noticed that for the medium density mesh in the linear region for the RS:X hydrofoil the turbulence model selection does not play a significant role, since the results were similar. The differences in drag coefficient were also within acceptable range. Therefore, from the strictly hydromechanical point of view the medium density mesh with DES approach or $k-\omega$ SST turbulence model should be used.

It was decided to perform the calculations for the range of angles of attack corresponding to the linear region. It allows to apply less conservative approach for the y^+ value. Since slight difference between the meshes is observed in linear region, then M3 would be the starting point for FSI calculations. Moreover, the $k-\omega$ SST turbulence was decided to be used. The possible reduction of the number of mesh elements for the FSI calculations was searched, because co-simulation significantly increases the time of one calculation case. For the coarse mesh DES would use in the end $k-\omega$ SST formulation anyway.

Although this approach is not the most accurate of all analysed, there is one point that needs to be underlined. The study focusses on the comparison of the hydroelastic properties of the windsurfing fins, and the same shape is assumed for all hydrofoils. Therefore, the detailed hydrodynamic analysis of the influence of possible shape variations on the hydrodynamic forces is not the primary interest of the study. Nevertheless, the CFD is well capable of indicating the differences between various shapes, even if the results are subject to a non-negligible systematic error. As long as the same mesh is used for all hydrofoils, and it allows to capture all main features of the flow, it can be assumed of sufficient accuracy.

4.3. Finite Element Method - discussion of results

The simplified optimisation tool build-in to FEMAP gave already quite accurate results within very short time and little effort. Therefore, it can be used as a first approximation, or when a very accurate determination of the stiffness distribution is not of the primary interest. The iterative procedure requires to evaluate each time the sensitivity vectors. If the convergence is slow, the entire procedure becomes quite time-consuming. For the analysed fins, the required number of iterations necessary to obtain convergence varied from two to five, so analysis time vary significantly. However, based on the comparison of the data presented in Chapter 3.2.1 and Chapter 3.2.3, it is evident that presented procedure of stiffness distribution identification improved the match to the experimental data and provided more precise results. The presented process of an identification using a displacement as a state variable allowed to achieve a very good agreement of the model response with the natural object behaviour.

Free vibrations tests were performed to obtain additional data for benchmark and validation of presented approach. What influences most the modes and eigenfrequencies of the structure is its mass and stiffness. It was double checked that the similarity of mass for numerical model and tested fin is preserved. In this case, any differences between the numerical and experimental results would result from faultily identified stiffness distribution. The differences between first four eigenfrequencies obtained numerically and experimentally were equal to 0.63%, 4.71%, 6.11% and 4.64%, respectively. Especially for the first mode, the error is small.

MOST WIEDZY Downloaded from mostwiedzy.pl

These results can be considered as more than satisfactory. Moreover, the identified modes are the same for experiment and calculations. It demonstrates that the calculations are correct both from the qualitative and quantitative points of view.

Presented results show that if there is a need to identify the stiffness distribution of a larger population of fins, it is unnecessary to introduce additional state variables to the identification process. Nevertheless, the identification can be extended to additional state variables – the subsequent eigenfrequencies.

As a part of the research, for comparative purposes, the identification of the stiffness distribution was done based solely on the first four eigenfrequencies. The procedure for stiffness distribution identification was analogous to the one described in detail in Chapter 2.6.6. The state variable λ was the structure eigenfrequency obtained from the free vibration test. Four iterations were required to obtain very good agreement between numerical and experimental results. Figure 4.1 presents the convergence of the state parameters. The subscripts 1 – 4 indicates the following eigenfrequencies.

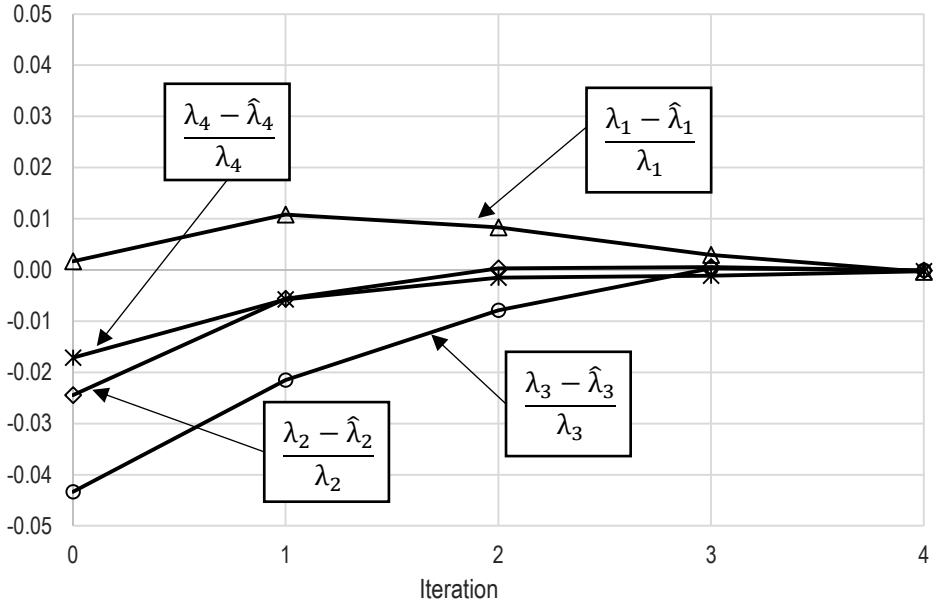

Figure 4.1 Convergence of the state parameters.

Figure 4.2 presents the changes of the Young Modulus values of all eight sections for every iteration of the identification procedure. The values of the Young Modulus values are quite different from the one obtained from the identification based on the static deformation. For such stiffness distribution the values of the static deformation determined by FEM are different from the one obtained from the experiments. The comparison is presented in Table 4.2.

Table 4.2. Stiffness identification based on various state parameters - Comparison of the displacement.

Identification type	**q_1 [m]**	**q_2 [m]**
Static displacement	0.0149	0.0410
Free vibration frequency	0.0135	0.0424

MOST WIEDZY Downloaded from mostwiedzy.pl

Obtained differences are large. Therefore, in this case determination of stiffness distribution based only on the structure eigenfrequencies is not the right approach. Especially if the determination of the structure deformation is the key interest.

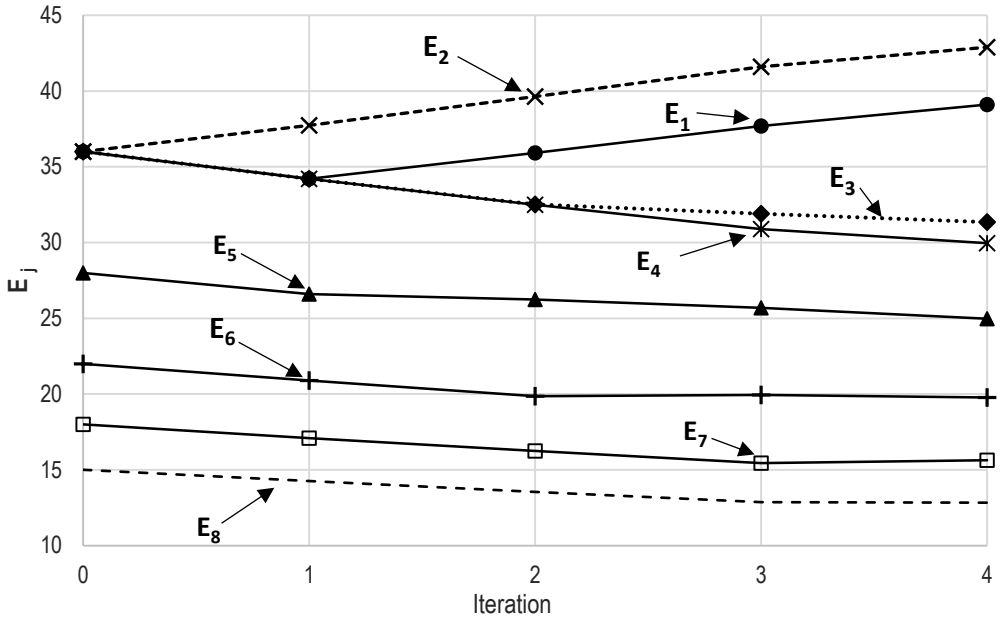

Figure 4.2 Convergence of the design variables.

During the identification based on the sensitivity analysis the sensitivity vectors are also determined. Figure 4.3 presents the values of the sensitivity vectors for the first eigenfrequency. It can be noticed that the main influence on the first eigenfrequency value has the first three sections.

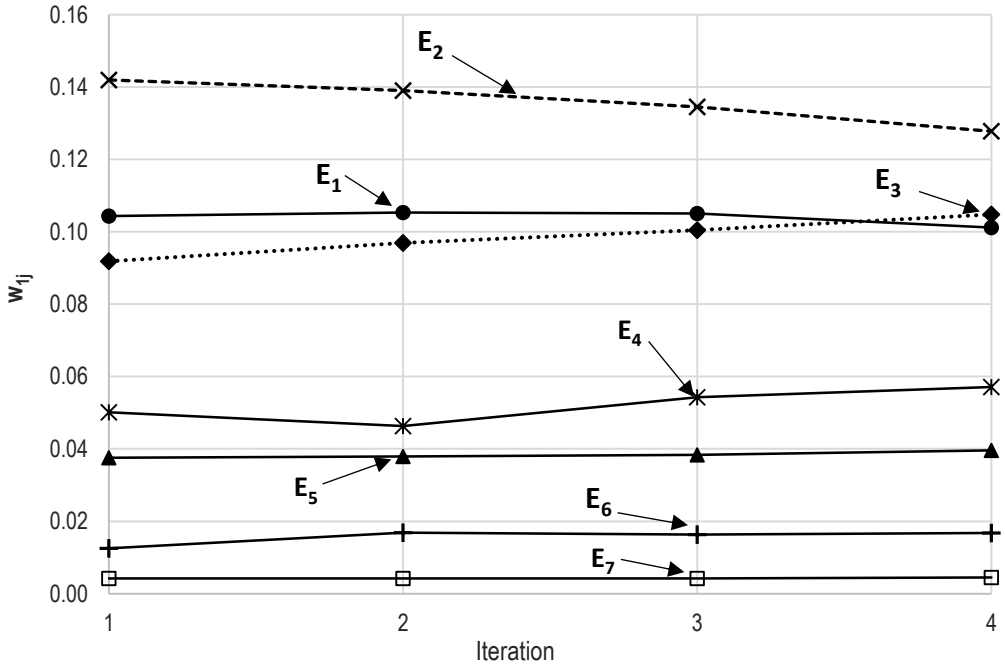

Figure 4.3 Convergence of the sensitivity vector for the first eigenfrequency.

MOST WIEDZY Downloaded from mostwiedzy.pl

Figure 4.4 presents the values of the sensitivity vectors for the second eigenfrequency. It can be noticed that the highest influence on the value of the second frequency value has the fifth and sixth section.

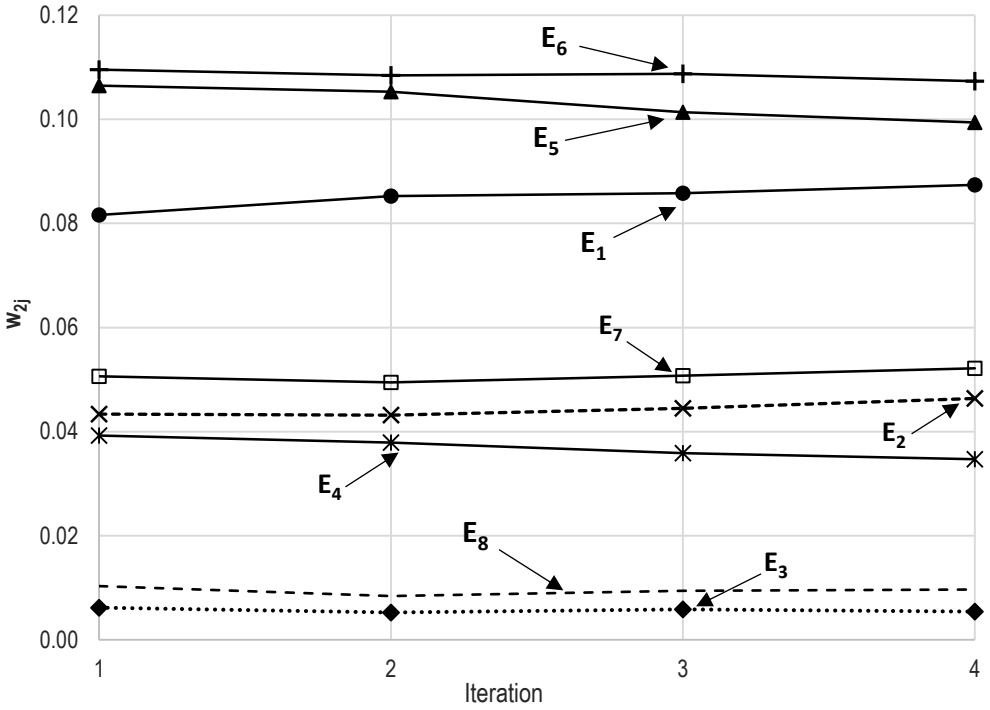

Figure 4.4 Convergence of the sensitivity vector for the second eigenfrequency.

Figure 4.5 presents the values of the sensitivity vectors for the third eigenfrequency. It can be noticed that the dominant influence has the stiffness of the seventh section.

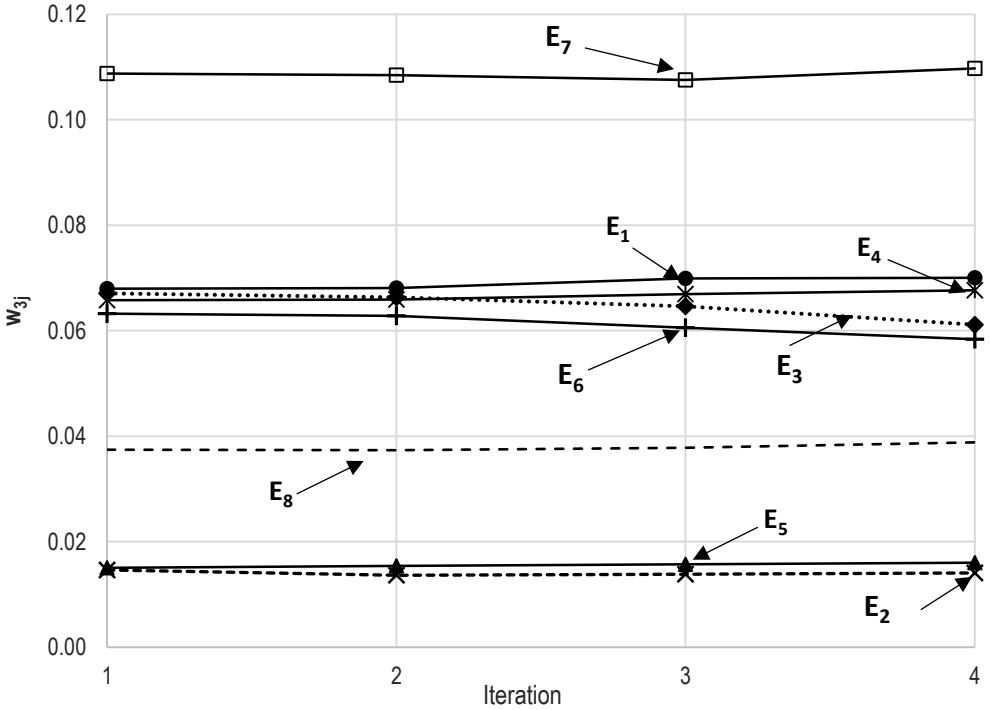

Figure 4.5 Convergence of the sensitivity vector for the third eigenfrequency.

MOST WIEDZY Downloaded from mostwiedzy.pl

Figure 4.6 presents the values of the sensitivity vectors for the fourth eigenfrequency. According to this picture the highest influence on the fourth mode frequency has the stiffness of the sections number two and three.

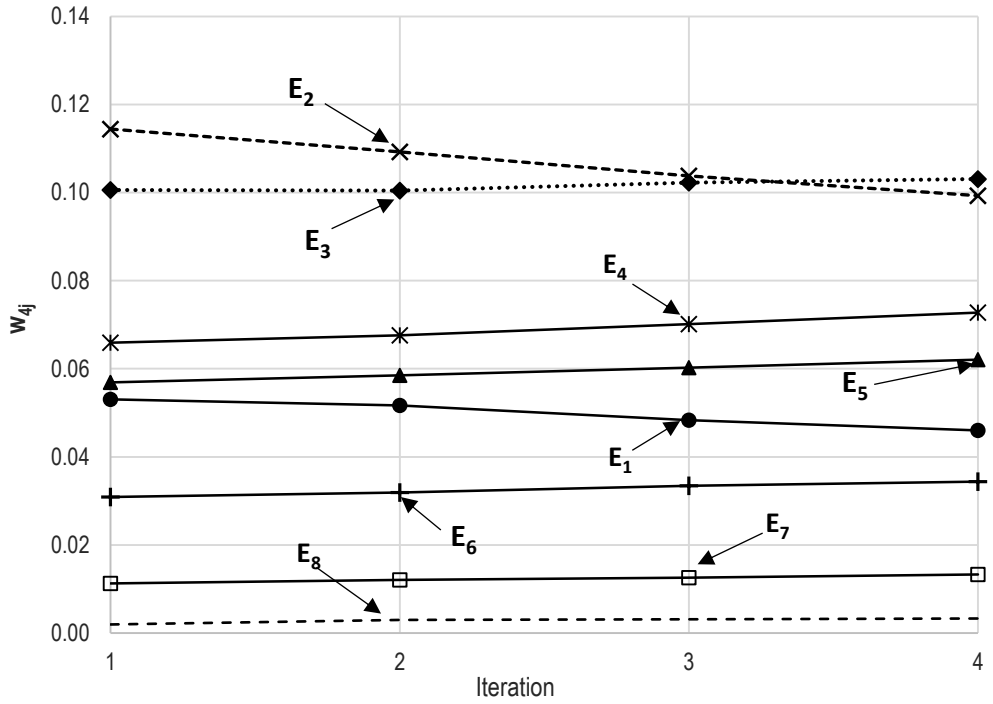

Figure.4.6 Convergence of the sensitivity vector for the fourth eigenfrequency.

Table 4.3 summarises the values of the sensitivity vectors for all design parameters (displacements q and eigenfrequencies λ).

Table 4.3. Stiffness identification based on various state parameters - comparison of the sensitivity vectors.

	q		λ			
	w_{1j}	w_{2j}	w_{1j}	w_{2j}	w_{3j}	w_{4j}
E_{i1}	0.314	0.197	0.101	0.087	0.070	0.046
E_{i2}	0.355	0.258	0.128	0.046	0.014	0.099
E_{i3}	0.175	0.180	0.105	0.005	0.061	0.103
E_{i4}	0.037	0.112	0.057	0.035	0.068	0.073
E_{i5}	0	0.097	0.040	0.099	0.016	0.062
E_{i6}	0	0.045	0.017	0.107	0.058	0.034
E_{i7}	0	0	0.004	0.052	0.110	0.013
E_{i8}	0	0	0	0.010	0.039	0.003

It can be noticed that sections number six and seven has quite significant influence on the eigenfrequencies of the second and third mode. At the same time, they have very little, or the impact on the values of the static displacement is almost negligible. It shows that for obtaining the

MOST WIEDZY Downloaded from mostwiedzy.pl

very accurate identification of the structure stiffness distribution, results of both experiments should be used, if possible.

The application of the modal analysis can be especially helpful in determination of the section stiffness at the tip of the fin. It seems that for the presented structure there are more than one stiffness distribution, which would satisfy the condition of the agreement with the first four eigenfrequencies. At the same time, they do not provide the stiffness distribution that results in desired values of the static displacement.

The identification based on the static deformation using multiple control points is preferred method. It provides with sufficiently accurate results; experiments can be done relatively simply, and the results are much easier to analyse and interpret than the free vibrations experiment results. Finally, the identification based on the static displacement gives the clear and unique results of stiffness distribution.

At the early stage of this study, the application of the orthotropic material was considered. It was found that the sensitivity of the structure bending modes due to Young Modulus in the longitudinal direction is one order of magnitude greater than other material constants relative variations. In case of the torsional mode the influence of the Shear Modulus was dominant. However, the eigenfrequency value of this mode is high (321.4 Hz) and is not expected to play a significant role. Due to very good accuracy achieved for simplified isotropic model it was decided that the Young Modulus will be the only design parameter. Thus, the stiffness distribution of the windsurfing fin determined using described identification procedure is used for coupled hydrodynamic analysis.

The limitation of the presented approach is the assumption that within the selected group of fins there are no significant differences in the composite lay-up with respect to different ply orientations. It was proven that for a unidirectional laminate, the induced bend-twist coupling can locally increase or decrease the angle of attack depending on the ply orientation with respect to the main material axis (Zarruk et al. 2014). At the same time, the laminate can have quasi-isotropic properties when the plies are oriented in multiple directions (Xu, Mkaddem, and El Mansori 2016). Therefore, any bending and twisting mechanism would be more likely to result from the fin sweep angle and the local centre of lift force relative to the shear centre of the section, rather than from the composite properties as described by Chiu, Kalaugher, and Broers (1995).

This approach is considered to be correct given the circumstances that the composite material constituents are glass mat, which can be treated as isotropic, and bi-directional woven. Unidirectional fibres would have to be used in the outer layer and the direction would have to be drastically different for different fins to observe different types of bending twist deformation. Attempting to model the exact composite lay-up would result in significant uncertainty as there could be many possible lay-ups that give similar performance. Therefore, the structural model based on the isotropic material is much more practical to build, calibrate and validate. In summary, the obtained FEA model is considered to be of sufficient accuracy despite the assumptions and limitations presented.

MOST WIEDZY Downloaded from mostwiedzy.pl

4.4. Fluid-Structure Interaction - discussion of results

4.4.1. Discussion of results of the validation study

One of the largest questions and uncertainties encountered during the research were the values of the Rayleigh damping coefficient. Due to an access to experimental data, it was decided to investigate the influence of the Rayleigh coefficient on the displacement and forces for the trapezoidal hydrofoil used for validation of the numerical models – see Chapter 3.5.1. Table 4.4 presents the combination of damping coefficients used for calculations.

Table 4.4. Values of the damping coefficient.

Case Number	α	β
1	1.8	0.05
2	1.8	0.1
3	1.8	0.2

Figure 4.7 presents the damping coefficient ζ_n of the n-th mode calculated according to Equation 2.2 presented in Chapter 2.4.3. Except cases presented in the Table 4.4 the damping coefficient was also plotted for values of damping coefficient that can be found in the literature for the aluminium plate fixed at one end according to Rahul, Dharani, and Balaji (2021) equal to α = 1.65 and $\beta = 2 \cdot 10^{-5}$.

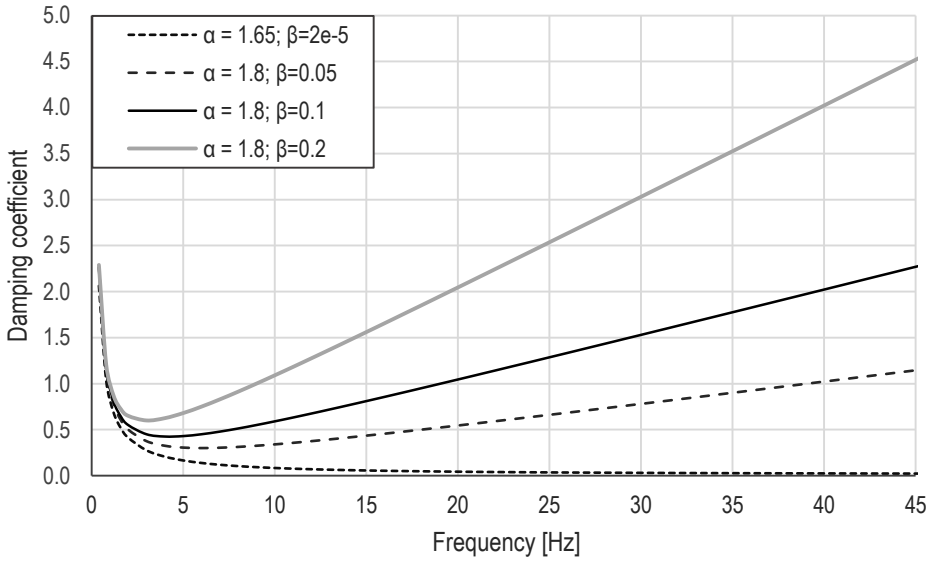

Figure 4.7 Values of damping coefficient depending on the frequency of vibrations.

According to Figure 4.7, it can be noticed that for higher values of eigenfrequencies the stiffness proportional damping coefficient β has a significant impact on the damping coefficient. For the tested hydrofoil, the first eigenfrequency in water was estimated to be equal to 42 Hz (Zarruk et al. 2014), so selection of stiffness proportional coefficient is crucial. The value of damping coefficient for aluminium plate presented in the literature is significantly lower than the one used for the calculations. However, if the suggested value of the material damping for aluminium is selected, the calculations are unstable and diverging.

MOST WIEDZY Downloaded from mostwiedzy.pl

For the sake of comparison, the calculations were performed for the values of the material damping as specified by Rahul, Dharani, and Balaji (2021), however the fluid acting on the structure was an air instead of water. The velocity of the air was selected in a way to obtain the same values of Reynolds number as in the Case 1 described in Chapter 3.5.1 of the validation study. In this case, the velocity of air was almost 14 times greater than water and obtained lift force about five times smaller. In this case, simulations were stable. It is in line with the findings presented by Förster, Wall, and Ramm (2007), that for sufficiently high numbers of fluid to solid mass ratio, the calculations can suffer from instability issues due to 'artificial added mass effect'. The remedy of this problem suggested by authors is application of iteratively staggered algorithms. Küttler and Wall (2008) introduced the relaxation method, which is implemented in STAR-CCM software for FSI calculations and was also applied in presented validation study. However, both solutions were not sufficient, and calculations were not stable. Tezduyar et al. (2006) proposed the artificial increase of the mass to obtained converged solution. However, the stabilising effect of the mass increase was demonstrated for membranes, which is far from the object of consideration of the current study. Finally, they argued that also damping has a stabilising effect, and introduction of the damping may be done in computations where time-accuracy is not required. Since in my study I seek for the quasi-steady solution, the application of the additional structural damping to obtain the converged solution is declared as the correct approach.

Figure 4.8 presents the comparison of time history of forces generated by the NACA 0009 hydrofoil tested by Zarruk et al. (2014) for various values of the stiffness proportional damping coefficient. Calculations were performed for the same velocity of water and hydrofoil angle of attack as for the Case 1 of the FSI validation study. Values presented in Table 3.10 were obtained for the stiffness proportional damping coefficient β=0.1. The results obtained for the coefficient β=2e-5 were not included, since the simulation diverged after initialisation of the calculations.

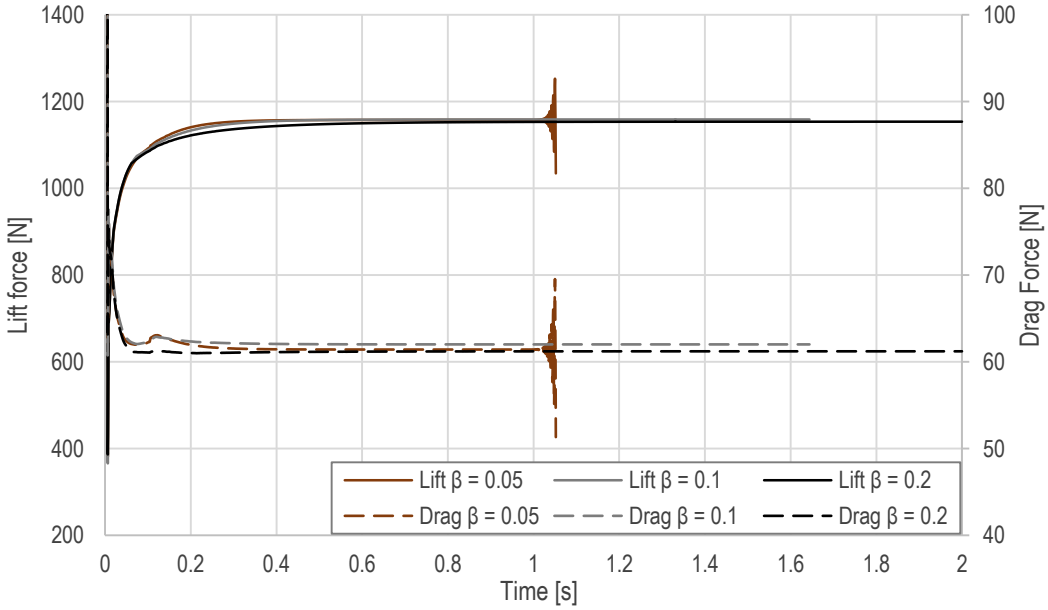

Figure 4.8 Comparison of the drag and lift forces for various stiffness proportional damping coefficients.

MOST WIEDZY Downloaded from mostwiedzy.pl

It can be noticed that for the stiffness proportional damping coefficient β =0.05 simulation also becomes unstable, and solution diverges. It happens even when results seem to converge. For the remaining two higher values of the stiffness proportional damping coefficient the calculations are stable, however, some differences can be noticed.

Figure 4.9 presents the time history of the tip displacement. Not only the rate of deformation is different, but also the converged value of the hydrofoil tip displacement. For the β=0.05, the tip displacement was equal to q = 12.98 mm before it starts to diverge. For the β=0.1, the tip displacement was equal to q = 12.65 mm, and for the β=0.2 the tip displacement was equal to q = 12.16 mm. Therefore, the increase of the β by 100% resulted in decrease of the tip displacement by 3.9%.

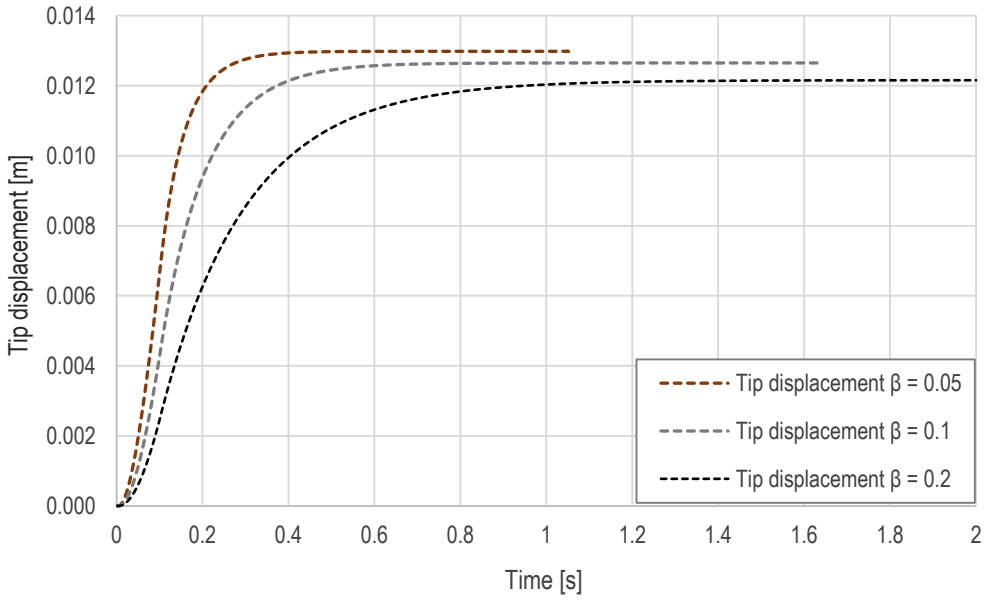

Figure 4.9 Comparison of the tip displacement for various stiffness proportional damping coefficients.

In terms of forces, the difference in the lift force generated by the hydrofoil for various damping coefficient values is 0.5%, and 1.3% for the drag force. Therefore, the sensitivity of the forces on the value of the damping coefficient exists, but it is rather small.

The conducted comparative study shows that the numerical models selected for the calculations are capable of providing credible results and can be utilised for solution of the main problem of the thesis.

4.4.2. Assessment of displacements and forces for RS:X windsurfing fin

The approach for determination of the hydroelastic properties of the windsurfing fin presented in this thesis allowed to study variations that occur between them. The main observation that can be drawn from the FSI calculations is that the fins are prone to deformation under the fluid loads (see Figure 3.30 and Figure 3.31) leading to reduction of the forces compared to undeformed structure (see Figure 3.27). However, significant differences in bending have a moderate influence on the variations in fluid forces acting on analysed RS:X fins. Those

MOST WIEDZY Downloaded from mostwiedzy.pl

findings are summarised in Figure 4.10 which presents the comparison of tip displacement, Figure 4.11 shows the differences in lift coefficient and Figure 4.12. presents the comparison of drag coefficient. In each comparison FIN1 was taken as the reference and results for the remaining fins were shown as a percent of reference FIN1.

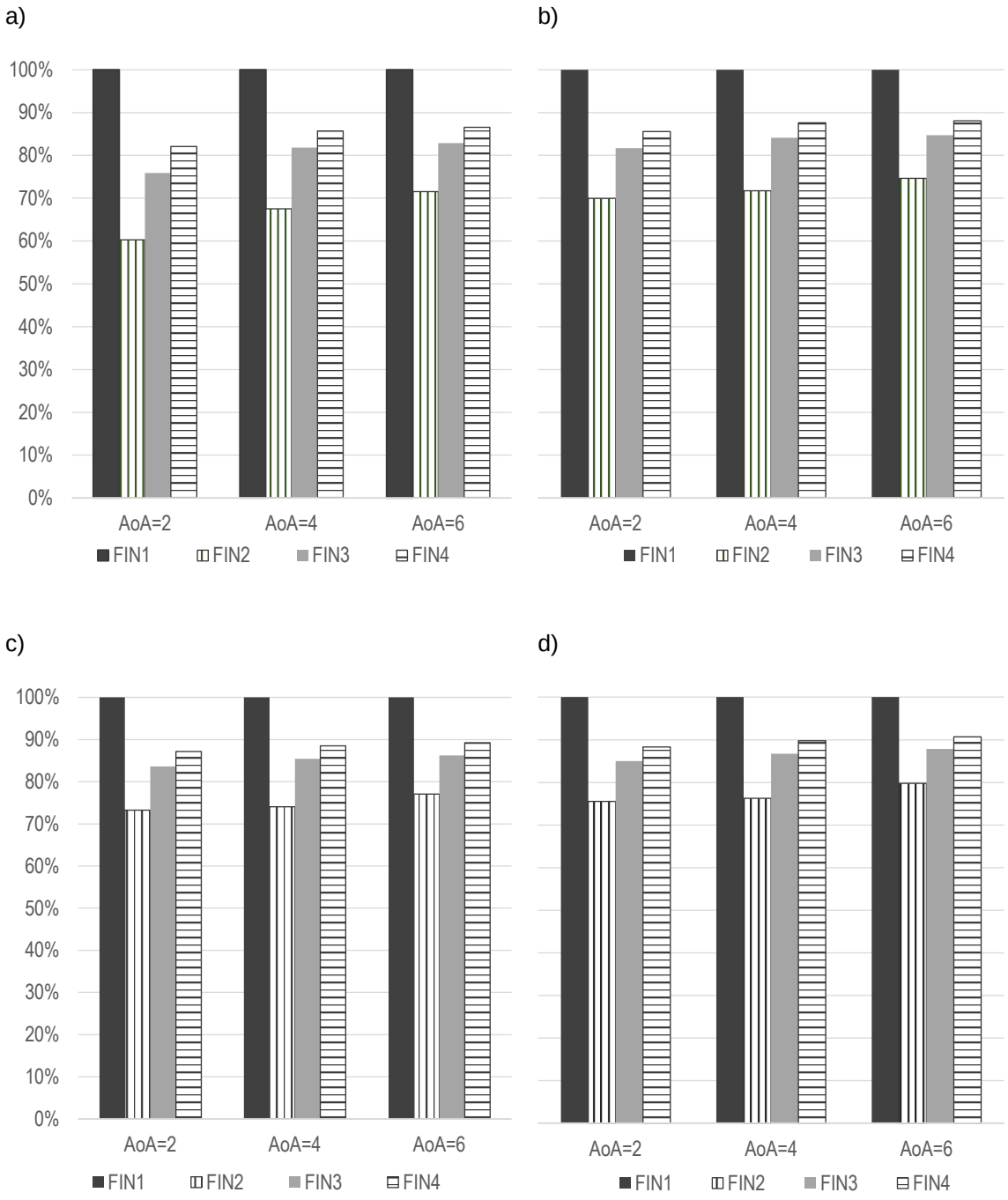

Figure 4.10 Comparison of the tip displacement for RS:X fin: a)Velocity 4 m/s b)Velocity 6 m/s c)Velocity 8 m/s d)Velocity 10 m/s.

According to Figure 4.10 it is clearly visible that FIN2, FIN3 and FIN 4 are less susceptible for fluid load. The difference between FIN1 and FIN2 reach even up to 40% for the lowest velocity, and 20% for the highest speed velocity of water inflow. Moreover, the percentage difference between FIN1 and remaining fins decrease with increasing speed.

MOST WIEDZY Downloaded from mostwiedzy.pl

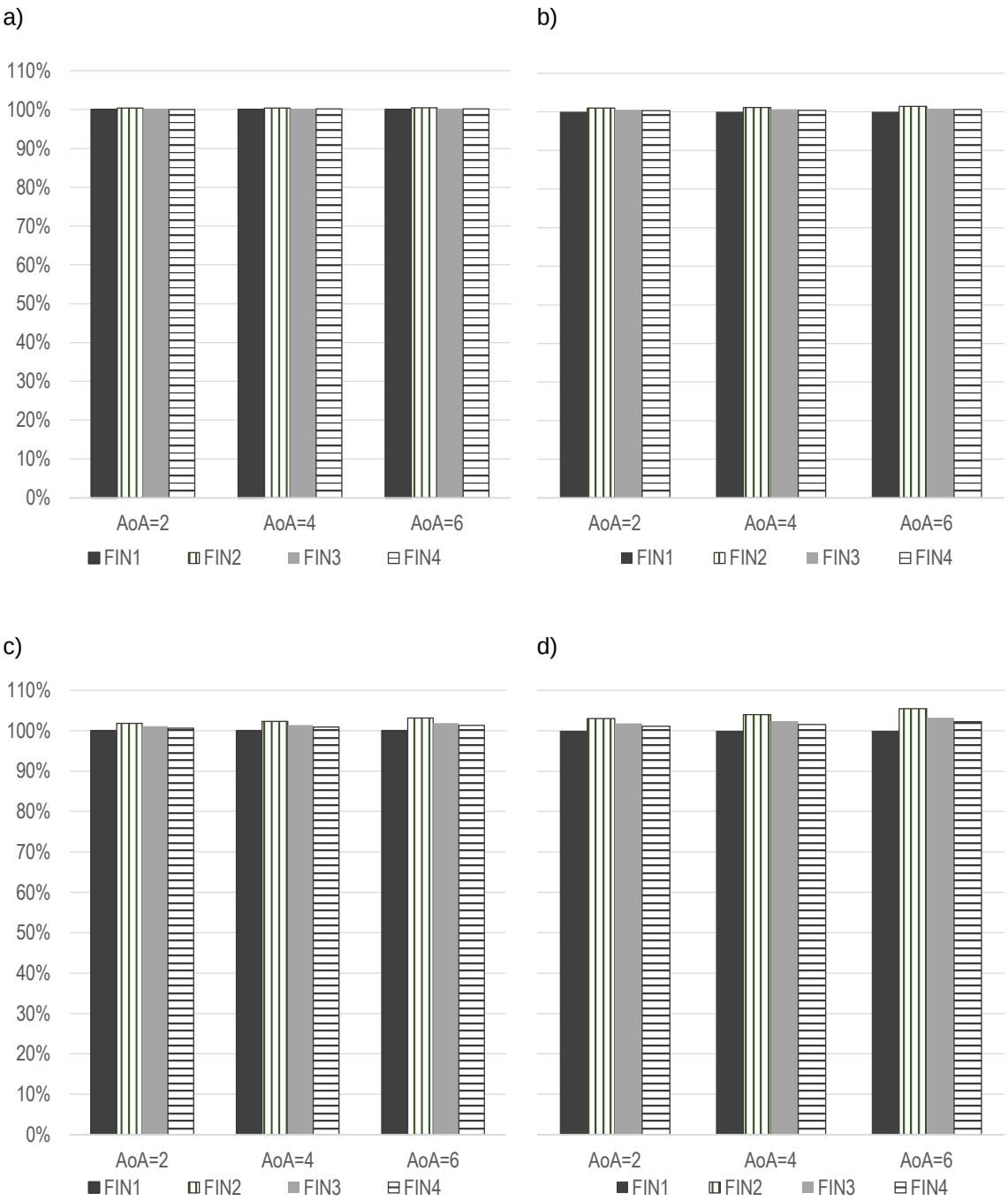

Figure 4.11 Comparison of the lift coefficient for RS:X fin: a)Velocity 4 m/s b)Velocity 6 m/s c)Velocity 8 m/s d)Velocity 10 m/s.

According to Figure 4.11 the percentage differences between lift coefficient for all fins are significantly smaller than the difference between tip displacement. It proves earlier statement that significant differences in deformation between analysed RS:X fins have an impact on the lift force, however, it is not so significant. The percentage difference between FIN1 and FIN2 varies from 0.4% to 5.4%, and naturally, it increases together with fluid load and tip displacement.

MOST WIEDZY Downloaded from mostwiedzy.pl

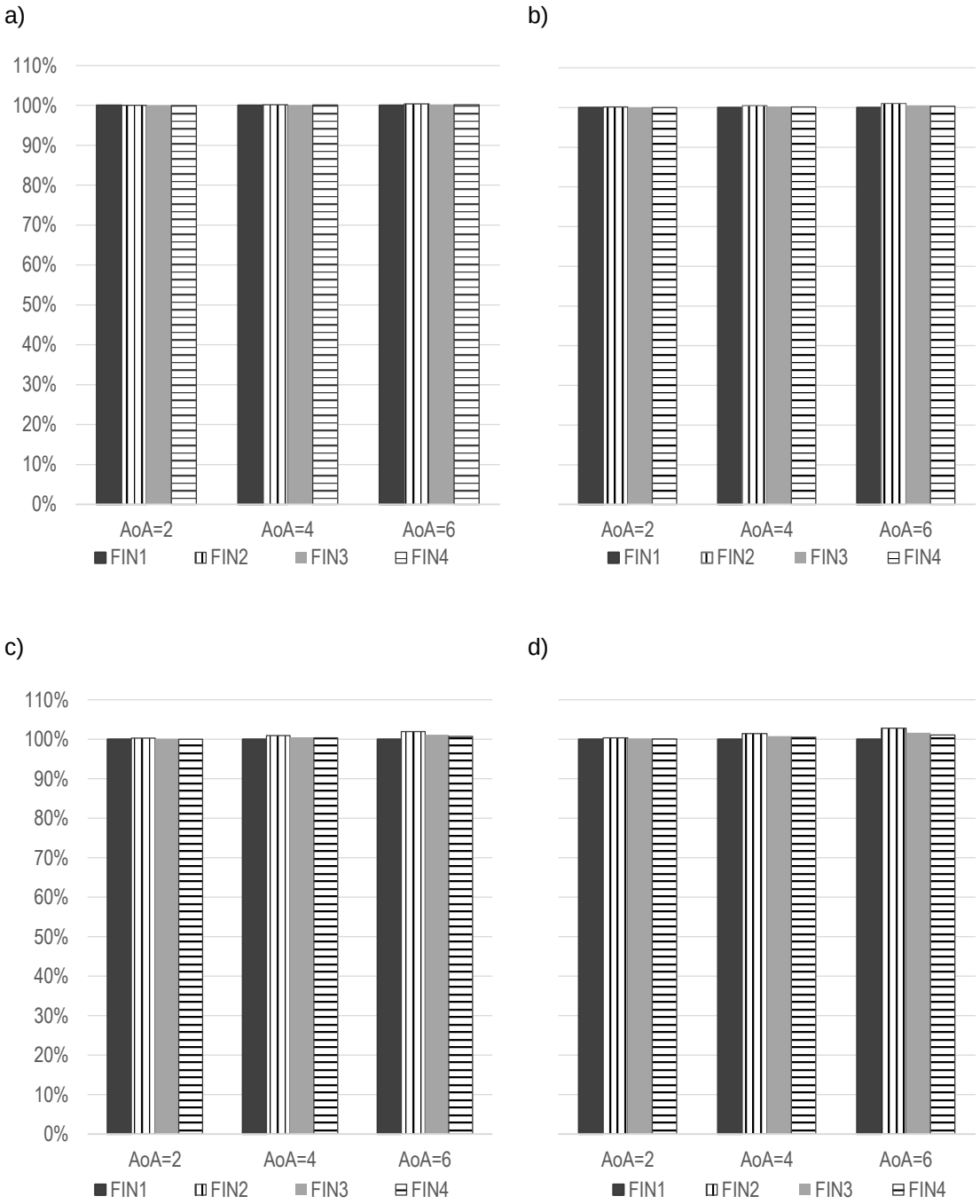

Figure 4.12 Comparison of the drag coefficient for RS:X fin: a)Velocity 4 m/s b)Velocity 6 m/s c)Velocity 8 m/s d)Velocity 10 m/s.

According to Figure 4.12 the percentage differences between drag coefficients for all fins are significantly smaller than the difference between tip displacement and smaller that between lift coefficients. The difference between FIN1 and FIN2 varies from 0.1% to 2.9%. It is believed that reduction of the drag force is mainly attributed to loss of lift and therefore lower induced drag.

As mentioned in Chapter 2.7.4, implicit and explicit coupling were compared with each other. It needs to be mentioned, that at the primary phase of the implicit coupling calculations solvers required several sub-iterations so that the normalised displacement residual drop below 0.01. However, in the further phase, the exchange took place only once in a time step, meaning that it was ambiguous with the explicit coupling approach. On the other hand, application of the

MOST WIEDZY Downloaded from mostwiedzy.pl

implicit coupling led to more stable calculations allowing to reduce the damping coefficient compared to explicit coupling. Table 4.5 presents the comparison of the forces and tip displacement for FIN4, angle of attack equals to 6 degrees with the velocity of 8 m/s.

Table 4.5. Values of the damping coefficient.

Coupling	Damping coefficient	Tip displacement	Lift force	Drag force
Explicit	α = 2.7 β = 1.7	0.128 m	974.6 N	39.66 N
Implicit	α = 2.7 β = 1.7	0.128 m	974.6 N	39.66 N
Implicit	α =1.35 β = 0.224	0.132 m	969.6 N	39.52 N

According to data in Table 4.5, for the case of RS:X fin the damping coefficient has even smaller influence on the forces generated by the fin, although again the differences in tip displacement are noticeable. The most significant difference between case with implicit coupling and low damping and explicit coupling is the convergence time, understood as the amount of time steps inside the simulation that need to be completed to obtain quasi-steady solution. The simulation time necessary to obtain stable converged solution was equal to 3 seconds of simulation time for implicit coupling compared to 15 seconds of simulation time for explicit coupling. Naturally, the implicit coupling requires more CPU time to finalise one time step due to inner iterations. However, it is more stable, and it allows to apply lower material damping values. As shown, the material damping is responsible for rate of deformation before achieving convergence. Therefore, it is clear, then if the structure dynamics is of the primary interest, the structure damping coefficients need to be used with care.

The orthotropy of the material is not applied, and fins have the same geometry. Therefore, various bending deformation is the only physical mechanism that causes differences in forces. It might explain why, in the end, observed differences are noticeable, but not so significant. Nevertheless, the fins should not be analysed only from the hydrodynamic point of view, because the effect of deformation plays an important role. It is especially well visible in Figure 3.32 and Figure 3.33. For some profiles and hydrofoils, the lift-drag characteristics are to some extent Reynolds number dependent. However, it is especially pronounced for the angles of attack close to stall. In general, for the undeformed fin, the forces coefficient should vary mostly due to angle of attack, not to velocity of the fluid. Differences between fins indicate that the variations in force coefficients for the same angle of attack are mainly the result of the hydrofoil deformation. The reduction in the lift coefficient compared to rigid hydrofoil varies between 12.8% and 8.1% for the velocity of 10 m/s angle of attack of 6 degrees, for the FIN1 and FIN2, respectively. It is accompanied by the reduction of the drag coefficient which is between 6.9% and 4.2% for the FIN1 and FIN2, respectively. Such variations show that for composite fins susceptible to fluid loads, the hydrodynamic forces cannot be done determined without taking into account the hydrofoil deformation.

In the light of the conducted research, it was recognised that the main limitation of the proposed method is the material modelling and assumption of the isotropy. It should not be used

MOST WIEDZY Downloaded from mostwiedzy.pl

if the hydrofoil structure is designed to exhibit particular bend-twist behaviour under the fluid loads – with the intended orthotropic behaviour. Moreover, if the hydrofoils vary in the significant way in terms of plies orientation proposed model also probably could not capture it. Therefore, it should not be treated as a universal approach for identification of every composite structure. In some cases, it should be enriched to take into account more material constants.

Another aspect of the identified limitation the influence of the damping coefficient. In my research it was artificially increased due to its stabilising effect on the calculations. The hydrofoil deformation described in this thesis are very significant and limited number of published works report the results for such a high level of bending. Therefore, no better solution for ensuring the results convergence was found in other works, than the one applied in this research. Large structure deformation under high fluid loads is believed to be the main reason for the calculations instability. It was observed that RS:X windsurfing fins vary between each other in terms of rate of free vibration decay. However, those differences cannot be used to differentiate fins between each other, because the damping coefficient obtained experimentally is much lower than the one which is required to stabilize the calculations.

Finally, I would like to address the issue of the numerical results accuracy. The FSI calculations were performed and validated for the hydrofoil similar to windsurfing RS:X fin. Results of that calculations were compared to experimental data according to Zarruk et al. (2014) proving high accuracy of FSI calculations. Nevertheless, the numerical results of FSI calculations for the RS:X fin were not compared directly to experiments. However, they were verified, and the same models were used for all analysed windsurfing fins. Even if there would be differences between experiment, the proposed model is still able to study differences between hydroelastic behaviour various fins, which was the main goal of the thesis. In reality, the fins vary between each other in both shape and material properties, and my analysis allowed to separate the influence of the stiffness distribution.

MOST WIEDZY Downloaded from mostwiedzy.pl

5. SUMMARY, CONCLUSION AND FUTURE WORKS

The thesis focuses on the issue of various hydroelastic performances of the flexible windsurfing fin of the RS:X monotype class. The scientific problem raised in the dissertation is vast complex since the forces acting on the elastic fin cause its deformation, which eventually influences the generated force. This leads to a feedback loop referred in the literature as the Fluid-Structure Interaction problem, which has not received enough attention up to this point. To a certain extent, this research advances the investigation of the FSI phenomenon. This thesis investigated the differences in hydrofoil stiffness distribution and the impact of stiffness variations on the hydrodynamic forces generated by the windsurfing fins that ideally should be under every aspect identical, practically are not, though. The study contributes to the knowledge regarding hydrostructural behaviour of hydrofoil that undergoes significant deformation, and consequences of structure various stiffness.

The ultimate goal of this research has been set to determine the range of variability of hydroelastic properties for the flexible composite windsurfing fins of the RS:X class, which has been fully accomplished. All the particular objectives that led to completing the main goal have been successfully achieved as well, in particular:

- the framework for analysis of the hydroelastic properties of windsurfing fins with unknown composite lay-up has been developed;
- the range of variations in the mechanical properties of the hydrofoils has been identified;
- the simplified substitute FEM model based on the investigation into internal structure has been proposed;
- the substitute Finite Element Method model of the hydrofoil internal structure has been developed;
- the flow around the fin by means of high fidelity unsteady CFD calculations has been modelled;
- CFD and FEM solvers to perform Fluid-Structure Interaction calculations have been coupled;
- the influence of the structural stiffness on the hydromechanical characteristics of the hydrofoil has been determined.

The answer to the research question that was asked, have been formulated and justified within the rigorous scientific approach.

The main achievements of the research are:

- obtaining high-quality 3D model of windsurfing fin based on laser scanning;
- successful implementation of the first-order sensitivity analysis for the accurate determination of the stiffness distribution;
- application of free vibration measurements and modal analysis for validation of FEM model of windsurfing fin and determining construction Rayleigh coefficients;

MOST WIEDZY Downloaded from mostwiedzy.pl

- successful coupling structural and fluid domains for performing Fluid-Structure Interaction calculation;
- determination of the hydroelastic properties range of variability and influence of the stiffness distribution on the forces generated by the windsurfing fin.

Methodology presented in this thesis allows for identifying the stiffness distribution of composite fins in the case when the composite lay-up and schedule are unknown. This method has been successfully adopted, with the tailored applications to the problem of fin hydoelasticity. It is capable to study the differences between the fins that are designed as identical, yet actually due to the imperfections of the realistic manufacturing process they have an unknown composite schedule, thus, they remain structurally different, which leads to various deflection under same loads. The quantified differences in the stiffness distribution were used to determine their influence on the hydrodynamic forces generated by fins. Finally, two solvers were coupled using available software solutions and Fluid-Structure Interaction calculations for four fins over a wide range of speed and angles of attack were performed. As a result, the range of variation of the hydrodynamic forces was also obtained, giving a comprehensive picture of the hydroelastic properties of theoretically identical fins. The proposed approach, specifically aiming at the actual fins with all their imperfections and manufacturing-originated structural variations, is claimed to be a novelty in the field.

The main findings of the conducted investigation can be divided into two groups, one related to technical aspects of performed calculations, and second, purely to physics of the studied phenomena:

1. As it is described in the literature, at certain conditions the FSI calculations can become unstable, due to large deformation and high values of the fluid to solid density ratio. The suggested solution is to artificially increase the mass of the structure or perform iteratively staggered calculations. It was noticed that another aspect, that significantly helps to stabilise the calculations is to increase the structure Rayleigh damping coefficients. Moreover, the experimental tests showed that the rate of structure damping can be various for fins, therefore it would be useful to investigate more deeply the influence of damping coefficient on the stability and accuracy of calculations.
2. It was found that the variations of deformation between theoretically identical fins can be significant. The tip displacement of the most flexible fin is approximately 20% higher than the stiffest one. Additionally, it was found that the relation between tip displacement and generated lift forces is almost linear for each fin. What distinguish fins from each other is different slope of the lift vs displacement line.
3. The differences in lift forces between analysed fins do not exceed 6%. The highest discrepancy between fins occurs for the largest external fluid loading. The highest lift force is generated by the stiffest fin. The general trend is in line with

MOST WIEDZY Downloaded from mostwiedzy.pl

experimental and numerical finding of other researchers. For the drag force the opposite trend than for the lift was observed. It is believed that this is mostly due to higher induced drag typical for fins that generate higher lift force.

The results and findings presented in this thesis have practical applications. It was demonstrated that the stiffness of the hydrofoil affects the hydrodynamic forces generated on the fin, and this influence was quantified. The results of this research can be interesting, first, for the scientific community of the researchers who investigate the aerodynamic and hydrodynamic properties of hydrofoils. It is crucial for them to realise that in some cases the deformation of the hydrofoil can cause the significant variations in generated forces, compared to undeformed shape. This work is also important for researchers who study the hydroelastic properties of hydrofoils by means of Fluid Structure Interaction calculations. This research shows that for composite hydrofoils that are theoretically identical, a large variation of deformation can occur; therefore, it can be sometimes difficult to draw a meaningful conclusion if the study is based on the limited number of samples.

This study can be interesting for the end users of the sailing equipment. The findings presented in this thesis can serve as a guide for windsurfers on which equipment features are desirable for improving performance. Moreover, the proposed method for modelling the composite hydrofoils with the unknown layup can be used for similar objects, such as other monotype classes for which alike problem occurs.

The next target group of this research are the hydrofoil designers and producers. The awareness of the differences that can occur during the fin production can be a motivation for improving the production processes to eliminate the influence of the equipment flaws on the racing performance. The method of hydrofoil testing based on the vibrations can be used for quality control to ensure better repeatability of the products.

This research was conducted assuming that the influence of the stiffness is isolated from the possible variations of the shape, and only this feature was investigated. It is known that differences in hydrofoil shape can also occur. Therefore, future works will focus on integrating two problems: the influence of the shape and stiffness of the hydrofoil on the hydroelastic performance. Moreover, verifying the presented method for composite material modelling would be interesting. To do so, it is planned to cooperate with the windsurfing fin producer and obtain data about the exact composite layup of the windsurfing fin. It would not be for the monotype class, but this would allow me to compare the presented method with an approach of modelling composite when the exact lamination plan is known.

Finally, it will be a significant achievement to investigate the hydrofoil performance under natural conditions. Therefore, developing a method for measuring and analysing the hydrofoil performance in the natural environment is desired.

MOST WIEDZY Downloaded from mostwiedzy.pl

PUBLISHED WORKS

Pruszko, Hanna, Maciej Reichel, Tomasz Mikulski. (2023). Influence of windsurfing fin stiffness distribution on the lift-drag characteristics. In *10th International Conference on Computational Methods in Marine Engineering – MARINE 2023*. https://doi.org/10.23967/marine.2023.101

Pruszko, Hanna. (2021). Mesh dependence study for numerical assessment of hydrodynamic characteristics of windsurfing fin. In *International Symposium on Hydrodynamics in Ship Design, Safety, Manoevring and Operation, Hydronav 2021*.

Pruszko, Hanna, Tomasz Mikulski. (2021). Modal Analysis of Windsurfing composite fins and struts. In *XX Szkoła Analizy Modalnej*.

Pruszko, Hanna, Tomasz Mikulski. (2021). Accelerometric measurements of windsufring fins vibrations. In. *International Conference on Postgraduate Research in Maritime Technology*.

MOST WIEDZY Downloaded from mostwiedzy.pl

REFERENCES

Abbott, Ira H., and Albert. E. Von Doenhoff. 1959. *Theory of Wing Sections, Including a Summary of Airfoil Data*. 1st ed. Dover Publications.

Akcabay, Deniz Tolga, Eun Jung Chae, Yin Lu Young, Antoine Ducoin, and Jacques Andre Astolfi. 2014. "Cavity Induced Vibration of Flexible Hydrofoils." *Journal of Fluids and Structures* 49: 463–84. https://doi.org/10.1016/j.jfluidstructs.2014.05.007.

Amman, Othmar H., Theodore von Kármán, and Glenn B. Woodruff. 1941. "The Failure of the Tacoma Narrows Bridge." Washington, DC.

Ausoni, Philippe, Mohamed Farhat, Xavier Escaler, Eduard Egusquiza, and François Avellan. 2007. "Cavitation Influence on von Kármán Vortex Shedding and Induced Hydrofoil Vibrations." *Journal of Fluids Engineering, Transactions of the ASME* 129 (8): 966–73. https://doi.org/10.1115/1.2746907.

Balze, Rémy, Nedeleg Bigi, Kostia Roncin, Jean B. Leroux, Alain Nême, Vincent Keryvin, Antoine Connan, Hervé Devaux, and Denis Gléhen. 2017. "An Innovative Tool to Study and Optimize Racing Yacht Appendages Using Fluid-Structure Interactions." In *7th International Conference on Computational Methods in Marine Engineering, MARINE 2017*, 2017-May:616–24.

Banks, Joseph., Laura. Marimon Giovannetti, Joshua. C. Taylor, and Stephen. R. Turnock. 2016. "Assessing Human-Fluid-Structure Interaction for the International Moth." In *11th Conference of the International Sports Engineering Association, ISEA 2016*, 147:311–16. Elsevier Ltd. https://doi.org/10.1016/j.proeng.2016.06.297.

Banks, Joseph., Laura. Marimon Giovannetti, X. Soubeyran, Alexander. M. Wright, Stephen. R. Turnock, and Stephen. W. Boyd. 2015. "Assessment of Digital Image Correlation as a Method of Obtaining Deformations of a Structure under Fluid Load." *Journal of Fluids and Structures* 58: 173–87. https://doi.org/10.1016/j.jfluidstructs.2015.08.007.

Barbero, Ever J. 2013. *Finite Element Analysis of Composite Materials Using ANSYS:, Second Edition*. *Finite Element Analysis of Composite Materials Using ANSYS:, Second Edition*.

Bergan, C. W., E. O. Tengs, B. W. Solemslie, and O. G. Dahlhaug. 2019. "An Experimental Investigation of the Hydrodynamic Damping of Vibrating Hydrofoils." *IOP Conference Series: Earth and Environmental Science* 240 (6). https://doi.org/10.1088/1755-1315/240/6/062008.

Blazek, Jiri. 2015. *Computational Fluid Dynamics: Principles and Applications: Third Edition*. *Computational Fluid Dynamics: Principles and Applications: Third Edition*. https://doi.org/10.1016/C2013-0-19038-1.

Boyd, Stephen W., Daniel Flannigan, Joseph Banks, and Stephen R. Turnock. 2015. "DESIGN OF COMPOSITE CONTROL SURFACES FOR TAILORED DEFORMATION USING FLUID STRUCTURE INTERACTIONS." In *LIMAS -2015: International Conference on Light Weight Design of Marine Structures*.

MOST WIEDZY Downloaded from mostwiedzy.pl

Brandner, Paul. A., and Bryce. W. Pearce. 2012. “Experimental Modelling of Steady Hydrofoil Fluid-Structure Interaction.” *Proceedings of the 18th Australasian Fluid Mechanics Conference, AFMC 2012*, no. December: 3–6.

Brennen, C. E. 1982. “A Review of Added Mass and Fluid Inertial Forces.”

Capuzzi, Marco, Alberto Pirrera, and Paul M. Weaver. 2014. “A Novel Adaptive Blade Concept for Large-Scale Wind Turbines. Part I: Aeroelastic Behaviour.” *Energy* 73. https://doi.org/10.1016/j.energy.2014.06.044.

Cardoso de Brito, Miguel, Leigh Stuart Sutherland, José Manuel C. Pereira, and Mário Rui Arruda. 2022. “Fluid-Structure Interaction Analyses for Hydro-Elastic Tailoring of a Windsurfer Fin.” *Journal of Marine Science and Engineering* 10 (10). https://doi.org/10.3390/jmse10101371.

Carvelli, V., T. Truong Chi, M. S. Larosa, S. V. Lomov, C. Poggi, D. Ranz Angulo, and I. Verpoest. 2004. “EXPERIMENTAL AND NUMERICAL DETERMINATION OF THE MECHANICAL PROPERTIES OF MULTI-AXIAL MULTI-PLY COMPOSITES.” In *ECCM 11 11th European Conference on Composite Materials*.

Çengel, Yunus A., and John M. Cimbala. 2018. *Fluid Mechanics A Fundamental Approach*. *Fluid Dyanmics*.

Chae, Eun Jung, Deniz Tolga Akcabay, Alexandra Lelong, Jacques Andre Astolfi, and Yin Lu Young. 2016. “Numerical and Experimental Investigation of Natural Flow-Induced Vibrations of Flexible Hydrofoils.” *Physics of Fluids* 28 (7). https://doi.org/10.1063/1.4954785.

Chae, Eun Jung, Deniz Tolga Akcabay, and Yin Lu Young. 2017. “Influence of Flow-Induced Bend–Twist Coupling on the Natural Vibration Responses of Flexible Hydrofoils.” *Journal of Fluids and Structures* 69 (January): 323–40. https://doi.org/10.1016/j.jfluidstructs.2016.12.008.

Chaphalkar, Pramod, and Ajit D. Kelkar. 2001. “Classical Laminate Theory Model for Twill Weave Fabric Composites.” *Composites - Part A: Applied Science and Manufacturing* 32 (9). https://doi.org/10.1016/S1359-835X(01)00101-4.

Chiu, T. W., P. G. Kalaugher, and C. A. M. Broers. 1995. “The Application of Photogrammetry in the Study of the Effects of Sailboard Fin Flexibility.” *Proceedings of the Institution of Mechanical Engineers, Part C: Journal of Mechanical Engineering Science* 209 (6): 373–81. https://doi.org/10.1243/PIME_PROC_1995_209_168_02.

Chróścielewski, Jacek, Tomasz Ferenc, Tomasz Mikulski, Mikołaj Miśkiewicz, and Łukasz Pyrzowski. 2019. “Numerical Modeling and Experimental Validation of Full-Scale Segment to Support Design of Novel GFRP Footbridge.” *Composite Structures* 213. https://doi.org/10.1016/j.compstruct.2019.01.089.

Degroote, Joris, Sebastiaan Annerel, and Jan Vierendeels. 2010. “Stability Analysis of Gauss-Seidel Iterations in a Partitioned Simulation of Fluid-Structure Interaction.” *Computers and Structures* 88 (5–6). https://doi.org/10.1016/j.compstruc.2009.09.003.

De La Torre, O., X. Escaler, E. Egusquiza, and M. Farhat. 2013. “Experimental Investigation of Added Mass Effects on a Hydrofoil under Cavitation Conditions.” *Journal of Fluids and Structures* 39. https://doi.org/10.1016/j.jfluidstructs.2013.01.008.

MOST WIEDZY Downloaded from mostwiedzy.pl

Ducoin, Antoine, Jacques André Astolfi, and Marie Laure Gobert. 2012. “An Experimental Study of Boundary-Layer Transition Induced Vibrations on a Hydrofoil.” *Journal of Fluids and Structures* 32: 37–51. https://doi.org/10.1016/j.jfluidstructs.2011.04.002.

Ducoin, Antoine, Jacques André Astolfi, and Jean François Sigrist. 2012. “An Experimental Analysis of Fluid Structure Interaction on a Flexible Hydrofoil in Various Flow Regimes Including Cavitating Flow.” *European Journal of Mechanics, B/Fluids* 36 (November): 63–74. https://doi.org/10.1016/j.euromechflu.2012.03.009.

Durbin, P. A. 1991. “Near-Wall Turbulence Closure Modeling without ‘Damping Functions.’” *Theoretical and Computational Fluid Dynamics* 3 (1). https://doi.org/10.1007/BF00271513.

Elham, Ali, and Michel J.L. Van Tooren. 2016. “Tool for Preliminary Structural Sizing, Weight Estimation, and Aeroelastic Optimization of Lifting Surfaces.” *Proceedings of the Institution of Mechanical Engineers, Part G: Journal of Aerospace Engineering* 230 (2). https://doi.org/10.1177/0954410015591045.

Faltinsen, Odd M. 2015. “Hydrodynamics of Marine and Offshore Structures.” *Journal of Hydrodynamics*. https://doi.org/10.1016/S1001-6058(14)60092-5.

Faltinsen, Odd M. 2000. “Hydroelastic Slamming.” *Journal of Marine Science and Technology* 5 (2). https://doi.org/10.1007/s007730070011.

Ferenc, Tomasz, and Tomasz Mikulski. 2020a. “Parametric Optimization of Sandwich Composite Footbridge with U-Shaped Cross-Section.” *Composite Structures* 246. https://doi.org/10.1016/j.compstruct.2020.112406.

Ferenc, Tomasz, and Tomasz Mikulski. 2020b. “Validation Process for Computational Model of Full-Scale Segment for Design of Composite Footbridge.” *Polish Maritime Research* 27 (2). https://doi.org/10.2478/pomr-2020-0037.

Ferziger, Joel H., and Milovan Peric. 2002. *Computational Methods for Fluid Dynamics*. Springer.

Förster, Christiane, Wolfgang A. Wall, and Ekkehard Ramm. 2007. “Artificial Added Mass Instabilities in Sequential Staggered Coupling of Nonlinear Structures and Incompressible Viscous Flows.” *Computer Methods in Applied Mechanics and Engineering* 196 (7). https://doi.org/10.1016/j.cma.2006.09.002

Frazer, R.A. 1929. “The Flutter of Aeroplane Wing.” *Journal of the Royal Aeronautical Society* 33: 407–54.

Garg, Nitin, Gaetan K.W. Kenway, Joaquim R.R.A. Martins, and Yin Lu Young. 2017. “High-Fidelity Multipoint Hydrostructural Optimization of a 3-D Hydrofoil.” *Journal of Fluids and Structures* 71 (May): 15–39. https://doi.org/10.1016/j.jfluidstructs.2017.02.001.

Garg, Nitin, Bryce W. Pearce, Paul A. Brandner, Andrew W. Phillips, Joaquim R.R.A. Martins, and Yin L. Young. 2019. “Experimental Investigation of a Hydrofoil Designed via Hydrostructural Optimization.” *Journal of Fluids and Structures* 84: 243–62. https://doi.org/10.1016/j.jfluidstructs.2018.10.010.

Giovannetti, Laura Marimon, Ali Farousi, Fabian Ebbesson, Alois Thollot, Alex Shiri, and Arash Eslamdoost. 2022. “Fluid-Structure Interaction of a Foiling Craft.” *Journal of Marine Science and Engineering* 10 (3). https://doi.org/10.3390/jmse10030372.

MOST WIEDZY Downloaded from mostwiedzy.pl

Gourlay, Tim, and Jon Martellotta. 2011. “Aero-Hydrodynamics of an RS: X Olympic Racing Sailboard.” *Cmst.Curtin.Edu.Au*.

Greene, C.F. 1927. “An Introduction to the Problem of Wing Flutter.” *Transactions of the American Society of Mechanical Engineers* Vol. 49-50.

Hansen, Ketesse, T Gourlay, and A King. 2011. “Analysis of Flow around an RS: X Racing 66 Windsurfing Fin.” *Cmst.Curtin.Edu.Au*.

Hansen, M. O.L., J. N. Sørensen, S. Voutsinas, N. Sørensen, and H. Aa Madsen. 2006. “State of the Art in Wind Turbine Aerodynamics and Aeroelasticity.” *Progress in Aerospace Sciences*. https://doi.org/10.1016/j.paerosci.2006.10.002.

Harwood, Casey M., Andrew J. Stankovich, Yin Lu Young, and Steven L. Ceccio. 2019. “Combined Experimental and Numerical Study of the Free Vibration of Surface-Piercing Struts.” *Open Archives of the 16th International Symposium on Transport Phenomena and Dynamics of Rotating Machinery, ISROMAC 2016*, 1–9.

Hayat, Khazar, and Sung Kyu Ha. 2015. “Load Mitigation of Wind Turbine Blade by Aeroelastic Tailoring via Unbalanced Laminates Composites.” *Composite Structures* 128. https://doi.org/10.1016/j.compstruct.2015.03.042.

Herath, Manudha T., S. Natarajan, B. Gangadhara Prusty, and Nigel St John. 2015. “Isogeometric Analysis and Genetic Algorithm for Shape-Adaptive Composite Marine Propellers.” *Computer Methods in Applied Mechanics and Engineering* 284 (February): 835–60. https://doi.org/10.1016/j.cma.2014.10.028.

Herath, Manudha T., B. Gangadhara Prusty, Andrew W. Phillips, and Nigel St. John. 2017. “Structural Strength and Laminate Optimization of Self-Twisting Composite Hydrofoils Using a Genetic Algorithm.” *Composite Structures* 176 (September): 359–78. https://doi.org/10.1016/j.compstruct.2017.05.012.

Herath, Manudha T., Andrew W. Phillips, Nigel St John, Paul Brandner, Bryce Pearce, and Gangadhara Prusty. 2021. “Hydrodynamic Response of a Passive Shape-Adaptive Composite Hydrofoil.” *Marine Structures* 80 (November). https://doi.org/10.1016/j.marstruc.2021.103084.

Hermundstad, Ole Andreas, Jan Vidar Aarsnes, and Torgeir Moan. 1999. “Linear Hydroelastic Analysis of High-Speed Catamarans and Monohulls.” *Journal of Ship Research* 43 (1). https://doi.org/10.5957/jsr.1999.43.1.48.

ITTC. 2008. “Uncertainty Analysis in CFD Verification and Validation Methodology and Procedures - 7.5-03 -01-01.” In *ITTC – Recommended Procedures and Guidelines*, 1–12.

ITTC. 2011. “Practical Guidelines for Ship CFD Applications - 7.5-03-02-03.” In *ITTC – Recommended Procedures and Guidelines*, 1–18.

ITTC. 2014. “Practical Guidelines for Ship Resistance CFD - 7.5-03-02-04.” In *ITTC – Recommended Procedures and Guidelines*, 1–9.

Kameyama, Masaki, and Hisao Fukunaga. 2007. “Optimum Design of Composite Plate Wings for Aeroelastic Characteristics Using Lamination Parameters.” *Computers and Structures* 85 (3–4). https://doi.org/10.1016/j.compstruc.2006.08.051.

MOST WIEDZY Downloaded from mostwiedzy.pl

Kreja, Ireneusz. 2007. “Geometrically Non-Linear Analysis of Layered Composite Plates and Shells.”

Kreja, Ireneusz, and Agnieszka Sabik. 2019. “Equivalent Single-Layer Models in Deformation Analysis of Laminated Multilayered Plates.” *Acta Mechanica* 230 (8). https://doi.org/10.1007/s00707-019-02434-7.

Kunz, Donald L. 1994. “Survey and Comparison of Engineering Beam Theories for Helicopter Rotor Blades.” *Journal of Aircraft* 31 (3). https://doi.org/10.2514/3.46518.

Küttler, Ulrich, and Wolfgang A. Wall. 2008. “Fixed-Point Fluid–Structure Interaction Solvers with Dynamic Relaxation.” *Computational Mechanics* 43 (1): 61–72. https://doi.org/10.1007/s00466-008-0255-5.

Lackner, Matthew A., and Mario A. Rotea. 2011. “Passive Structural Control of Offshore Wind Turbines.” *Wind Energy* 14 (3). https://doi.org/10.1002/we.426.

Lardeau, S, and R Manceau. 2012. “Computations of Complex Flow Configurations Using a Modified Elliptic-Blending Reynolds-Stress Model.” *10th International ERCOFTAC Symposium on Engineering Turbulence Modelling and Measurements*, no. 2002.

Liao, Yingqian, Nitin Garg, Joaquim R.R.A. Martins, and Yin L. Young. 2019. “Viscous Fluid–Structure Interaction Response of Composite Hydrofoils.” *Composite Structures* 212 (March): 571–85. https://doi.org/10.1016/j.compstruct.2019.01.043.

Lien, F. S., and M. A. Leschziner. 1994. “Assessment of Turbulence-Transport Models Including Non-Linear Rng Eddy-Viscosity Formulation and Second-Moment Closure for Flow over a Backward-Facing Step.” *Computers and Fluids* 23 (8). https://doi.org/10.1016/0045-7930(94)90001-9.

Liu, Jialun, and Robert Hekkenberg. 2017. “Sixty Years of Research on Ship Rudders: Effects of Design Choices on Rudder Performance.” *Ships and Offshore Structures* 12 (4). https://doi.org/10.1080/17445302.2016.1178205.

Liu, Zhanke, and Yin L. Young. 2009. “Utilization of Bend-Twist Coupling for Performance Enhancement of Composite Marine Propellers.” *Journal of Fluids and Structures*. https://doi.org/10.1016/j.jfluidstructs.2009.04.005.

Malcolm, David J., and Daniel L. Laird. 2003. “Modeling of Blades as Equivalent Beams for Aeroelastic Analysis.” In *ASME 2003 Wind Energy Symposium, WIND2003*. https://doi.org/10.1115/wind2003-870.

Manceau, Rémi, and Kermal Hanjalić. 2002. “Elliptic Blending Model: A New near-Wall Reynolds-Stress Turbulence Closure.” *Physics of Fluids* 14 (2). https://doi.org/10.1063/1.1432693.

Mangano, Marco, Sicheng He, Yingqian Liao, Denis Gabriel Caprace, and Joaquim R.R.A. Martins. 2022. “Towards Passive Aeroelastic Tailoring of Large Wind Turbines Using High-Fidelity Multidisciplinary Design Optimization.” In *AIAA Science and Technology Forum and Exposition, AIAA SciTech Forum 2022*. https://doi.org/10.2514/6.2022-1289.

Marimon Giovannetti, L., J Banks, S. W. Boyd, and S. R. Turnock. 2015. “Fluid Structure Interaction in High Performance Catamaran C-Foils under Load.” In *5th High Performance Yacht Design Conference, HPYD 2015*, 171–79.

MOST WIEDZY Downloaded from mostwiedzy.pl

Marimon Giovannetti, Laura, Joseph Banks, Stephen W. Boyd, and Stephen R. Turnock. 2016. “Developing Tools for Assessing the Fluid Structure Interaction of Passive Adaptive Composite Foils.” In *Insights and Innovations in Structural Engineering, Mechanics and Computation - Proceedings of the 6th International Conference on Structural Engineering, Mechanics and Computation, SEMC 2016*, 586–91. https://doi.org/10.1201/9781315641645-97.

Marimon Giovannetti, L., J. Banks, M. Ledri, S. R. Turnock, and S. W. Boyd. 2018. “Toward the Development of a Hydrofoil Tailored to Passively Reduce Its Lift Response to Fluid Load.” *Ocean Engineering* 167 (November): 1–10. https://doi.org/10.1016/j.oceaneng.2018.08.018.

Marimon Giovannetti, L, J. Banks, S. R. Turnock, and S. W. Boyd. 2017a. “Uncertainty Assessment of Coupled Digital Image Correlation and Particle Image Velocimetry for Fluid-Structure Interaction Wind Tunnel Experiments.” *Journal of Fluids and Structures* 68: 125–40. https://doi.org/10.1016/j.jfluidstructs.2016.09.002.

Marimon-Giovannetti, Laura, J. Banks, M. Ledri, S. W. Boyd, and S. R. Turnock. 2017b. “Fluid Structure Interaction Design Development of Passive Adaptive Composite International Moth Foil.” *Fourth International Conference on Innovation in High Performance Sailing Yachts (INNOV'SAIL)*, no. Dic: 31–40.

Marimon Giovannetti, Laura. 2017c. “Fluid Structure Interaction Testing, Modelling and Development of Passive Adaptive Composite Foils.” PhD thesis, University of Southampton.

Matusiak, Jerzy. 2022. Kul - 24.1 17 Laivahydrodynamiikan jatkokurssi, Aalto Univeristy.

Matthies, Hermann G., Rainer Niekamp, and Jan Steindorf. 2006. “Algorithms for Strong Coupling Procedures.” *Computer Methods in Applied Mechanics and Engineering* 195 (17–18). https://doi.org/10.1016/j.cma.2004.11.032.

Maung, Phyo Thu, B. Gangadhara Prusty, Ginu Rajan, Enbang Li, Andrew W. Phillips, and Nigel A. St John. 2017. “Distributed Strain Measurement Using Fibre Optics in a High Performance Composite Hydrofoil.” *ICCM International Conferences on Composite Materials* 2017-August.

Maung, Phyo Thu, B. Gangadhara Prusty, Md Shamsuddoha, Andrew W. Phillips, and Nigel A. St John. 2021. “Static and Dynamic Response of a Carbon Composite Full-Scale Hydrofoil Manufactured Using Automated Fibre Placement.” *Composites Part C: Open Access* 6: 100218. https://doi.org/10.1016/j.jcomc.2021.100218.

Maute, K., and M. Allen. 2004. “Conceptual Design of Aeroelastic Structures by Topology Optimization.” *Structural and Multidisciplinary Optimization* 27 (1–2). https://doi.org/10.1007/s00158-003-0362-z.

Menter, F. R. 1994. “Two-Equation Eddy-Viscosity Turbulence Models for Engineering Applications.” *AIAA Journal* 32 (8). https://doi.org/10.2514/3.12149.

Menter, F. R., and M. Kuntz. 2004. “Adaptation of Eddy-Viscosity Turbulence Models to Unsteady Separated Flow Behind Vehicles.” In . https://doi.org/10.1007/978-3-540-44419-0_30.

MOST WIEDZY Downloaded from mostwiedzy.pl

Mustafa, Ghulam, Afzal Suleman, and Curran Crawford. 2015. “Probabilistic Micromechanical Analysis of Composite Material Stiffness Properties for a Wind Turbine Blade.” *Composite Structures* 131. https://doi.org/10.1016/j.compstruct.2015.06.070.

Müzel, Sarah David, Eduardo Pires Bonhin, Nara Miranda Guimarães, and Erick Siqueira Guidi. 2020. “Application of the Finite Element Method in the Analysis of Composite Materials: A Review.” *Polymers*. https://doi.org/10.3390/POLYM12040818.

Navagally, Rahul Reddy. 2017. “Composite Materials - History, Types, Fabrication Techniques, Advantages, and Applications.” *International Journal of Mechanical And Production Engineering* 5 (9).

Ng, Bing Feng, Rafael Palacios, Eric C. Kerrigan, J. Michael R. Graham, and Henrik Hesse. 2016. “Aerodynamic Load Control in Horizontal Axis Wind Turbines with Combined Aeroelastic Tailoring and Trailing-Edge Flaps.” *Wind Energy* 19 (2): 243–63. https://doi.org/10.1002/we.1830.

Nicholls-Lee, R. F., S. R. Turnock, and S. W. Boyd. 2013. “Application of Bend-Twist Coupled Blades for Horizontal Axis Tidal Turbines.” *Renewable Energy* 50. https://doi.org/10.1016/j.renene.2012.06.043.

Otero, F., S. Oller, X. Martinez, and O. Salomón. 2015. “Numerical Homogenization for Composite Materials Analysis. Comparison with Other Micro Mechanical Formulations.” *Composite Structures* 122. https://doi.org/10.1016/j.compstruct.2014.11.041.

Patel, M. H. 1988. *Dynamics of Offshore Structures.* https://doi.org/10.1016/0141-0296(85)90054-9.

Pernod, Laetitia, Antoine Ducoin, Hervé Le Sourne, Jacques André Astolfi, and Pascal Casari. 2019. “Experimental and Numerical Investigation of the Fluid-Structure Interaction on a Flexible Composite Hydrofoil under Viscous Flows.” *Ocean Engineering* 194. https://doi.org/10.1016/j.oceaneng.2019.106647.

Ponte, R., L. Sutherland, and Y. Garbatov. 2022. “Structural Analysis of a ‘Foiling Moth’ Sailing Dinghy Hydrofoil.” In *Trends in Maritime Technology and Engineering Volume 1*, 185–91. CRC Press. https://doi.org/10.1201/9781003320272-21.

Rahmani, Hossein, S. Heydar Mahmoudi Najafi, and Alireza Ashori. 2014. “Mechanical Performance of Epoxy/Carbon Fiber Laminated Composites.” *Journal of Reinforced Plastics and Composites*. https://doi.org/10.1177/0731684413518255.

Rajpal, D., C. Kassapoglou, and R. De Breuker. 2019. “Aeroelastic Optimization of Composite Wings Including Fatigue Loading Requirements.” *Composite Structures* 227. https://doi.org/10.1016/j.compstruct.2019.111248.

Rahul, B., J. Dharani, and R. Balaji. 2021. “Optimal Method for Determination of Rayleigh Damping Coefficients for Different Materials Using Modal Analysis.” *International Journal of Vehicle Structures and Systems* 13 (1). https://doi.org/10.4273/ijvss.13.1.20.

Rakowski, Gustaw, and Zbigniew Kacprzyk. 2016. *Metoda Elementów Skończonych w Mechanice Konstrukcji*. III. Warszawa: Oficyna Wydawnicza Politechniki Warszawskiej.

Reichel, Maciej. 2019. „Equivalent standard manoeuvres for pod-driven ships”. Ocean

MOST WIEDZY Downloaded from mostwiedzy.pl

Engineering 187 (2019) 106165

Sacher, Matthieu, Mathieu Durand, Élisa Berrini, Frédéric Hauville, Régis Duvigneau, Olivier Le Maître, and Jacques André Astolfi. 2018. “Flexible Hydrofoil Optimization for the 35th America’s Cup with Constrained EGO Method.” *Ocean Engineering* 157: 62–72. https://doi.org/10.1016/j.oceaneng.2018.03.047.

Sacher, Matthieu, Jean Baptiste Leroux, Alain Nême, and Christian Jochum. 2020. “A Fast and Robust Approach to Compute Nonlinear Fluid-Structure Interactions on Yacht Sails – Application to a Semi-Rigid Composite Mainsail.” *Ocean Engineering* 201 (October). https://doi.org/10.1016/j.oceaneng.2020.107139.

Sailing Energy. “Windsurfing in the Olympics: Who Is Representing Team GB At Rio 2016 & Who to Watch Out For.” https://mpora.com/windsurfing-kitesurfing/windsurfing-olympics-team-gb-rio-2016/. *Access 15.05.2022.*

Siemens PLM Software. 2017. “User Guide Star CCM+ V12.04.”

Sinou, J. J. 2022. “Flutter Instability and Active Aeroelastic Control with Time Delay for a Two-Dimensional Airfoil.” *European Journal of Mechanics, A/Solids* 92. https://doi.org/10.1016/j.euromechsol.2021.104465.

Speziale, Charles G., Sutanu Sarkar, and Thomas B. Gatski. 1991. “Modelling the Pressure-Strain Correlation of Turbulence: An Invariant Dynamical Systems Approach.” *Journal of Fluid Mechanics* 227. https://doi.org/10.1017/S0022112091000101.

Stasiak, Janusz. 2005. “Nurzania pionowego cylindra kołowego - Eksperymentalne wyznaczanie charakterystyki amplitudowej nurzań”. In Polish. Ćwiczenie Laboratoryjne, Wydział Oceanotechniki i Okrętownictwa. Politechnika Gdańska.

Stier, Bertram, Jaan Willem Simon, and Stefanie Reese. 2015. “Numerical and Experimental Investigation of the Structural Behaviour of a Carbon Fiber Reinforced Ankle-Foot Orthosis.” *Medical Engineering and Physics* 37 (5). https://doi.org/10.1016/j.medengphy.2015.02.002.

Sun, Zeyu, Jie Xiao, Lei Tao, Yuanping Wei, Shijie Wang, Hui Zhang, Shu Zhu, and Muhuo Yu. 2018. “Preparation of High-Performance Carbon Fiber-Reinforced Epoxy Composites by Compression Resin Transfer Molding.” *Materials*. https://doi.org/10.3390/ma12010013.

Sutherland, L., and P.A. Wilson. 1994. “Fin Hydrodynamics of a Windsurfer.” *Transactions on the Built Environment* 5.

Sutherland, L.S., M. Cardoso de Brito, J. Chaves Pereira, M.R. Arruda, and S. Benson. 2022. “Fluid-Structure Interaction Analyses of a Composite Windsurf Fin.” In *Trends in Maritime Technology and Engineering Volume 1*, 223–31. CRC Press. https://doi.org/10.1201/9781003320272-25.

Szymczak, C., Mikulski, T. 2004. “Zastosowanie Analizy Wrażliwości Do Identyfikacji Parametrycznej Konstrukcji.” In Polish. *Konferencja Naukowa Komitetu Inżynierii Lądowej i Wodnej PAN i Komitetu Nauki PZITB – Krynica 2004*.

Taketani, Tadashi, Koyu Kimura, Satoko Ando, and Koutaku Yamamoto. 2013. “Study on Performance of a Ship Propeller Using a Composite Material.” In *Third International Symposium on Marine Propulsors*.

MOST WIEDZY Downloaded from mostwiedzy.pl

Tan, W., F. Naya, L. Yang, T. Chang, B. G. Falzon, L. Zhan, J. M. Molina-Aldareguía, C. González, and J. Llorca. 2018. “The Role of Interfacial Properties on the Intralaminar and Interlaminar Damage Behaviour of Unidirectional Composite Laminates: Experimental Characterization and Multiscale Modelling.” *Composites Part B: Engineering* 138. https://doi.org/10.1016/j.compositesb.2017.11.043.

Temtching Temou, Vanilla, Benoit Augier, and Benoit Paillard. 2021. “Hydro-Elastic Response of Composite Hydrofoil with FSI.” *Ocean Engineering* 221 (February). https://doi.org/10.1016/j.oceaneng.2020.108230.

Temtching Temou, Vanilla, Odran Fagherazzi, Benoit Augier, Jacques André Andr, Jacques André Astolfi, and David Raison. 2018. “AN EXPERIMENTAL AND NUMERICAL STUDY OF FSI APPLIED TO SAIL YACHT FLEXIBLE HYDROFOIL WITH LARGE DEFORMATIONS.” In *Proceedings of 9th International Symposium on Fluid-Structure Interactions, Flow-Sound Interactions, Flow-Induced Vibration & Noise July 8-11, 2018, Toronto, Ontario, Canada*.

Tezduyar, Tayfun E., Sunil Sathe, Ryan Keedy, and Keith Stein. 2006. “Space-Time Finite Element Techniques for Computation of Fluid-Structure Interactions.” *Computer Methods in Applied Mechanics and Engineering* 195 (17–18). https://doi.org/10.1016/j.cma.2004.09.014.

Toledo, Mario W.E., Liz G. Nallim, and Bibiana M. Luccioni. 2008. “A Micro-Macromechanical Approach for Composite Laminates.” *Mechanics of Materials* 40 (11). https://doi.org/10.1016/j.mechmat.2008.05.004.

Visonneau, M., E. Guilmineau, and G. Rubino. 2018. “Computational Analysis of the Flow around a Surface Combatant at 10◦ Static Drift and Dynamic Sway Conditions.” *32nd Symposium on Naval Hydrodynamics*, no. August.

Volpi, S., M. Diez, D. Kim, F. Stern, and J. L. Grenestedt. 2016a. “Full-Scale Fluid-Structure Interaction Simulation and Experimental Validation of High-Speed Planing-Hull Slamming with Composite Panels,” no. September: 11–16. In *31st Symposium on Naval Hydrodynamics*. Monterey.

Volpi Silvia, Matteo Diez, Hamid Sadat-Hosseini, and Kim Dong-Hwan. 2016b. “Full-Scale Fluid-Structure Interaction Simulation and Experimental Validation of High-Speed Planing-Hull Slamming with Composite Panels Multifidelity Metamodels and Adaptive Grid Refinement for Shape Optimistion View Project ONR-NICOP View Project.” https://www.researchgate.net/publication/308889815.

Volpi Silvia, Matteo Diez, and Frederick Stern. 2017. “Towards the High-Fidelity Multidisciplinary Design Optimization of a 3D Composite Material Hydrofoil.” *7th International Conference on Computational Methods in Marine Engineering, MARINE 2017* 2017-May (May): 119–30.

Xu, Jinyang, Ali Mkaddem, and Mohamed El Mansori. 2016. “Recent Advances in Drilling Hybrid FRP/Ti Composite: A State-of-the-Art Review.” *Composite Structures*. https://doi.org/10.1016/j.compstruct.2015.09.028.

MOST WIEDZY Downloaded from mostwiedzy.pl

Yao, Zhifeng, Fujun Wang, Matthieu Dreyer, and Mohamed Farhat. 2014. “Effect of Trailing Edge Shape on Hydrodynamic Damping for a Hydrofoil.” *Journal of Fluids and Structures* 51: 189–98. https://doi.org/10.1016/j.jfluidstructs.2014.09.003.

Young, Yin Lu, Nitin Garg, Paul A. Brandner, Bryce W. Pearce, Daniel Butler, David Clarke, and Andrew W. Phillips. 2018a. “Load-Dependent Bend-Twist Coupling Effects on the Steady-State Hydroelastic Response of Composite Hydrofoils.” *Composite Structures* 189 (April): 398–418. https://doi.org/10.1016/j.compstruct.2017.09.112.

Young, Yin Lu, Casey Harwood, and Jacob Ward. 2018. “Sensing and Control of Flexible Hydrodynamic Lifting Bodies in Multiphase Flows.” In *Sensors and Smart Structures Technologies for Civil, Mechanical, and Aerospace Systems*, 59. https://doi.org/10.1117/12.2303821.

Young, Yin Lu, Hyunse Yoon, Tristan Wright, Casey M. Harwood. 2018. “The Effect of Waves and Ventilation on the Dynamic Response of a Surface-Piercing Hydrofoil.” *The 32nd Symposium on Naval Hydrodynamics*, no. August: 5–10.

Zarruk, Gustavo A., Paul A. Brandner, Bryce W. Pearce, and Andrew W. Phillips. 2014a. “Experimental Study of the Steady Fluid-Structure Interaction of Flexible Hydrofoils.” *Journal of Fluids and Structures*. https://doi.org/10.1016/j.jfluidstructs.2014.09.009.

Zienkiewicz, Olek, Robert Taylor, and J. Z. Zhu. 2013. *The Finite Element Method: Its Basis and Fundamentals: Seventh Edition*. *The Finite Element Method: Its Basis and Fundamentals: Seventh Edition*. https://doi.org/10.1016/C2009-0-24909-9.

Zhang, Kaomin, Yizhuo Gu, Min li, and Zuoguang Zhang. 2014. “Effect of Rapid Curing Process on the Properties of Carbon Fiber/Epoxy Composite Fabricated Using Vacuum Assisted Resin Infusion Molding.” *Materials and Design*. https://doi.org/10.1016/j.matdes.2013.08.065.

MOST WIEDZY Downloaded from mostwiedzy.pl

APPENDIX I – SUPPLEMENTARY RESULTS OF THE FREE VIBRATIONS EXPERIMENT IN AIR AND WATER

Apart from the study presented in the main part of the thesis some fins were tested to compare the values of the eigenfrequencies and rate of free vibrations decay. Five fins were compared; however, these are different that those presented in the main body of the dissertation. For differentiation they will be numbered FIN-I to FIN-V. The time history of accelerations along the Z-axis and angular velocities around the Y-axis were processed using Fast Fourier Transform to transit from the time to frequency domain. It allowed the assessment of the eigenfrequencies of each fin. Additionally, the damping coefficients for all four modes were evaluated.

The results of the FFT analysis from two sensors located at the leading and trailing edge are presented in figures from Figure AI-1 to Figure AI-5. On the right-hand side is the record from the sensor placed at the leading edge. On the left-hand side are placed the records from the sensors positioned at the trailing edge. Figure AI.1 presents the FFT for FIN-I. The left axis corresponds to the spectral power density of the angular velocity about Y axis (in this convention along the fin span) and right axis to the spectral power density of the accelerations along the Z axis (corresponding to bending motion).

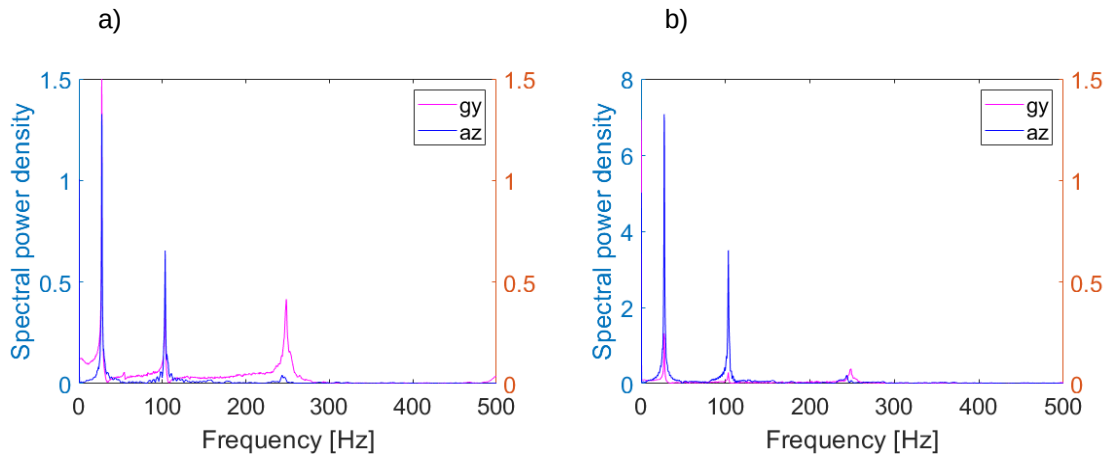

Figure AI.1 The magnitude of Spectral Power Density – FIN-I a) sensor on the leading edge b) sensor on the trailing edge.

Figure AI.2 presents the FFT for FIN-II. The left axis corresponds to the spectral power density of the angular velocity about Y axis and right axis to the spectral power density of the accelerations along the Z axis.

MOST WIEDZY Downloaded from mostwiedzy.pl

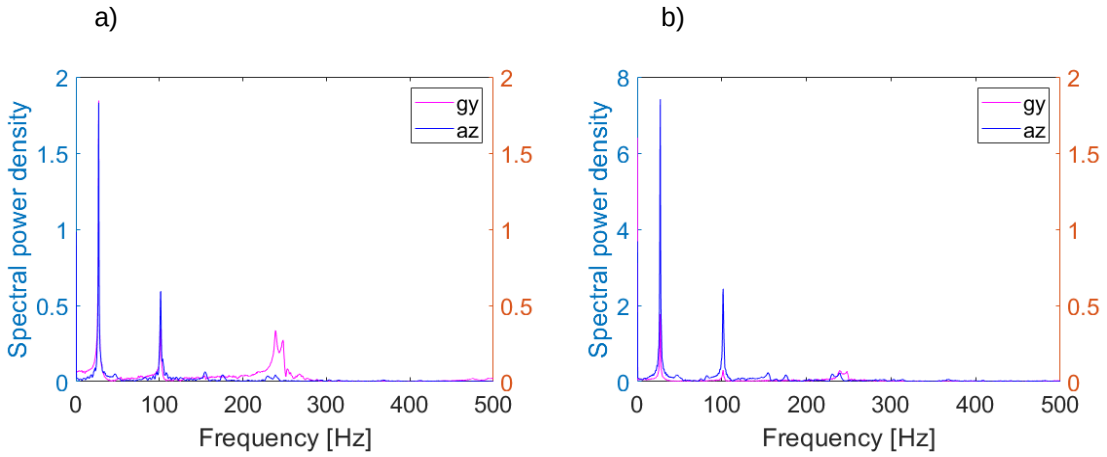

Figure AI.2 The magnitude of Spectral Power Density – FIN-II a) sensor on the leading edge b) sensor on the trailing edge.

Figure AI.3 presents the FFT for FIN-III. The left axis corresponds to the spectral power density of the angular velocity about Y axis and right axis to the spectral power density of the accelerations along the Z axis.

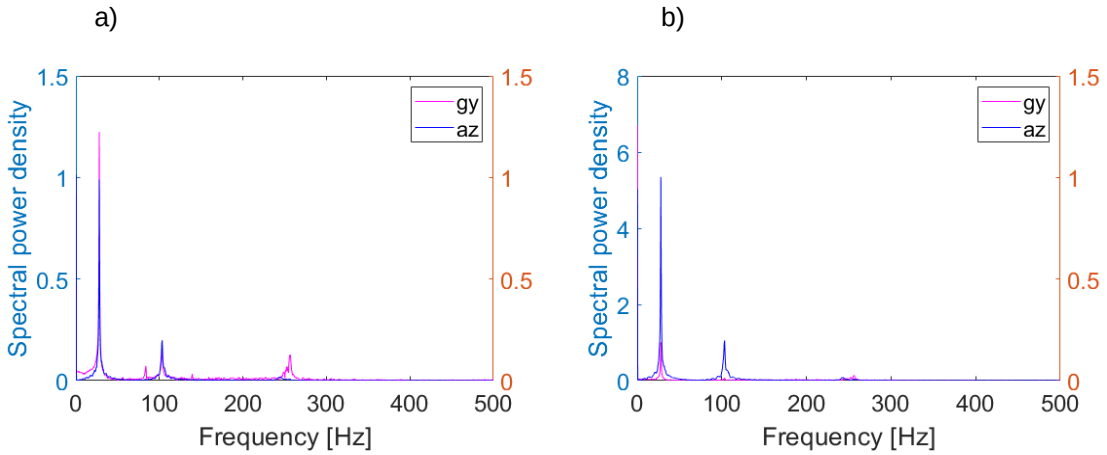

Figure AI.3 The magnitude of Spectral Power Density – FIN-III a) sensor on the leading edge b) sensor on the trailing edge.

Figure AI.4 presents the FFT for FIN-IV. The left axis corresponds to the spectral power density of the angular velocity about Y axis and right axis to the spectral power density of the accelerations along the Z axis.

MOST WIEDZY Downloaded from mostwiedzy.pl

a) b)

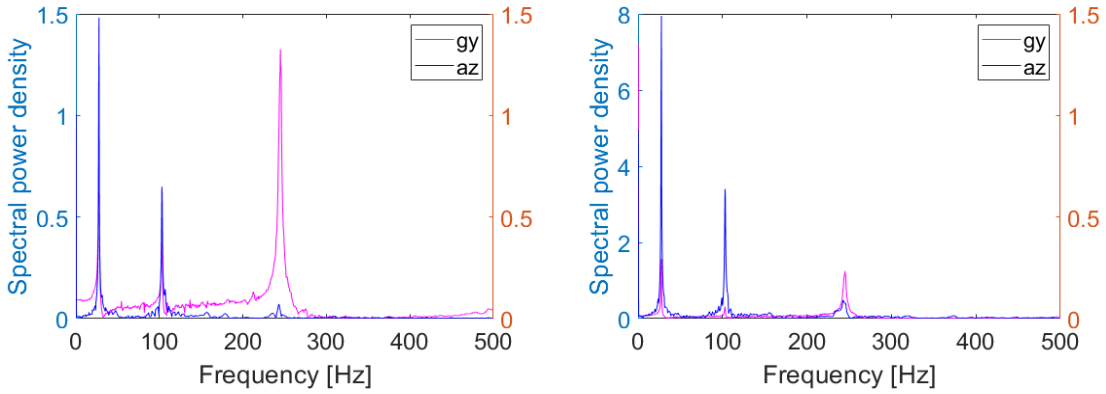

Figure AI.4 The magnitude of Spectral Power Density – FIN-IV a) sensor on the leading edge b) sensor on the trailing edge.

Figure AI.5 presents the FFT for FIN-V. The left axis corresponds to the spectral power density of the angular velocity about Y axis and right axis to the spectral power density of the accelerations along the Z axis.

a) b)

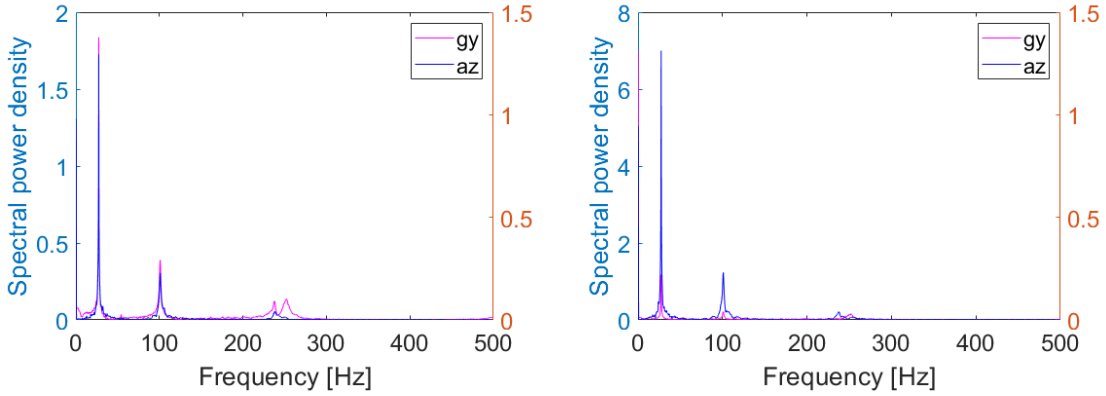

Figure AI.5 The magnitude of Spectral Power Density – FIN-V a) sensor on the leading edge b) sensor on the trailing edge.

The values of the eigenfrequencies for identified eigenmodes are summarized in Table AI.1.

Table AI.1. Measurement of accelerations - comparison of the eigenfrequencies.

Mode	FIN-I	FIN-II	FIN-III	FIN-IV	FIN-V
1	27.33 Hz	27.32 Hz	27.99 Hz	27.66 Hz	27.32 Hz
2	103.3 Hz	101.6 Hz	103.3 Hz	103 Hz	100.6 Hz
3	243.3 Hz	154.3/175.6	242.3 Hz	242.9 Hz	237.6 Hz
4	248.7 Hz	230.6/239.3 Hz	256.6 Hz	244.9 Hz	252.2 Hz
5		238.9/247.9 Hz			

MOST WIEDZY Downloaded from mostwiedzy.pl

Measured time history of accelerations and angular velocities showed significant differences between the fins. In order to quantify them, the damping coefficient B was searched.

Equation AI-1 defines the function for the envelope of the dampened signal:

$$N(t) = -N_0 e^{-B \cdot t} \cdot \cos(T_N \cdot t) \tag{AI.1}$$

Where:

N_0 – The amplitude of acceleration (angular velocity) at t = 0

T_N – Period of dampened oscillations [s]

t – time [s]

B – damping coefficient

The period of oscillations T_N was evaluated from the Fast Fourier Transform analysis, initial amplitude N_0 was known from the time history analysis, and values of damping coefficient were modified to find a good fit with the measured signal time history. For smoothing the data, the running mean of nine samples was calculated and presented. The damping coefficient was evaluated for the running mean of the signal of the accelerations time history. The results of the damping coefficient evaluation are presented in figures from Figure AI.0.6 to Figure AI.10. Figure AII.6 presents the results for the FIN-I.

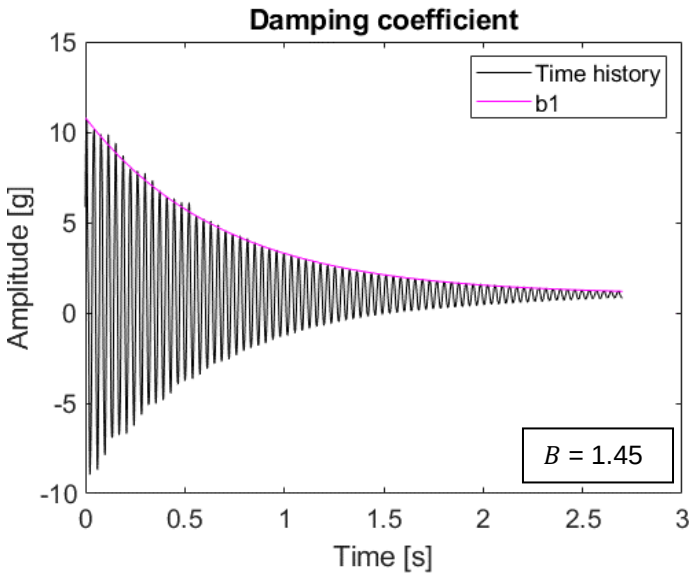

Figure AI.6 The time history of the accelerations and envelope based on the damping coefficient B for FIN-I.

Figure AI.7 presents the results for the FIN-II.

MOST WIEDZY Downloaded from mostwiedzy.pl

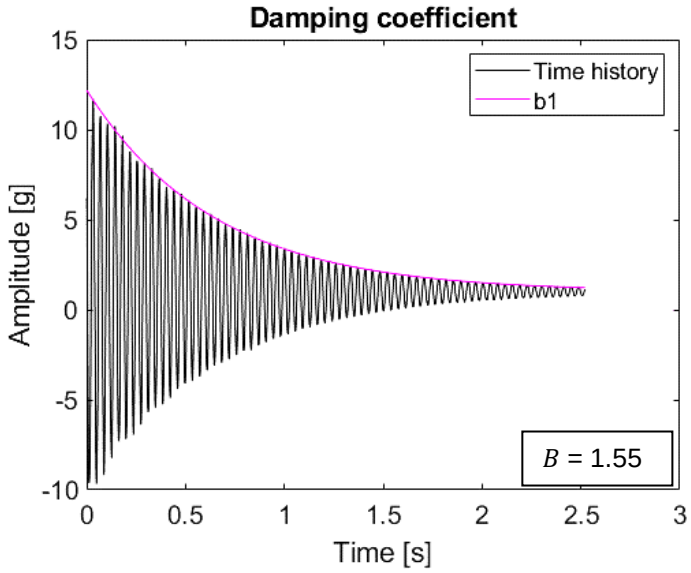

Figure AI.7 The time history of the accelerations and envelope based on the damping coefficient B for FIN-II.

Figure AI.8 presents the results for the FIN-III. It can be noticed that for FIN-III one damping coefficient for the entire time history of the accelerations cannot be fitted, which means that it is variable in time.

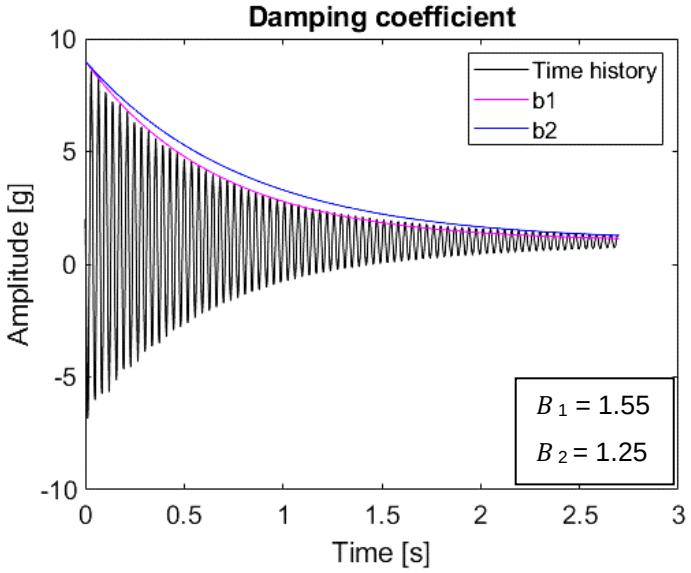

Figure AI.8 The time history of the accelerations and envelope based on the damping coefficient B for FIN-III.

Figure AI.9 presents the results for the FIN-IV.

MOST WIEDZY Downloaded from mostwiedzy.pl

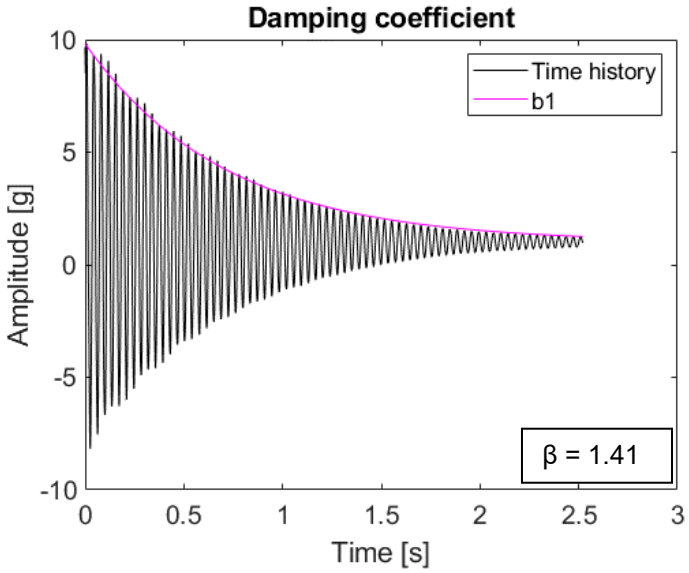

Figure AI.9 The time history of the accelerations and envelope based on the damping coefficient β for FIN-IV.

Finally, Figure AI.10 presents the time history of the accelerations for FIN-V. It can be very clearly visible that the rate of the free vibrations decay is slower than for the remaining four fins.

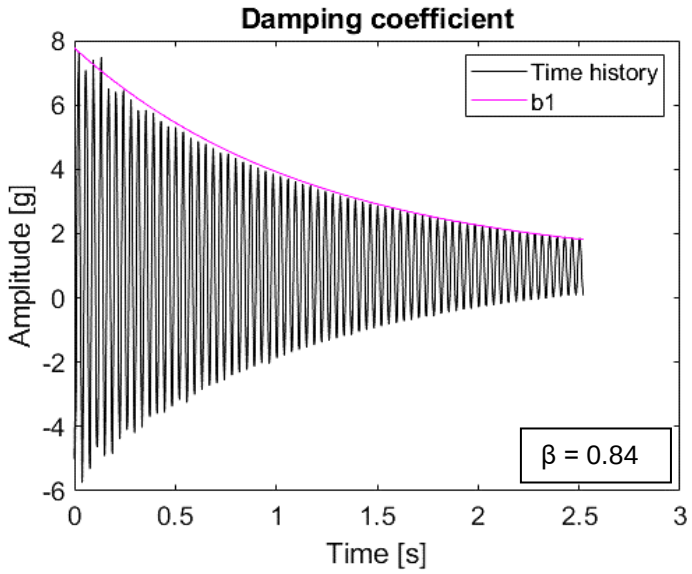

Figure AI.10 The time history of the accelerations and envelope based on the damping coefficient β for FIN-V.

The results presented so far refers to the experiments conducted in air. Following figures will refer to the experiments conducted in water for FIN4. The time history of the accelerations and FFT of the accelerations along the Z-axis are presented for various types of vibration excitation: by hitting with the rubber hummer and pulling the tip of the fin with the soft rope then releasing. Figure AI.11 to Figure AI.13 presents the results of the three trials of the excitation with the hummer. The obtained signal is quite noisy with more peak frequencies that can be observed with the soft rope excitation – Figure AI.14.

MOST WIEDZY Downloaded from mostwiedzy.pl

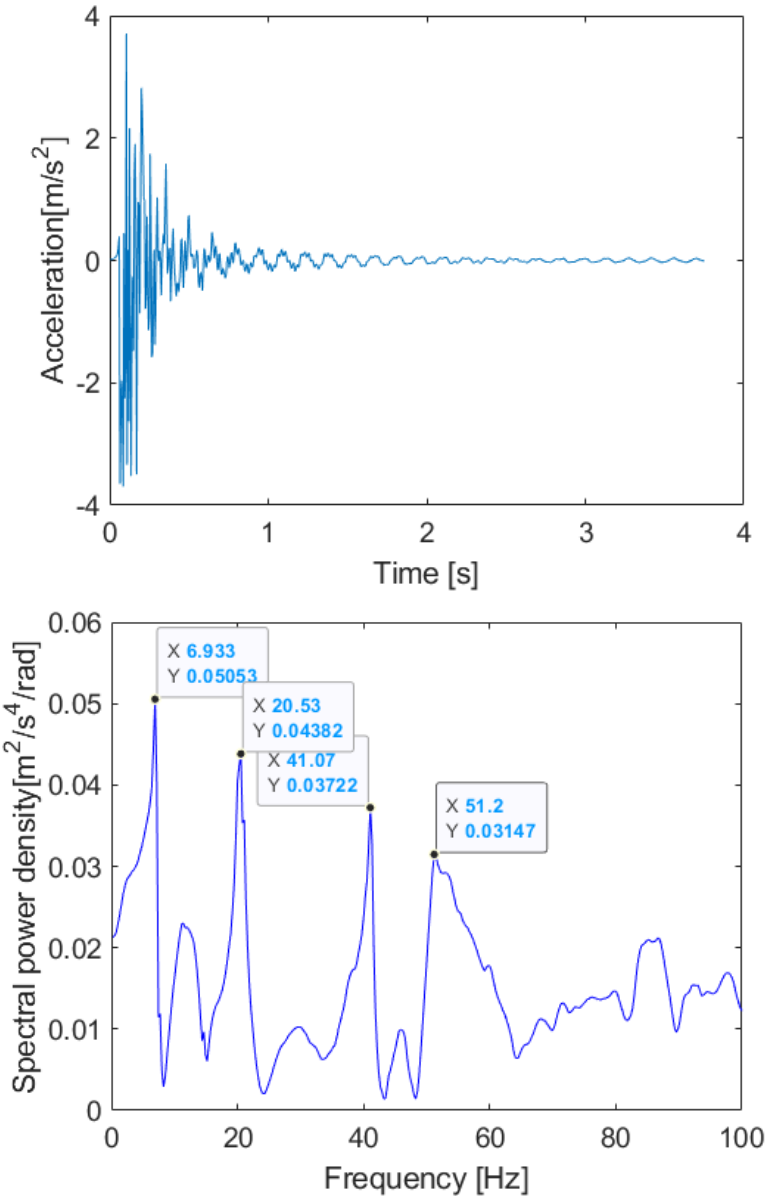

Figure AI.11 Time history of the accelerations along Z axis (top) and FFT of the signal (bottom)- excitation with the hummer – trial 1.

MOST WIEDZY Downloaded from mostwiedzy.pl

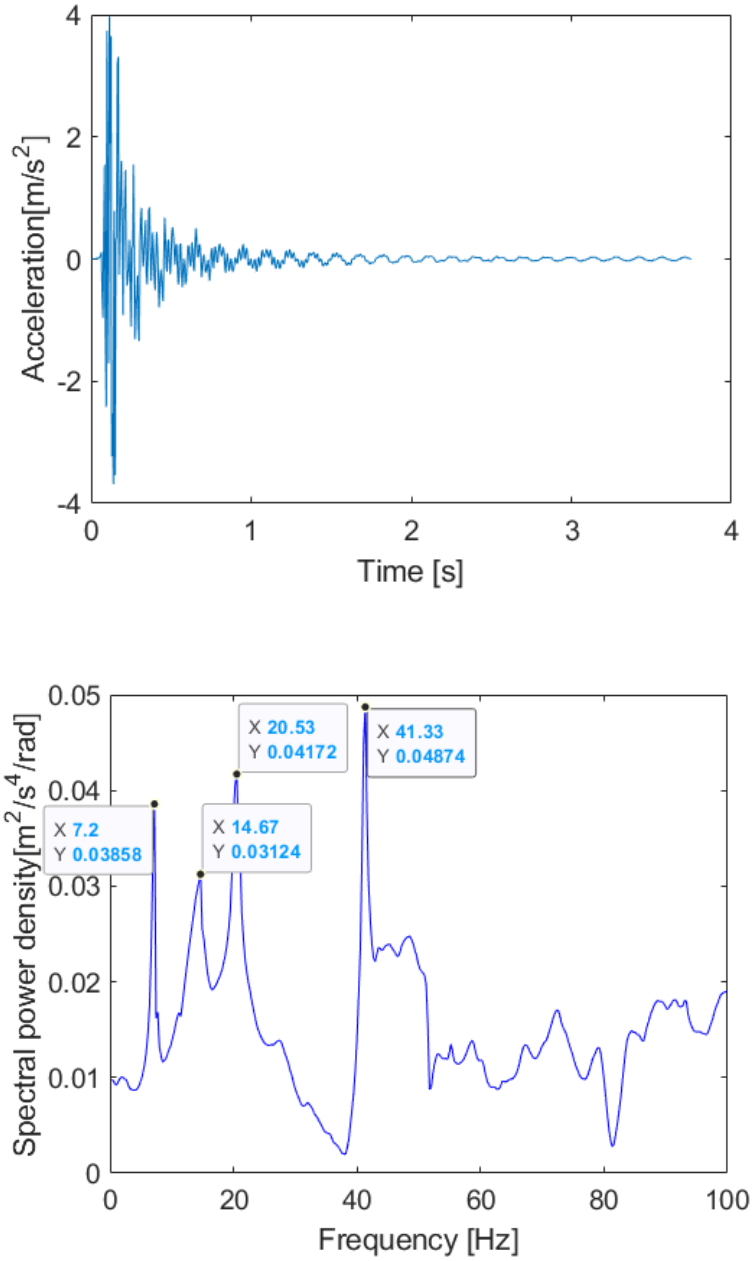

Figure AI.12 Time history of the accelerations along Z axis (top) and FFT of the signal (bottom)- excitation with the hummer – trial 2.

MOST WIEDZY Downloaded from mostwiedzy.pl

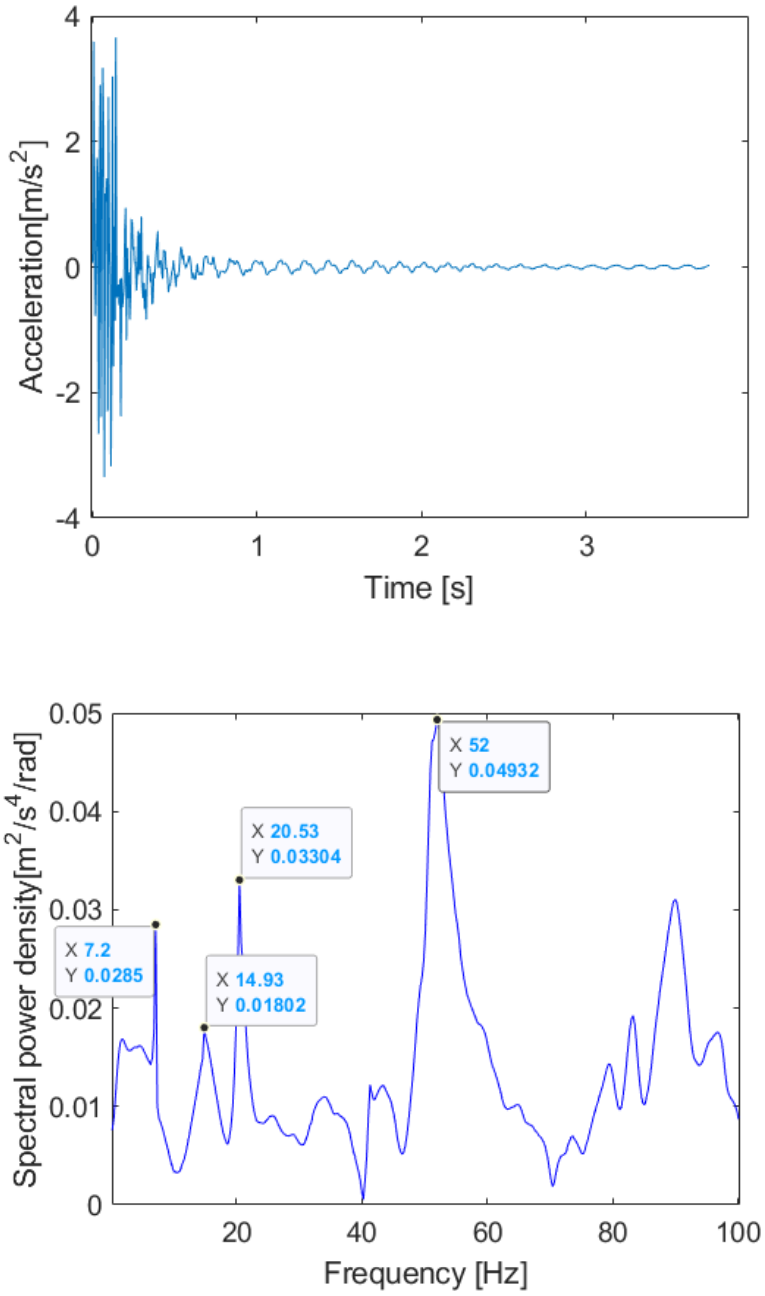

Figure AI.13 Time history of the accelerations along Z axis (top) and FFT of the signal (bottom)- excitation with the hummer – trial 3.

It can be noticed that it is very difficult to indicate the modes in the water, especially that some frequencies are dominant in one attempt and not so much pronounced in another trial. Moreover, the variations between the values of the Eigenmodes is more significant than observed in air.

Compared to Figures AI.11, AI.12 and AI.13 the time history of accelerations in Figure AI.15 are less noisy, and therefore, less frequencies are dominant. This method, but another trial was used for the results presented in the main body of the thesis.

MOST WIEDZY Downloaded from mostwiedzy.pl

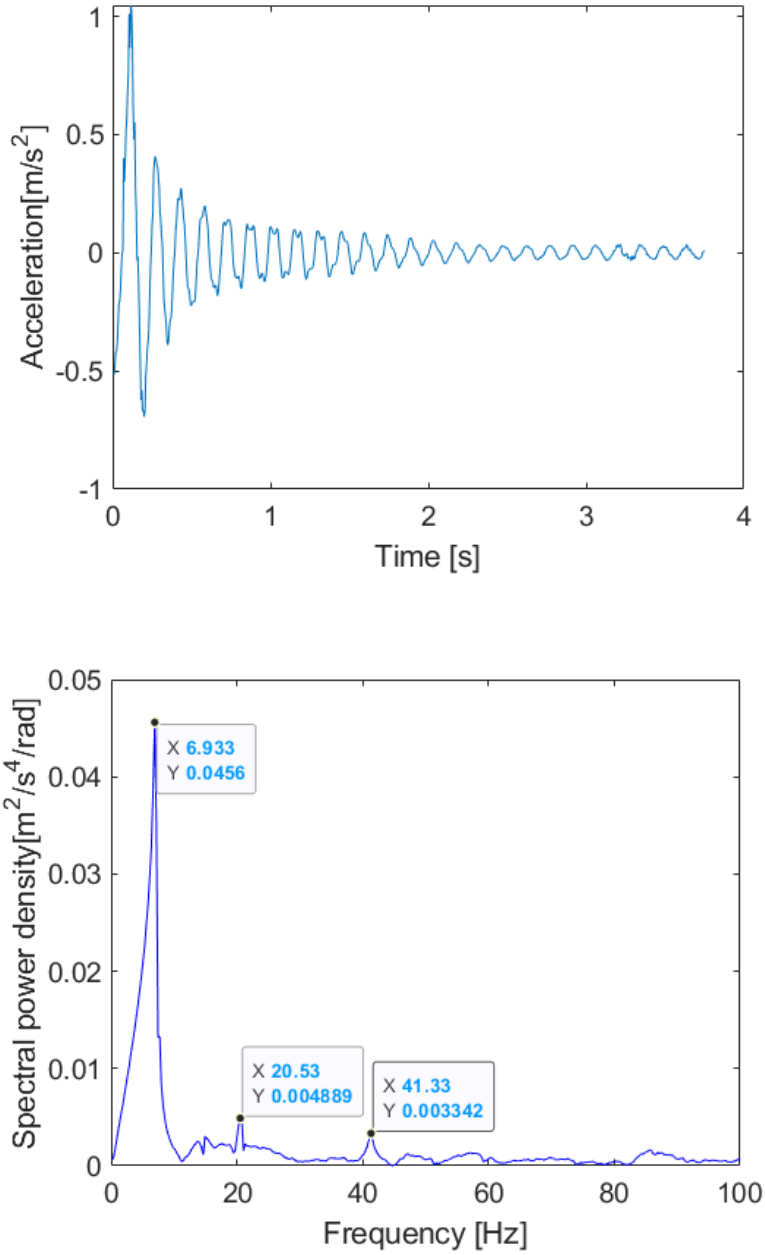

Figure AI.14 Time history of the accelerations along Z axis (top) and FFT of the signal (bottom)- excitation with the soft rope – trial 1

It can be noticed that the results of the acceleration in water are more difficult and less straightforward to interpret. Additionally, I would like to mention, that based on the accelerations only it was not possible to evaluate the added mass of the water together with total damping coefficient and added stiffness of the structure. It was noticed that the coefficients of the Eq. 2.103 are not constant, and it turns into a bit more complicated relation to be directly solved based on the single measurement of the accelerations.

MOST WIEDZY Downloaded from mostwiedzy.pl

LIST OF FIGURES

MOST WIEDZY Downloaded from mostwiedzy.pl

MOST WIEDZY Downloaded from mostwiedzy.pl

MOST WIEDZY Downloaded from mostwiedzy.pl

MOST WIEDZY Downloaded from mostwiedzy.pl

LIST OF TABLES

MOST WIEDZY Downloaded from mostwiedzy.pl